UNIVERSIDADE FEDERAL DO PARÁ
INSTITUTO DE GEOCIÊNCIAS
PROGRAMA DE PÓS-GRADUAÇÃO EM GEOLOGIA E GEOQUÍMICA

TESE DE DOUTORADO Nº 167

EVOLUÇÃO SUPERGÊNICA DO DEPÓSITO CUPRÍFERO ALVO 118 - PROVÍNCIA MINERAL DE CARAJÁS

Tese apresentada por:

PABLLO HENRIQUE COSTA DOS SANTOS
Orientador: Prof. Dr. Marcondes Lima da Costa (UFPA)

BELÉM – PARÁ
2022

Dados Internacionais de Catalogação na Publicação (CIP) de acordo com ISBD
Sistema de Bibliotecas da Universidade Federal do Pará
Gerada automaticamente pelo módulo Ficat, mediante os dados fornecidos pelo autor

S237e Santos, Pabllo Henrique Costa dos.
Evolução supergênica do depósito cuprífero Alvo 118 - Província Mineral de Carajás / Pabllo Henrique Costa dos Santos. — 2022.
xviii, 145 f. : il. color.

Orientador: Prof. Dr. Marcondes Lima da Costa
Tese (Doutorado) - Universidade Federal do Pará, Instituto de Geociências, Programa de Pós-Graduação em Geologia e Geoquímica, Belém, 2022.

1. Mineralogia. 2. Geoquímica. 3. Intemperismo. 4. Cobre. I. Título.

CDD 549

Universidade Federal do Pará

Instituto de Geociências
Programa de Pós-Graduação em Geologia e Geoquímica

EVOLUÇÃO SUPERGÊNICA DO DEPÓSITO CUPRÍFERO ALVO 118 - PROVÍNCIA MINERAL DE CARAJÁS

TESE APRESENTADA POR:

PABLLO HENRIQUE COSTA DOS SANTOS

Como requisito parcial à obtenção de Grau de Doutor em Ciências na Área de GEOQUÍMICA E PETROLOGIA, linha de pesquisa MINERALOGIA E GEOQUÍMICA

Data de Aprovação: 15 / 12 / 2022

Banca Examinadora:

Prof. Marcondes Lima da Costa
Orientador – UFPA

Prof.ª Dr.ª Adriana Maria Coimbra Horbe
Membro – UnB

Prof.ª Dr.ª Edi Mendes Guimarães
Membro – UnB

Prof. Dr. Luiz Carlos Bertolino
Membro – CETEM

Prof. Dr. Rômulo Simões Angélica
Membro – UFPA

Dedico este trabalho à minha mãe, Vera Lúcia da Costa, pela sua dedicação para sempre me proporcionar o melhor.

AGRADECIMENTOS

Ao Prof. Dr. Marcondes Lima da Costa pela orientação e constante esforço em proporcionar a infraestrutura analítica e os recursos financeiros necessários ao desenvolvimento desta pesquisa.

Ao Programa de Pós-graduação em Geologia e Geoquímica pela da infraestrutura laboratorial e recursos financeiros.

Ao Conselho Nacional de Desenvolvimento Científico e Tecnológico pelos recursos financeiros (Grants 305015/2016-8 e 442871/2018-0).

Ao apoio da Vale, que permitiu acesso às áreas de exploração, mina-piloto, testemunhos de sondagem, mapas, sessões e dados analíticos, além de disponibilizar funcionários muito atenciosos para nos receber e orientar, como os geólogos Arthur Cardoso, Wolney Rosa e Bruno Assis.

Ao Dr. Clóvis Maurity, que foi o primeiro a encorajar o desenvolvimento desta pesquisa e não mediu esforços para intermediar a cooperação com a Vale.

Ao empenho daqueles que, mesmo diante das restrições da pandemia Covid-19, conseguiram dar prosseguimento às nossas análises: Prof.ª Drª Desiree Roedink (University of Bergen), Dr. Matthew Locke (Louisiana State University) e Prof.ª Drª Mariella Alzamora (Universidade Federal do Rio de Janeiro).

Ao Prof. Dr. Nilson Ferreira pelos ensinamentos em Espectroscopia Mössbauer e pela atenciosidade com que me recebeu na Universidade Federal de Sergipe.

Ao Prof. Cláudio Nery Lamarão e Cleida Freitas pelos direcionamentos e palavras de incentivo nos momentos de dificuldade.

Aos meus colegas de trabalho, técnicos de laboratórios do Instituto de Geociências, sempre disponíveis para atender meus pedidos: Joelma Lobo Bruno Veras (Oficina de Laminação), Gisele Marques e Ana Paula (Laboratório de Microanálises), Natália Oliveira (Laboratório de Análises Químicas), Everaldo Lira (Laboratório de Sedimentologia).

Aos integrantes do Grupo de Mineralogia e Geoquímica Aplicada (GMGA), em especial Dr.ª Glayce Jholy, pelo companheirismo nas atividades cotidianas do Mugeo e Lamiga.

Aos amigos que acompanharam de perto minha caminhada acadêmica: Lívia Beatriz, Ailton Brito, Priscilla Gozzi, Leonardo Negrão, Quezia Alencar, Aline Silva, Roseane Norat,

Darilena Porfírio, Lynette Bhabha, Fernanda Sobrinho, Socorro Progene, Daiveson Abreu, Bruno Apolo, Suyanne Flávia.

Ao companheirismo da minha esposa, Rayara Silva, que foi minha grande incentivadora em todos os momentos.

Aos meus pais, Vera Costa e José Santos, pelo esforço em me proporcionar uma boa educação e estarem sempre disponíveis para me ajudar no que for preciso.

RESUMO

A Província Mineral de Carajás abriga um dos maiores cinturões cupríferos do mundo, em que as mineralizações hipogênicas sulfetadas foram parcialmente transformados em gossans e estes lateritizados e/ou truncados durante a evolução da paisagem. Estas coberturas representam fonte de informações para a explorção mineral e, em alguns casos, podem ser lavradas juntamente com as mineralizações hipogênicas parentais. Os platôs da Superfície Sul-americana hospedam gossans completos e lateritizados, enquanto as áreas denudadas no entorno, típicas da Superfície Velhas, exibem gossans incompletos ou imaturos, tendo como um exemplar deste último o depósito Alvo 118. Neste corpo, a mineralização hipogênica foi convertida em um gossan imaturo localizado em profundidade, enquanto as rochas hospedeiras foram intemperizados próximo à superfície, formando um saprólito mineralizado. O gossan é formado por uma zona de oxidação, que inclui goethita, malaquita, pseudomalaquita, cuprita, tenorita, cobre nativo, ramsbeckita, crisocola e libethenita; com relictos de uma zona de sulfeto secundário, representada por calcocita. Estes minerais estão distribuídos em zonas de domínio da goethita, malaquita, cuprita e libethenita, com evolução independente, em que suas sucessões minerais refletem a transição das soluções mineralizantes de condições ácidas para levemente alcalinas e aumento no potencial de oxirredução. Este ambiente foi estabelecido a partir da interação das soluções ácidas, derivadas da dissolução da calcopirita, com os minerais de ganga (calcita e apatita) e das rochas hospedeiras, granodioritos e, secundariamente, cloritítos, que atuaram no tamponamento do sistema, favorecendo a formação de novos minerais carreadores do cobre. As fortes correlações do CuO com Ag, Te, Pb, Se, Bi, Au, In, Y, U e Sn na mineralização hipogênica refletem as inclusões de petzita, altaíta, galena, cassiterita e estannita na calcopirita. No gossan, Ag, Te, Pb, Se e Bi permaneceram associados e foram incorporados aos minerais de cobre neoformados. Por outro lado, Au, In, Y, U e Sn exibem maior afinidade com os oxi-hidróxidos de ferro, assim como, Zn, As, Be, Ga, Mo e Ni. Os valores de δ^{65}Cu reforçam que o gossan investigado é imaturo e não foi intensamente afetado por processos de lixiviação. As principais fases minerais identificadas no saprólito são caulinita (dominante), associada com clorita, esmectita e vermiculita, além de quartzo e oxihidróxidos de ferro. No saprólito, os oxi-hidróxidos de ferro apresentam forte correlação com Ga, Sc, Sn, V, Mn, Co e Cr, em parte derivados do intemperismo das rochas parentais. Adicionalmente, dados de espectroscopia Mössbauer apontam importante papel da ferridrita e goethita como incorporadores de cobre no saprólito. Não há evidências da incorporação de sua pelos argilominerais. Os valores de δ^{56}Fe indicam pouca contribuição da mineralização primária para

os conteúdos de Fe do saprólito, que é mais influenciado pelo intemperismo da clorita. A associação Al_2O_3, Hf, Zr, Th, TiO_2, Ce, La, Ba, Sr representa a assinatura geoquímica das rochas hospedeiras, que influenciam a composição química dos três tipos de mineralização. Por outro lado, os principais elementos rastreadores da mineralização hipogênica são a associação In, Y, Te, Pb, Bi, Se. O conhecimento detalhado do fracionamento mineral e geoquímico supergênico torna o depósito Alvo 118 um referencial para a investigação de gossans imaturos e saprólitos mineralizados em áreas denudadas da Província Mineral de Carajás ou em terrenos equivalentes.

Palavras-chave: mineralogia, geoquímica, intemperismo, cobre.

ABSTRACT

The Carajás Mineral Province is home to one of the most extensive cupriferous belts in the world, where hypogene mineralizations were partially transformed into gossans, later lateritized and/or truncated during landscape evolution. These covers represent an information source for mineral exploration and, in some cases, can be mined together with parental hypogene mineralizations. The plateaus of the South American Surface host complete and lateritized gossans, while the surrounding denuded areas, typical of the Velhas Surface, exhibit incomplete or immature gossans, with the Alvo 118 deposit as an example. In this orebody, the hypogene mineralization was converted into an immature gossan located at depth, while the host rocks were weathered near the surface, forming a mineralized saprolite. The gossan comprises an oxidation zone, which includes goethite, malachite, pseudomalachite, cuprite, tenorite, native copper, ramsbeckite, chrysocolla, and libethenite, with relics of a secondary sulfide zone, represented by chalcocite. These minerals are distributed in the goethite, malachite, cuprite, and libethenite zones, with their mineral successions reflecting the transition of mineralizing solutions from acidic to slightly alkaline conditions and an increase in oxidation potential. This environment was established from the interaction of acid solutions, derived from chalcopyrite dissolution, with the gangue minerals (calcite and apatite) and the host rocks, granodiorites and, secondarily, chloritites, which acted in buffering the system, favoring the formation of new copper-bearing minerals. The strong correlations of CuO with Ag, Te, Pb, Se, Bi, Au, In, Y, U, and Sn in the hypogene mineralization reflect the inclusions of petzite, altaite, galena, uraninite, cassiterite, and stannite in chalcopyrite. In the gossan, Ag, Te, Pb, Se, and Bi remained associated and were incorporated into neoformed copper minerals. On the other hand, Au, In, Y, U, and Sn exhibit greater affinity with iron oxyhydroxides, as well as Zn, As, Be, Ga, Mo and Ni. The $\delta^{65}Cu$ values reinforce that the investigated gossan is immature and was not intensely affected by leaching processes. The main mineral phases identified in the saprolite are kaolinite (predominant), associated with chlorite, smectite, vermiculite, quartz, and iron oxyhydroxides. Iron oxyhydroxides are strongly correlated with Ga, Sc, Sn, V, Mn, Co, and Cr, partly derived from the weathering of parent rocks. Additionally, Mössbauer spectroscopy data point to the important role of ferrihydrite and goethite as copper-bearing phases. There is no evidence of copper incorporation by clay minerals. The $\delta^{56}Fe$ values indicate a little contribution of primary mineralization to the Fe content of the saprolite, which is more influenced by chlorite weathering. The association Al_2O_3, Hf, Zr, Th, TiO_2, Ce, La, Ba, and Sr represents the geochemical signature of the host rocks, which influence the chemical

composition of the three types of mineralization. On the other hand, the association In, Y, Te, Pb, Bi, and Se comprise the main pathfinder elements of the hypogene mineralization. Detailed knowledge of the supergene mineral and geochemical fractionation makes the Alvo 118 deposit a reference guide for investigating immature gossans and mineralized saprolites in denuded areas of the Carajás Mineral Province or equivalent terrains.

Keywords: mineralogy, geochemistry, weathering, copper.

LISTA DE ILUSTRAÇÕES

CAPÍTULO 1

CAPÍTULO 4

CAPÚTULO 6

SUMÁRIO

1. INTRODUÇÃO

1.1. APRESENTAÇÃO

A Província Mineral de Carajás (PMC) abriga um dos maiores agrupamentos de depósitos cupríferos do mundo, formados a partir de dois principais eventos hipogênicos desenvolvidos no Neoarqueano e Paleoproterozóico (Grainger *et al*. 2008, Torresi *et al*. 2012). As mineralizações em geral consistem em corpos sulfetados, hospedados por sequencias metavulcanosedimentares intensamente hidrotermalizadas. Dada a elevada reatividade dos sulfetos, muitos desses corpos foram ao menos parcialmente convertidos em gossans (Costa *et al.* 1996).

Os perfis gossânicos da PMC naturalmente foram afetados pelo intemperismo tropical tipicamente desenvolvido na região durante o Cenozóico. Desse modo, muitos desses corpos e suas rochas hospedeiras se encontram lateritizados e, adicionalmente, associados com depósitos coluvionares e perfis de solo (Costa *et al*. 1999, Porto 2016). Nos platôs que constituem a Serra dos Carajás, os regolitos tendem a apresentar esta sucessão completa. Por outro lado, as áreas denudadas no entorno da serra exibem perfis lateríticos trucados, representados por horizontes saprolíticos (Toledo-Groke *et al.* 1985, Ildefonse *et al.* 1986, Mano *et al.* 2020). Consequentemente, os gossans identificados nestas áreas também estão incompletos, sem o capeamento ferruginoso característico.

O depósito de cobre Alvo 118 corresponde a um caso peculiar, em que um gossan imaturo se formou em profundidade a partir da mineralização hipogênica e não foi afetado pela lateritização e erosão. Ele é envolvido e recoberto por rochas ainda bem preservadas, que passaram por um grau incipiente de intemperismo, causado pela interação com as soluções ácidas liberadas a partir da dissolução dos sulfetos primários. Muito acima do gossan, as rochas hospedeiras são então convertidas em um horizonte saprolítico, que se estende até a superfície. Regolitos com esta configuração eram até então pouco documentados na PMC, onde as investigações mais avançadas estavam até então restritas ao depósito Salobo (Toledo-Groke *et al.* 1985, Ildefonse *et al*. 1986, Veiga *et al.* 1991).

Do ponto de vista metalogenático, o gossan do depósito Alvo 118 registra um estágio adicional para a evolução supergênica da PMC, em que se formaram gossans imaturos em profundidade. Em contraste, o horizonte saprolítico que está acima marca a transição para uma zona afetada pelo clima tropical, com forte influência do lençol freático e domínio das reações de hidrólise. Este segundo cenário corresponde a um halo de dispersão que ainda preserva

elevados teores de cobre, cujos mecanismos de retenção representam informações relevantes para a indústria mineral (Veiga *et al.* 1991, Albuquerque *et al.* 2001).

Nesta tese, foram investigados os principais aspectos mineralógicos, micromorfológicos e químicos da porção supergênica do depósito Alvo 118. Serão aqui apresentadas: (1) as condições de formação do gossan imaturo, com implicações metalogenéticas; (2) o fracionamento geoquímico entre mineralização hipogênica, gossan e saprólito, com reflexos exploratórios; (3) os mecanismos de incorporação do cobre pelos minerais derivados do intemperismo das rochas hospedeiras, um aspecto de interesse metalúrgico. Estas linhas de investigação serão respectivamente apresentadas na forma dos seguintes manuscritos:

(1) "Mineralogical and textural evolution of the Alvo 118 copper-bearing gossan: Implications for supergene metallogenesis in Carajás Mineral Province, Brazil", publicado no Journal of South American Earth Sciences (https://doi.org/10.1016/j.jsames.2022.104108);

(2) "Geochemical and isotopic fractionation in the hypogene ore, gossan, and saprolite of the Alvo 118 deposit: Implications for copper exploration in regoliths of the Carajás Mineral Province", submetido ao corpo editorial do Geochemical Journal (ANEXO A);

(3) "The geochemical importance of iron oxyhydroxides and associated minerals for copper enrichment in saprolite from a denuded area in the Carajás Mineral Province", que deverá ser submetido ao International Journal of Earth Sciences.

1.2. JUSTIFICATIVA

Durante séculos, gossans aflorantes ou subaflornates foram minerados em diversas regiões do mundo, principalmente para a obtenção de cobre, chumbo, zinco, níquel, ouro e platinóides (Taylor 2011). Já no início do século XXI, o avanço do conhecimento exploratório demonstrou sua aplicabilidade para a descoberta dos corpos sulfetados subjacentes ou próximos, em geral muito mais volumosos (Taylor 2011, Andreu *et al.* 2015, Yesares *et al.* 2017, Pires *et al.* 2020). Além do potencial exploratório, os gossans foram investigados como registro da evolução supergênica de grandes províncias minerais sulfetadas. Destacam-se neste contexto o Lacan Fold Belt e Golden Grove District, na Austália; Bathust Mining Camp, no Canadá; e Iberian Pirite Belt, na Espanha. Nestas regiões, de clima árido, os gossans são em geral aflorantes (Boyle 1993, Scott *et al.* 2001, Smith e Singh 2007, Velasco *et al.* 2013).

Na PMC, a obliteração dos gossans por processos lateríticos e a densa cobertura vegetal limitaram seu uso como guias exploratórios. Destaca-se neste contexto o depósito de

ouro de Igarapé-Bahia, reconhecido como um gossan lateritizado quando já estava em lavra (Costa *et al.* 1999, Porto 2016, Monteiro *et al.* 2018). Atualmente, na busca por viabilidade econômica, muitas mineradoras têm optado por lavrar pelo menos uma parte dos gossans juntamente com os depósitos sulfetados, que em geral são de maior interesse (Velasco *et al.* 2013).

Assim, as campanhas exploratórias realizadas no depósito Alvo 118 investigaram não apenas a mineralização hipogênica, mas também o gossan e saprólito sobrejacentes. Foram então reconhecidas reservas hipogênicas (sulfetadas) da ordem de 170 Mt a 1,21% de Cu e 3 ppm de Au; e mineralização supergênica de 55 Mt a 0,92% de Cu e 0,3 ppm de Au, dos quais 30% são referentes ao gossan e 70 % ao saprólito. Além da maior tonelagem de minério, a lavra conjunta resultaria na redução das pilhas de estéril.

Os elevados teores de cobre registrados na zona de alteração supergênica do depósito Alvo 118 suscitam questionamentos quanto aos processos de dispersão e mecanismos de fixação destes e outros metais no gossan e saprólito. Estas informações são cruciais para os processos de mineração, incluindo, exploração, lavra, beneficiamento e disposição de estéril e resíduos (Nordstrom 2011, Peterson *et al*. 2014, Stavinga *et al.* 2017). Por outro lado, o depósito Alvo 118 é um representante da história evolutiva dos regolitos distribuídos ao longo da Superfície Velhas/Itacaiúnas na PMC, que ainda são restritamente documentados (Toledo-Groke *et al.* 1985; Ildefonse *et al.* 1986, Silva e Kotschoubey 2000).

1.3. OBJETIVOS

1.3.1. Objetivos gerais

Os objetivos gerais desta tese são (1) estabelecer as condições de formação do gossan desenvolvido no depósito Alvo 118, a fim consolidá-lo como representante de um cenário evolutivo da PMC em que se formaram gossans imaturos em profundidade, não afetados pela lateritização; (2) estabelecer o fracionamento geoquímico e isotópico entre a mineralização hipogênica, gossan e saprólito, buscando estabelecer o caminho de dispersão ou incorporação supergênica do cobre e outros metais; (3) compreender os mecanismos de incorporação do cobre no saprólito, uma vez que ele não apresenta nenhum mineral que seja portador deste elemento como componente principal.

1.3.2. Objetivos específicos

Os objetivos específicos são (1) estabelecer as sucessões mineralógicas no gossan e saprólito, a partir das relações texturais; (2) reconstituir as propriedades físico-químicas do ambiente que favoreceu a desestabilização da mineralização hipogênica para formação do gossan; (3) estabelecer as associações geoquímicas típicas da mineralização primária gossan e saprólito, de modo a determinar os minerais carreadores do cobre e outros metais; (4) acompanhar processos e mecanismos envolvidos na formação do gossan e saprólito, a partir do comportamento de isótopos Cu e Fe; (5) identificar e quantificar os oxi-hidróxidos de ferro no saprólito.

2. REFERENCIAL TEÓRICO

2.1. DEPÓSITOS SULFETADOS E SUA RESPOSTA AO INTEMPERISMO

Quando depósitos minerais hipogênicos e suas rochas hospedeiras, formados sob temperaturas e pressões elevadas, são submetidos às condições superficiais (T_{atm} ~15 °C; P_{atm} ~1 bar; and pO_2 ~0,2 bar), seu equilíbrio é redistribuído, resultando em modificações supergênicas (Reich e Vasconcelos 2015). Este processo ocorre de modo diferenciado entre os corpos sulfetados e as rochas hospedeiras. Os sulfetos são mais reativos e sua decomposição é dominada por processos de oxirredução que resultam na formação dos gossans. Por sua vez, os silicatos formadores das rochas hospedeiras são submetidos a reações de hidrólise, em geral mais dependentes das condições hidrológicas superficiais (Thornber e Taylor 1992, Taylor 2011).

Nos dois contextos descritos acima, podem se desenvolver zonas de enriquecimento ou halos de dispersão supergênica em que elementos como Cu, Al, Fe, Ni, Mn, U, Au e Zn podem ser parcialmente retidos, contribuindo para a viabilidade dos projetos de mineração (Reich e Vasconcelos 2015). Adicionalmente, depósitos supergênicos são de grande importância paleoambiental, registrada ao longo do seu fracionamento mineralógico, geoquímico e isotópico (Mathur e Fantle 2015). Os principais aspectos relacionados à formação e evolução dos gossans e perfis de intemperismo, considerados no desenvolvimento desta tese, serão tratados nos itens a seguir. Ressalta-se que a formação dos gossans é normalmente referida na literatura como um tipo especial de intemperismo, para a o qual se aplica o termo *oxidative weathering*. Por isso, optou-se por trata-lo separadamente do intemperismo das rochas hospedeiras.

2.1.1. Formação de gossans

Os gossans são produtos de reações de oxirredução desenvolvidas a partir de corpos sulfetados principalmente maciços. O modelo mais aceito para sua formação os descreve como uma pilhas galvânicas, em que elétrons fluem através do corpo sólido, migrando de zonas mais reativas do corpo sulfetado, que atuam como anodo, em direção a interfaces extremas, que atuam como catodo. Este processo depende da disponibilidade de oxigênio dissolvido nas águas percolantes, que é então reduzido no catodo, enquanto o sulfeto primário é oxidado no anodo (Thornber e Taylor 1992, Chávez 2021, Taylor 2011).

Um importante fator controlador da natureza e assembléia mineral do gossan é a separação espacial entre as reações que ocorrem no anodo e catodo. Um exemplo clássico é o

depósito de Kambalda (Austrália), onde a reação de oxidação do sulfeto ocorre 100 m ou mais abaixo da zona de redução do oxigênio, que, neste caso, coincide com o limite inferior do lençol freático (Thornber e Taylor 1992). Por outro lado, nas porções em que os grãos de sulfeto estão disseminados, ou seja, isolados um do outro por silicatos, anodo e catodo estarão a alguns micros de distância (Fig. 1).

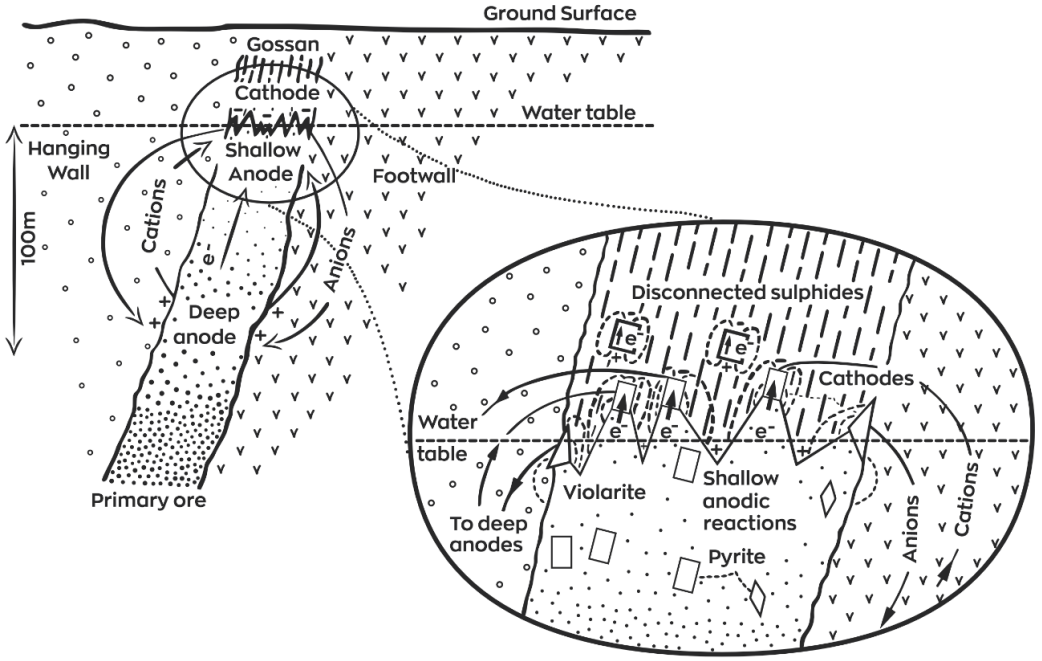

Fig. 1 Seção representativa do posicionamento das reações anódicas profundas e catódicas que ocorrem próximo ao nível freático no depósito de sulfeto maciço niquelífero de Kambalda, Austrália (Thornber e Taylor 1992).

Portanto, a formação dos gossans não depende necessariamente do contato direto com o lençol freático. Assim, eles podem de desenvolver sob condições climáticas variáveis, desde que haja mínima disponibilidade de água, com certo aporte de oxigênio dissolvido (Alpers e Brimhall 1989, Reich *et al*. 2009). Nestes diferentes cenários, as reações de oxirredução envolvidas na desestabilização dos sulfetos hipogênicos tendem a acidificar o ambiente, o que por sua fez acelera a decomposição dos minerais de ganga e constituintes das rochas hospedeiras (Andrew 1984, Thornber e Taylor 1992, Taylor 2011, Chávez 2021). Em contrapartida, a decomposição destes minerais consome H^+, contribuindo para a neutralização do ambiente.

Além disso, são liberados íons ou compostos iônicos capazes de se ligar aos metais provenientes dos sulfetos primários. Isto resulta na formação de um amplo espectro de minerais no perfil gossânico, em que elementos como Cu, Pb, Zn, Ni, Co, Cr, Mn, Au, Ag, e EGP podem ser parcialmente incorporados (Thornber e Taylor 1992, Scott 2001). Assim, a base dos perfis gossânicos é normalmente constituída por sulfetos secundários, formados ainda em ambiente

redutor (Belogub *et al*. 2008, Dill 2015). A zona intermediária pode apresentar um amplo espectro mineral, que inclui sulfatos, carbonatos, fosfatos, silicatos, oxi-hidróxidos e elementos nativos. Esses minerais são formados pela interação das rochas encaixantes com as soluções ácidas produzidas pela decomposição dos sulfetos primários e secundários (Chávez 2000, Reich *et al*. 2009, Vasconcelos *et al*. 2015). Já o topo do gossan classicamente consiste em uma zona de lixiviação, constituída principalmente por oxi-hidróxidos de ferro e manganês (Robb 2005, Haldar 2018).

Os perfis gossânicos podem ser classificados em maturos, quando apresentam o zoneamento mineralógico completo; e imaturos, quando as zonas superiores não se desenvolveram (Scott *et al*. 2001, Atapour e Aftabi 2007). No primeiro caso, a zona de oxi-hidróxido de ferro, ao se formar próxima à superfície, frequentemente exibe a morfologia do tipo chapéu de ferro (Oliveira *et al*. 1991, Taylor 2011). Por ser a expressão superficial do perfil gossânico, muitos autores optam por se referir à zona de oxi-hidróxido de ferro como gossan, embora seja crescente o uso do termo leached capping ou leaching zone para se referir a esta porção do corpo gossânico (Taylor 2011).

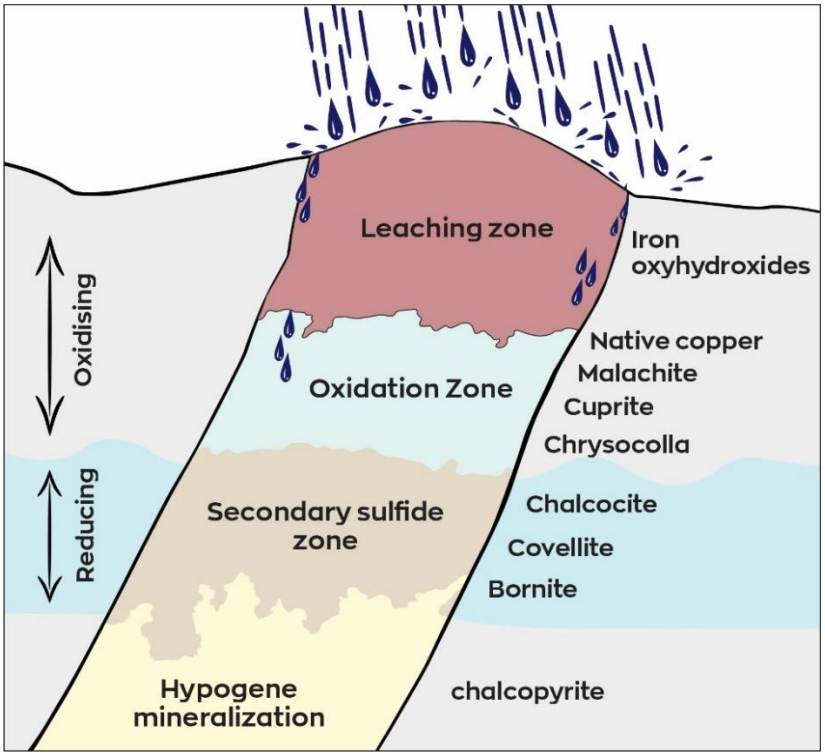

Fig. 2 Zoneamento típico do perfil gossânico, incluindo a mineralização primária e as zonas de enriquecimento supergênico, oxidação e lixiviação, modificado de Asmus (2013).

Seu estudo se tornou importante ferramenta para prospecção deste tipo de depósito, especialmente aqueles mineralizados em Cu, Pb, Zn, Au, Ag e Mo (Taylor 2011). Por isso, em paralelo às campanhas exploratórias, vários trabalhos se dedicaram ao entendimento de sua

origem e mecanismos de formação (Moeskops 1977, Taylor e Appleyard 1983, Taylor 1984, Nickel 1984) ou ao mapeamento da distribuição espacial dos *iron hats*, expressões superficiais da zona oxi-hidróxido de ferro que usualmente capeia o perfil gossânico. Além disso, o próprio corpo gossânico normalmente representa uma zona de enriquecimento supergênico com potencial econômico (Atapour e Aftabi 2007).

As ocorrências mais famosas de gossans estão na Austrália, Lacan Fold Belt (Scott *et al*. 2001) e Golden Grove District (Smith e Sing 2007); no Canadá, Bathurst Mining Camp (Boyle 1993); e ainda na Espanha, Iberian Pyrite Belt (Velasco *et al*. 2013). No Brasil, os corpos mais conhecidos são Igarapé Bahia, no Pará (Costa *et al*. 1996); São Bartolomeu, em Goiás (Oliveira 1991); Canoas, no Paraná; O' Toole, em Minas Gerais (Imbernon 1998); e Irecê, na Bahia (Oliveira *et al*. 1995). Em algumas dessas regiões, muitos gossans foram durante séculos minerados para a obtenção de cobre e outros metais (Hunt *et al*. 2016) e, nas últimas décadas, passaram a ser utilizados como guias prospectivos dos depósitos sulfetados subjacentes.

2.1.2. Intemperismo das rochas hospedeiras

A formação dos perfis de intemperismo é em geral dominada por reações de hidrólise, que ocorrem quando as águas superficiais, levemente ácidas, reagem com os minerais primários. Neste processo, elementos mais solúveis (Ca, Na, K, Mg) e parte da sílica são liberados e lixiviados, causando enriquecimento relativo dos elementos menos solúveis (principalmente Fe e Al), que formam minerais mais estáveis nas condições supergênicas (Dixon *et al*. 2009; Millot *et al*. 2002, Macheyeki *et al*. 2020). Assim, os perfis são em geral compostos por uma mistura de caulinita, hematita, goethita e, as vezes, gibbsita, nos horizontes superiores, com minerais menos estáveis em profundidade, próximo às rochas do embasamento. Este termo vem do inglês *bedrocks*, usado para fazer referência às rochas não intemperizadas subjacentes, que não necessariamente são precursoras do perfil de intemperismo (Lebedeva *et al*. 2007, Butt 2016).

O intemperismo dos silicatos é influenciado pela composição e textura da rocha-mãe, pH e o Eh do ambiente, além de fatores regionais, como o clima, relevo e condições tectônicas. A atuação conjunta destes fatores controla o grau de lixiviação dos minerais primários e a consequente formação dos minerais secundários (Toledo-Groke *et al.* 1985, White e Blum 1995, White Brantley 2003, Price *et al.* 2005). Espessos regolitos representam numerosos desafios, pois podem ser encontrados em diversas condições climáticas, de úmidas a áridas, tropicais a temperadas que obliteram as feições iniciais (Dixon *et al.* 2009). Por outor lado, eles também constituem oportunidades exploratórias, pois as características petrográficas,

mineralógicas e químicas comuns podem ser utilizadas como referencial para o estudo de terrenos equivalentes (Butt 2016).

Em geral os perfis de intemperismo estão melhor preservados em regiões que permaneceram tectonicamente estáveis por períodos prolongados ou quando recobertos por crostas ferruginosas (Butt 2016, Goodfellow *et al*. 2016; Callahan *et al*. 2019). Ainda assim, a geomorfologia dos regolitos é um aspecto dominante na determinação dos padrões de dispersão geoquímica dos depósitos minerais. Assim, a erosão, juntamente como as mudanças ambientais resultam em um mosaico de formas de relevo, que incluem regolitos preservados ou truncados em diversos níveis (Fig. 3).

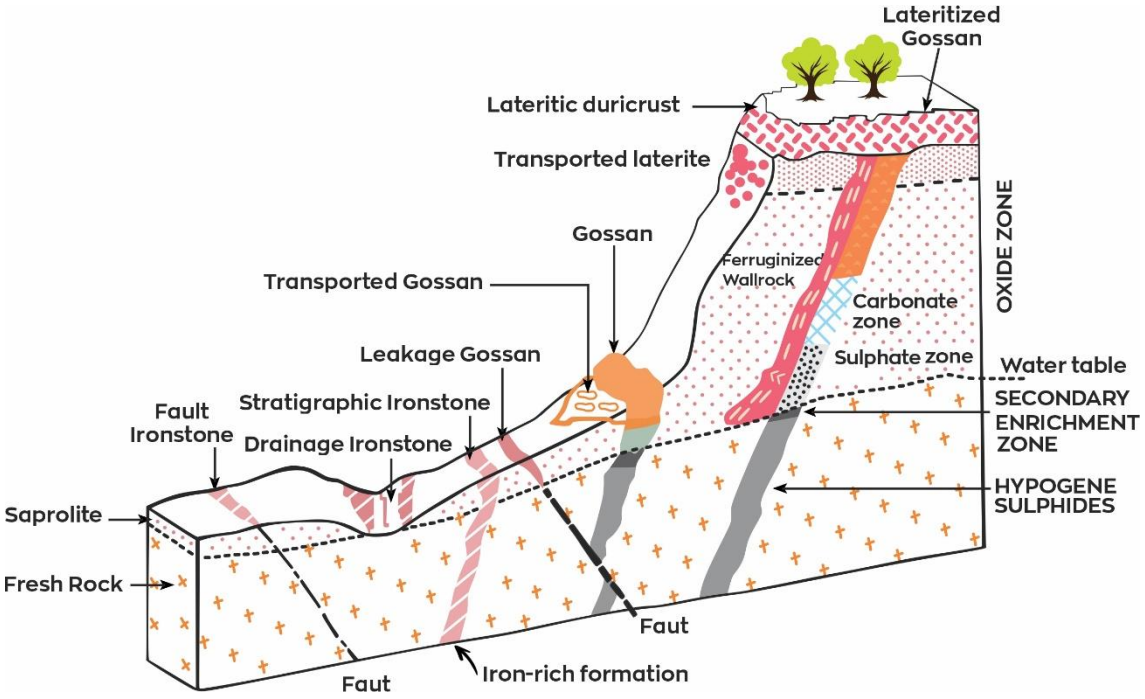

Fig. 3 Arcabouço típico dos regolitos formados em regiões tropicais, posteriormente transformados e truncados em diversos níveis pela evolução da paisagem, modificado de Taylor e Thornber (1992).

2.2. PROVÍNCIA MINERAL DE CARAJÁS

A PMC hospeda vários depósitos de sulfeto de cobre maciço de classe mundial, como Salobo (Siqueira e Costa 1991), Sossego (Monteiro *et al*. 2008), Cristalino (Soares *et al*. 2001) e Alemão (Galarza *et al*. 2008); além de depósitos menores, como Alvo 118 (Torresi *et al*. 2012), Gameleira (Lindenmayer *et al*. 2001), Estrela (Volp *et al*. 2006), Breves (Tallarico 2003), Igarapé Cinzento (Silva *et al*. 2006), Águas Claras (Silva e Villas 1998) e Serra Verde (Reis e Villas 2002). Estas mineralizações constituem o ambiente propício para a formação de perfis gossânicos.

Os gossans da Província Mineral de Carajás são em parte aflorantes, como verificado em Serra Verde (Costa e Costa 1985); recobertos por horizontes saprolíticos, a exemplo do Salobo (Toledo-Groke *et al*. 1985; Veiga *et al*. 1991); e em parte lateritizados, como em Águas Claras e Igarapé Bahia (Costa *et al*. 1996, Porto 2016). O processo de denudação que avança sobre os regolitos de Carajás há pelo menos 10 Ma resultou em um aprofundamento regional do lençol freático, de modo que depósitos mais profundos, inicialmente preservados, foram progressivamente submetidos a modificações supergênicas, a depender do nível de truncamento dos regolitos (Silva e Kotschoubey 2000, Monteiro *et al*. 2018).

3. MATERIAIS E MÉTODOS

3.1 AMOSTRAGEM

Foram realizadas duas atividades de campo à área do depósito, totalizando dez dias. Nestas ocasiões foram selecionados e descritos os furos de sondagem A118-484 e A118-505, e deles extraídas 90 amostras. Os dados de subsuperfície foram complementados com a coleta de 10 amostras adicionais na frente de lavra da cava piloto do projeto, já desativada.

3.1. MEDIDAS DE Eh E pH

Doze amostras foram selecionadas para medidas e pH e Eh. Alíquotas de 1 g pulverizadas foram adicionadas a 10 ml de água destilada em tubos falcon, conforme os procedimentos propostos por Teixeira *et al.* (2017). Foram realizadas cinco medidas em cada amostra, empregando-se o medidor Orion Star A211 (Thermo Scientific).

3.2. DIFRAÇÃO DE RAIOS-X

A caracterização mineralógica foi realizada por difração de raios-X (DRX). Analisaram-se amostras totais e alíquotas pontuais, visando detectar fases mineralógicas isoladas. As amostras foram pulverizadas em gral de ágata e analisadas no difratômetro Bruker D2 PHASER, com ânodo de Cu, operando a 300 W (30 kV x 100 mA), na faixa angular de 5 a 75 °2θ, com tempo de passo de passo de 0,02 s. Todos os procedimentos analíticos foram realizados no Laboratório de Mineralogia, Geoquímica e Aplicações da Universidade Federal do Pará.

3.3. ESPECTROSCOPIA NO INFRAVERMELHO

Espectros de infravermelho com transformada de Fourier foram adquiridos no equipamento Bruker Vertex 70, com detector L-alanina deuterada, dopada com sulfato de triglicina e operando a temperatura ambiente (RT-DLaTGS). As análises foram controladas no software Opus 7, na região de 4000 a 400 cm^{-1}, em modo de transmissão, com resolução espectral de 4 cm^{-1} e velocidade de movimentação do espelho de 10 kHz. As leituras foram realizadas no LAMIGA-UFPA. Todos os procedimentos analíticos foram realizados no Laboratório de Mineralogia, Geoquímica e Aplicações da Universidade Federal do Pará.

3.4. ESPECTROSCOPIA MÖSSBAUER

Para identificação e quantificação dos minerais de ferro, empregou-se análises por espetroscopia Mössbauer ^{57}Fe das amostras in natura na temperatura ambiente (298 K). As medidas foram realizadas em espectrômetro convencional, com geometria de transmissão e aceleração constante da fonte (^{57}Co). Os espectros foram coletados na faixa de velocidade de

aproximadamente ± 10 mm/s. A velocidade foi calibrada em relação ao α-Fe à temperatura ambiente; e os espectros obtidos foram ajustados usando o software WinNormos-for-Igor. Todos os procedimentos analíticos foram realizados no Centro Brasileiro de Pesquisas Físicas.

3.5. ESTEREOMICROSCOPIA E MICROSCOPIA ÓPTICA

As investigações microtexturais e aprofundamento mineralógico foram realizados a partir de vinte lâminas delgadas polidas, analisadas ao Microscópio Óptico LEICA DM 2700 P, com câmera LEICA MC 170 HD acoplada.

3.6. MICROSCOPIA ELETRÔNICA DE VARREDURA

Estes dados foram complementados por imagens via elétrons retroespalhados, obtidas ao Microscópio Eletrônico de Varredura (MEV) HITACHI TM 3000; e análises químicas semiquantitativas por Sistema de Energia Dispersiva (SED) Oxford SwiftED 3000. As condições analíticas utilizadas foram 15 kV, para a voltagem de aceleração; 50 µm como diâmetro do feixe; e filamento de tungstênio como fonte de elétrons. As análises micromorfológicas foram realizadas no Laboratório de Mineralogia, Geoquímica e Aplicações (Universidade Federal do Pará).

3.7. MICROSSONDA ELETRÔNICA

A composição química mineral foi obtida por Microssonda Eletrônica (ME), após metalização das seções polidas com uma película de 5 nm de carbono. Empregou-se o equipamento JEOL JXA-8230, com potencial de aceleração de 20 kV, corrente do feixe em 20 nA e spot com 5 µm de diâmetro. Os dados foram processados no software JEOL, com utilização do método matemático φρZ-XPP para correção dos efeitos de matriz. A seleção dos elementos a serem analisados ocorreu a partir de testes preliminares em que foram identificados os constituintes maiores e traços detectáveis em cada mineral. Estas investigações foram realizadas no Chevron Geomaterials Characterization Laboratory (Louisiana State University).

3.8. ANÁLISES QUÍMICAS TOTAIS

Um grupo de 400 amostras com 10 Kg cada foi analisado para determinação da composição química total da rocha. Para análise de Ag, Al, As, Ba, Be, Bi, Cd, Ce, Co, Cr, Cs, Fe, Ga, Ge, Hf, In, K, La, Li, Mg, Mn, Mo, Na, Nb , Ni, P, Pb, Rb, Re, S, Sb, Sc, Se, Sn, Sr, Ta, Te, Th, Ti, Tl, U, V, W, Y, Zn e Zr, amostras de 0,25 g foram digeridas com ácidos perclórico, nítrico, fluorídrico e clorídrico. O resíduo é completado com ácido clorídrico diluído e analisado por espectrometria de emissão atômica com plasma acoplado indutivamente. Após esta análise, os resultados foram revisados para altas concentrações de Bi, Hg, Mo, Ag e W e

diluídos apropriadamente. As amostras que atenderam a este critério foram então analisadas por espectrometria de massa de plasma acoplado indutivamente. Au foi determinado por ensaio de fogo seguido por análise em ICP-AES e Cu foi analisado por Niton X Ray Fluorescence. Os resultados dessas análises foram gentilmente cedidos pela Vale.

Adicionalmente, 12 amostras coletadas em contextos mineralógicos específicos também foram analisadas, para esclarecer a associação entre mineralogia e composição química total. Para determinação de SiO_2, Al_2O_3, Fe_2O_3, CaO, Na_2O, K_2O, Cr_2O_3, TiO_2, MnO, P_2O_5, SrO e BaO, 0,1 g de amostras foram adicionados ao fluxo de borato de lítio bem misturados e fundidos em um forno a 1025°C. A massa fundida resultante foi então arrefecida e dissolvida numa mistura ácida contendo ácidos nítrico, clorídrico e fluorídrico. Esta solução foi então analisada pelo ICP-AES. Bário, Ce, Cr, Cs, Dy, Er, Eu, Ga, Gd, Ge, Hf, Ho, La, Ku, Nb, Pr, Rb, Sm, Sn, Sr, Ta, Tb, Th, Tm, U, V, W, Y, Yb e Zr foram digeridos pelo mesmo método, mas com uma fusão adicional de borato de lítio e analisados por ICP-MS. A perda ao fogo foi determinada pelo método gravimétrico, usando um forno de decomposição térmica e enxofre total e carbono foram analisados por espectroscopia de infravermelho LECO.

Para Ag, Cd, Co, Cu, Li, Mo, Ni, Pb, Sc e Zn, uma amostra de 0,25g foi digerida com os ácidos perclórico, nítrico, fluorídrico e clorídrico. O volume do resíduo foi completado com ácido clorídrico diluído e a solução resultante é analisada por ICP-AES. Para Cu, amostras de 0,4 g foram digeridas em água régia e analisadas por ICP-MS. Para As, Bi, Hg, In, Re, Sb, Se, Te e Tl, uma amostra de 0,50 g foi digerida com água régia por 45 minutos. Após resfriamento, a solução resultante foi diluída para 12,5 mL com água desionizada, misturada e analisada por ICP-MS. Ouro, Pt e Pd foram determinados por ensaio de fogo e acabamento ICP-AES. Todos os dados químicos foram adquiridos nas instalações dos laboratórios da ALS.

3.9. ISÓTOPOS ESTÁVEIS

Oito amostras pulverizadas foram aquecidas a 1000°C por 1,5 h, para remover compostos orgânicos. Em seguida, o material foi dissolvido em béqueres de teflon com HF, HNO_3 e HCl concentrados, a 130 °C. As soluções foram divididas em duas alíquotas, posteriormente secas e redissolvidas. Foi utilizado 1 ml de HCl 6N para análises de isótopos de Fe e 1 ml de HCl 10N para isótopos de Cu. Apenas ácidos duplamente destilados foram usados no procedimento e o material de laboratório foi pré-limpo com HCl a 10% para minimizar contaminações.

3.9.1. Isótopos de ferro

Oito alíquotas de amostra correspondentes a 500-1000 µg Fe foram carregadas em colunas com cerca de 1 ml de resina troca aniônica AG1-X8 (100-200 mesh) em uma capela de fluxo laminar classe A100. Os elementos da matriz foram eluídos usando 5 ml de HCl 6M, e o Fe foi subsequentemente eluído usando 2 ml de água ultrapura e 4,5 ml de HNO_3 5M (Moeller *et al*. 2014). A amostra eluída foi seca e adicionada a 0,3 M de HNO_3. As amostras foram então analisadas quanto às concentrações de Fe usando um espectrômetro de massa com plasma indutivamente acoplado e multicoletor Nu Plasma II (MC-ICP-MS), em que a interface Plasma 3 foi aprimorada na Universidade de Bergen. Uma amostra de ácido (branco) carregada nas mesmas colunas de troca aniônica produziu valores de 4 ng de Fe, que corresponde a menos de 0,002% do Fe contido nas amostras.

As soluções foram diluídas para 2 ppm de Fe em frascos de teflon limpos com ácido e analisados para isótopos de Fe no modo de plasma úmido em pseudo-resolução média (R5-95% = 9899) com ^{54}Fe em Faraday cup L5, ^{56}Fe em H1 e ^{57}Fe em H4. Os zeros foram medidos pela deflexão ESA por 30 segundos antes de cada bloco e as amostras foram analisadas em 2 blocos de 20 medições de 8 segundos. Cada amostra foi executada em duplicata e um padrão interno (Han Fe, $\delta^{56}Fe = 0,29 \pm 0,07‰$, Moeller *et al*. 2014) foi medido regularmente para confirmar as proporções precisas de isótopos de Fe.

As razões de isótopos de Fe foram corrigidas para viés de massa usando bracketing de amostra padrão (SSB) com o padrão de bracketing IRMM-014, seguindo a equação: $\delta^{56}Fe_{spl,\ corr} = \{((^{56}Fe/^{54}Fe)_{spl,\ meas} / [0.5 \times (^{56}Fe/^{54}Fe)_{std1,\ meas} + 0.5 \times (^{56}Fe/^{54}Fe)_{std2,\ meas}]) -1\} \times 1000$ e similarmente para $\delta^{57}Fe$. Um gráfico de $\delta^{57}Fe$ versus $\delta^{56}Fe$ confirmou que todas as amostras e padrão caem (dentro do erro) na linha de fracionamento dependente de massa terrestre com uma inclinação de 1,47. Com base em análises repetidas de Han Fe (n = 15), a precisão externa em $\delta^{56}Fe$ foi de 0,10 (2s). As análises do padrão de basalto BCR-2 produziram um $\delta^{56}Fe$ médio de $0,07 \pm 0,05‰$ (n = 3), o que está em excelente acordo com o valor publicado de $0,09 \pm 0,01‰$ (Craddock e Dauphas 2011).

3.9.2. Isótopos de cobre

Oito alíquotas de amostra correspondentes a 1000 µg Cu foram carregadas em colunas de Teflon feitas sob medida com 1 ml de resina de troca aniônica AG-MP1 (100-200 mesh) em uma capela de fluxo laminar classe A100. Para amostras em que menos de 100 µg de Fe foi carregado na coluna, os elementos da matriz foram eluídos usando 4 ml de HCl 10M, e Cu foi

subsequentemente eluído usando 6 ml de HCl 5M (modificado de Borrok *et al.* 2007). A calibração da coluna mostrou que maiores teores de Fe resultam em eluição mais precoce do Cu. Para amostras com mais de 100 µg Cu, os elementos da matriz foram, portanto, eluídos com apenas 3 ml de HCl 10 M. As amostras eluídas foram secas, refluxadas com HNO_3 concentrado por 4 horas e recolhidas em HNO_3 0,3 M.

As amostras foram posteriormente analisadas para concentrações de Cu usando um Nu Plasma II MC-ICP-MS na Universidade de Bergen. Uma amostra de ácido em branco que foi executada nas mesmas colunas de troca aniônica produziu um branco de 1 ng Cu, que corresponde a menos de 0,001% do Cu nas amostras. As soluções foram diluídas para 100 ppb Cu em frascos de Teflon limpos com ácido e analisados para isótopos de Cu no modo de plasma úmido em baixa resolução com ^{63}Cu no copo axial de Faraday e ^{65}Cu em H4. As abundâncias de zinco foram monitoradas em copos Faraday H6 (^{66}Zn) e H9 (^{68}Zn) e os sinais totais de Zn foram tipicamente inferiores a 1% do sinal total de Cu. Os zeros foram medidos pela deflexão ESA por 30 segundos antes de cada bloco, e as amostras foram analisadas em 2 blocos de 20 medições de 8 segundos.

Cada amostra foi executada em duplicata e um padrão interno (Bergen Cu, $\delta^{65}Cu$ = -0,06 ± 0,06‰) (Moeller *et al.* 2012) foi medido regularmente para confirmar as proporções precisas de isótopos de Cu. As razões de isótopos de Cu foram corrigidas para viés de massa usando bracketing de amostra padrão (SSB) com o padrão de bracketing ERM AE647, seguindo a equação: $\delta^{65}Cu_{spl,\ corr} = \{((^{65}Cu/^{63}Cu)_{spl,\ meas} / [0.5 \times (^{65}Cu/^{63}Cu)_{std1,\ meas} + 0.5 \times (^{65}Fe/^{63}Cu)_{std2,\ meas}]) -1\} \times 1000$. Os valores foram subsequentemente recalculados para o padrão SRM976 como: $\delta^{65}Cu_{SRM976} = \delta^{65}Cu_{ERM\ AE647} + 0.21$ (Moeller *et al.* 2012). Com base em análises repetidas de Bergen Cu (n = 8), a precisão externa em $\delta^{65}Cu$ foi de 0,08 (2s).

4. MINERALOGICAL AND TEXTURAL EVOLUTION OF THE ALVO 118 COPPER-BEARING GOSSAN: IMPLICATIONS FOR SUPERGENE METALLOGENESIS IN CARAJÁS MINERAL PROVINCE, BRAZIL

https://doi.org/10.1016/j.jsames.2022.104108

Pabllo Henrique Costa dos Santos and Marcondes Lima da Costa

Abstract

The Carajás Mineral Province is home to one of the most extensive copper-gold belts globally, where hypogene orebodies were partially transformed into gossans. The Carajás Mountains host mature gossan profiles modified by lateritization. Conversely, the surrounding denuded landscape holds deep immature gossans characterized by generation mechanisms that remain poorly understood. Alvo 118 is a typical deposit from this area, with numerous drill cores available for evaluation. Mineralogical, textural, and mineral chemistry investigations showed that the hypogene mineralization, consisting of massive and disseminated chalcopyrite with minor nukundamite, was partially oxidized. The resulting gossan comprises a range of copper-bearing minerals, including malachite, pseudomalachite, cuprite, tenorite, native copper, ramsbeckite, chrysocolla, and libethenite, with relics of a secondary sulfide zone represented by chalcocite. The host rocks are relatively well-preserved from supergene alteration near the gossan due to the chalcopyrite's low acidifying potential and the deep occurrence of the gossan orebody, resulting in an immature profile. The gossan orebody is sectioned into four zones; the mineral succession of each zone indicates independent evolution, with a general transition from slightly acidic to alkaline conditions and increasing oxidation potential, with local oscillations related to water table fluctuations. This environment was established by the interaction of acid solutions derived from sulfide dissolution with gangue minerals (calcite and apatite) and secondarily with host rocks (chloritites and granodiorites), leading to system buffering. Ti, Mn, Zn, Ni, V, and Co were incorporated into the gossan mainly by goethite, while malachite contains Ba, Ca, Cr, Mn, and Zn. Gold and Pb were detected in goethite, cuprite, tenorite, and native copper. This set of mineralogical zones and mineral successions record an important and unique stage of the supergene evolution of the Carajás Mineral Province, with prominent copper-gold mineralization showing no effects from lateritization.

Keywords: mineralization, regolith, oxidoreduction, Itacaiúnas Surface

1 Introduction

Oxidation reactions involving sulfide deposits produce mineralogically zoned orebodies known as gossans (Andrew 1984; Thornber and Taylor 1992; Taylor 2011). They usually comprise a supergene enrichment zone, formed of secondary sulfides; an oxidation zone, including sulfates, carbonates, phosphates, oxides, and silicates (Belogub et al. 2008; Reich et al. 2009; Števko et al. 2012; Dill 2015; Vasconcelos et al. 2015); and a leaching zone rich in iron oxyhydroxides, typically displaying an iron hat form near the surface (Taylor 2011; Haldar 2018; Ozdemir and Sahinoglu 2018). Gossans are considered mature when they display a complete profile (e.g., secondary sulfide, oxidation, and leaching zones) or immature if the leaching zone is not formed (Scott et al. 2001; Atapour and Aftabi 2007).

For decades, gossans have been used as guides for exploring hypogene sulfide orebodies, especially those mineralized in Cu, Pb, Zn, Mo, Ni, Au, and platinoids (Andreu et al. 2015; Yesares et al. 2017; Pires et al. 2020). Additionally, numerous gossans have been mined with their parent sulfides, increasing the reserves and profitability of the deposits (Throop and Buseck 1971; Velasco et al. 2013). Gossans have also been used to constrain the supergene evolution of large sulfide mineral provinces, such as the Lacan Fold Belt and Golden Grove District in Australia, the Bathurst Mining Camp in Canada, and the Iberian Pyrite Belt in Europe (Boyle 1993; Scott et al. 2001; Smith and Singh 2007; Velasco et al. 2013).

The Gossan formation in the Carajás Mineral Province (CMP) was strongly affected by landscape evolution. The set of plateaus that form the Carajás Mountains (South American/Carajás geomorphic surface) houses mature gossans subjected to lateritization across the Cenozoic, as observed in the Águas Claras and Igarapé Bahia deposits (King 1956; Costa et al. 1999; Porto 2016; Monteiro et al. 2018). Conversely, the dissected and flattened areas surrounding the Carajás Mountains (Velhas/Itacaiúnas geomorphic surface) host deep immature gossans, whose host rocks usually evolve to saprolite near the surface, as in the Salobo and Sossego mines and in the Sequeirinho, Furnas, and Alvo 118 deposits (King 1956; Ildefonse 1986; Monteiro et al. 2018; Mano et al. 2020) (Fig. 1A). Gossan formation in these dissected areas represents a poorly documented stage of CMP supergene evolution.

Alvo 118 is a typical immature gossan formed at the expense of hydrothermal copper-gold orebodies in the CMP, southeastern Amazon. The massive hypogene ore was not exhumed by erosion, which prevented the development of a prominent leaching zone and led to the formation of a deep oxidation zone. The top of the gossan orebody is capped by relatively fresh host rocks and is progressively weathered near the surface. This type of gossan occurrence is

known to comprise significant supergene deposits, the formation of which requires further investigation. In the case of Alvo 118, the hypogene reserves reach 170 Mt @ 1 % Cu and 0.3 g/t Au, while the supergene reserves reach 55 Mt, 30 % of which corresponds to the gossan and 70 % to the saprolite derived from the host rocks (Docegeo 1991; Grainger et al. 2008).

The advancement of drilling in the Alvo 118 deposit and excavation of a pilot open-pit mine allowed the investigation of deep gossan drill cores. These new data are especially valuable because CMP is home to one of the most extensive copper-bearing sulfide belts worldwide, including several deposits under exploration and four copper-gold mines in operation (Monteiro et al. 2008; Moreto et al. 2015; Del Real et al. 2021), Fig. 1A. Therefore, numerous gossans are spread across the region as components of the regoliths that cover the hypogene deposits and their host rocks, including saprolites, laterites, and colluviums (Veiga et al. 1991; Costa et al. 1996).

This paper presents the supergene processes involved in the formation of the Alvo 118 gossan, considering it a reference guide for the generation of deep copper-gold-bearing gossans that are typical in the dissected areas of the CMP. These data may also support the improved selection of exploration and mining techniques, metallurgical Cu recovery methods, and mining waste conditioning methods (Nordstrom 2011; Peterson et al. 2014; Stavinga et al. 2017).

2 Geological setting

2.1 Carajás Mineral Province

The CMP is located in the southeastern Amazon Craton. Its copper-gold mineralizations are mainly distributed in the Carajás Tectonic Domain (2.86–2.55 Ga; Dall'Agnol et al. 2006; Schutesky and Oliveira 2020). The basement of this domain comprises tonalitic-trondhjemitic gneisses and migmatites of the Xingu Complex and orthogranulites of the Pium Complex (Pidgeon et al. 2000). These units are overlain by the Itacaiúnas Supergroup, which consists of basic, intermediate, and felsic metavolcanic sequences interspersed with clastic metasedimentary rocks and banded iron formations (Machado et al. 1991; Trendall et al. 1998; Araújo Filho et al. 2020). This set was intruded by syntectonic alkaline granites of 2.74–2.76 Ga; rhyolitic and dacitic intrusions of 2.64 and 2.65 Ga; and sub-alkaline Paleoproterozoic intrusions of 1.87–1.88 Ga (Grainger et al. 2008; Machado et al. 1991; Dall'Agnol et al. 1994).

The intrusions described above are related to the main hydrothermal events that mark regional metallogenetic evolution. The oldest of these (2.57 Ga) produced the Salobo, Sossego, Cristalino, and Alemão copper-gold deposits, while the youngest (1.88 Ga) formed the

Gameleira, Estrela, Breves, Igarapé Cinzento, and Serra Verde ones (Grainger et al. 2008). Alvo 118 is the only deposit that records the overlap of both events (Torresi et al. 2012).

2.2. Geology of the deposit

The Alvo 118 area predominantly comprises mafic to intermediate metavolcanic sequences from the Grão Pará Group (Itacaiúnas Supergroup). They are intruded by granodiorites, tonalites, and gabbros in addition to dacitic to rhyolitic and diabasic dikes (Grainger et al. 2008; Torresi et al. 2012), Fig. 1B. This set hosts two tabular sub-vertical copper-gold-bearing sulfide orebodies. They reach 4.5 km of continuous extension with a width of 450 m and are distributed in a set of hills aligned in the NW–SE direction. Near the mineralized zone, the host rocks were progressively subjected to hydrothermal alteration, represented by albite, scapolite, biotite, alkali feldspar, chlorite, quartz, and sericite (Torresi et al. 2012).

The hypogene mineralization comprises (1) massive sulfide, containing chalcopyrite (~60 %), bornite (~20 %), hematite (~10 %), magnetite (~10 %), locally associated with calcite, quartz, chlorite, and apatite; and (2) disseminated sulfide, formed of quartz-rich stockwork veins, with varying amounts of apatite, biotite, chalcopyrite, and hematite, dated to 1.87 Ga (Grainger et al. 2008; Torresi et al. 2012). Hypogene mineralization was converted into a gossan orebody with progressive transformation of primary sulfides into chalcocite, digenite, malachite, pseudomalachite, native copper, cuprite, and tenorite (Albuquerque et al. 2001). At the top, the gossan is overlain by fresh host rocks, which are then weathered to form saprolite (Fig. 1C) consisting of kaolinite, chlorite, smectite, and iron oxyhydroxides, which are partly recognized as Cu-bearing minerals (Mano et al. 2020; Veiga et al. 1991). The supergene alteration profile (gossan and saprolite) reaches a depth of 80 m from the highest sites of the hills (Fig. 1D) and 50 m in the eroded flanks.

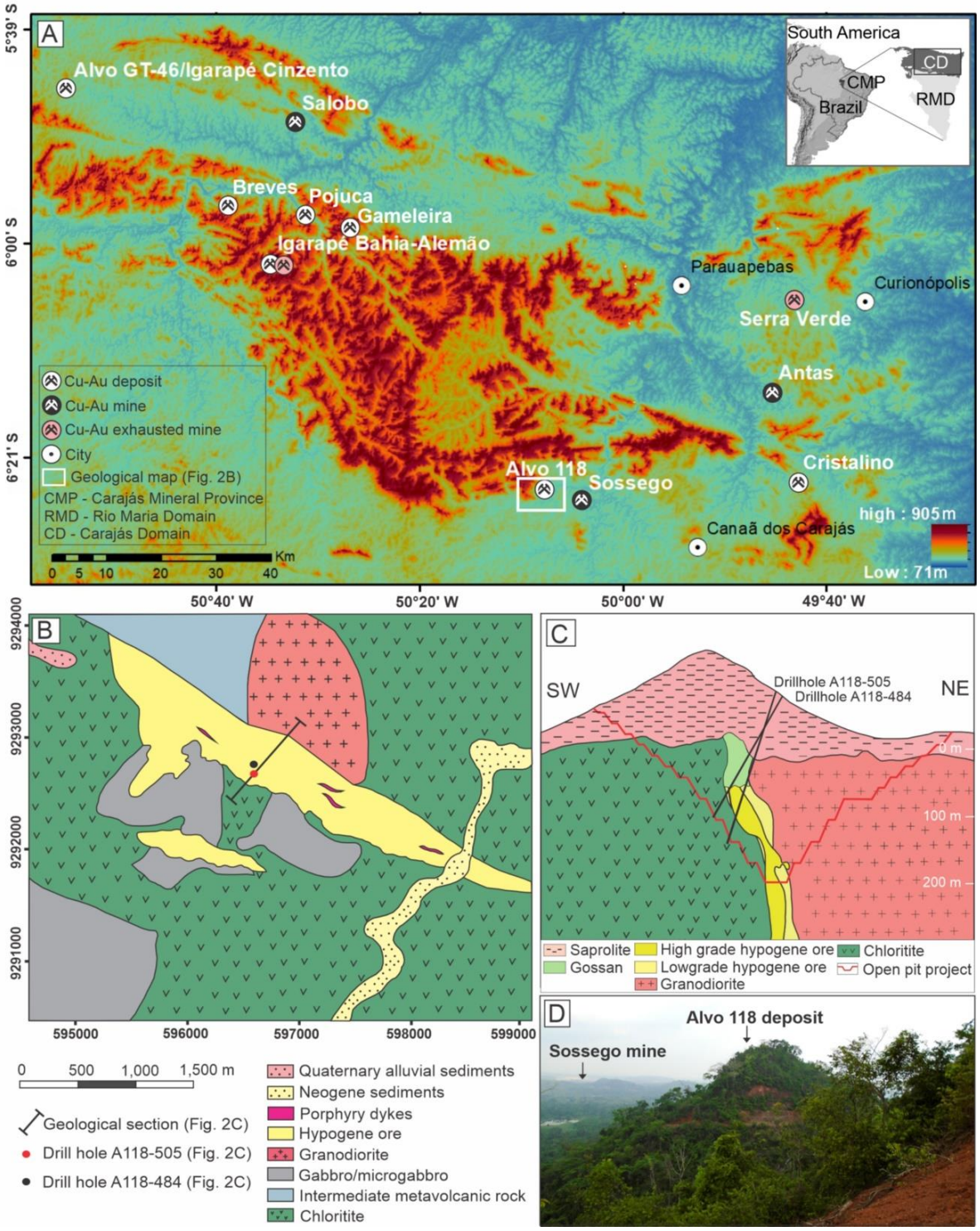

Fig. 1 A) Digital elevation model of northern CMP (USGS 2006), with the locations of the major copper-gold deposits and mines marked. Red to yellow coloring represent the South American/Carajás surface and the blue to green coloring indicates the Velhas/Itacaiúnas surface. B) Simplified geological map of area surrounding the Alvo 118 deposit emphasizing the distribution of hypogene mineralization, compiled and modified from Vasques et al. (2008) and Torresi et al. (2012). C) Geological section of the Alvo 118 deposit with the arrangement of the hypogene mineralization, gossan, and saprolite (modified from Vale S.A.). D) Landscape surrounding a hill of the Alvo 118 deposit showing the Sossego copper-gold mine in the background.

3 Materials and methods

Two field campaigns were conducted in the deposition area. Boreholes A118–484 (182 m deep) and A118–505 (210 m deep) were described, and 90 samples were collected. To complement the subsurface data, 20 additional samples were collected from the benches of a disabled pilot open-pit mine.

The initial mineralogical characterization was performed by X-ray diffraction (XRD) of whole and hand-picking samples to identify locally distributed phases. The samples were powdered in an agate mortar and analyzed using a Bruker D2 PHASER diffractometer with a Cu anode operating at 300 W (30 kV × 100 mA) in the angular range of 5 °to 75° 2θ, with a step time of 0.02 s. All analytical procedures were performed at the Mineralogy, Geochemistry, and Applications Laboratory (Federal University of Pará).

Mineralogical and microtextural investigations were performed on 20 polished thin sections, using a LEICA DM 2700 P optical microscope, with an attached MC 170 HD camera. These data were enhanced by backscattered electron images, obtained with a HITACHI TM 3000 scanning electron microscope (SEM); and semi-quantitative chemical analyses obtained with an Oxford SwiftED 3000 energy dispersive system. The analytical conditions were an acceleration voltage of 15 kV, beam diameter of 50 µm, and tungsten filament as the electron source. The analyses were performed at the Mineralogy, Geochemistry, and Applications Laboratory (Federal University of Pará). Descriptive textural terminology is after Delvigne (1999) and Stoops (2003).

Mineral chemistry investigations were performed using a JEOL JXA-8230 electron probe microanalyzer (EPMA) with an acceleration voltage of 20 kV, 20 nA beam current, and 5 µm diameter spot, after coating the sections with a 5 nm carbon film. The data were processed in JEOL software using the φρZ-XPP mathematical method to correct the matrix effects. Prior evaluations determined the elements to be analyzed by identifying the major and detectable trace components in each phase. Thus, the analyzed elements and respective standards were Ti (rutile), Cr (chromite), Zn (sphalerite), Al (chromite), Mg (diopside), Si (diopside), Ca (apatite), Mn (Mn), Cl (Cal-STD), Ba (barite), P (apatite), V (V), Co (cobaltite), As (cobaltite), Au (Au), Pb (galena), Cd (Cd), and Ni (pentlandite). Standard hematite was used to analyze Fe in phosphates, silicates, and oxides (trivalent state iron); while marcasite was applied to sulfides (bivalent state iron). For S analyses, the applied standards were barite (phosphates and silicates) and marcasite (oxides and sulfides). For Cu, the standards were Cu (phosphates, silicates, and

oxides) and chalcopyrite (sulfides). These investigations were performed at the Chevron Geomaterials Characterization Laboratory (Louisiana State University).

4 Results

4.1 Host rocks

Chloritites and granodiorite host the hypogene mineralization and gossan. In the investigated boreholes, the chloritites range from ~35–43 m and ~80–150 m in depth. In comparison, the granodiorites occur from ~43–80 m (Fig. 2A). The chloritites contains chlorite (80 %), plagioclase (15 %), and quartz (5 %), with accessory magnetite and weak foliation. Granodiorites contains ~40 % quartz, ~35 % oligoclase, and ~15 % orthoclase, with accessory biotite and hornblende. Granodiorite is often crosscut by chlorite veinlets, which reflect the hydrothermal alteration event described by Torresi et al. (2012). Notably, near the gossan orebody, chloritites and granodiorites are relatively preserved, with little to no evidence of supergene alteration, while the granodiorite minerals are moderately weathered.

4.2 Hypogene mineralization

Hypogene mineralization was identified only in the subsurface, ~110–150 m deep, in the two analyzed drill holes (Fig. 2A). It comprises a disseminated sulfide zone represented by stockwork veins of quartz and chalcopyrite in addition to accessory calcite, apatite, fluorite, and siderite, intercepting chloritites (Fig. 2G); and a massive sulfide zone represented by veins of chalcopyrite (with accessory nukundamite) crosscutting chloritites. The veins present breccia-like texture in which chalcopyrite surrounds millimetric fragments of chloritites, in addition to quartz grains, calcite, fluorite, and apatite (Fig. 2H). Thus, the massive and disseminated mineralizations are not continuous, but interspersed with zones of non-mineralized chloritite and granodiorite.

4.3 Mineralogical and textural zonation of the gossan profile

The gossan profile displays an average thickness of 60 m in the two analyzed drill holes and exhibits significant textural and mineralogical variance. This allowed it to be divided into four zones, from the bottom to the top, according to the dominant mineral: goethite, malachite, cuprite, and libethenite (Fig. 2A). The gossan profile is originally entirely located above 35 m deep, however, the malachite zone was partially exposed during the excavation of a pilot open-pit mine (Fig. 2B-F). The deep and outcropping sections of the gossan orebody are detailed below.

The goethite zone is hosted by chloritites and comprises three distinct facies, according to the distribution pattern of the iron oxyhydroxide, named cavity-filling, fracture-filling and breccia facies (Figs. 2A; 6A, B). In this zone, goethite is locally associated with malachite, chalcocite, native copper and pseudomalachite.

The cavity-filling facies occurs in the lowest part of the gossan profile (A118-484 drill hole), with ~6 m thick. In this section, chalcopyrite dissolution results in numerous cavities in the stockwork veins that previously formed disseminated hypogene ore. These cavities present irregular shapes and are up to 20 mm in length. Additionally, they are commonly coated with goethite (Figs. 3A, B), often covered with malachite (Figs. 3C, D; 6A).

The fracture-filling facies corresponds to goethite coating or completely filling the fracture system that crosscuts the chlorites. This facies ranges from ~20 m to ~50 m thick on drill holes A118-505 and A118-484, respectively, following the fractures distribution. In part of this system, goethite is covered by chalcocite (Figs. 3G, H; 6A).

The breccia facies is 2 m thick on A118-484 and 6 m thick on A118-505 drill hole. In this section of the gossan, dissolution of the massive hypogene ore produced a breccia-like texture, in which goethite micromass surrounds anedric quartz grains up to 10 mm in length (Figs. 3E, F; 6B). In portions, these breccias consist dominantly of quartz; in others, the surrounding massive goethite prevails.

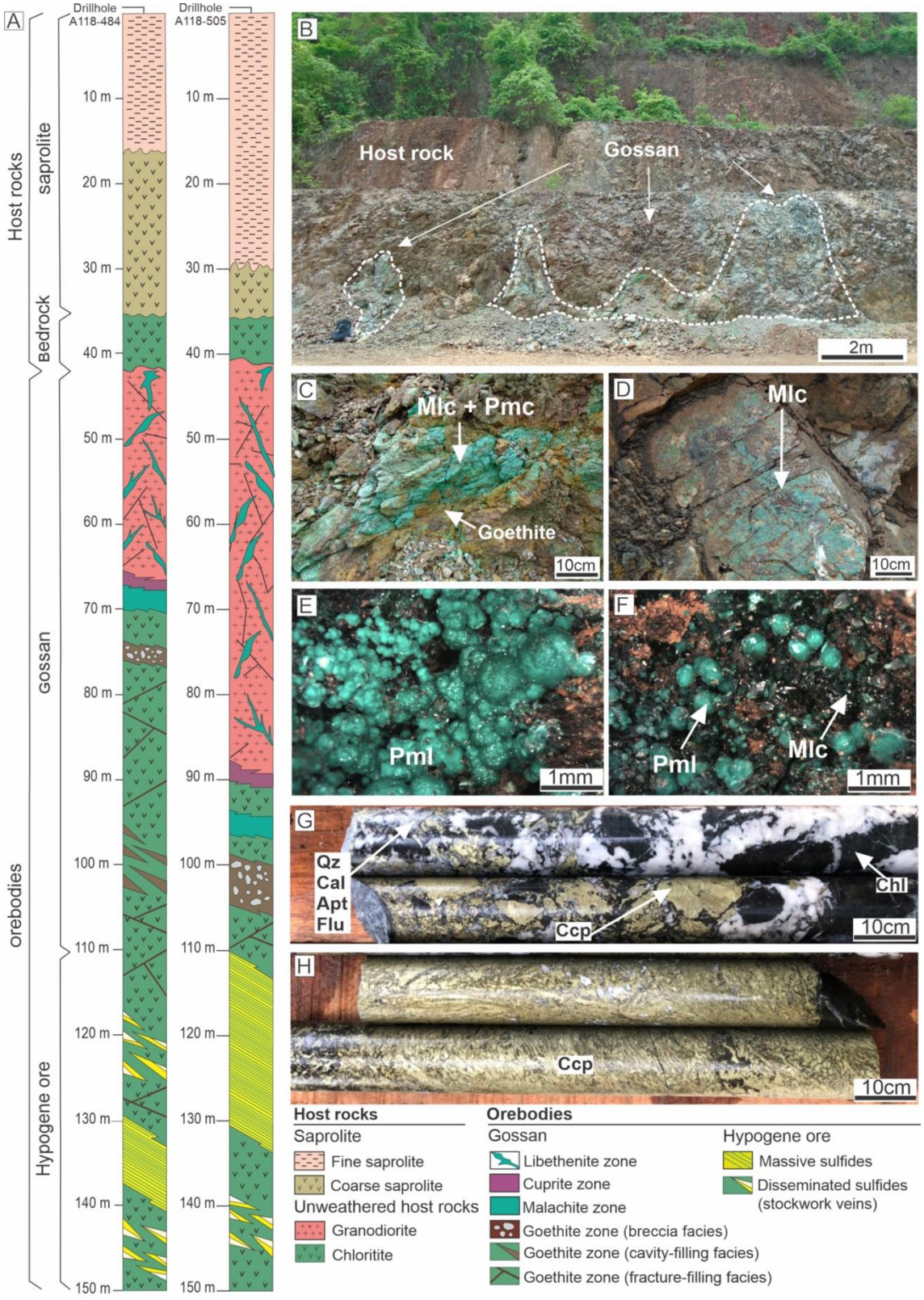

Fig. 2 A) Geological sections of the Alvo 118 deposit emphasizing the arrangement of orebodies (hypogene mineralization and gossan) and host rocks (bedrock and saprolite). B) Gossan outcrop in Alvo 118 pilot open-pit mine. C) Lenses of malachite, pseudomalachite, and goethite. D) Fracture surface covered with malachite. Stereo microscope images of botryoidal pseudomalachite (E) associated with malachite crystallites (F) in fracture planes. Drill cores showing disseminated (G) and massive (H) hypogene ore. Abbreviations: Mlc (malachite); Pml (pseudomalachite); Gth (goethite); Ccp (chalcopyrite); Qz (quartz); Cal (calcite); Apt (apatite); Flu (fluorite); Chl (chloritite).

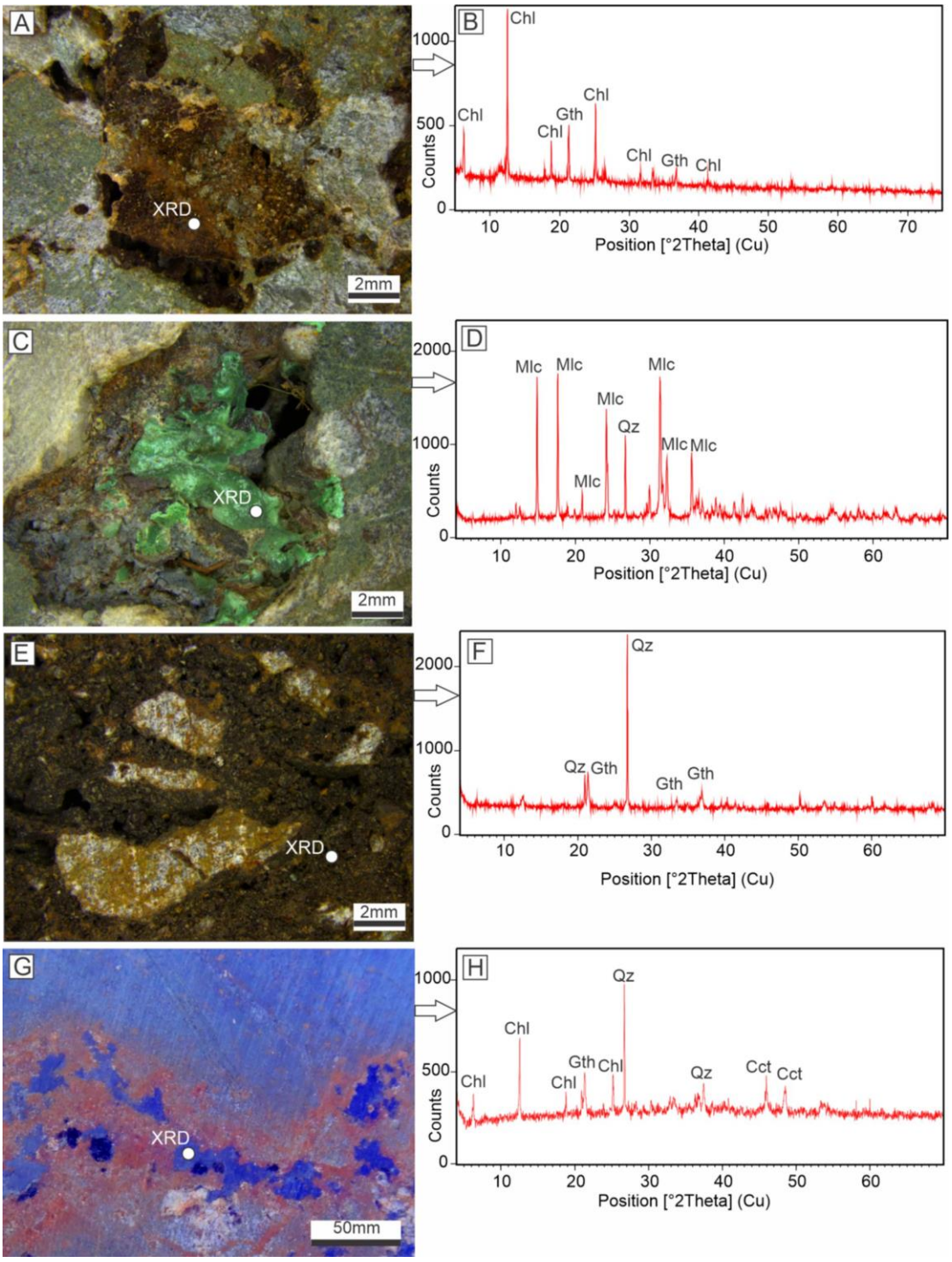

Fig. 3 Textural relationships on the goethite zone obtained with a stereo microscope. Dissolution cavities coated with goethite (A, B). Malachite covering goethite in dissolution cavities (C, D). Breccia facies with massive goethite surrounding quartz grains (E, F). Fracture in chlorite filled with goethite and chalcocite (G, H). Abbreviations: Chl (chlorite); Gth (goethite); Qz (quartz); Mlc (malachite); Cct (chalcocite). White spots indicate sites selected for XRD analysis.

The malachite zone is ~4 m thick in both analyzed drill holes. This zone is hosted by the chloritites, apparently filling the spaces previously occupied by massive hypogene mineralization. In the A118-484 drill hole, the bottom contact is with chloritite and top contact with the cuprite zone. In comparison, in A118-505, both contacts are with chloritite. The framework of the malachite zone comprises massive malachite, interspersed with portions of chrysocolla and ramsbeckite. These minerals surround black nodules of copper oxide, which can include cuprite, tenorite or both (Fig. 4A, B; 6C). The massive malachite is often associated with kaolinite pockets, suggesting local weathering of chlorite from the host rock (Figs. 4C, D; 6C). Additionally, chlorite is commonly identified by XRD within the massive malachite domain.

The malachite zone was the only zone observed in the pilot open-pit mine (Fig. 2B). The outcrop shows pockets of the oxidation zone evolved and caped by chloritites, which are progressively weathered toward the top, forming a saprolite. In the gossan pockets, malachite occurs as massive lenses associated with pseudomalachite and goethite (Fig. 2C) and coating or filling the fracture system (Fig. 2D). Locally, botryoidal pseudomalachite and malachite crystallites are coating dissolution cavities (Figs. 2E, F).

The cuprite zone is ~1 m thick and can display bottom contact with the malachite zone or with chloritites, depending on the analyzed drill hole, while the top contact is with the granodiorites. The framework of this zone consists dominantly of massive cuprite associated with goethite, forming a red to purple micromass that surrounds quartz grains. Brown lenses of goethite with minor cuprite, surrounding quartz grains, are interspersed with the cuprite-dominated portions (Fig. 4E, F; 6D)

The libethenite zone is ~25 m and ~45 m thick in drill holes A118-485 and A118-505, respectively. The gossan newly formed minerals are disseminated in fractures of the host rocks, which comprise granodiorites. This zone consists dominantly of libethenite, pseudomalachite, and malachite, which together occur as a greenish friable micromass (Figs. 4G, H; 6E). The libethenite zone represents the top of the gossan orebody. This zone is overlain by relatively fresh host rocks, represented mainly by chloritite, which are weathered near the surface, forming a ~35 m thick saprolite.

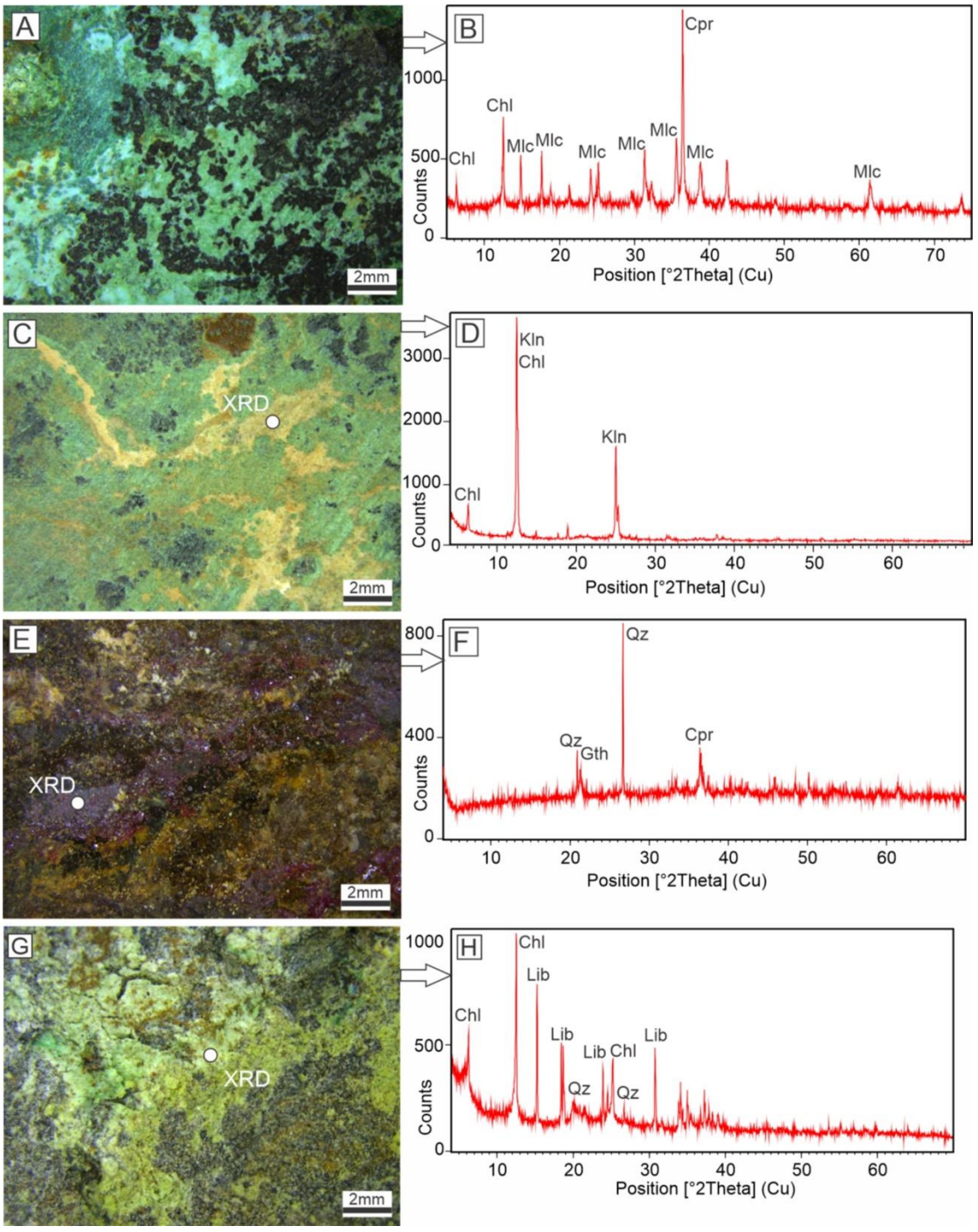

Fig. 4 Textural relationships on the malachite (A-D), cuprite (E, F) and libethenite (G, H) zones obtained with a stereo microscope. Malachite and chrysocolla surrounding cuprite and tenorite nodules (A, B). Irregular kaolinite pockets crosscutting massive malachite (C, D). Cuprite micromass interspersed with lenses on goethite with minor cuprite (E, F). Micromass formed of libethenite and malachite arranged in granodiorite fracture (G, H). Abbreviations: Chl (chlorite); Gth (goethite); Qz (quartz); Mlc (malachite); Pml (pseudomalachite); Cpr (cuprite); Kln (kaolinite); Lib (libethenite). White spots indicate sites selected for XRD analysis.

4.4 Micromorphology and mineral chemistry

Optical microscopy coupled with SEM and EPMA confirmed and detailed the mineral successions of the goethite (breccia facies), malachite, and cuprite zones. The libethenite zone was not analyzed using these methods because of its friable texture.

Under the microscope, the goethite micromass typical of the breccia facies (goethite zone) exhibits numerous chlorite plates inherited from the host rocks (Fig. 5A). Still on the framework of the breccias, quartz grains are locally involved by subhedral native copper crystals, in turn surrounded by goethite (Figs. 5B, C; 6B). Additionally, irregular microcavities and microfractures in the goethite micromass are coated or filled with pseudomalachite (Figs. 5D). Under SEM, goethite microboxwork features are commonly found, presenting angular vugs typical of chalcopyrite dissolution (Gandhi and Sarkar 2016), also filled with pseudomalachite (Fig. 5E; 6B). Finally, in the contact between the chloritites and the breccia facies, there was a clear penetrative relationship between goethite and chlorite in which the former occurred in the cleavage plains of the latter, resulting in local ferruginization of the host rock (Fig. 5F).

In the malachite zone, malachite exhibits coliform to botryoidal habits and often surrounds tenorite nodules. This framework is associated with a sub-translucent brownish kaolinite micromass (Figs. 5G, H). Chrysocolla was interspersed with massive malachite and also surrounds tenorite nodules (Fig. 5I). Under SEM, the fine association between malachite and tenorite nodules was confirmed (Fig. 5J; 6C). The same association was found with cuprite, which comprises subhedral crystals and exhibits local concavities suggestive of dissolution, in addition to alteration edges consisting of tenorite (Fig. 5K). SEM/EPMA also revealed the local occurrence of ramsbeckite surrounding tenorite (Fig. 5L; 6C).

In the cuprite zone, microanalysis allowed two domains to be distinguished. The first comprises massive cuprite associated with goethite (Fig. 5M), both surrounding fractured quartz grains with cuprite and native copper filling some of the fracture spaces (Fig. 5N; 6D). The second domain comprises goethite surrounding the skeletal chalcocite, possibly as a remnant of a former secondary sulfide zone (Fig. 5O; 6D).

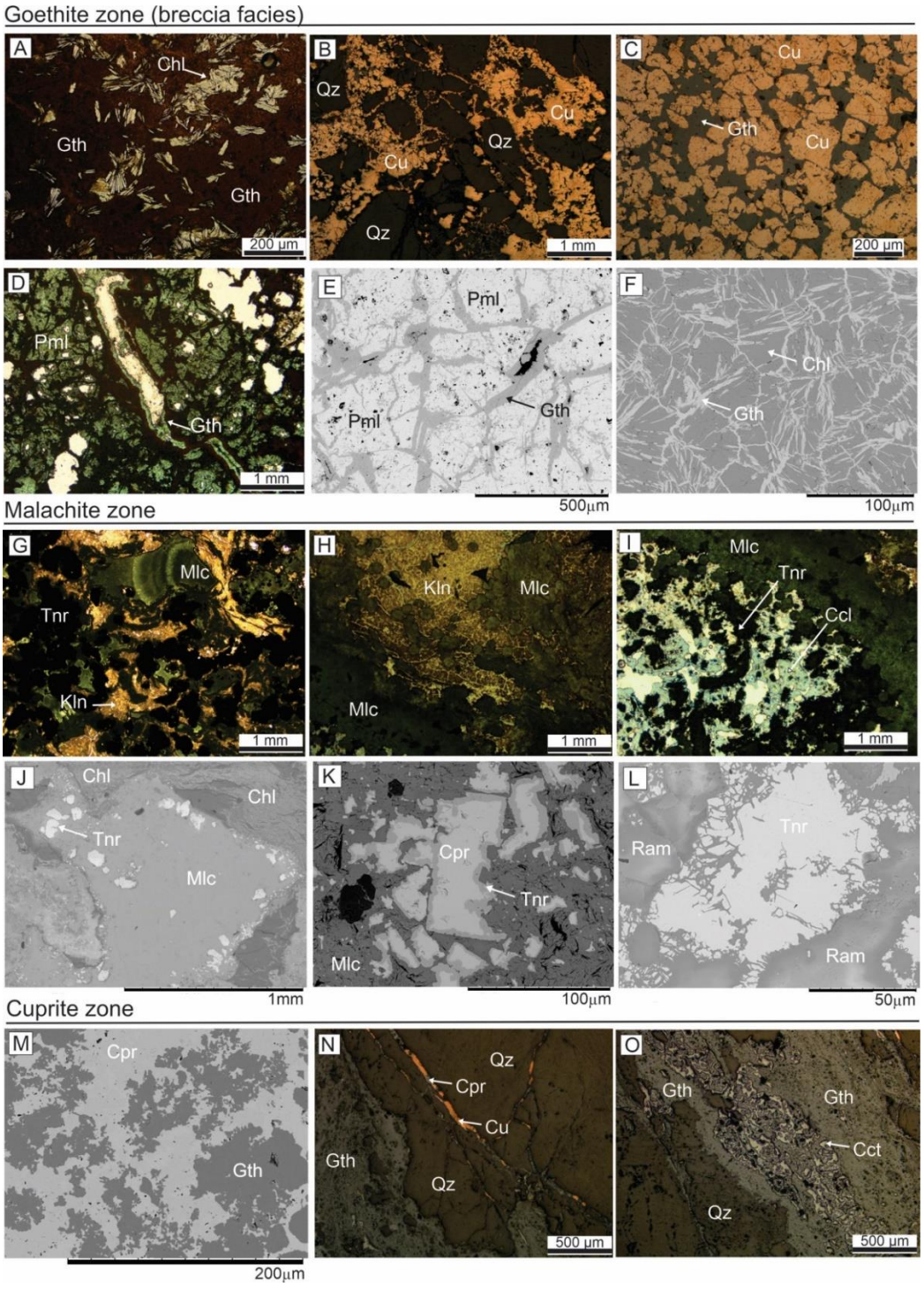

Fig. 5 Massive goethite with chlorite plates, OM/PPL (A). Native copper surrounding quartz grains, CPL (B). Subhedral crystals of native copper surrounded by goethite, OM/CPL (C). Pseudomalachite filling porosity and microfractures, OM/ PPL (D). Microboxwork feature in goethite filled with pseudomalachite, SEM (E). Chloritite crosscut by goethite, SEM (F). Malachite and tenorite crosscut by kaolinite, OM/PPL (G). Botryoidal malachite with kaolinite, OM/PPL (H). Chrysocolla interspersed with malachite and involving tenorite nodules, OM/PPL (I). Massive malachite involving tenorite (J). Subhedral crystals of cuprite with borders of tenorite, SEM (K). Ramsbeckite involving tenorite, SEM (L). Cuprite micromass involving associated with goethite, SEM (M). Cuprite and native copper veinlets in quartz, OM/RL (N). Skeletal chalcocite surrounded by goethite, OM/RL (O). Abbreviations: Chl (chlorite); Gth (goethite); Qz (quartz); Cu (native copper); Mlc (malachite); Pml (pseudomalachite); Cpr (cuprite); Tnr (tenorite); Ccl (chrysocolla); Kln (kaolinite); optical microscopy (OM); plane polarized light (PPL); cross polarized light (CPL); reflected light (RL); Scanning electron microscopy (SEM).

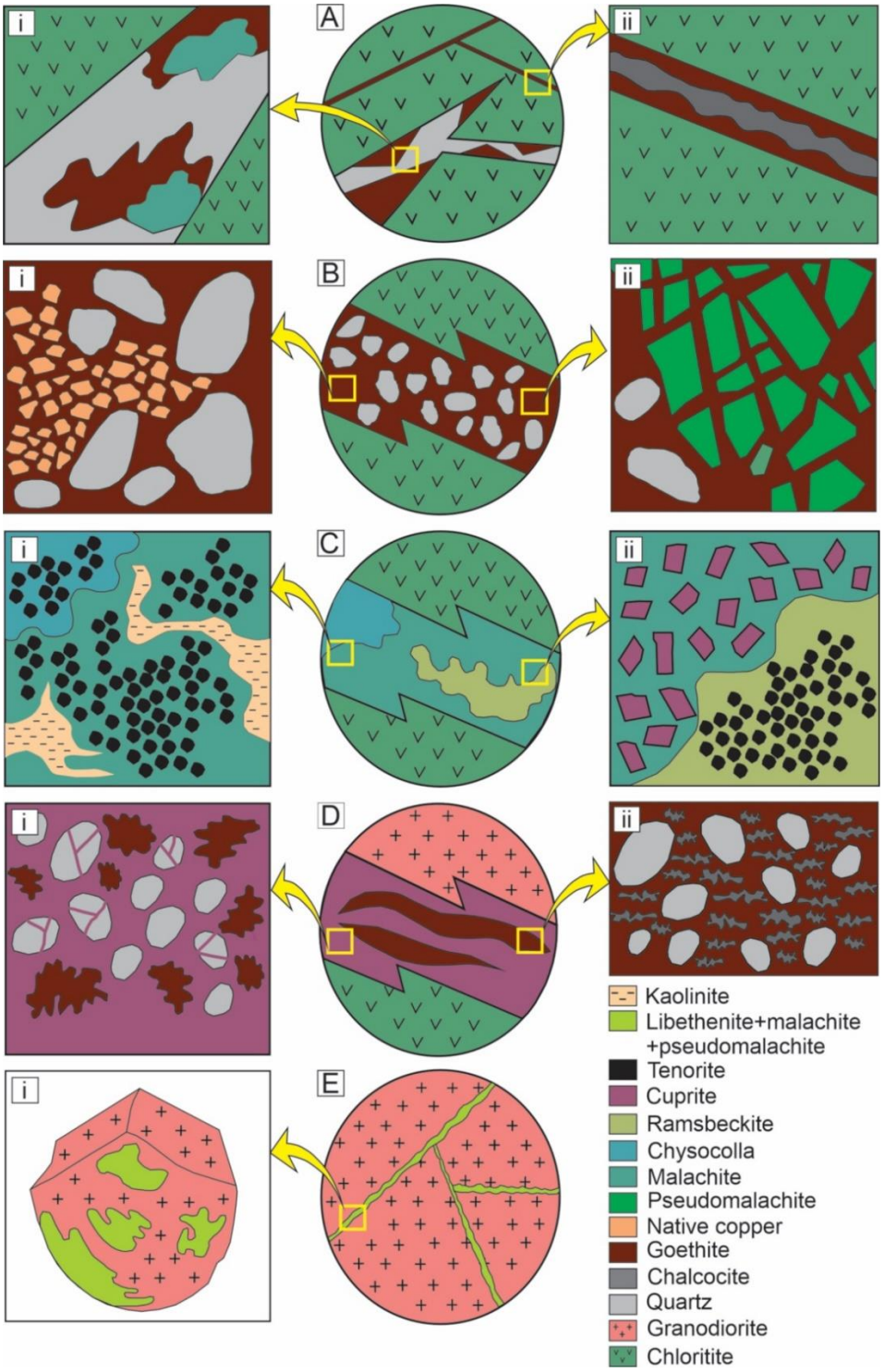

Fig. 6 Schematic model of the Alvo 118 gossan zones, highlighting the espacial distribution and texture, based on macro and microscopic features. A) Cavity-filling and fracture-filling facies of the goethite zone, highlighting dissolution cavities coated with goethite and malachite (i) and fractures filled with goethite and chalcocite (ii). B) Breccia facies of the goethite zone, showing native copper crystal in the goethite micromass, both surrounding quartz grains (i) and microboxwork texture in goethite filled with pseudomalachite (ii). C) Malachite zone, comprising of malachite and chrysocolla micromasses associated with kaolinite and surrounding cuprite/tenorite nodules (i) or malachite and ramsbeckite micromasses surrounding subhedral cuprite and cuprite/tenorite nodules, respectively (ii). D) Cuprite zone, comprising a cuprite micromass, with goethite lenses, in which the former comprises cuprite associated with goethite and surrounding quartz grains (i) and the later include goethite micromass with skeleton chalcocite (ii). E) Libethenite zone, formed of malachite, pseudomalachite, in addition to libethenite micromass, spread in the fractures of granodiorites (i).

Determining the chemical compositions of the selected minerals facilitated the phase identification and estimation of the preferential distribution of trace elements along the newly formed phases (Tab. 1). However, these results should be considered with caution, as the most minerals are very fine, so each analysis may reflect the composition of more than one phase.

Chalcopyrite contains high concentrations of Ti, Al, Mn, Mg, Si, Zn, Ni, and V. These elements were also identified in the gossan minerals, mainly goethite, native copper, malachite, pseudomalachite, and chrysocolla. The latter three also containing high Ba, Cr, and Ca concentrations, which were not detected in the hypogene minerals.

Goethites were analyzed in the goethite and cuprite zones where mean values of 0.59 % and 0.69 % Cu were detected, respectively. The average concentrations of trace elements in the goethite zone is 298 ppm Pb, 166 ppm Zn, 592 ppm Co, and 584 ppm Ni, while the cuprite zone reach values of 330 ppm Pb, 655 ppm Zn, 585 ppm Co, and 995 ppm Ni. These concentrations were higher than the values of chalcopyrites from hypogene mineralization (Pb not detected, 46 ppm Zn, 370 ppm Co, and 147 ppm Ni).

Although it was not identified in the hypogene minerals (chalcopyrite, nukundamite, and magnetite), gold was found in high average concentrations especially in the breccia facies of the goethite zone, where it was detected in native copper (mean: 56 ppm) and goethite (mean: 274 ppm); and in the malachite zone, identified in cuprite (mean: 48 ppm) and tenorite nodules surrounded by ramsbeckite (mean: 55 ppm).

Tab. 1. Chemical composition of selected minerals in hypogene mineralization and gossan zones as basic statistical parameters: minimum (Min.): maximum (max), mean and standard deviation (SD).

Massive hypogene mineralization (chalcopyrite + nukundamite + magnetite)															
Chalcopyrite (n=7); $Cu_{0.98}Fe_{1.01}S_{1.96}$ / Theoretical formula: $CuFeS_2$															
	Wt. %			Ppm											Wt. %
	Cu	**Fe**	**S**	**Ti**	**Al**	**Mn**	**Mg**	**Si**	**Zn**	**Ni**	**V**	**Pb**	**Co**	**Au**	**Total**
Min.	34.32	29.95	33.36	-	-	-	-	-	-	-	-	-	110	-	98.80
Max.	34.81	31.07	34.57	490	3340	140	4250	3410	140	320	200	-	510	-	99.95
Mean	34.53	30.77	34.22	173	503	59	646	493	46	147	53	-	310	-	99.76
SD	0.21	0.39	0.40	182	1253	67	1592	1286	60	117	91	-	137	-	0.42
Nukundamite (n=4); $Cu_{5.07}Fe_{0.97}S_{5.87}$ / Theoretical formula: Cu_5FeS_6															
	Wt. %			Ppm											Wt. %
	Cu	**Fe**	**S**	**Ti**	**Al**	**Mn**	**Mg**	**Si**	**Zn**	**Ni**	**V**	**Pb**	**Co**	**Au**	**Total**
Min.	56.45	9.45	32.75	-	-	-	40	-	-	-	-	-	100	-	99.92
Max.	57.74	9.88	33.71	70	-	-	250	-	150	230	-	-	270	-	99.97
Mean	56.94	9.67	33.29	18	-	-	183	-	38	63	-	-	203	-	99.95
SD	0.57	0.18	0.46	35	-	-	97	-	75	112	-	-	72	-	0.02
Magnetite (n=5); $Fe_{2.92}O_{3.01}$ / Theoretical formula: Fe_3O_4															
	Wt. %		Ppm												Wt. %
	Fe	**O**	**Ti**	**Al**	**Mn**	**Mg**	**Cu**	**Si**	**Zn**	**S**	**Ni**	**V**	**Pb**	**Co**	**Au**	**P**	**Total**
Min.	70.40	20.35	-	-	-	-	-	550	-	100	160	-	10	590	-	-	91.22
Max.	70.94	21.69	60	4270	150	5820	1520	4980	230	3370	360	630	560	1160	-	-	93.97
Mean	70.66	20.80	24	938	60	1202	558	1782	86	888	274	180	358	798	-	-	92.17
SD	0.19	0.54	26	1866	78	2583	661	1851	99	1408	80	266	228	223	-	-	1.08

Tab. 1 (continuation). Chemical composition of selected minerals in hypogene mineralization and gossan zones as basic statistical parameters: minimum (Min.): maximum (max), mean and standard deviation (SD).

Breccia facies of goethite zone (goethite + native copper)																	
Goethite (n=12); $Fe_{1.0}O_{0.68}(O_{0.68}H)$ / Theoretical formula: FeO(OH)																	
	Wt. %						Ppm										Wt. %
	Al	**Cu**	**Si**	**Fe**	**P**	**O**	**Ti**	**Mn**	**Mg**	**Zn**	**S**	**Ni**	**V**	**Pb**	**Co**	**Au**	**Total**
Min.	3.56	0.31	0.61	62.47	0.40	22.63	-	-	120	-	-	640	-	50	490	-	90.62
Max.	6.14	0.81	3.19	63.28	0.50	27.93	820	110	540	390	-	1360	200	750	790	520	101.50
Mean	4.39	0.59	1.45	62.71	0.43	24.34	343	40	347	166	-	984	35	298	592	274	94.22
SD	0.88	0.15	0.95	0.24	0.03	1.90	275	39	141	125	-	241	59	228	96	165	3.89
Native copper (n=12); Cu/ Theoretical formula: Cu																	
	Wt. %	Ppm														Wt. %	
	Cu	**Ti**	**Al**	**Mn**	**Mg**	**Si**	**Zn**	**Fe**	**S**	**Ni**	**V**	**Pb**	**Co**	**Au**		**Total**	
Min.	98.94	-	130	-	-	-	-	290	-	-	-	-	-	-		99.83	
Max.	99.94	280	3190	180	190	2740	220	10780	360	140	110	230	130	370		100.70	
Mean	99.72	65	841	33	16	312	46	3940	142	27	31	46	60	56		100.28	
SD	0.30	101	1007	58	55	809	74	3104	126	50	40	79	48	111		0.29	
Pseudomalachite (n=5); $Cu_{3.66}(P_{1.73}O_4)_2(OH)_4$ / Theoretical formula: $Cu_5(PO_4)_2(OH)_4$																	
	Wt. %					Ppm										Wt. %	
	P_2O_5	**CuO**	**BaO**	**SiO_2**	**FeO**	**TiO_2**	**Al_2O_3**	**Cr_2O_3**	**MnO**	**MgO**	**CaO**	**SO_3**	**Cl**	**ZnO**	**CO_2**	**Total**	
Min.	22.54	68.41	0.27	0.24	0.26	-	180	-	-	-	-	-	-	-	-	93.11	
Max.	23.41	69.10	0.33	0.70	1.19	750	1210	420	-	180	230	-	-	420	-	94.10	
Mean	22.95	68.73	0.30	0.49	0.88	294	666	110	-	36	140	-	-	176	-	93.49	
SD	0.37	0.33	0.03	0.19	0.42	282	429	178	-	80	85	-	-	189	-	0.42	

Tab. 1 (continuation). Chemical composition of selected minerals in hypogene mineralization and gossan zones as basic statistical parameters: minimum (Min.): maximum (max), mean and standard deviation (SD).

Malachite zone (ramsbeckite + tenorite + cuprite + malachite+ chrysocolla)

Malachite (n=7); $Cu_{1.6}C_{0.99}O_3(OH)_2$ / Theoretical formula: $Cu_2CO_3(OH)_2$

	Wt. %					ppm										Wt. %
	P_2O_5	**CuO**	**BaO**	**SiO_2**	**CO_2**	**TiO_2**	**Al_2O_3**	**Cr_2O_3**	**MnO**	**MgO**	**CaO**	**SO_3**	**Cl**	**ZnO**	**FeO**	**Total**
Min.	0.44	71.02	0.25	0.06	19.65	-	390	-	-	-	-	-	-	-	-	91.71
Max.	0.89	71.89	0.31	0.17	19.89	450	1000	100	10	280	140	300	-	550	510	92.89
Mean	0.60	71.52	0.28	0.12	19.78	94	620	23	3	43	39	73	-	259	121	92.41
SD	0.16	0.32	0.02	0.04	0.09	175	216	39	5	105	66	116	-	230	179	0.40

Chrysocolla (n=2); $(Cu,Al)_{1.6}H_2Si_2O_5(OH)_4.n(H_2O)$ / Theoretical formula: $(Cu,Al)2H_2Si_2O_5(OH)_4.n(H_2O)$

	Wt. %							Ppm								Wt. %
	Al_2O_3	**MgO**	**CaO**	**CuO**	**BaO**	**SiO_2**	**FeO**	**TiO_2**	**Cr_2O_3**	**MnO**	**P_2O_5**	**SO_3**	**Cl**	**ZnO**	**CO_2**	**Total**
Mean	3.64	0.23	0.40	42.14	0.12	36.71	0.21	-	-	-	735	805	750	30	-	83.69

Ramsbeckite (n=3)

	Wt. %			ppm												Wt. %
	Cu	**S**	**O**	**Ti**	**Al**	**Mn**	**Mg**	**Si**	**Zn**	**Fe**	**Ni**	**V**	**Pb**	**Co**	**Au**	**P**	**Total**
Min.	44.08	20.01	35.55	-	-	-	-	-	120	-	-	-	-	10	-	-	99.91
Max.	44.30	20.13	35.72	320	90	80	60	-	270	200	-	30	-	140	-	-	100.02
Mean	44.19	20.07	35.63	107	30	37	30	-	213	130	-	10	-	80	-	-	99.95
SD	0.11	0.06	0.09	185	52	40	30	-	81	113	-	17	-	66	-	-	0.06

Cuprite (n=10); $Cu_{2.0}O_{1.0}$ / Theoretical formula: Cu_2O

	Wt. %						Ppm										Wt. %
	Ti	**Al**	**Mn**	**Mg**	**Cu**	**O**	**Si**	**Zn**	**Fe**	**S**	**Ni**	**V**	**Pb**	**Co**	**Au**	**P**	Total
Min.	-	-	-	-	88.46	11.19	-	-	-	-	-	-	-	-	-	-	99.77
Max.	260	260	120	150	89.27	11.36	30	210	340	1070	280	80	530	130	320	-	100.58
Mean	59	19	34	18	88.77	11.25	2	49	117	383	35	27	164	27	48	-	100.12
SD	85	67	42	48	0.21	0.05	8	69	123	308	73	33	182	52	85	-	0.21

Tenorite nodules surrounded by malachite (n=11); $Cu_{1.0}O_{1.0}$ / Theoretical formula: CuO

	Wt. %		ppm													Wt. %
	Cu	**O**	**Ti**	**Al**	**Mn**	**Mg**	**Si**	**Zn**	**Fe**	**S**	**Ni**	**V**	**Pb**	**Co**	**Au**	**P**	**Total**
Min.	79.68	20.09	-	-	-	-	-	-	-	-	-	-	-	-	-	-	99.83
Max.	80.06	20.19	120	50	190	90	20	440	550	230	230	140	480	140	-	-	100.33
Mean	79.89	20.14	11	5	64	15	2	144	102	83	62	43	92	21	-	-	100.10
SD	0.13	0.03	36	15	66	30	6	169	156	83	88	49	172	42	-	-	0.16

Tenorite nodules surrounded by ramsbeckite (n=6); $Cu_{1.0}O_{1.01}$/ Theoretical formula: CuO

	Wt. %		ppm													Wt. %
	Cu	**O**	**Ti**	**Al**	**Mn**	**Mg**	**Si**	**Zn**	**Fe**	**S**	**Ni**	**V**	**Pb**	**Co**	**Au**	**P**	**Total**
Min.	79.54	20.15	-	-	-	-	-	-	-	110	-	-	-	-	-	-	99.97
Max.	80.10	20.60	80	590	100	6150	600	200	260	490	250	210	110	60	330	-	100.93
Mean	79.87	20.35	22	277	27	2238	198	80	90	237	68	57	22	20	55	-	100.56
SD	0.22	0.16	35	305	39	2288	246	94	99	146	98	82	44	25	135	-	0.36

Tab. 1 (continuation). Chemical composition of selected minerals in hypogene mineralization and gossan zones as basic statistical parameters: minimum (Min.): maximum (max), mean and standard deviation (SD).

Cuprite zone (chalcocite + goethite + cuprite + tenorite)																	
Cuprite (n=2); $Cu_{2.0}O_{1.01}$ / Theoretical formula: Cu_2O																	
	Wt. %		ppm														Wt. %
	Cu	**O**	**Ti**	**Al**	**Mn**	**Mg**	**Si**	**Zn**	**Fe**	**S**	**Ni**	**V**	**Pb**	**Co**	**Au**	**P**	Total
Mean	88.90	11.25	170	-	-	45	-	195	95	230	-	5	25	70	-	-	100.24
Tenorite (n=2); $Cu_{1.0}O_{1.0}$ / Theoretical formula: CuO																	
	Wt. %		Ppm														Wt. %
	Cu	**O**	**Ti**	**Al**	**Mn**	**Mg**	**Si**	**Zn**	**Fe**	**S**	**Ni**	**V**	**Pb**	**Co**	**Au**	**P**	Total
Mean	79.81	20.15	120	-	30	-	-	100	250	230	45	-	-	15	-	-	100.04
Goethite (n=4); $Fe_{1.0}O_{0.58}(O_{0.58}H)$ / Theoretical formula: FeO(OH)																	
	Wt. %					ppm											Wt. %
	Al	**Cu**	**Si**	**Fe**	**O**	**Ti**	**Mn**	**Mg**	**Zn**	**S**	**Ni**	**V**	**Pb**	**Co**	**Au**	**P**	**Total**
Min.	1.20	0.58	0.54	62.29	20.37	-	200	480	370	-	600	20	190	550	-	-	86.42
Max.	3.06	0.86	0.77	63.16	21.46	80	480	1100	890	-	1440	210	440	630	-	-	88.32
Mean	2.15	0.69	0.65	62.64	20.90	28	298	795	655	-	995	100	330	585	-	-	87.41
SD	0.98	0.12	0.11	0.38	0.62	38	128	254	236	-	377	80	120	41	-	-	1.05
Chalcocite (n=4); $Cu_{1.99}S_{0.99}$ / Theoretical formula: Cu_2S																	
	Wt. %			ppm												Wt. %	
	Cu	**Fe**	**S**	**Ti**	**Al**	**Mn**	**Mg**	**Si**	**Zn**	**Ni**	**V**	**Pb**	**Co**	**Au**	**Total**		
Min.	78.91	0.27	19.38	-	-	-	40	-	-	-	-	-	-	-	99.92		
Max.	79.75	1.06	20.26	170	240	330	330	-	-	90	-	-	150	-	99.97		
Mean	79.33	0.62	19.93	73	60	128	208	-	-	38	-	-	63	-	99.94		
SD	0.35	0.34	0.39	86	120	147	126	-	-	38	-	-	75	-	0.03		

5 Discussion

5.1 Mineralogical successions

In each gossan zone (e.g., goethite, malachite, cuprite, and libethenite zones), mineralogical successions were defined. Namely, mineral phases whose textural relationships suggest variations in the physicochemical conditions of the mineralizing environment were determined regardless of equilibrium and summarized in Fig. 7. The successions presented below are influenced by percolating solutions, carrying ions released by hypogene minerals, which migrate downwards and laterally until reaching microenvironments with specific pH and Eh that allow the formation of cupper-bearing newly formed minerals (Thornber, 1985; Thornber and Taylor, 1992).

5.1.1 Succession I: Goethite - malachite (cavity-filling facies of goethite zone)

The cavity-filling facies of the goethite zone was formed by the dissolution of chalcopyrite from hypogene mineralization (Fig. 3A), as suggested by their partially angular shapes (Gandhi and Sarkar, 2016). Iron was retained as goethite at practically the same site where it was released by chalcopyrite due to the oxidation of Fe^{2+} to Fe^{3+}, suggesting slightly acidic conditions (Fig. 8A). This pH is in accordance with the low acidification potential of chalcopyrite when compared to other sulfide minerals with higher sulfur contents (Nickel 1984; Chávez 2000; Atapour and Aftabi 2007). The subsequent coating of the goethite films by malachite (Fig. 3C; 6Ai) marks the transition from a slightly acidic to an alkaline environment (Fig. 8B). This process was conditioned by the availability of Cu^{2+} derived from chalcopyrite and CO_3^{2-}/HCO_3^- released during the dissolution of calcite, unstable under acidic conditions (e.g., Brown 2005; Putter et al. 2010; Papineau 2020).

5.1.2 Succession II: Goethite - chalcocite (fracture-filling facies of goethite zone)

The coating of goethite by chalcocite along the fracture-filling facies of the goethite zone (Fig. 3G; 6Aii) shows fluctuations between oxidizing and reducing conditions owing to the vertical movement of the water table. In this context, local solutions containing SO_4^{2-} and Cu^{2+} (derived from chalcopyrite dissolution) formed a secondary sulfide zone superimposed on the oxidizing environment in which goethite was previously stablished (e.g., Sato 1992; Atapour and Aftabi 2007).

5.1.3 Succession III: Goethite - native copper (breccia facies of goethite zone)

In some portions of the breccia facies of the goethite zone, subhedral crystals of native copper were the first minerals to occupy the cavities left by chalcopyrite dissolution (Fig. 5B, C; 6Bi). The involvement of these crystals by goethite suggests that in the first stage, more reducing conditions dominated, becoming more oxidizing later (Thornber 1985; Bigham and Nordstrom 2000; Pires et al. 2020). The presence of native copper also limits this portion of the mineralizing environment to pH <6. Cu^{+} convolution occurs only under these conditions, according to the reaction $2Cu^{+} \rightarrow Cu^{2+} + Cu$, which subsequently converged to the slightly acidic pH at which goethite was formed (Thornber, 1985; Bigham and Nordstrom, 2000).

5.1.4 Succession IV: Goethite - pseudomalachite (breccia facies of goethite zone)

The partial filling of the boxwork features with goethite walls by pseudomalachite (e.g., Fig. 5D, E; 6Bii) reflects the transition to more alkaline conditions required to form this mineral compared to goethite (Magalhães et al. 1986; Bigham and Nordstrom 2000; Crane et al. 2001). The availability of $H_2PO_4^{-}{}_{(aq)}$ or $HPO_4^{2-}{}_{(aq)}$ for pseudomalachite formation depends on the presence of apatite as a gangue mineral in hypogene mineralization (e.g., Crane et al. 2001). This process is also controlled by gossan evolution in distinct pulses with a variable capacity to dissolve apatite.

5.1.5 Succession V: Malachite - tenorite - chrysocolla (malachite zone)

Tenorite was the first phase to form, subsequently surrounded by malachite and chrysocolla micromasses, suggesting an increase in the Eh (Fig. 8B). Under these conditions, malachite precipitation was made possible by the availability of CO_3^{2-}, leading to the reaction $2Cu^{2+} + CO_3^{2-} + 2OH^{-} \rightarrow Cu^{2}(CO_3)(OH)_2$ typical of alkaline conditions (Anderson, 1982; Nickel, 1984; Siuda and Kruzzewski 2013). Simultaneously, supersaturation in $H_4SiO_4^{-}{}_{(aq)}$, possibly derived from the partial dissolution of chlorite, and slightly acidic to alkaline pH (Williamson 1994; Yates et al. 1998; Crane et al. 2001) allowed the polymerization of silica and formation of the colloidal precursor to chrysocolla (Krauskopf 1959; Putter et al. 2010), Figs. 5I and 6Ci.

5.1.6 Succession VI: Malachite - cuprite - tenorite - ramsbeckite (malachite zone)

The presence of cuprite suggests a pH of <6, under which Cu^{2+} tends to act as a catalyst for the interaction of Fe^{3+} with water, according to the reaction $7H_2O + Fe^{2+} + Cu^{2+} \rightarrow 2Fe(OH)_3 + Cu_2O + 8H^{+}$, forming cuprite as a product (Blanchard 1968). The formation of tenorite at the

edges of cuprite crystals indicates the presence of water in the interstices, which produces favorable conditions for Cu oxidation along with the reduction of dissolved oxygen in the water. This process is in accordance with the partial reactions $Cu_2O + H_2O \rightarrow 2CuO + 2H^+ + 2e^-$ and $1/2H_2O + H_2O + 2e^- \rightarrow 2OH^-$, which results in the overall reaction $Cu_2O + ½O_2 \rightarrow 2CuO$ (Echavarría et al. 2009) during which tenorite is formed, indicating an increase in Eh (Fig. 8C). As discussed in Section 5.1.5, the involvement of cuprite/tenorite by malachite suggests a pH increase (Fig. 5J; 6Cii).

5.1.7 Succession VII: Cuprite- tenorite - native copper - goethite - chalcocite (cuprite zone)

The occurrence of cuprite-tenorite-goethite with native copper and chalcocite provides evidence for the fluctuation of the oxidation potential of the mineralizing environment (Figs. 5M-O; 6D). The formation of chalcocite occurred in a previous reducing zone (e.g., Belogub et al. 2008). The skeletal aspect suggests that it is a relic, now subordinated to minerals typical of the oxidation zone, such as goethite, cuprite, and tenorite. The latter may have been formed from cuprite oxidation (as described in Section *5.1.6.*) or via the direct oxidation of S in the chalcocite, according to the reaction $Cu_2S + 3O_2 + H_2O \rightarrow CuSO_4 + CuO + 2OH^-$ (Blanchard 1968). Conversely, native copper, which usually forms under more reducing conditions than cuprite, tenorite, and goethite (Thornber 1985), is superimposed on these minerals given their arrangement along the fracture zones. This indicates local Eh fluctuations, suggesting vertical migration of the water table.

5.1.8 Succession VIII: Libethenite - malachite - pseudomalachite (libethenite zone)

The dissolution of apatite, identified as an accessory mineral in massive and disseminated mineralization, provided $H_2PO_4^-{}_{(aq)}$ or $HPO_4^{2-}{}_{(aq)}$ in interstitial solutions to induce the formation of libethenite. This phase, distributed along the fractures of granodiorites (Fig. 6Ei), requires high concentrations of phosphate ions to form, leading to the lower concentrations in which pseudomalachite can still precipitate (e.g., Robie and Hemingway 1995; Clissold 2007), as indicated in Fig. 8D. The presence of malachite in this succession reflects the dissolution of calcite associated with chalcopyrite in the hypogene ore.

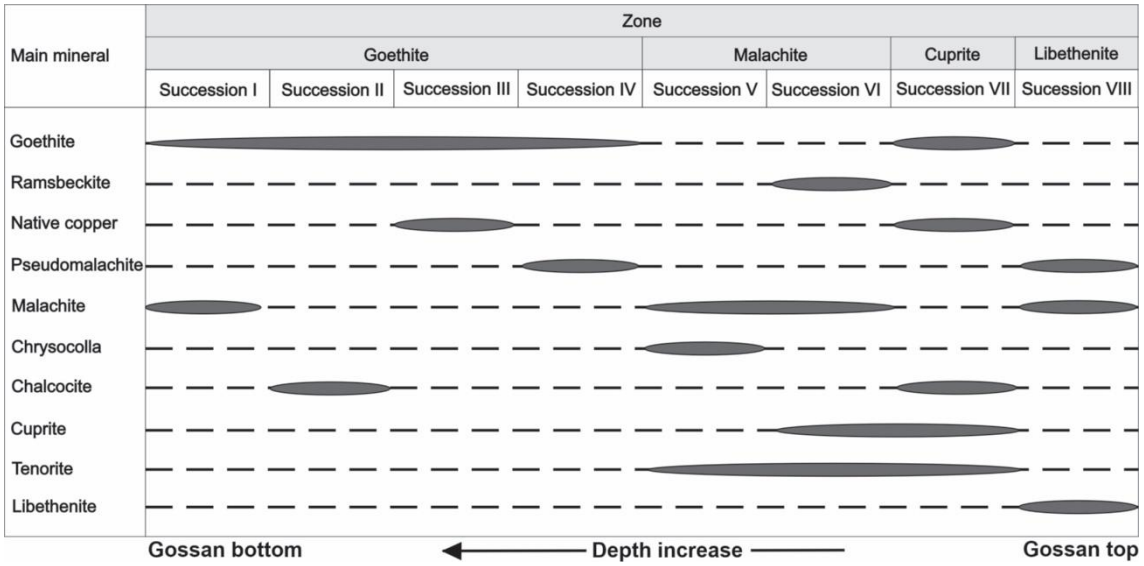

Fig. 7 Distribution of newly formed minerals in the Alvo 118 gossan, grouped in mineral successions.

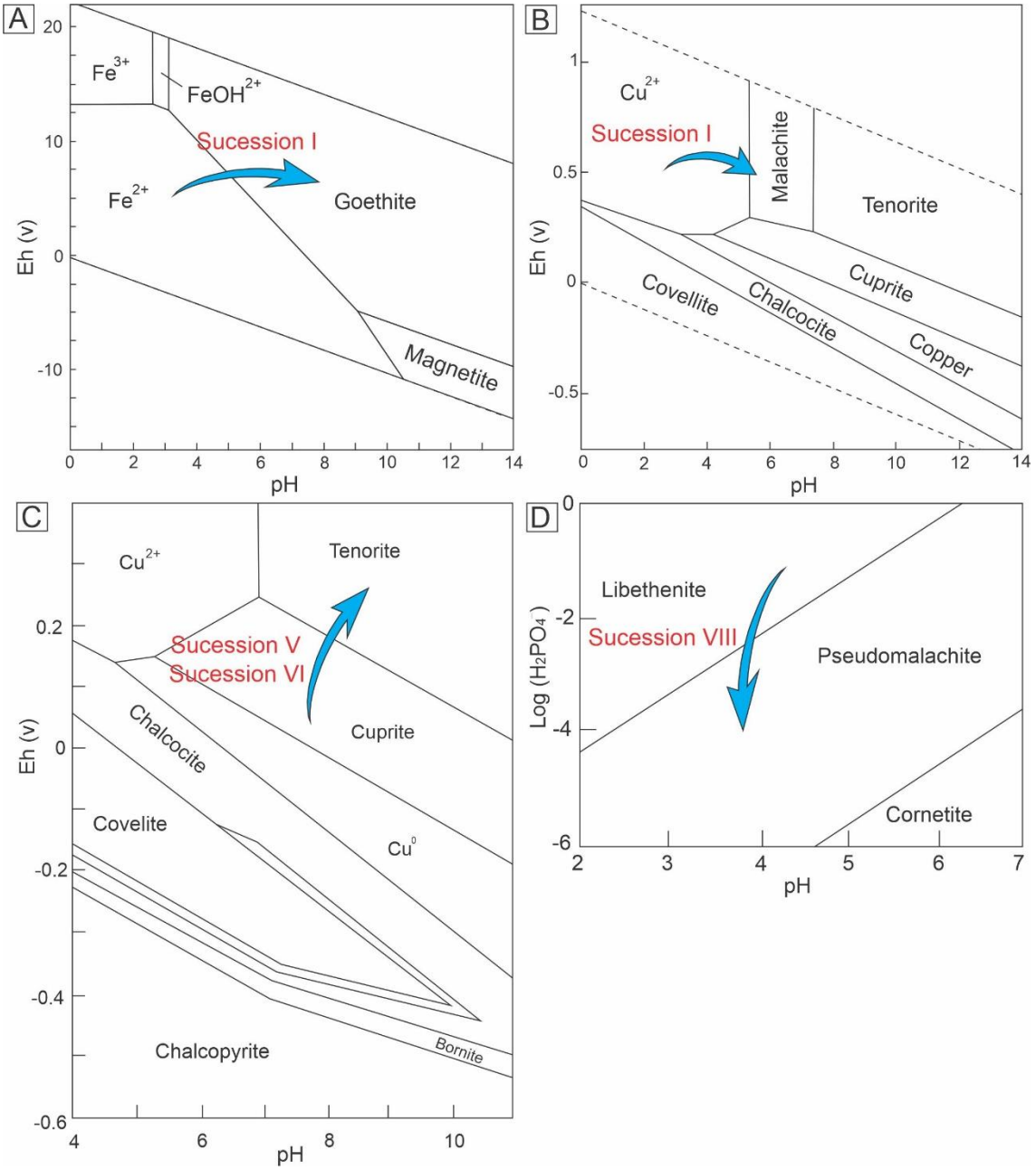

Fig. 8 Variations in the prevailing pH-Eh conditions during gossan formation indicated by arrows. A) Goethite and Fe^{2+} stability fields at 8 °C (Samolczyk et al. 2012). B) Stability diagrams for copper and its ionic species considering groundwater as a reference, $PCO_2 = 10^{-2}$ (Putter et al. 2010). C) Cu-Fe-SOH system at 25 °C and 1 atm, considering S activity as 0.1, within and near the hematite stability field (Sato 1992). D) pH-$H_2PO_4^{2-}$ equilibrium diagram for secondary copper phosphates at 25 °C, where the boundaries between the fields refer to equations in which copper activity is invariable (Crane et al. 2001).

5.2 Geochemical fractionation

Among the main trace elements identified in chalcopyrite (Mn, Zn, Co, Ni, Ti, Al, Mg, Si, and V), Mn, Zn, and Co are typically incorporated into the structure of this mineral, particularly in hydrothermal deposits, and Ni has also been detected (Demir et al. 2008; Helmy et al. 2014; Wang et al. 2014; Sadati et al. 2016; George et al. 2018). Chalcopyrite may show a higher content and variety of trace elements when other sulfide minerals with greater

incorporation capacity, such as sphalerite and galena, are absent, which is the case for the Alvo 118 deposit (Cook et al. 2009; George et al., 2015, 2016).

Although chalcopyrite is formed by covalent bonds between $Cu^{+}Fe^{3+}S_2^{3-}$ and $Cu^{2+}Fe^{3+}S_2^{2-}$ (Li et al. 2013), Goldschmidt rules can be used to explain the high contents of Mn, Zn, Co, and Ni. The ionic rays of these elements in the divalent state and tetrahedral coordination are in the interval between the values of Fe^{3+} and Fe^{2+} (e.g., George et al. 2018). Conversely, the presence of Ti, Al, Mg, Si, and V indicates some interference from gangue minerals, especially chlorite plates, associated with chalcopyrite (Fig. 5A). The non-detection of Ag, Pb, and Au supports that these elements are restricted to solid inclusions.

Nukundamite, locally associated with chalcopyrite, with a mean stoichiometric ratio of $Cu_{5.07}Fe_{0.97}S_{5.87}$, which is very close to its ideal chemical formula, Cu_5FeS_6, is usually formed by hydrothermal processes (e.g., Sillitoe and Clark 1969; Clark 1970; Rice et al. 1979; Hatert 2003). Significant concentrations of Ti, Mg, Ni, Zn, or Co in nukundamite have not been reported in previous research.

Magnetite ($Fe_{2.92}O_{3.01}$) is slightly nonstoichiometric, suggesting the beginning of its transformation into hematite, which can occur even under hydrothermal conditions (Zhao et al. 2019). The main trace elements identified in magnetites from Alvo 118 (i.e., Ti, Al, Mn, Mg, Cu, Si, Zn, Ni, and Co) are commonly detected in magnetites from magmatic and hydrothermal deposits worldwide (Dare et al. 2014; Mavrogonatos et al. 2019). Silicon is uncommon in magnetites, although it has been detected in rare skarn-type deposits (Shimazaki 1998; Dare et al. 2014; Nadoll et al. 2014).

Goethite shows high contents of Al and Si due to its ability to trap minuscule silicate particles during its formation (Velasco et al. 2013); that is, Al would not be in isomorphic substitution, as usually occurs in supergene environment (e.g., Fitzpatrick and Schwertmann 1982; Carlson 1995; Liu et al. 2014). This was confirmed by the identification of chlorite crystallites associated with goethite, which also clarifies the high Mg contents in goethite (Figure 5A). Likewise, The P contents in goethites are attributed to pseudomalachite filling cavities in goethite micromass (Fig. 5D).

Goethite also contains various trace elements partially equivalent to those identified in the minerals from hypogene mineralization (chalcopyrite, nukundamite, magnetite), mainly Ti, Mn, Zn, Ni, V, and Co, in accordance with its strong ability to adsorb metals and metallic

compounds (Dzombak and Morel 1990; Rose and Bianchi-Mosquera 1993). Gold (mean: 274 ppm) and Pb (mean: 298 ppm) were identified in the goethite, although the former was not detected in hypogene mineralization and the later was only detected in magnetite.

Due to its wide distribution, malachite is also an important trace element-bearing mineral in the Alvo 118 gossan, mainly Ba, Ca, Cr, Fe, Mn, and Zn (e.g., Papineau 2020). This can be partly attributed to the presence of other minerals from the malachite-rosasite group with the general formula $M_2^{2+}(CO_3)(OH)_2$, in which bivalent metals (M) can replace copper at two octahedral sites (Perchiazzi 2006; Driscoll et al. 2011; Perchiazzi et al. 2018). Pseudomalachite, chrysocolla, cuprite, tenorite, native copper, and chalcocite are secondary carriers of trace elements because they are less abundant than goethite and malachite.

5.3 Mineralizing environment

Mineralogical and textural data were used to determine physicochemical characteristics of the mineralizing environment. The domain of chalcopyrite and its low S/Cu ratio compared with other more acidifying sulfide minerals resulted in the formation of a slightly acidic environment (Chávez 2000; Atapour and Aftabi 2007). These conditions were favorable for the *in-situ* precipitation of iron oxyhydroxides (i.e., goethite zone) after the oxidation of Fe^{2+} released by chalcopyrite, forming a halo adjacent to the hypogene mineralization. This halo should not be confused with leached cappings, which are typical of the outcropping top of mature gossans (Taylor 2011; Kříbek et al. 2016).

The occurrence of skeletal chalcocite in the cuprite zone indicates the initial formation of a secondary sulfide zone, which is subsequently destabilized by the continuous increase in Eh. Thus, the relics of the secondary sulfide zone (i.e., chalcocite) are surrounded by superimposed mineral phases such as cuprite, tenorite, and goethite (Cuadra and Rojas 2001; Kříbek et al. 2016)

The increase in Eh was confirmed by the involvement of native copper by goethite (Fig. 5B, C) and the replacement of cuprite by tenorite (Fig. 5K) in the goethite and malachite zones, respectively. Therefore, this appears to be a general trend the studied mineralizing environment. Conversely, there were local fluctuations in Eh, as evidenced by a second generation of chalcocite superimposed on iron oxyhydroxides in the fracture of the goethite zone (Fig. 3G) as well as the native copper veinlets crosscutting iron oxyhydroxides and copper oxides in the cuprite zone (Fig. 5N).

The acid solutions produced by chalcopyrite oxidation were gradually neutralized by gangue minerals and host rocks. Some of these are essential sources of cations that can consume hydrogen ions via hydrolysis. This favored the formation of a broad spectrum of copper minerals in gossan (Amcoff and Holényi 1996). Thus, the mineral successions reflect the progressive alkalinization of the mineralizing environment, as revealed by the coating of goethite by malachite (Fig. 3B) and by the development of the malachite and libethenite zones.

Although the mineralogical successions point to a broad trend of increasing pH, the gossan formation was marked by development in microenvironments with independent evolutions. This was favored by the heterogeneous distribution of hypogene mineralization, interspersed with non-mineralized zones, and the presence of host rocks with distinct buffering capacity (chloritites and granodiorites). Thus, the isolated microenvironments were precursors of goethite, malachite, cuprite, and libethenite zones.

The low reactivity of chloritites is due to the chlorite domain formed by hydrothermal phyllic alteration, which has a lower cation exchange capacity than feldspars (Chávez 2000; Nash 2004). In contrast, granodiorites were more affected by the acidity of the gossan environment, which accelerated the hydrolysis reactions of plagioclase and alkali feldspar, resulting in neutralization of the percolating solutions (e.g., Chávez, 2000, 2021). Calcite and apatite (gangue minerals) also contribute significantly to fluid neutralization and the release of ionic compounds such as CO_3^- and PO_4^- to the precipitation of newly formed minerals (e.g., Verhaert et al. 2018).

5.4 Gossan generation

Chalcopyrite dissolution controlled the initial stage of supergene evolution; this finding is compatible with the electrochemical model widely used to explain gossan formation (Sato and Mooney 1960; Nickel et al. 1974; Thornber 1985). In this model, at the lower limit of the water table, the reduction of oxygen (cathode) dissolved in the water is induced by an upward electron flow along the solid surface of the hypogene sulfide, (Fig. 9), resulting in the oxidation of the more reactive end of the sulfide orebody (anode) (Thornber, 1985; Thornber and Taylor, 1992). Thus, the oxidation of S and consequent decomposition of chalcopyrite develops according to the reaction $CuFeS_2 + 4.25O_2 + 1.5H_2O \rightarrow Cu^{2+} + 2SO_4^{2-} + 4H^+ +$ FeO(OH) (Siuda and Kruszewski, 2013). Further studies are needed to verify the role of bacteria in the formation of Alvo 118 gossan, as bioinduced oxidoreduction in natural environments is considered increasingly relevant (Enders et al. 2006; Nordstrom 2011; Zammit et al. 2015).

The oxi-reductive nature of the mineralizing environment allowed on the other hand the formation of chalcocite (secondary sulfide) in the initial stage of gossan development. However, the continuous deepening of the water table destabilized this mineral, as evidenced by the skeletal relics identified in the cuprite zone, compatible with more oxidizing conditions (Taylor et al., 1980; Kříbek et al., 2016).

The relative preservation of minerals forming the host rock around and just above the gossan, with little evidence of weathering, suggests that gossan formation occurred predominantly below the water table. Based on the development of the weathering profile on the covering host rocks, it was possible to interpret that the lower limit of the water table was ~35 m. Above this depth, the chlorites evolved to form saprolite by hydrolysis reactions and intense leaching. However, seasonal downward trend of the water table, facilitate by the fracture system (Fig. 9), played an important role in bringing oxygen-bearing water to the deep hypogene mineralization (e.g., Alpers and Brimhall, 1989; Reich et al. 2009; Vasconcelos et al. 2015). This was revealed by mineral successions, compatible with Eh oscillations, and by the distribution of the newly formed minerals along fractures, suggesting chemical transportation by water.

This process exerts a considerable influence on gossan development because even in small amounts, water with dissolved oxygen is crucial for destabilizing chalcopyrite. In this scenario, Eh became oxidizing for sulfur in the chalcopyrite structure but still allowed chalcocite formation, which is typical of a reducing environment. Despite the common precursor, that is, massive or disseminated chalcopyrite, the gossan zones evolved independently because the non-mineralized sections of the host rock physically separated them. Thus, the development of each gossan zone was mainly affected by interactions with gangue minerals (especially calcite and apatite) and secondarily by chloritites and granodiorites.

The dissolution of chalcopyrite produced slight acidic pH, favoring the dissolution of calcite following the reaction $CaCO_3 + H^+ \rightleftharpoons Ca^{2+} + HCO_3^-$ (Sverdrup 1984; Horta et al. 2017). Under similar pH conditions, apatite was also dissolved according to $Ca_{10}(PO_4)_6(F,OH)_2 + 14H^+ \rightleftharpoons 10Ca^{2+} + 6H_2PO_4^- + 2HF, H_2O$ (Dorozhkin 1997; Tõnsuaadu et al. 2021). Both reactions show that calcite and apatite consume H^+ when interacting with acidic solutions (Rose et al. 1979; Chávez 2000; Kahou et al. 2021). In addition, HCO_3^- and $H_2PO_4^-$ were released, allowing the formation of malachite, pseudomalachite, and libethenite.

The most abundant and reactive minerals in the chloritites were chlorite and plagioclase. The decomposition of chlorite can be expressed as $(Mg,Fe,Al)_6[AlSi_3O_{10}](OH)_8 + 16H^+ \rightarrow [6(Mg,Fe,Al)]^{13+} + Al^{3+} + 3H_4SiO_4 + 6H_2O$ (Lowson et al. 2005; Alekseyev 2007), and plagioclase decomposition follows the reaction $CaAl_2Si_2O_8 + H_2O + 2H^+ \rightarrow Ca^{2+} + Al_2Si_2O_5(OH)_4$, which has kaolinite as a by-product, as often identified as irregular pockets associated with malachite (e.g., Dayal 2007), Fig. 4C. The hydrolysis of plagioclase was dominant in the mineralization portions hosted by granodiorites, as previously described. Orthoclase was also decomposed, following the reaction $2KAlSi_3O_8 + 2H^+ + H_2O \rightarrow 2\ K^+ + Al_2Si_2O_5(OH)_4 + 4SiO_2$, with kaolinite formation and silica release (Clark 2015).

The association of hypogene mineralization styles and host rocks with the corresponding gossan zone is shown in Fig. 9. The massive hypogene ore was converted into the breccia facies of the goethite zone due to the poor interaction with the hosting chloritites and possibly a lack of reactive gangue minerals. Therefore, Cu and sulfate were lost by the system, and only Fe, which is the least mobile component of hypogene sulfides, concentrated as massive goethite surrounding relic quartz grains. In some portions where Cu was still available, due to a slightly higher pH, the cuprite zone was developed, also following the massive style of the precursor hypogene mineralization. The malachite zone formation took place in a similar context, reflecting the local availability of phosphate and carbonate ions. Conversely, disseminated hypogene mineralization in stockwork veins hosted by chloritites produced portions of the cavity-filling facies of the goethite zone in the sites previously occupied by chalcopyrite; and disseminated hypogene ore hosted by granodiorites resulted in the formation of the libethenite zone along the fracture system.

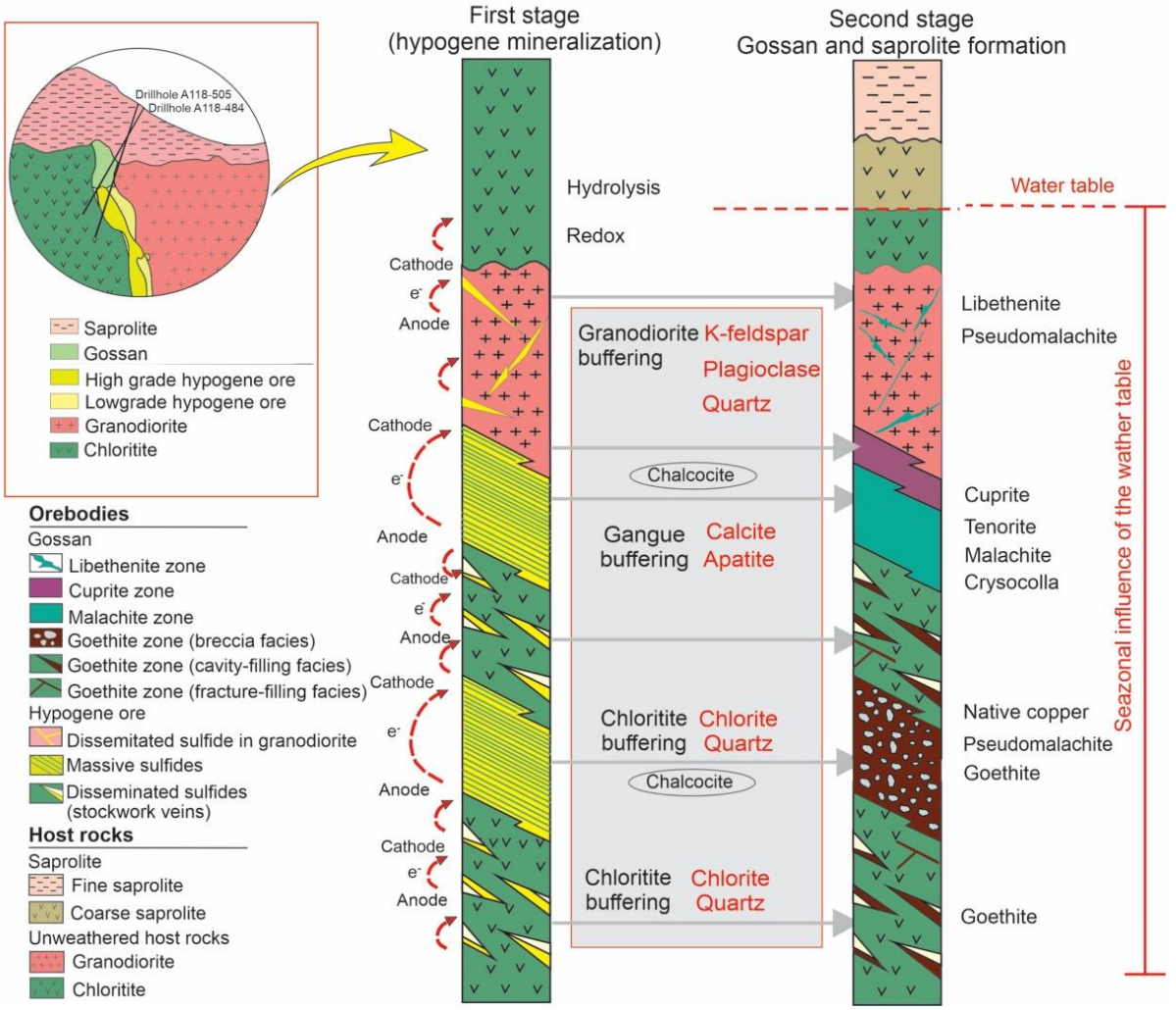

Fig. 9 Alvo 118 supergene evolution stages emphasizing distinct hypogene mineralization styles, host rocks, and corresponding gossan zones. The first stage represents interpreted distribution os the hypogene mineralization, while the second stage shows gossan formation in the zone of influence of the water table and weathering of the host rocks near the surface.

6 Conclusions

The Alvo 118 deposit presents a polyphasic metallogenetic evolution in which gossan-type mineralization is superimposed on hydrothermal sulfide ore. The mineral successions identified in the gossan reflect the progressive evolution of mineralizing solutions from slightly acidic to neutral or slightly alkaline conditions, which is mainly influenced by the interaction with gangue minerals (calcite and apatite), and, at a lower intensity, with granodiorites and chloritites. Mineral successions in each gossan zone point to a continuous increase in the oxidation potential of the supergene mineralizing environment, with some oscillations related to water table fluctuations.

The goethite (breccia facies), malachite, and cuprite zones were formed from massive hypogene mineralization. The precursors of the first two were hosted by chloritites and the latter

by granodiorite. In contrast, the cavity-filling facies of the goethite zone and the libethenite zone are derived from disseminated mineralization hosted by chloritites and granodiorites, respectively. The main trace elements in the hypogene mineralization (Ti, Mn, Zn, Ni, V, Co) were incorporated into the gossan mainly by goethite. Malachite is mostly related to retention of Ba, Ca, Cr, Mn, and Zn. Gold and Pb are restricted to cuprite, tenorite, and native copper.

In the CMP, the development of the Alvo 118 gossan represents a supergene metallogenetic stage preserved from lateritization events that widely affected the region, hosted by relatively well-preserved chlorites and granodiorites. Thus, Alvo 118 differs from most gossans that have been studied so far in the CMP, and other equivalent orebodies must be distributed in the flattened areas around the Carajás Mountains and in deep hypogene sulfide deposits worldwide.

A**cknowledgments**

The authors thank Vale S.A. for access to exploration areas, logistical support during field activities, and access to drill records and exploratory data; the geologist Clóvis Maurity for the intermediation of the partnership with Vale S.A.; and the Geosciences Institute of the Federal University of Pará for the analytical facilities. This work was supported by the National Council for Scientific and Technological Development (CNPq) [305015/2016-8; 442871/2018-0].

References

Albuquerque, M . A . C ., Andrade, P . J . M . B ., Maurity, C ., Kwitko, R ., 2001. Geologia e características das mineralizações cupríferas do depósito Alvo 118, Província Mineral de Carajás, Pará, Brasil. VII Simpósio de Geologia da Amazônia. 5–8.

Alekseyev, V . A ., 2007. Equations for the dissolution reaction rates of montmorillonite, illite, and chlorite. Geochem. Int. 45 (8), 770–780. https://doi.org/10.1134/S0016702907080046.

Alpers, C . N ., Brimhall, G . H ., 1989. Paleohydrologic evolution and geochemical dynamics

of cumulative supergene metal enrichment at La Escondida, Atacama Desert, Northern. Chile. Econ. Geol. 84, 229–255. https://doi.org/10.2113/gsecongeo.84.2.229.

Amcoff, Ö ., Holényi, K ., 1996. Mineral Formation on Metallic Copper in a “Future Repository Site Environment. Swedish Nuclear Power Inspectorate, Stockholm.

Anderson, A . J ., 1982. Characteristics of leached capping and techniques of appraisal. In:

Titley, S . R . (Ed.), Advances in Geology of the Porphyry Copper Deposits. first ed., University Arizona Press, Tucson, pp. 275–295. https://doi.org/10.1029/EO064i009p00085. Southwesten North America.

Andreu, E ., Torró, L ., Proenza, J . A ., Domenech, C ., García-Casco, A ., Villanova de Benavent, C ., Chavez, C ., Espaillat, J ., Lewis, J . F ., 2015. Weathering profile of the Cerro de Maimón VMS deposit (Dominican Republic): textures, mineralogy, gossan evolution and mobility of gold and silver. Ore Geol. Rev. 65, 165–179. https://doi.org/10.1016/j.oregeorev.2014.09.015.

Andrew, R . L ., 1984. The geochemistry of selected base-metal gossans, southern Africa. J. Geochem. Explor. 22, 161–192. https://doi.org/10.1016/0375-6742(84)90011-6.

Araújo Filho, R . C ., Nogueira, A . C . R ., Araújo, R . N ., 2020. New stratigraphic proposal of a Paleoproterozoic siliciclastic succession: implications for the evolution of the Carajás Basin, Amazonian craton, Brazil. J South Amer Earth Sci 102, 102665. https:// doi.org/10.1016/j.jsames.2020.102665.

Atapour, H ., Aftabi, A ., 2007. The geochemistry of gossans associated with Sarcheshmeh porphyry copper deposit, Rafsanjan, Kerman, Iran: implications for exploration and the environment. J. Geochem. Explor. 93 (1), 47–65. https://doi.org/10.1016/j.gexplo.2006.07.007.

Belogub, E . V ., Novoselov, K . A ., Yakovleva, V . A ., Spiro, B ., 2008. Supergene sulphides and related minerals in the supergene profiles of VHMS deposits from the South Urals. Ore Geol. Rev. 33, 239–254. https://doi.org/10.1016/j.oregeorev.2006.03.008.

Bigham, J . M ., Nordstrom, D . K ., 2000. Iron and aluminum hydroxysulfates from acid sulfate waters. Rev. Mineral. Geochem. 40, 351–403. https://doi.org/10.2138/rmg.2000.40.7.

Blanchard, R ., 1968. Interpretation of leached outcrops. Nev. Bur. Mine. Bull. 66, 1–196.

Boyle, D . R ., 1993. Oxidation of massive sulfide deposits in the Bathurst mining Camp, new brunswick. In: Alpers, C . N ., Blowes, D . W . (Eds.), Environmental Geochemistry of Sulfide Oxidation. American Chemical Society, Washington, pp. 535–550. https://doi.org/10.1021/bk-1994-0550.ch032.

Brown, A . C ., 2005. Refinements for footwall red-bed diagenesis in the sediment-hosted stratiform copper deposits model. Econ. Geol. 100, 765–771. https://doi.org/10.2113/gsecongeo.100.4.765.

Carlson, L ., 1995. Aluminum substitution in goethite in lake ore. Bull. Geol. Soc. Finland 67 (1), 19–28.

Chávez, W ., 2000. Supergene oxidation of copper deposits: zoning and distribution of copper oxide minerals. Soc of Econ Geol News 41, 10–21. https://doi.org/10.5382/SEGnews.2000-41.fea.

Chávez, W . X ., 2021. Weathering of copper deposits and copper mobility: mineralogy, geochemical stratigraphy, and exploration implications. Soc Econ Geol Discov 126, 16–27. https://doi.org/10.5382/SEGnews.2021-126.fea-01.

Clark, A . H ., 1970. An occurrence of the assemblage native sulfurcovellite-"Cu5.5xFexS6.5x", Aucanquilcha, Chile. Am. Mineral. 55 (5–6), 913–918.

Clark, Y ., 2015. Groundwater Geochemistry and Isotopes. CRC Press, Boca Raton. https://doi.org/10.1201/b18347.

Clissold, M . E ., 2007. Aspects of the Supergene Geochemistry of Copper, Nickel and Bismuth. Thesis. Western Sydney University.

Cook, N . J ., Ciobanu, C . L ., Pring, A ., Skinner, W ., Shimizu, M ., Danyushevsky, L ., Saini-

Eidukat, B ., Melcher, F ., 2009. Trace and minor elements in sphalerite: a LA-ICP-MS study. Geochem. Cosmochim. Acta 73, 4761–4791. https://doi.org/10.1016/j.gca.2009.05.045.

Costa, M . L ., Angélica, R . S ., Costa, N . C ., 1999. The geochemical association Au–As–B–(Cu) –Sn–W in latosol, colluvium, lateritic iron crust and gossan in Carajás, Brazil: for primary ore identification. J. Geochem. Explor. 67, 33–49. https://doi.org/10.1016/S0375-6742(99)00065-5.

Costa, M . L ., Angélica, R . S ., Fonseca, L . R ., 1996. Geochemical exploration for gold in deep weathered lateritized gossans in the Amazon region-Brazil: a case history of the Igarapé Bahia deposit. Geochim. Bras. 13–26.

Crane, M . J ., Sharpe, J . L ., Williams, P . A ., 2001. Formation of chrysocolla and secondary copper phosphates in the highly weathered supergene zones of some Australian deposits. Record Aust. Mus. 53 (1), 49–56. https://doi.org/10.3853/j.0067-1975.53.2001.1323.

Cuadra, P ., Rojas, G ., 2001. Oxide mineralization at the radomiro tomic porphyry copper deposit, northern Chile. Econ. Geol. 96, 387–400. https://doi.org/10.2113/gsecongeo.96.2.387.

Dall'Agnol, R ., Lafon, J . M ., Macambira, M . J . B ., 1994. Proterozoic anorogenic magmatism

in the central amazonian province, amazonian craton: geochronological, petrological and geochemical aspects. Min. Pet. 50, 113–138. https://doi.org/10.1007/BF01160143.

Dall'Agnol, R ., Oliveira, M . A ., Almeida, J . A . C ., Althoff, F . J ., Leite, A . A . S ., Oliveira, D . C ., Barros, C . E . M ., 2006. Archean and paleoproterozoic granitoids of the Carajás metallogenetic province, eastern amazonian craton. In: Dall'Agnol, R ., Rosa Costa, L . T ., Klein, E . L . (Eds.), Symposium on Magmatism, Crustal Evolution, and Metallogenesis of the Amazonian Craton. pp. 99–150.

Dare, S . A . S ., Barnes, S . J ., Beaudoin, G ., et al., 2014. Trace elements in magnetite as petrogenetic indicators. Miner. Deposita 49 (7), 785–796. https://doi.org/10.1007/s00126-014-0529-0.

Dayal, A . M ., 2017. Exploration technique. In: Dayal, A . M . (Ed.), Shale Gas Exploration and Environmental and Economic Impacts. pp. 65–93. https://doi.org/10.1016/B978-0-12-809573-7.00005-6.

Del Real, I ., Reich, M ., Simon, A . C ., et al., 2021. Formation of giant iron oxide-copper-gold deposits by superimposed, episodic hydrothermal pulses. Commun Earth Environ 2, 192. https://doi.org/10.1038/s43247-021-00265-w.

Delvigne, J . E ., 1999. Atlas of Micromorphology of Mineral Alteration and Weathering, vol. 3. Mineralogical, Canadian Mineralogist Special Publication, Ottawa, Ontario, p. 495.

Demir, Y ., Uysal, I ., Sadiklar, M . B ., Sipahi, F ., 2008. Mineralogy, mineral chemistry, and fluid inclusion investigation of Kostere hydrothermal vein-type deposit (Gumushane, NE-Turkey). Neu Jahr Für Min 185 (2), 215–232. https://doi.org/10.1127/0077-7757/2008/0122.

Dill, H . G ., 2015. Supergene alteration of ore deposits: from nature to humans. Elements 11 (5), 311–316. https://doi.org/10.2113/gselements.11.5.311.

Docegeo, 1991. Departamento Nacional de Produção Mineral internal report.

Dorozhkin, S . V ., 1997. Surface reactions of apatite dissolution. J. Colloid Interface Sci. 191, 489–497. https://doi.org/10.1006/jcis.1997.4942.

Driscoll, R ., Hageman, P ., Benzel, W ., et al., 2011. Assessment of the geoavailability of trace elements from minerals in mine wastes: analytical techniques and assessment of selected copper minerals. U.S. Geol Sur Sci Inv Rep 2011–5211. (pamphlet).

Dzombak, D . A ., Morel, F . M ., 1990. Surface Complexation Modeling: Hydrous Ferric Oxide. Wiley, New York.

Echavarría, A ., Echeverría, F ., Arroyave, C ., Gil, H ., 2009. Study of the copper corrosion mechanism in the presence of propionic acid vapors. J. Braz. Chem. Soc. 20 (10), 1841–1848. https://doi.org/10.1590/S0103-50532009001000011.

Enders, M . S ., Knickerbocker, C ., Titley, S . R ., Southam, G ., 2006. The role of bacteria in the supergene environment of the morenci porphyry copper deposit, greenlee county, Arizona. Econ. Geol. 101 (1), 59–70. https://doi.org/10.2113/gsecongeo.101.1.59.

Fitzpatrick, R . W ., Schwertmann, U ., 1982. Al-substituted goethite—an indicator of pedogenic and other weathering environments in South Africa. Geoderma 27 (4), 335–347. https://doi.org/10.1016/0016-7061(82)90022-2.

Gandhi, S . M ., Sarkar, B . C ., 2016. Essentials of Mineral Exploration and Evaluation, Elsevier, New York, pp. 199–234. (Chapter 8): Drilling.

George, L ., Cook, N . J ., Ciobanu, C . L ., Wade, B . P ., 2015. Trace and minor elements in galena: a reconnaissance LA-ICP-MS study. Am. Mineral. 100, 548–569. https://doi.org/10.2138/am-2015-4862.

George, L . L ., Cook, N . J ., Ciobanu, C . L ., 2016. Partitioning of trace elements in co-crystallized sphalerite-galena-chalcopyrite hydrothermal ores. Ore Geol. Rev. 77, 97–116. https://doi.org/10.1016/j.oregeorev.2016.02.009.

George, L . L ., Cook, N . J ., Crowe, B . B . P ., Ciobanu, C . L ., 2018. Trace elements in hydrothermal chalcopyrite. Min. Mag. 82 (1), 59–88. https://doi.org/10.1180/minmag.2017.081.021.

Grainger, C . J ., Groves, D . I ., Tallarico, F . H . B ., Fletcher, I . R ., 2008. Metallogenesis of the Carajás mineral province, southern Amazon craton, Brazil: varying styles of archean through paleoproterozoic to neoproterozoic base- and precious-metal mineralisation. Ore Geol. Rev. 33, 451–489. https://doi.org/10.1016/j.oregeorev.2006.10.010.

Haldar, S . K ., 2018. Exploration geochemistry. In: Mineral Exploration Principles and Applications. second ed., Elsevier, Amsterdam, pp. 85–101. https://doi.org/10.1016/B978-0-12-814022-2.00005-8.

Hatert, F ., 2003. Occurrence of sulphides on the bornite-idaite join from vielsalm, Stavelot massif, Belgium. Eur. J. Mineral 15 (6), 1063–1068. https://doi.org/10.1127/0935-1221/2003/0015-1063.

Helmy, H . M ., Shalaby, I . M ., Abdel Rahman, H . B ., 2014. Large-scale metal zoning in a late-Precambrian skarn-type mineralization, Wadi Kid, SE Sinai, Egypt. J. Earth Sci. 90,

77–86. https://doi.org/10.1016/j.jafrearsci.2013.11.015.

Horta, D . G ., Monte, M . B ., Leal-Filho, L . S ., 2017. Effect of dissolution kinetics on flotation response of calcite with oleate. Braz J of Chel Eng 34 (4), 1035–1042.

Ildefonse, P ., 1986. Hydroxy-Cu-Vermiculite formed by the weathering of Fe-biotites at Salobo, Carajás, Brazil. Clay Clay Miner. 34 (3), 338–345. https://doi.org/10.1346/CCMN.1986.0340315.

Kahou, Z . S ., Duchêne, S ., Brichau, S ., et al., 2021. Mineralogical and chemical characterization of supergene copper-bearing minerals: examples from Chile and Burkina Faso. Ore Geol. Rev. 133, 104078. https://doi.org/10.1016/j.oregeorev.2021.104078.

King, L . C ., 1956. A geomorfologia do brasil oriental. Rev. Bras. Geogr. 18, 147–265.

Krauskopf, K . B ., 1959. The geochemistry of silica in sedimentary environments. In: Ireland HA Silica in Sediments. SEPM, Tulsa. https://doi.org/10.2110/pec.59.01.0004.

Kříbek, B ., Zachariáš, J ., Knésl, I ., et al., 2016. Geochemistry, mineralogy, and isotope composition of Pb, Zn, and Cu in primary ores, gossan and barren ferruginous crust from the Perkoa base metal deposit, Burkina Faso. J. Geochem. Explor. 168, 49–64. https://doi.org/10.1016/J.GEXPLO.2016.05.007.

Li, Y ., Kawashima, N ., Li, J ., Chandra, A ., Gerson, A . R ., 2013. A review of the structure, and fundamental mechanisms and kinetics of the leaching of chalcopyrite. Adv. Colloid Interface Sci. 197–198, 1–32. https://doi.org/10.1016/j.cis.2013.03.004.

Liu, H ., Chen, T ., Frost, R . L ., 2014. An overview of the role of goethite surfaces in the environment. Chemosphere 103, 1–11. https://doi.org/10.1016/j.chemosphere.2013.11.065.

Lowson, R ., Comarmond, M . C ., Rajaratnam, G ., Brown, P . L ., 2005. The kinetics of the dissolution of chlorite as a function of pH and at 25°C. Geochem. Cosmochim. Acta 69 (7), 1687–1699. https://doi:10.1016/j.gca.2004.09.028.

Machado, N ., Lindenmayer, Z ., Krogh, T . E ., Lindenmayer, D ., 1991. U-Pb geochronology of Archean magmatism and basement reactivation in the Carajás area, Amazon shield, Brazil. Precambrian Res. 49, 329–354. https://doi.org/10.1016/0301-9268(91)90040-H.

Magalhães, M . C . F ., Jesus, J . D . P ., Williams, P . A ., 1986. Stability constraints and formations of Cu (II) and Zn (II) phosphate minerals in the oxidized zone of base metal orebodies. Mineral. Mag. 50, 33–39. https://doi.org/10.3749/canmin.1400066.

Mano, E . S ., Caner, L ., Petit, S ., Chaves, A . P ., 2020. Mineralogical characterization of copper lateritic ore from the Furnas deposit - Carajás, Brazil. Int Eng J 73 (3), 329–335. https://doi.org/10.1590/0370-44672019730113.

Mavrogonatos, C ., Voudouris, P ., Berndt, J ., et al., 2019. Trace elements in magnetite from the pagoni rachi porphyry prospect, NE Greece: implications for ore genesis and exploration. Minerals 9 (12), 725. https://doi.org/10.3390/min9120725.

Monteiro, H . S ., Vasconcelos, P . M . P ., Farley, K . A ., Lopes, C . A . M ., 2018. Age and evolution of diachronous erosion surfaces in the Amazon: combining (U-Th)/He and cosmogenic 3He records. Geochem. Cosmochim. Acta 229, 162–183. https://doi.org/10.1016/j.gca.2018.02.045.

Monteiro, L . V . S ., Xavier, R . P ., Hitzman, M . W ., et al., 2008. Mineral chemistry of ore and hydrothermal alteration at the Sossego iron oxide–copper–gold deposit, Carajás Mineral Province, Brazil. Ore Geol. Rev. 34 (3), 317–336. https://doi.org/10.1016/j.oregeorev.2008.01.003.

Moreto, C . P . N ., Monteiro, L . V . S ., Xavier, R . P ., et al., 2015. Timing of multiple hydrothermal events in the iron oxide–copper–gold deposits of the Southern Copper Belt, Carajás Province, Brazil. Miner. Deposits 50 (5), 517–546. https://doi.org/10.1007/s00126-014-0549-9.

Nadoll, P ., Angerer, T ., Mauk, J . L ., French, D ., Walshe, J ., 2014. The chemistry of hydrothermal magnetite: a review. Ore Geol. Rev. 61, 1–32. https://doi.org/10.1016/j.oregeorev.2013.12.013.

Nash, J . T ., 2004. Hydrogeochemical studies of historical mining area in the Humboldt River Basin and adjacent areas, northern Nevada. Sci Invest Rep 2004–5236. https://doi.org/10.3133/SIR20045236.

Nickel, E . H ., 1984. The mineralogy and geochemistry of the weathering profile of the Teutonic Bore Cu-Pb-Zn-Ag sulphide deposit. J. Geochem. Explor. 22, 239–263. https://doi.org/10.1016/0375-6742(84)90014-1.

Nickel, E . H ., Ross, J . R ., Thornber, M . R ., 1974. The supergene alteration of pyrrhotite-pentlandite ore at Kambalda, Western Australia. Econ. Geol. 69 (1), 93–107. https://doi.org/10.2113/gsecongeo.69.1.93.

Nordstrom, D . K ., 2011. Mine waters: acidic to circumneutral. Elements 7 (6), 393–398. https://doi.org/10.2113/gselements.7.6.393.

Ozdemir, A ., Sahinoglu, A ., 2018. Important of gossans in mineral exploration: a case study in northern Turkey. Int J Earth Sci Geoph 4, 19. https://doi.org/10.35840/2631-5033/1819.

Papineau, D ., 2020. Chemically oscillating reactions in the formation of botryoidal malachite. Am. Mineral. 105 (4), 447–454. https://doi.org/10.2138/am-2020-7029.

Perchiazzi, N ., 2006. Crystal structure determination and Rietveld refinement of rosasite and mcguinnessite. Zeit Für Krist Sup 23, 505–510. https://doi.org/10.1524/zksu.2006.suppl_23.505.

Perchiazzi, N ., Dragone, R ., Demitri, N ., Vignola, P ., Biagioni, C ., 2018. Incorporation of Co in the rosasite–malachite carbonate group of minerals: crystal structure studies of kolwezite and synthetic cobaltoan malachites. Eur. J. Mineral 30 (3), 609–620. https://doi.org/10.1127/ejm/2018/0030-2743.

Peterson, R . C ., Williamson, M . C ., Rainbird, R . H ., 2014. Gossan Hill, Victoria Island, Northwest Territories: an analogue for mine waste reactions within permafrost and implication for the subsurface mineralogy of Mars. Earth Planet Sci. Lett. 400, 88–93. https://doi.org/10.1016/j.epsl.2014.05.010.

Pidgeon, R . T ., Macambira, M . J . B ., Lafon, J . M ., 2000. Th–U–Pb isotopic systems and internal structures of complex zircons from an enderbite from the Pium Complex, Carajás Province, Brazil: evidence for the ages of granulite facies metamorphism and the protolith of the enderbite. Chem. Geol. 166, 159–171. https://doi.org/10.1016/S0009-2541(99)00190-4.

Pires, G . L . C ., Renac, C ., Bongiolo, E . M ., Neumann, R ., 2020. Gossan mineralogy, textures, and gold enrichment over the Au (As, Bi, Ag) deposit in the Buracão Area (Brasília Fold Belt, Brazil): implications for gold prospecting in weathering profiles. J. Geochem. Explor. 218, 106615. https://doi.org/10.1016/j.gexplo.2020.106615.

Porto, C . G ., 2016. Geochemical exploration challenges in the regolith dominated Igarapé Bahia gold deposit, Carajás, Brazil. Ore Geol. Rev. 73, 432–450. https://doi.org/10.1016/j.oregeorev.2015.10.027.

Putter, T ., Mees, F ., Decrée, S ., Dewaele, S ., 2010. Malachite, an indicator of major Pliocene Cu remobilization in karstic environment (Katanga, Democratic Republic of Congo). Ore Geol. Rev. 38, 90–100. https://doi.org/10.1016/j.oregeorev.2010.07.001.

Reich, M ., Palacios, C ., Vargas, G ., Luo, S ., Cameron, E . M ., Leybourne, M . I ., Parada, M . A .,Zúñiga, A ., You, C . F ., 2009. Supergene enrichment of copper deposits since the onset of modern hyperaridity in the Atacama Desert, Chile. Miner. Deposita 44 (5), 497–504. https://doi.org/10.1007/s00126-009-0229-3.

Rice, C . M ., Atkin, D ., Bowles, J . F . W ., Criddle, A . J ., 1979. Nukundamite, a new mineral, and idaite. Mineral. Mag. 43, 193–200. https://doi.org/10.1180/minmag.1979.043.326.01.

Robie, R . A ., Hemingway, B . S ., 1995. Thermodynamic properties of minerals and related substances at 298.15K and 1 bar (105 Pascals) pressure and at higher temperatures. Uni Sta Geol Surv Bul 2131. https://doi.org/10.3133/b2131.

Rose, A . W ., Bianchi-Mosquera, G . C ., 1993. Adsorption of Cu, Pb, Zn, Co, Ni, and Ag, on goethite and hematite: a control on metal mobilization from red-beds into stratiform copper deposits. Econ. Geol. 88, 1226–1236. https://doi.org/10.2113/gsecongeo.88.5.1226.

Rose, W . R ., Hawkes, H . E ., Webb, J . S ., 1979. Geochemistry in Mineral Exploration. Academic Press, New York.

Stoops, G ., 2003. Guidelines for Analysis and Description of Soil and Regolith Thin Sections. Soil Science Society of America, Madison, Wisconsin, p. 184.

Sadati, S . N ., Yazdi, M ., Mao, J ., Behzadi, M ., Adabi, M . H ., Lingang, X ., Zhenyu, C ., Mokhtari, M . A . A ., 2016. Sulfide mineral chemistry investigation of sediment-hosted stratiform copper deposits, Nahand-Ivand area, NW Iran. Ore Geol. Rev. 72, 760–776. https://doi.org/10.1016/j.oregeorev.2015.09.018.

Samolczyk, M . A ., Spooner, I . S ., Stanley, C . R ., 2012. A model for uranium mobility in groundwater in the Grand Pré region, Nova Scotia, Canada. Atl. Geol. 48, 1–13. https://doi.org/10.4138/atlgeol.2012.001.

Sato, M ., 1992. Persistency-field Eh-pH diagrams for sulfides and their application to supergene oxidation and enrichment of sulfide ore bodies. Geochem. Cosmochim. Acta 56 (8), 3133–3156. https://doi.org/10.1016/0016-7037(92)90294-S.

Sato, M ., Mooney, H . M ., 1960. The electrochemical mechanism of sulfide self-potentials. Geophysics 25 (1), 226–249. https://doi.org/10.1190/1.1438689.

Schutesky, M . E ., Oliveira, C . G ., 2020. From the roots to the roof: an integrated model for the Neoarchean Carajás IOCG System, Brazil. Ore Geol. Rev. 127, 103833. https://doi.org/10.1016/j.oregeorev.2020.103833.

Scott, K . M ., Ashley, P . M ., Lawie, D . C ., 2001. The geochemistry, mineralogy and maturity of gossans derived from volcanogenic Zn–Pb–Cu deposits of the eastern Lachlan Fold Belt, NSW, Australia. J. Geochem. Explor. 72 (3), 169–191. https://doi.org/10.1016/S0375-6742(01)00159-5.

Shimazaki, H ., 1998. On the occurrence of silician magnetites. Resor Geol 48. https://doi.org/10.1111/j.1751-3928.1998.tb00004.x. . 233–29. .

Sillitoe, R . H ., Clark, A . H ., 1969. Copper and copper-iron sulfides as the initial products of supergene oxidation, Copiapó mining district, northern Chile. Am. Mineral. 54,1684–1710.

Siuda, R ., Kruszewski, L ., 2013. Recently formed secondary copper minerals as indicators of geochemical conditions in an abandoned mine in Radzimowice (SW Poland). Geol. Q. 57 (4), 583–600. https://doi.org/10.7306/gq.1114.

Smith, R . E ., Singh, B ., 2007. Recognizing, in lateritic cover, detritus shed from the Archaean Gossan Hill Cu–Zn–Au volcanic-hosted massive sulphide deposit, Western Australia. Geochem. Explor. Environ. Anal. 7 (1), 71–86. https://doi.org/10.1144/1467-7873/06-120.

Stavinga, D ., Jamieson, H ., Layton-Matthews, D ., Paradis, S ., Falck, H ., 2017. Geochemical and mineralogical controls on metal(loid) mobility in the oxide zone of the Prairie Creek Deposit, NWT. Geochem. Explor. Environ. Anal. 17 (1), 21–33. https://doi.org/10.1144/geochem2015-378.

Števko, M ., Sejkora, J ., Bačík, P ., 2012. Mineralogy and origin of supergene mineralization at the Farbište ore occurrence near Poniky, central Slovakia. J. Geom. 56 (3), 273–298. https://doi.org/10.3190/jgeosci.098.

Sverdrup, H . U ., 1984. Calcite dissolution and acidification mitigation strategies. Lake Reservoir Manag. 1 (1), 345–355. https://doi.org/10.1080/07438148409354537.

Taylor, G . F ., Wilmshurst, J . R ., Butt, C . R . M ., Smith, R . E ., 1980. Gossans. J. Geoch. Expl. 22, 30–32.

Taylor, R ., 2011. Gossans and Leached Cappings Field Assessment. Springer, Townsville.

Thornber, M . R ., 1985. Supergene alteration of sulphides. Chem. Geol. 53, 279–301. https://doi.org/10.1016/0009-2541(85)90075-0.

Thornber, M . R ., Taylor, G . F ., 1992. The mechanisms of sulphide oxidation and gossan formation 4, 119–138. https://doi.org/10.1016/B978-0-444-89095-5.50015-8.

Throop, A . H ., Buseck, P . R ., 1971. Nature and origin of black chrysocolla at the Inspiration Mine, Arizona. Econ. Geol. 66 (8), 1168–1175. https://doi.org/10.2113/gsecongeo.66.8.1168.

Torresi, I ., Xavier, R . P ., Bortholoto, D . F . A ., Monteiro, L . V . S ., 2012. Hydrothermal alteration, fluid inclusions and stable isotope systematics of the Alvo 118 iron oxide–copper–gold deposit, Carajás Mineral Province (Brazil): implications for ore genesis. Miner. Deposita 47 (3), 299–323. https://doi.org/10.1007/s00126-011-0373-4.

Tõnsuaadu, K ., Kallas, J ., Kuusik, R ., Hacialioglu-Erlenheim, G ., Trikkel, A ., 2021. A new perspective on fluorapatite dissolution in hydrochloric acid: thermodynamic calculations and experimental study. INORGA 9, 65. https://doi.org/10.3390/inorganics9080065.

Trendall, A . F ., Basei, M . A . S ., Laeter, J . R ., Nelson, D . R ., 1998. SHRIMP zircon U–Pb constraints on the age of the Carajás formation, Grão Pará group, Amazon craton. J of South Ame Ear Sci 11 (3), 265–277. https://doi.org/10.1016/S0895-9811(98)00015-7.

USGS, 2006. Shuttle Radar Topography Mission (SRTM).

Vasconcelos, P . M ., Reich, M ., Shuster, D . L ., 2015. The paleoclimatic signatures of supergene metal deposits. Elements 11 (5), 317–322. https://doi.org/10.2113/gselements.11.5.317.

Vasques, M . L ., Sousa, C . S ., Carvalho, J . M . L ., 2008. Mapa geológico e de recursos minerais do estado do Pará: Programa geologia do brasil, integração, atualização e difusão de dados da geologia do Brasil. escala 1:1.000.000.

Veiga, M . M ., Schorscher, H . D ., Fyfe, W . S ., 1991. Relationship of copper with hydrous ferric oxides: Salobo, Carajás, PA, Brazil. Ore Geol. Rev. 6, 245–255. https://doi.org/10.1016/0169-1368(91)90025-3.

Velasco, F ., Herrero, J . M ., Suárez, S ., Yusta, I ., Alvaro, A ., Tornos, F ., 2013. Supergene features and evolution of gossans capping massive sulphide deposits in the Iberian Pyrite Belt. Ore Geol. Rev. 53, 181–203. https://doi.org/10.1016/j.oregeorev.2013.01.008.

Verhaert, M ., Bernard, A ., Saddiqi, O ., Dekoninck, A ., Essalhi, M ., Yans, J ., 2018. Mineralogy and genesis of the polymetallic and polyphased low grade Fe-Mn-Cu ore of jbel rhals deposit (eastern high atlas, Morocco). Minerals 8 (2), 39. https://doi.org/10.3390/min8020039.

Wang, G ., Wang, Z ., Shi, R ., Zhang, Y ., Wang, K ., 2014. Mineralogy and isotope geochemical characteristics for Xiaozhen copper deposit, Langao County, Shaanxi Province and their constraint on genesis of the deposit. Geol. J. 19 (2), 281–294. https://doi.org/10.1007/s12303-014-0044-4.

Williamson, M . A ., 1994. Precipitation and Solubility of Chrysocolla in Near-Neutral pH Mine Drainage Solutions, South-Central Wyoming, Geological Society of America, p. A353. Abstracts.

Yates, D . M ., Joyce, K . J ., Heaney, P ., 1998. Complexation of copper with polymeric sílica in aqueous solution. Appl. Geochem. 13 (2), 235–241. https://doi.org/10.1016/S0883-2927(97)00062-0.

Yesares, L ., Sáez, R ., Ruiz, A . G ., Nieto, J . M ., Gómez, C ., Ovejero, G ., 2017. Mineralogical evolution of the Las Cruces gossan cap (Iberian Pyrite Belt): from subaerial to underground conditions. Ore Geol. Rev. 80, 377–405. https://doi.org/10.1016/j.oregeorev.2016.05.018.

Zammit, C . M ., Shuster, J . P ., Gagen, E . J ., Southam, G ., 2015. The geomicrobiology of supergene metal deposits. Elements 11 (5), 337–342. https://doi.org/10.2113/gselements.11.5.337.

Zhao, J ., Brugger, J ., Pring, A ., 2019. Mechanism and kinetics of hydrothermal replacement of magnetite by hematite. Geosci. Front. 10 (1), 29–41. https://doi.org/10.1016/j.gsf.2018.05.015.

5. GEOCHEMICAL AND ISOTOPIC FRACTIONATION IN THE HYPOGENE ORE, GOSSAN, AND SAPROLITE OF THE ALVO 118 DEPOSIT: IMPLICATIONS FOR COPPER EXPLORATION IN REGOLITHS OF THE CARAJÁS MINERAL PROVINCE

Pabllo Henrique Costa dos Santos[1]*, Marcondes Lima da Costa[1], Desiree Lisette Roerdink[2]

[1]Universidede Federal do Pará, Instituto de Geociências / Rua Augusto Corrêa, 01, Guamá, Belém, Pará, Brazil

[2]University of Bergen, Department of Earth Science / Realfagbygget, Allegaten 41, Bergen, 5007 Bergen, Norway

*Corresponding author, phsantos@ufpa.br

Abstract

In the Carajás Mineral Province, gossan formation and lateritization produced numerous supergene orebodies at the expense of IOCG deposits and host rocks. The Alvo 118 deposit comprises massive and disseminated hypogene copper sulfides associated with gossan and mineralized saprolites. The hypogene reserves are 170 Mt, with 1% Cu and 0.3 ppm Au, while the supergenes are 55 Mt, comprised of 30% gossan and 70% saprolite, with 0.92% Cu and 0.03 ppm Au. The gossan includes goethite, malachite, cuprite, and libethenite zones. The saprolite comprises kaolinite, vermiculite, smectite, and relics of chlorite. In the hypogene mineralization, Ag, Te, Pb, Se, Bi, Au, In, Y, Sn, U are mainly hosted by chalcopyrite and petzite, altaite, galena, uraninite, stannite, and cassiterite. In the gossan, Ag, Te, Pb, Se, Bi are hosted by Cu minerals, while Au, In, Y, Sn, U are associated with iron oxyhydroxides, in addition to Zn, As, Be, Ga, Ga, Mo, Ni, Sc. The $\delta^{65}Cu$ values indicate that the gossan is immature and not affected by leaching. In the saprolite, Ga, Sc, Sn, V, Mn, Co, Cr are associated with the iron oxyhydroxides, partially derived from the host rock weathering. The $\delta^{56}Fe$ values indicate that hypogene low contribution of the hypogene mineralization to the saprolite iron content. The association of Al_2O_3, Hf, Zr, Th, TiO_2, Ce, La, Ba, Sr represents the geochemical signature of the host rocks, with dominant contributions from chloritites, while In, Y, Te, Pb, Bi, and Se are main pathfinders of Cu and Au mineralizations.

Keywords: Chalcopyrite, petzite, chlorite, stable isotopes.

1 Introduction

Gossan generation involves sulfide dissolution and release of sulfate and metal ions, which can be lost or retained by the supergene system (Andreu *et al.*, 2015; Yesares *et al.*., 2017; Pires *et al*., 2020). This retention comprises the generation of newly formed minerals, establishing a mineralogical zoning, which can include secondary sulfides, sulfates, arsenates, phosphates, carbonates, and oxyhydroxides, carrying copper or other metals (Williams *et al*., 1999). These zones represent exploratory guides for the generally much larger hypogene deposits (e.g., Atapour and Aftabi, 2007; Suaréz *et al.*, 2012; Ozdemir and Shinoglu, 2018).

In tropical regions like the Amazon, gossan and their host rocks have been modified by weathering, producing thick saprolite blankets that include lateritic profiles and soils (Angelica *et al*., 1996; Costa *et al*., 1996; Porto, 2016). In this context, ions or ionic compounds not incorporated by gossan are partially retained by the weathering products of the host rocks, forming a geochemical dispersion halo (Veiga *et al*., 1991; Silva and Kotschoubey, 2000; Porto, 2016). This incorporation typically involves clay minerals and iron oxyhydroxides (Ildefonse, 1986; Veiga *et al*., 1991).

Thus tropical weathering makes mineral exploitation particularly complex because it modifies the gossans' classical mineralogical and textural aspects, which are preserved in arid regions (e.g., Scott *et al*., 2001; Atapour and Aftabi, 2007; Taylor, 2011). However, the weathering products of the host rocks can form economically attractive mineralizations, increasing the profitability of the deposit and reducing mining waste (e.g., Tornos *et al*., 2016).

The Carajás mineral province (CMP) has been subjected to tropical weathering and lateritization over the past 70 Ma, modifying the preexisting gossans, especially those located at the top of the Carajás Mountains, which is bounded by the South American/Carajás geomorphic surface (Costa *et al*., 1996; Monteiro *et al*., 2018). Additionally, denudation of the surrounding areas, which commenced at 10 Ma, now represented by the Velhas/Itacaiúnas geomorphic surface, exposed immature and truncated mature gossans. These secondary orebodies are generally capped by saprolite horizons and colluvial deposits (Ildefonse, 1986; Costa *et al*., 1996; Silva and Kotschoubey, 2000; Porto, 2016). Thus, mineral exploration in these terrains should consider the evolutionary degree of the gossans (mature or immature), lateritic profiles (complete or truncated), and their metal-retention capacity (Ildefonse, 1986; Veiga *et al*., 1991).

The Alvo 118 deposit consists of Cu-Au mineralization, typical of the denuded areas of the CMP. It comprises three ore types formed during distinct evolutionary stages: 1) hydrothermal massive and disseminated copper sulfide orebodies, 2) immature gossan, and 3) saprolite (Grainger *et al*., 2008; Torresi *et al*., 2012; Santos and Costa, 2022). The hypogene reserves reach 170 Mt at 1% Cu and 0.3 ppm Au, while those of supergene ores are approximately 55 Mt, of which 30% correspond to the gossan orebody and 70% to the saprolite, with 0.92% Cu and 0.03 ppm Au (Docegeo, 1991).

This research investigated the Alvo 118 deposit to acknowledge the patterns of fixation and dispersion of copper and other chemical components in the secondary mineralizations (gossan and saprolite) typical of the Itacaiúnas denuded areas. Additionally, mineralogical, textural, and isotopic data were used to evaluate the response of the hypogene mineralization and host rocks to oxidoreduction and hydrolysis reactions, respectively. Both approaches produced implications for mineral exploration.

2 Geological setting

The Carajás Mineral Province is located in the southeastern Amazon Craton and is home to one of the world's largest and oldest IOCG belts (Schutesky and Oliveira, 2020; Santiago *et al*., 2021). Most deposits are located in the Carajás tectonic domain, in the northern portion of the province (Fig. 1A), affected by two mineralizing hydrothermal events. The first (2.57 Ga) produced the Salobo, Sossego, Cristalino, and Alemão deposits; and the second (1.88 Ga) formed the Gameleira, Estrela, Breves, Igarapé Cinzento, and Serra Verde deposits (Grainger *et al*., 2008). Alvo 118 is the only hybrid orebody, recording the overlapping of both events (Torresi *et al*., 2012).

The Alvo 118 is a Cu and Au deposit related to shear zone hydrothermal alteration (Grainger *et al*., 2008). The hypogene IOCG mineralization comprises NW-SE sub-vertical tabular orebodies aligned with the neighboring Sossego, and Cristalino deposits (Grainger *et al*., 2008). The first mineralization style includes hydrothermal breccias comprising chalcopyrite and bornite matrix (with minor magnetite and pyrite), surrounding granite, gabbro, and schist clasts (Rigon *et al*., 2000). Stockwork veins formed of quartz, calcite, and chalcopyrite represent the second mineralization style. Hydrothermal xenotimes have been dated to 1869±9 Ma in the breccia zone matrix and to 1868±7 Ma in the stockwork veins (Grainger *et al*., 2008).

The deposit area houses mafic to intermediate volcanic sequences, with mylonitic foliation and intense chloritic alteration correlated with the Grão Pará Group. These rocks are then intruded by granodioritic, tonalitic, and gabbroic bodies, finally crosscut by dacitic-rhyolitic and diabasic dykes (Torresi *et al*., 2012), Fig. 1C. Toward the sulfide ore, the host rocks were progressively subjected to sodic (albite and scapolite), potassic (biotite and alkali feldspar), chloritic, and quartz-sericitic hydrothermal alteration (Torresi *et al*., 2012).

The gossan overlying the sulfide mineralization presents a mineralogical zonation, with progressive replacement of primary sulfides by secondary sulfides and then by carbonates, phosphates, and copper oxides (Albuquerque *et al*., 2001). In the overlying saprolite, copper is supposed to be carried by the alteration products of the primary silicates, that is, clay minerals and iron oxyhydroxides, such as in Salobo and Furnas deposits (Toledo-Groke *et al*., 1985; Ildefonse *et al*., 1986; Mano *et al*., 2020), Fig. 1D. The Alvo 118 deposit was initially explored in the 1990s, by Docegeo, and investigations were resumed in 2017 by Vale.

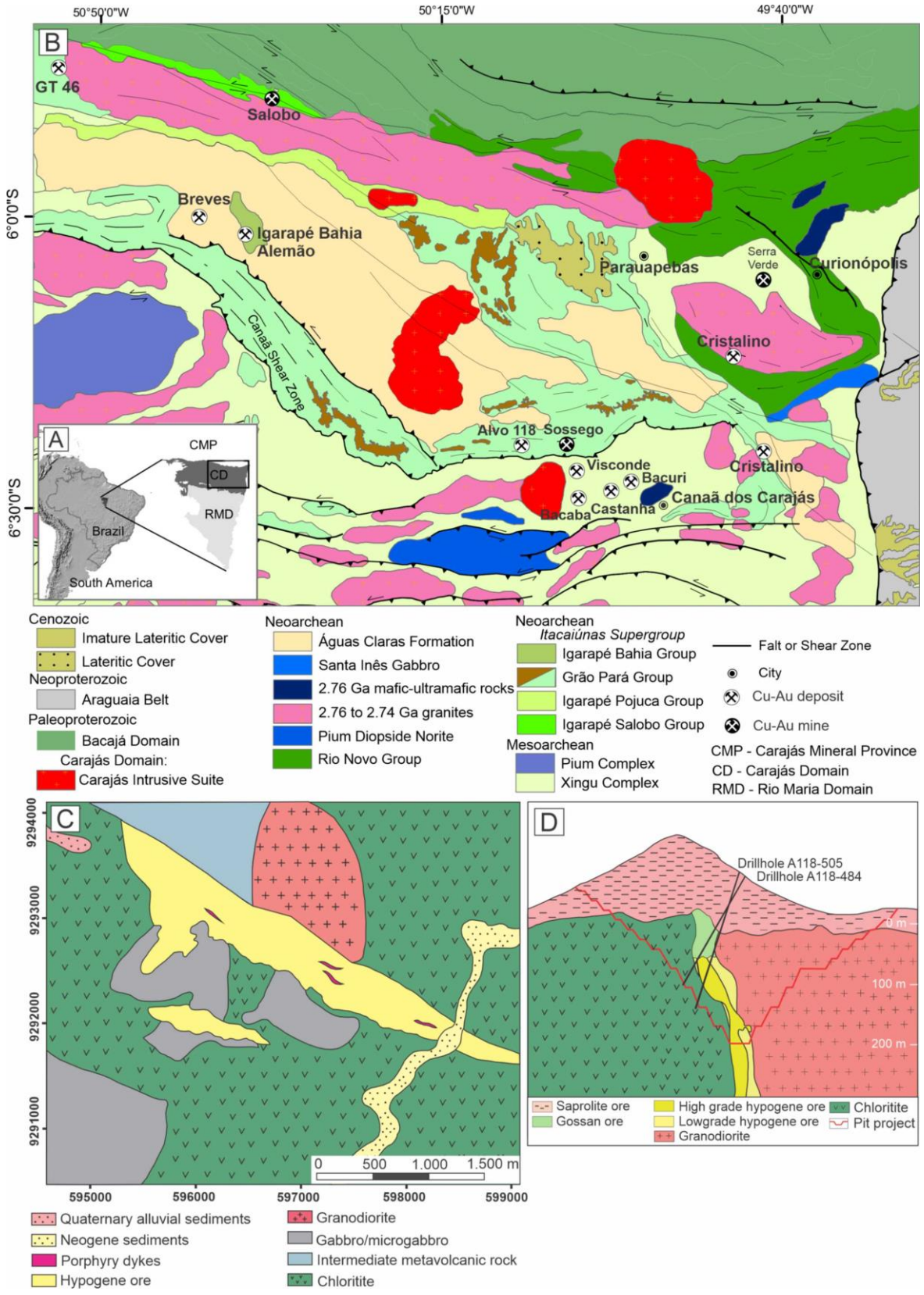

Fig. 1 A) Location of the Carajás tectonic domain in northern CMP. B) Geology of the Carajás domain, with the location of the main copper deposits, modified from Vasquez *et al*. (2008) and Grainger *et al*. (2008). C) Geology of the area surrounding the Alvo 118 deposit, according to Torresi *et al*. (2012) and Santos and Costa (2022). D) Geological section of the Alvo 118 deposit, with hypogene mineralization, gossans, and saprolite locations (Santos and Costa, 2022) (D).

3 Materials and methods

3.1 Sampling

Petrographic descriptions were performed on drill cores and outcrops in the Alvo 118 pilot mine, followed by the collection of 112 samples, including host rock, hypogene mineralization, gossan, and saprolite. Vale collected four hundred samples from two additional drill holes for whole-rock chemical analyses and made the results available for this research.

3.2 Optical and electron microscopy

The microtextural aspects were investigated through polished sections analyzed in a LEICA DM 2700 P petrographic microscope with a LEICA MC 170 HD camera. These data were enhanced with scanning electron microscopy (SEM) images (backscattered electrons) taken in the Hitachi TM3000 equipment. The target minerals were analyzed with an Oxford SwiftED3000 energy dispersive system (EDS). The voltage acceleration was from 5 to 15kV, using an SDD detector (161 eV Cu-Kα). The microtextural analyzes were carried out in the Mineralogy, Geochemistry, and Applications Laboratory (Federal University of Pará).

3.3 X-ray diffraction (XRD)

Mineral identification was enhanced with powder XRD in a Bruker D2 PHASER, with Cu anode, Lynxeye detector (1D mode); increment of 0.02 °2θ; 0.2 s step time; and 0.1 mm slit; operating at 300 W (30 kV and 10 mA), in the angular range 5 - 75°2θ. For clay minerals identification, 150 g aliquots from 20 samples were previously deflocculated in an ultrasonic vat and wet sieved at 63 μm. The passing fraction was centrifuged for 2 min at 1000 rpm. The suspension was centrifuged again at 1800 rpm for 10 min. Then, the suspension was decanted in another recipient and dried at 40 °C. Finally, the isolated clay particles were mounted in oriented sections; ethylene glycol solvated for 48 h; and heated at 540 °C for 2 h. The respective mineralogical response to each treatment was followed by DRX analyses in the angular range 4 - 75°2θ. These procedures were carried out in the Mineralogy, Geochemistry, and Applications Laboratory (Federal University of Pará).

3.4 Whole-rock chemical analysis

Four hundred samples with 10 Kg each were analyzed to determine whole-rock chemical composition. The analyzed elements were Ag, Al, As, Ba, Be, Bi, Cd, Ce, Co, Cr, Cs, Fe, Ga, Ge, Hf, In, K, La, Li, Mg, Mn, Mo, Na, Nb, Ni, P, Pb, Rb, Re, S, Sb, Sc, Se, Sn, Sr, Ta, Te, Th, Ti, Tl, U, V, W, Y, Zn, and Zr. Aliquots of 0.25 g were digested with perchloric, nitric, hydrofluoric, and hydrochloric acids. The residue was diluted with hydrochloric acid and

analyzed in an atomic emission spectrometer with inductively coupled plasma (ICP-AES). Following this analysis, the results were reviewed for high concentrations of Bi, Hg, Mo, Ag, and W and diluted accordingly. Samples meeting this criterion are then analyzed in a mass spectrometer with inductively coupled plasma (ICP-MS). Au was determined by fire essay with ICP-AES finish, and Cu was analyzed by Niton X-Ray Fluorescence. The results were kindly provided by Vale.

Additionally, 12 samples collected in specific mineralogical contexts were analyzed to clarify the association between mineralogy and chemical composition. The analyzed elements were SiO_2, Al_2O_3, Fe_2O_3, CaO, Na_2O, K_2O, Cr_2O_3, TiO_2, MnO, P_2O_5, SrO, and BaO. Aliquots of 0.1 g were added to lithium borate and fused at 1025°C. The resulting melt was then cooled and dissolved in a mixture of nitric, hydrochloric and hydrofluoric acids. This solution was then analyzed by ICP-AES. Barium, Ce, Cr, Cs, Dy, Er, Eu, Ga, Gd, Ge, Hf, Ho, La, Ku, Nb, Pr, Rb, Sm, Sn, Sr, Ta, Tb, Th, Tm, U, V, W, Y, Yb, and Zr were digested by the same method, but with an additional lithium borate fusion and analyzed by ICP-MS. Loss on ignition was determined by gravimetric method, using a thermal decomposition furnace. Total S and C were analyzed by LECO infrared spectroscopy.

For Ag, Cd, Co, Cu, Li, Mo, Ni, Pb, Sc, and Zn, 0.25g aliquots were digested with perchloric, nitric, hydrofluoric, and hydrochloric acids. The residue was made up to volume with dilute hydrochloric acid, and the resulting solution was analyzed by ICP-AES. For Cu, 0.4 g samples were digested in aqua regia and analyzed by ICP-MS. For As, Bi, Hg, In, Re, Sb, Se, Te, and Tl, 0.50 g aliquots were digested with aqua regia for 45 minutes. After cooling, the solution was diluted to 12.5 ml with deionized water and analyzed by ICP-MS. Gold, Pt, and Pd were determined by fire essay and ICP-AES finish. All the chemical data were acquired in the facilities of ALS laboratories.

3.5 Stable isotopes

Eight powdered samples were heated at 1000°C for 90 min, to remove organic compounds, and dissolved in concentrated HF, HNO_3, and HCl in Teflon beakers at 130°C. Solutions were split into two aliquots, dried down, and redissolved in 1 ml of 6M HCl (for Fe isotope analyses) and 1 ml of 10M HCl (for Cu isotope analyses). Only double-distilled acids were used in the procedure, and labware was pre-cleaned with 10% HCl to minimize contamination.

3.5.1 Iron isotopes

Eight aliquots corresponding to 500-1000 µg Fe were loaded onto anion exchange columns with approximately 1 ml of AG1-X8 resin (100-200 mesh) in a class A100 laminar flow hood. Matrix elements were eluted using 5 ml of 6M HCl, Fe was eluted using 2 ml ultrapure water and 4.5 ml of 5M HNO_3 (Moeller *et al*., 2014). The eluted sample was dried overnight and taken up in 0.3M HNO_3. Samples were subsequently analyzed for Fe concentrations using a Nu Plasma II multi-collector inductively coupled plasma mass spectrometer (MC-ICP-MS) with an upgraded Plasma 3 interface at the University of Bergen. A blank acid sample run over the same anion exchange columns yielded a blank of 4 ng Fe, corresponding to less than 0.002% of the Fe in the samples.

Solutions were diluted to 2 ppm Fe in acid-cleaned Teflon vials and analyzed for Fe isotopes in wet plasma mode at pseudo-medium-resolution (R5-95% = 9899) with ^{54}Fe in Faraday cup L5, ^{56}Fe in H1 and ^{57}Fe in H4. Zeros were measured by ESA deflection for 30 seconds before each block, and samples were analyzed in 2 blocks of 20 measurements of 8 seconds. Each sample was run in duplicate, and an internal standard (Han Fe, $\delta^{56}Fe = 0.29 \pm 0.07$‰ (Moeller *et al*., 2014)) was regularly measured to confirm accurate Fe isotope ratios. Fe isotope ratios were corrected for mass bias using standard-sample bracketing (SSB) with the bracketing standard IRMM-014, following the equation: $\delta^{56}Fe_{spl,\,corr} = \{((^{56}Fe/^{54}Fe)_{spl,\,meas} / [0.5 \times (^{56}Fe/^{54}Fe)_{std1,\,meas} + 0.5 \times (^{56}Fe/^{54}Fe)_{std2,\,meas}]) - 1\} \times 1000$ and similarly for $\delta^{57}Fe$.

A plot of $\delta^{57}Fe$ versus $\delta^{56}Fe$ confirmed that all samples and standard fall (within error) on the terrestrial mass-dependent fractionation line with a slope of 1.47. Based on repeated analyses of Han Fe (n = 15), the external precision on $\delta^{56}Fe$ was 0.10 (2s). Analyses of the BCR-2 basalt standard yielded an average $\delta^{56}Fe$ of 0.07 ± 0.05‰ (n = 3), which is in excellent agreement with the published value of 0.09 ± 0.01‰ (Craddock and Dauphas 2011).

3.5.2 Copper isotopes

Eight aliquots corresponding to 1000 µg Cu were loaded onto custom-made Teflon columns with 1 ml of AG-MP1 anion exchange resin (100-200 mesh) in a class A100 laminar flow hood. For samples less than 100 µg Fe was loaded onto the column, matrix elements were eluted using 4 ml of 10M HCl, and Cu was subsequently eluted using 6 ml of 5M HCl (modified after Borrok *et al.*, 2007). Column calibration showed that higher Cu contents result in earlier elution of Cu. For samples with more than 100 µg Cu, the matrix elements were eluted with

only 3 ml of 10M HCl. The eluted samples were dried overnight, refluxed with concentrated HNO_3 for 4 hours, and taken up in 0.3M HNO_3.

Samples were subsequently analyzed for Cu concentrations using a Nu Plasma II MC-ICP-MS at the University of Bergen. A blank acid sample run over the same anion exchange columns yielded a blank of 1 ng Cu, corresponding to less than 0.001% of the Cu in the samples. Solutions were diluted to 100 ppb Cu in acid-cleaned Teflon vials and analyzed for Cu isotopes in wet plasma mode at low resolution with ^{63}Cu in the axial Faraday cup and ^{65}Cu in H4. Zinc abundances were monitored in Faraday cups H6 (^{66}Zn) and H9 (^{68}Zn), and total Zn signals were typically less than 1% of the total Cu signal. Zeros were measured by ESA deflection for 30 seconds before each block, and samples were analyzed in 2 blocks of 20 measurements of 8 seconds.

Each sample was run in duplicate, and an internal standard (Bergen Cu, $\delta^{65}Cu = -0.06 \pm 0.06‰$, Moeller *et al.*, 2012) was regularly measured to confirm accurate Cu isotope ratios. Cu isotope ratios were corrected for mass bias using standard-sample bracketing (SSB) with the bracketing standard ERM AE647, following the equation: $\delta^{65}Cu_{spl,\ corr} = \{((^{65}Cu/^{63}Cu)_{spl,\ meas} / [0.5 \times (^{65}Cu/^{63}Cu)_{std1,\ meas} + 0.5 \times (^{65}Fe/^{63}Cu)_{std2,\ meas}]) -1\} \times 1000$. Values were subsequently recalculated to the SRM976 standard as: $\delta^{65}Cu_{SRM976} = \delta^{65}Cu_{ERM\ AE647} + 0.21$ (Moeller *et al.*, 2012). Based on repeated analyses of Bergen Cu (n = 8), the external precision on $\delta^{65}Cu$ was 0.08 (2s).

4. Results

4.1. Structure and zonation of the deposit

The investigated drill cores exhibit three distinct kinds of mineralization: hypogene, gossan, and saprolite. The hypogene and gossan mineralizations are typically interspersed with fresh host rocks (Fig. 2A). The base of the profile is comprised of chloritites, consisting of approximately 80 vol% chlorite, 15 vol% plagioclase, 5 vol% quartz, with accessory magnetite, and occasional zones of potassic alteration, indicated by the presence of alkali feldspar. Above that, the host rocks are granodiorites, composed of quartz (40 vol%), oligoclase (35 vol%), and orthoclase (15 vol%), in addition to biotite and hornblende which together make up approximately 10 vol%. The main accessory minerals in the granodiorites are apatite, zircon, and titanite.

Hypogene mineralization occurs approximately between 110 and 140 m deep, comprising massive ore interspersed disseminated ore, and chloritite zones. The disseminated-

style mineralization corresponds to stockwork veins formed of quartz with chalcopyrite, alkali feldspar, and calcite, with traces of siderite and fluorite (Figs. 2B). The massive-style is composed of chalcopyrite (with traces of nukundamite) surrounding millimetric fragments of chloritite (Figs. 2C). Chalcopyrite exhibits numerous inclusions, like apatite, magnetite, petzite, altaite, galena, uraninite, stannite, and cassiterite (Fig. 3).

The gossan was divided into four zones according to the dominant minerals: goethite, malachite, cuprite, and libethenite. Chloritites host the first two zones, and the last two are hosted by granodiorites. The *goethite zone* is at the base of the gossan profile and presents three main faciological variations: (1) cavity-filling, (2) fracture-filling, (3) and breccia facies. The cavity-filling facies comprises quartz-rich stockwork veins with numerous cavities formed by the dissolution of chalcopyrite. These cavities are invariably coated with goethite (Fig. 2D) and sometimes malachite. The fracture-filling facies consists of goethite and chalcocite locally filling chloritite fractures. The breccia facies consists of a goethite micromass surrounding quartz grains up to 4 cm in diameter (Fig. 2E, F). Native copper crystals and pseudomalachite are often identified within the goethite matrix.

The *malachite zone* is predominantly massive and up to 2 m thick. It consists of a malachite micromass with subordinate chrysocolla and ramsbeckite, surrounding black nodules of cuprite and tenorite (Fig. 2G). Massive goethite is often associated with this zone. The *cuprite zone* is predominantly massive, approximately 1 m thick, and is characterized by the intercalation of (1) reddish portions formed of cuprite and goethite surrounding millimetric quartz grains; and (2) brownish sections, consisting of goethite, chalcocite, and quartz (Fig. 2H). The *libethenite zone* is located approximately 43 to 80 m deep and represents the gossan top. Its distribution is restricted to the granodiorite fracture system, and the main Cu-bearing phase is libethenite, with minor pseudomalachite and malachite (Fig. 2I).

The saprolite extends from the surface to approximately 35 m deep, overlying fresh chloritites. Its base is composed of weakly weathered chloritites, partially preserving the primary foliation, thus comprising a coarse saprolite (Fig. 2J). From the bottom to the top, the saprolite is progressively kaolinized, with the development of fine saprolite, displaying clayey zones with alternating colors, ranging from red to light red, with white stains; and yellow (Figs. 2K-M). Numerous quartz veins crosscut all the saprolite zones.

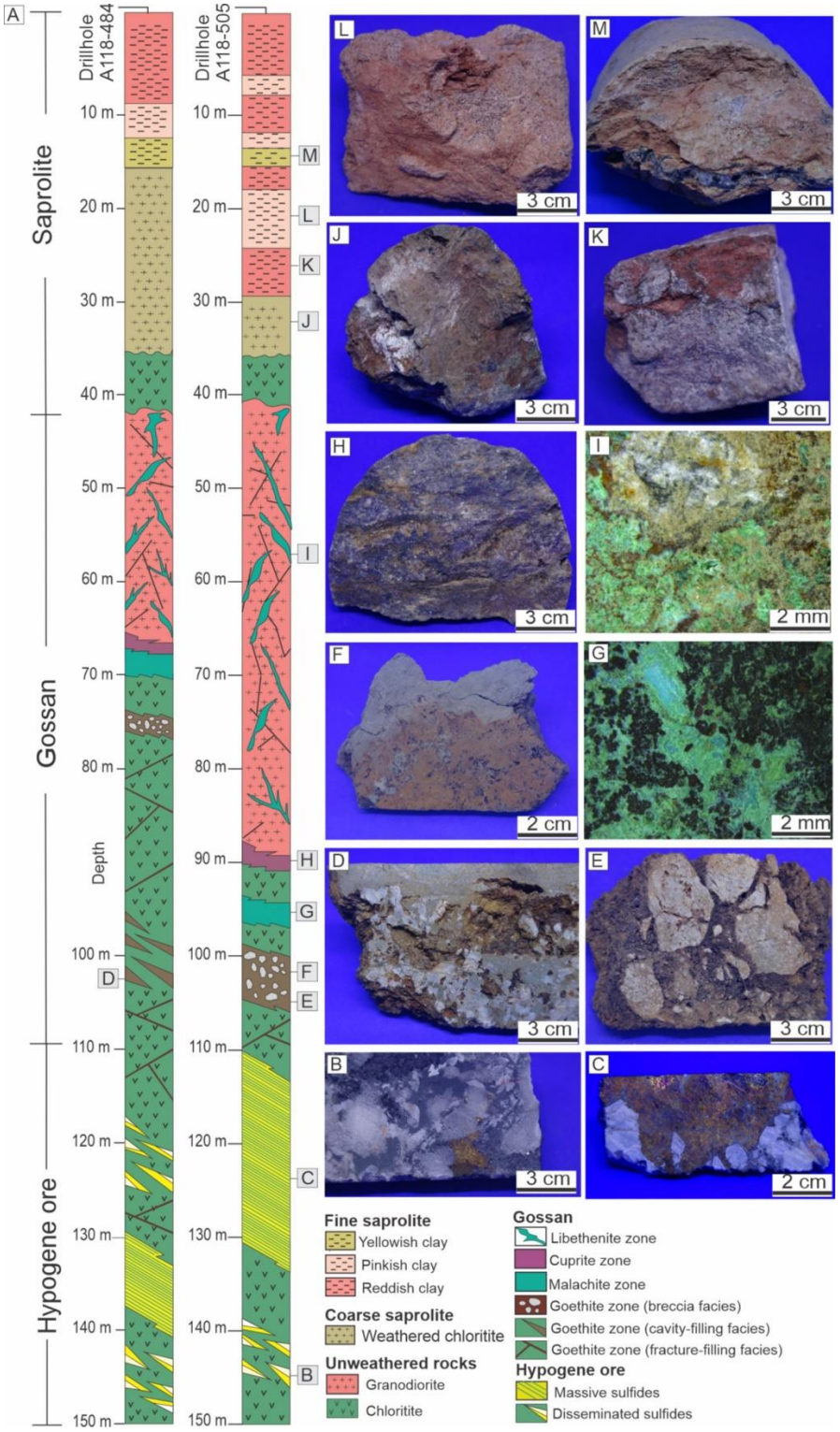

Fig. 2 Distribution of hypogene mineralization, gossan, and saprolite in the investigated drill holes, modified from Santos and Costa (2022) (A). Disseminated hypogene mineralization, comprising quartz veins with chalcopyrites crosscutting chloritite (B). Massive hypogene mineralization (B). Gossan: goethite (D, E, F), malachite (G), cuprite (H), and libethenite (I) zones. Saprolite: coarse saprolite (J) and fine saprolite (K, L, M).

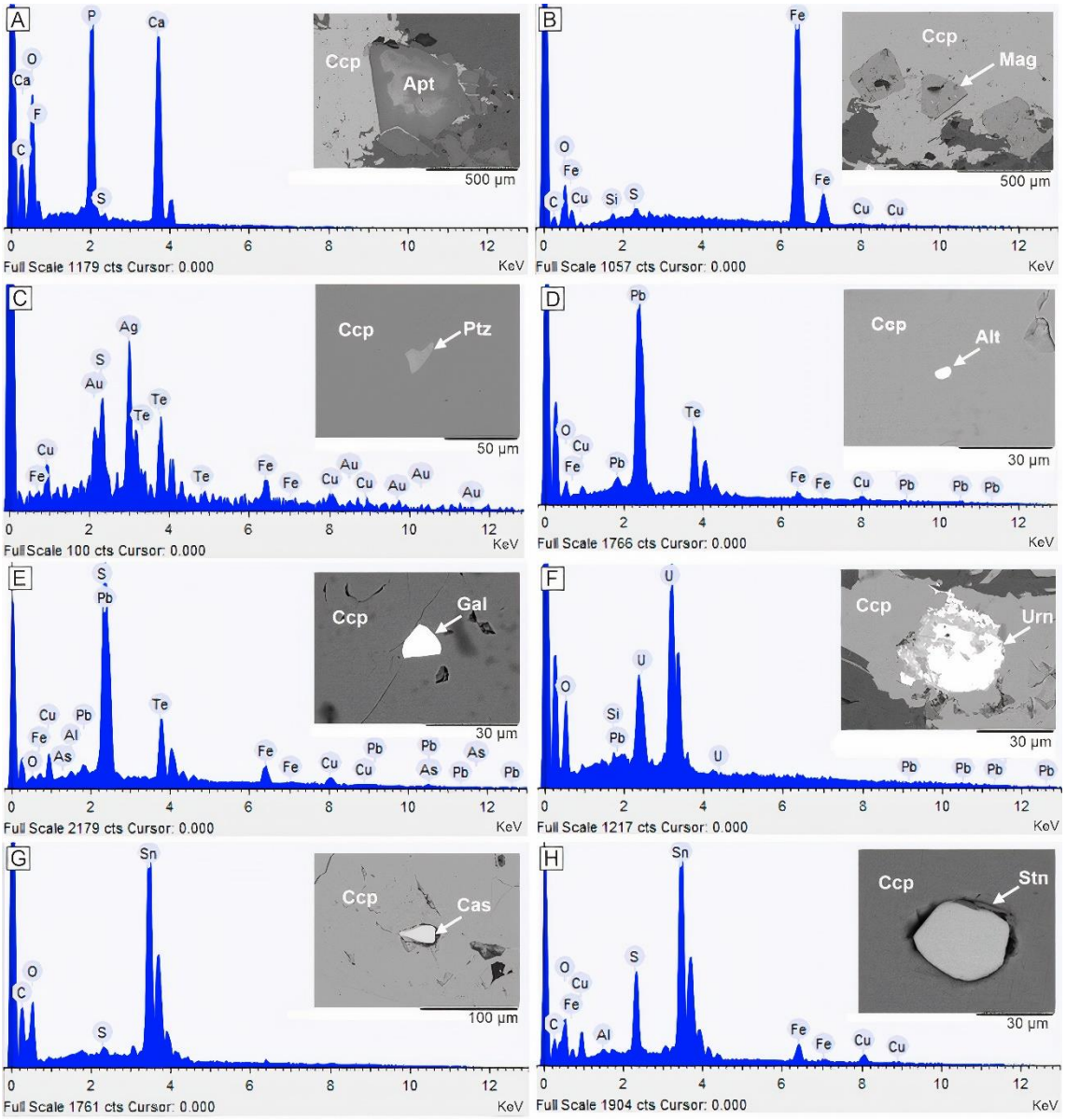

Fig. 3 SEM images and respective EDS spectra of accessory minerals from hypogene mineralization, identified as chalcopyrites inclusions: Apatite, Apt (A); magnetite, Mag (B); petzite, Ptz (C); altaite, Alt (D); galena, Gal (E); uraninite, Urn (F); cassiterite, Cas (G); and stannite, Stn (H).

Kaolinite is the predominant mineral all over the fine saprolite. It was identified from its 001 peak in 7.12 Å in the natural samples, which was not displaced after treatment with ethylene glycol but disappeared after heating at 550 °C. Across the profile, kaolinite may be associated with chlorite, vermiculite, smectite, or both (Figs. 4A-D).

Chlorite was identified from its highest intensity peak at 14 Å in the natural sample, whose position remains unchanged after glycolation and heating at 550 °C (Fig. 4A). Vermiculite was indicated by the 14.18 Å and 14.25 Å peaks in natural samples (Figs. 4B and D), which remain unchanged after glycolation and collapse to 12.46 and 12.28 Å, respectively, after heating (Figs. 4B and D). Smectite peaks appear at 14.49 Å and 14.05 Å in the natural

samples (Figs. 14C and D), expanding to 16.54 and 17.12 Å in the glycolated samples (Figs. 14C and D); and collapsing to 9.91 and 9.89 Å after heating (Figs. 14C and D). Quartz and goethite are present throughout the thin saprolite as resistate and newly formed minerals, respectively.

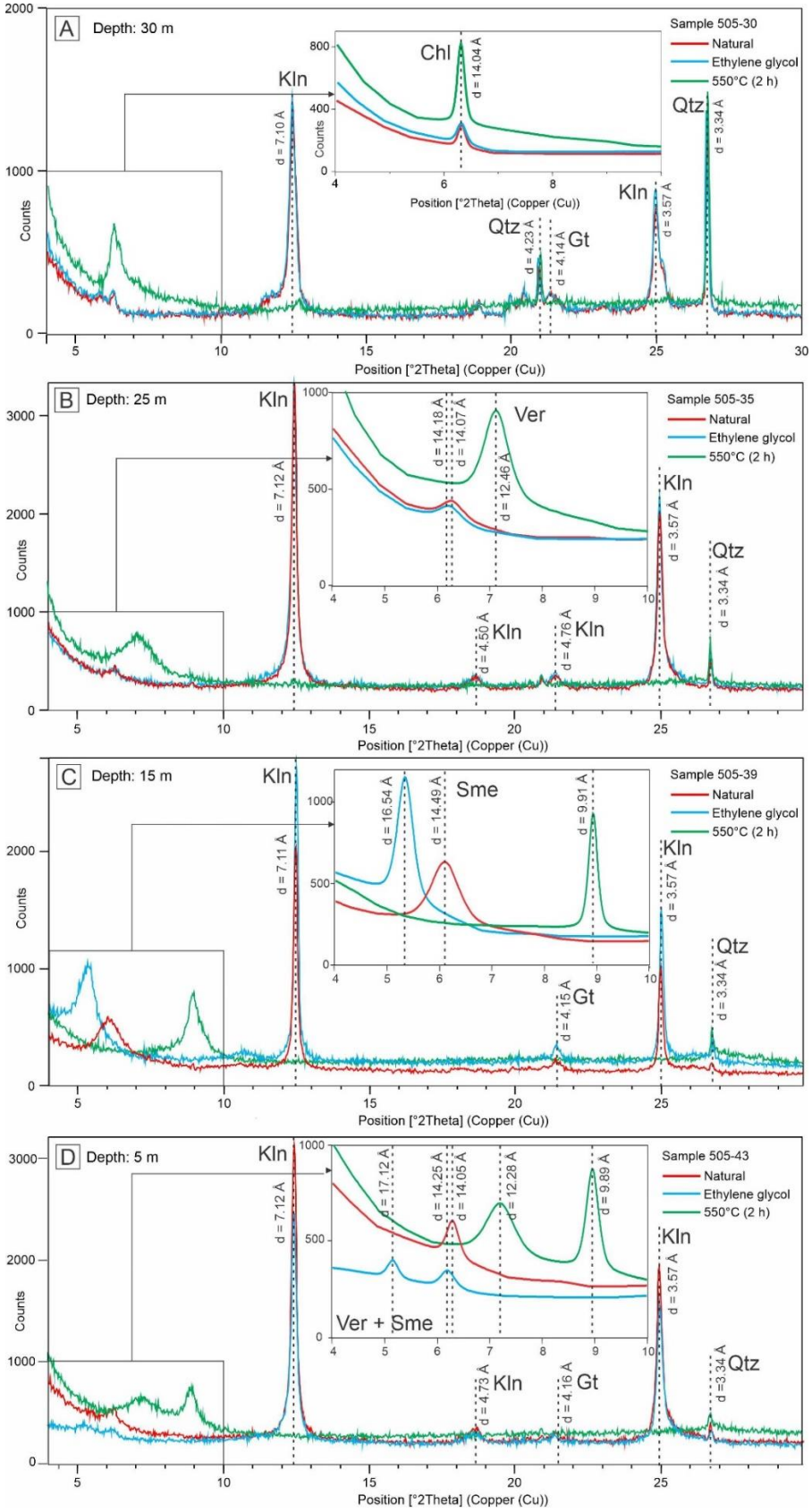

Fig. 4 X-ray diffractograms of selected samples of the fine saprolite, analyzed on oriented sections (red spectra); subjected to an ethylene glycol atmosphere for 24 h (blue spectra); and heated at 550 °C for 2 h (green spectra). Saprolite at 30 m deep (A); saprolite at 25 m deep (B); saprolite at 15 m deep (C); saprolite at 5 m deep (D). Kln (kaolinite); Chl (chlorite); Ver (vermiculite); Sme (smectite); Gt (goethite); Qtz (quartz).

4.2 Chemical composition of the hypogene mineralization, gossan, and saprolite

Aluminum (Al_2O_3), SiO_2, Fe_2O_3, CaO, MgO, K_2O, and LOI are the main components of the hypogene mineralization, gossan, and saprolite, followed by CaO, MgO, K_2O, TiO_2, MnO, and P_2O_5 (Tab. 1). Sodium (Na_2O) was detected only in the saprolite, averaging 0.038%. The CuO contents vary from 26.29 to 29.79% in the analyzed samples of the massive hypogene mineralization. However, in the gossan, CuO oscillates according to the mineralogical composition of each zone, goethite (0.9 to 0.91% CuO), malachite (46 to >50% CuO), and cuprite (7.9% CuO). This oscillation is also present in the saprolite (1.15 to 4.79% CuO). The Au values are higher in the hypogene mineralization (average 2.19 ppm), reduced in the gossan (0.05 to 0.47 ppm), and strongly decreased in the saprolite (from not detected to 0.55 ppm).

In the hypogene mineralization, the high Fe_2O_3, CuO, and S contents reflect the predominance of chalcopyrite, while SiO_2, Al_2O_3, MgO, and part of the Fe_2O_3 correspond mostly to chlorite. The gossan exhibits a substantial variation in Fe_2O_3 contents (0.77 to 71.4%), in which the lowest values correspond to the malachite and cuprite zones, and the highest naturally delimit the goethite zone. Intermediate Fe_2O_3 values are found in the interspersed chloritites, exhibiting the highest SiO_2, Al_2O_3, and MgO contents. In the saprolite, the Fe_2O_3 contents (6.35 to 20.2%) are controlled by the distribution of iron oxyhydroxides and exhibit very similar behavior to MgO, reflecting relic chlorites and iron release during chlorite weathering.

Among the trace elements, Sn, Pb, U, Te, and Ag concentrations are much higher than those of the UCC in the hypogene mineralization because of the inclusions of stannite, cassiterite, galena, uraninite, altaite, and petzite in chalcopyrite. These elements generally show substantially lower values in gossan and saprolite than in hypogene mineralization but are still above UCC.

Tab. 1. Chemical compositions of selected samples from the hypogene mineralization, gossan, and saprolite, expressed in wt% (major elements) and ppm (trace elements) and average composition of the upper continental crust, UCC (Rudnick and Gao, 2003).

	Hypogene ore		Gossan zone					Saprolite ore					UCC
			Goethite		Malachite		Cuprite						
Depth	129 m	127 m	98 m	70 m	69 m	68 m	94 m	15 m	12 m	10 m	7 m	5 m	
SiO_2 Wt.%	13.4	10.35	36.8	7.11	3.78	14.2	43.5	55	48.8	55.3	52	41.2	66.6
Al_2O_3	4.08	3.25	3.41	5.89	2.56	10	5.19	21.1	22.2	17.75	17.7	20.9	15.4
Fe_2O_3	25.8	35.4	49.8	71.4	0.77	6.07	36.8	9.85	13.0	6.33	16.6	20.2	5.04
CaO	1.93	1.67	0.08	0.06	0.03	0.04	0.07	0.03	0.03	0.07	0.04	0.02	3.59
MgO	4.6	3.61	0.48	2.55	0.15	1.63	0.6	2.38	1.37	1.41	2.75	1.73	2.48
Na_2O	<0.01	<0.01	<0.01	<0.01	<0.0	<0.01	<0.01	0.03	0.07	0.19	0.02	0.04	3.27
K_2O	2.51	1.85	0.27	0.07	0.05	0.15	0.21	1.33	0.76	2.25	0.28	1.11	2.80
TiO_2	0.13	0.11	0.24	0.16	0.09	0.29	0.41	1.12	1.14	1.9	1.01	1.01	0.64
MnO	0.02	0.02	0.05	0.06	<0.0	0.03	0.03	0.02	0.08	0.08	0.02	0.12	0.1
P_2O_5	1.28	1.1	1.48	1.28	<0.0	0.29	0.83	0.12	0.27	0.47	0.11	0.19	0.15
CuO	26.29	29.79	0.91	0.94	>50	46.32	7.90	1.51	1.65	4.79	2.95	1.15	0.0035
LOI	11.15	11.7	8.44	11.7	15.1	22.6	7.1	9.61	12.8	10.35	9.86	11.5	-
Total	91.20	98.86	101.96	101.22	>72.	101.62	102.65	102.16	102.	100.93	103.	99.20	-
C	0.02	0.05	0.02	0.09	2.95	3.15	0.06	0.04	0.06	0.08	0.07	0.04	-
S	21.3	23.8	0.04	0.01	0.67	0.48	0.76	0.01	<0.0	<0.01	<0.0	<0.01	-
Au ppm	2.72	3.32	0.047	0.432	0.08	0.397	0.277	0.016	0.01	0.004	0.55	<0.001	0.0015
Ag	16.2	22.3	3.6	0.8	43.8	26.8	3	<0.5	<0.5	0.7	0.5	0.5	0.053
Ba	84.8	68.3	27.2	30.6	123.	40.4	64.5	495	253	372	89.1	206	628
Co	135	118	22	55	2	13	22	29	66	45	28	113	17.3
Cr	<10	<10	<10	10	<10	10	20	70	70	10	100	80	92
Cs	2.35	1.91	1.27	0.42	0.02	0.06	2.59	1.1	0.77	0.58	1.82	1.11	4.9
Ga	18.6	14.3	12.2	37.2	8.8	30.2	22.4	32.6	33.1	15	33.9	37.6	17.5
Hf	<0.1	<0.1	0.7	0.3	0.1	0.9	1.6	6.2	7.4	9.2	7	6.1	5.3
Li	30	20	10	10	<10	10	10	10	10	<10	10	10	24
Mo	<1	<1	60	57	8	5	9	<1	2	<1	<1	<1	1.1
Nb	13.8	9.9	4.8	6.5	1.9	7.7	6.4	8.6	11.3	16.8	13.8	12.8	12
Ni	127	139	187	905	26	133	398	182	102	121	281	65	47
Pb	16	10	<2	185	20	113	<2	6	<2	14	5	<2	17
Pd	0.002	<0.001	0.001	<0.001	0.01	0.026	<0.001	0.007	0.01	0.002	0.00	0.013	0.0005
Pt	0.005	<0.005	<0.005	<0.005	0.02	0.015	<0.005	0.009	0.00	<0.005	0.00	<0.005	0.0005
Sn	198	278	21	13	7	21	29	42	24	6	31	28	2.1
Sr	5.9	8.8	4.8	1.5	0.9	3.7	4.2	24.1	10.9	29.8	10.1	4.9	320
Ta	1.3	1.1	0.2	0.5	0.3	0.5	0.2	0.7	0.9	1.3	0.9	0.6	0.9
Th	7.11	3.04	1.53	2.09	0.73	2.76	4.46	12.9	9.17	16.1	17.9	12.95	10.5
U	7.55	4.9	5.42	28	2.13	8.24	6.81	3.24	5.77	3.86	4.42	5.17	2.7
V	52	46	122	229	20	94	190	255	171	60	229	256	97
W	2	4	7	5	22	3	3	5	5	10	4	5	1.9
Y	1120	623	99.2	253	173.	1065	163.5	39.7	104	175	41.6	142.5	21
Zr	2	2	38	24	14	50	70	213	280	344	276	244	193
As	4.3	2.2	1.8	1.2	0.7	4.1	0.6	0.2	0.7	0.5	0.3	0.6	4.8
Bi	0.84	0.3	1.35	10.7	2.49	6.78	2.21	0.24	0.03	0.07	0.01	0.01	0.16
Hg	0.024	0.01	0.016	0.017	0.19	1.31	0.023	<0.005	0.01	0.008	0.01	0.01	0.05
In	4.42	5.29	0.133	0.462	0.13	0.38	0.127	0.04	0.02	0.022	0.03	0.03	0.056
Rb	300	234	37.9	6.3	1.8	6.2	44.5	104	84.7	115	66.6	77.1	84
Re	0.007	0.004	<0.001	0.001	0.00	0.008	0.001	0.001	<0.0	0.001	<0.0	0.001	0.198
Sc	9	8	16	17	16	84	27	41	32	17	44	36	14.0
Se	34.7	25.9	1.3	3.9	101.	30.3	15.9	0.2	0.3	2.3	1.2	2.7	0.09
Te	18.8	18.9	0.65	1.2	2.79	0.73	2.41	0.05	0.05	0.05	0.05	0.07	n. a.
Tl	0.42	0.31	0.05	0.02	<0.0	<0.02	0.1	0.12	0.15	0.07	0.14	0.16	0.9
Zn	42	36	117	793	34	120	231	103	59	89	108	51	67
La	8.5	7.2	4	13	11.1	150.5	7	74.9	16.4	38.2	15.4	40.6	31
Ce	38.6	27.7	10.2	28.4	25.1	318	14.6	151	28.4	81.8	18.8	76.8	63
Pr	8.7	5.82	1.18	3.48	3.18	39.6	1.72	16.7	3.29	9.68	3.14	12.25	7.1
Nd	67.5	42.9	6.2	17.1	15.6	179	7.7	60.6	13.9	42.1	13.3	53.7	27
Sm	47.3	28.1	2.54	7.31	5.27	48.4	3.23	9.25	3.5	8.7	2.61	11.45	4.7
Eu	12.65	7.66	1.07	3.03	2.11	16.25	1.36	2.7	1.55	3	1.01	3.85	1.0
Gd	122	69.7	6.53	18.75	12.5	85.9	9.4	8.07	8.25	13.3	4.08	17.05	4
Tb	25	14.7	1.32	4.01	2.6	16.7	2	1.18	1.57	2.34	0.68	2.8	0.7
Dy	176	100.5	9.79	28.7	19.3	123	15.65	6.54	11.3	16.35	4.42	17.8	3.9
Ho	38	21.5	2.54	7.24	4.88	31.7	4.05	1.31	2.82	4.22	1.05	3.9	0.83
Er	111.5	62.4	8.41	23.7	16.1	109	13.35	3.71	8.98	12.55	3.35	11.45	2.3
Tm	18.35	10.05	1.66	4.59	3.35	21.5	2.49	0.67	1.52	2.07	0.59	1.95	0.30
Yb	101.5	56.7	11.75	32.3	25.2	164.5	15.85	3.81	9.82	11.5	3.64	10.95	1.96
Lu	14.45	8.05	2.21	5.96	4.92	32.6	2.7	0.65	1.77	1.93	0.65	1.81	0.31
∑ REE	790.05	462.98	69.4	197.57	151.	1336.6	101.1	341.09	113.	247.74	72.7	266.36	125
$(La/Lu)_N$	0.06	0.09	0.19	0.23	0.23	0.48	0.27	11.96	0.96	2.05	2.46	2.33	-

The proportions of SiO_2, Al_2O_3, and Fe_2O_3 in selected samples from the hypogene mineralization, gossan, and saprolite demonstrate the compositional heterogeneity of the gossan compared with the saprolite, which forms a more homogeneous group (Fig. 5). The assemblage formed by the three types of mineralization shows a trend of increasing Fe_2O_3+MgO content. In hypogene mineralization, this reflects the predominance of chalcopyrite; in gossan and saprolite, it is related to iron oxyhydroxides and chlorite contents.

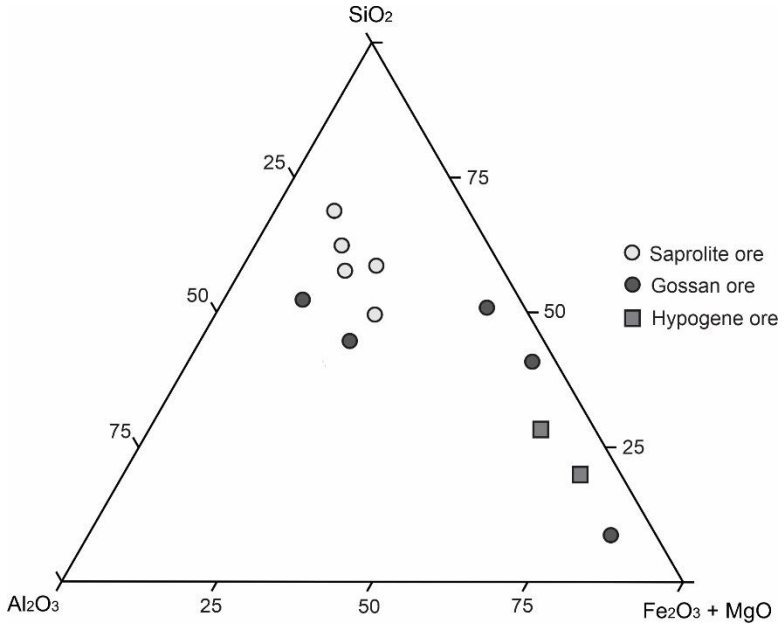

Fig. 5 Triangular diagram SiO_2–Al_2O_3–Fe_2O_3+MgO for selected samples from the hypogene mineralization, gossan, and saprolite.

The CuO and Au contents oscillate strongly and similarly along the investigated boreholes (Fig. 6). In the hypogene mineralization, this oscillation reflects the alternation between massive and disseminated sulfide domains. In the gossan, the highest contents correspond to the malachite and cuprite zones, which are massive, while the lowest contents are in the libethenite zone, restricted to the fracture system, with a disseminated distribution. The CuO and Au contents in the saprolite are higher than those in the libethenite zone located in the upper portion of the gossan but lower than those of the goethite, malachite, and cuprite zones.

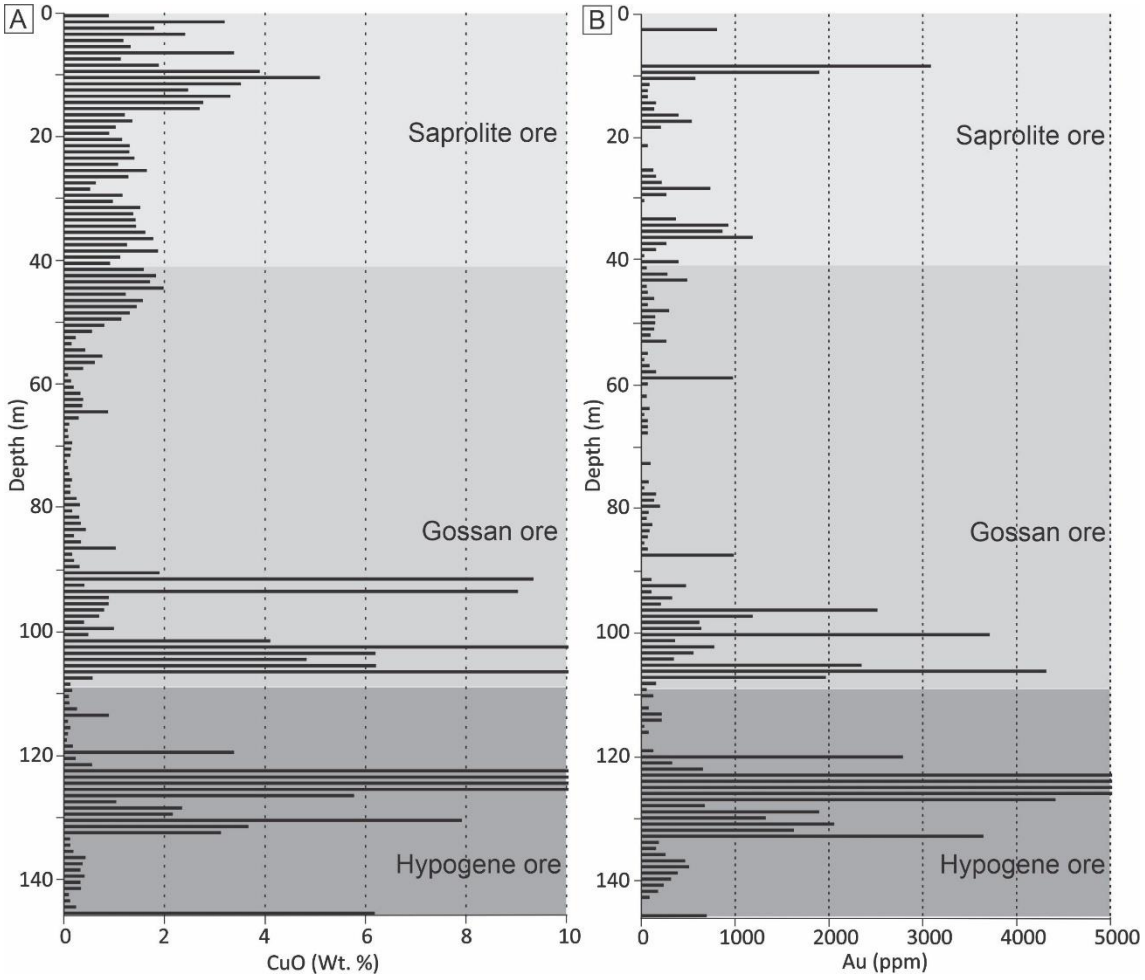

Fig. 6 Vertical distribution of CuO (Wt.%) and Au (ppm) along the A118-505 drill hole, crosscutting the hypogene mineralization, gossan, and saprolite.

3.3 Copper and Fe isotopes

The isotopic composition of the analyzed samples initially reflects chalcopyrite dissolution (the main Cu and Fe carrier in the hypogene ore) and the newly formation of Cu/Fe-bearing minerals in the gossan zones. Additionally, the overlying saprolite represents a new Cu and Fe isotopic fractionation stage.

The hypogene mineralization is enriched in the heavy copper isotope ($\delta^{65}Cu$ = +0.13 and +0.06‰), as well as the iron oxyhydroxide zone of the gossan, where the $\delta^{65}Cu$ value is even heavier ($\delta^{65}Cu$ = +0.73‰). However, the malachite zone of the gossan is isotopically lighter ($\delta^{65}Cu$ = −0.69 and −0.70‰). The saprolite overlying the gossan is also enriched in heavy isotopes, showing values similar to those observed in the hypogene mineralization ($\delta^{65}Cu$ = +0.07, 0.08, and +0.09‰). Therefore, there is no apparent isotopic fractionation between the hypogene mineralization and saprolite, while the zones that make up the gossan show significant positive and negative values (Table 2).

The heavy Fe isotope is enriched in the hypogene mineralization ($\delta^{56}Fe$ = +0, 36, and +0.45‰) and further increased in the malachite zone of the gossan ($\delta^{56}Fe$ = +0, 57, and +1.00‰). However, the iron oxyhydroxide zone of the gossan is depleted ($\delta^{56}Fe$ = −0.56‰). The saprolite overlying the gossan is enriched in the heavy isotope, as in the hypogene mineralization and malachite zone ($\delta^{56}Fe$ = +0.02, +0.14, and +0.22‰)(Tab. 2).

Tab. 2. ^{65}Cu and $\delta^{56}Fe$ values for samples from hypogene mineralization, gossan, and saprolite.

Sample	Cu Wt. %	$\delta^{65}Cu$	SE*	Fe Wt. %	$\delta^{56}Fe$	SE*
Hypogene ore						
505-07	21.00	0.13	0.123	18.04	0.36	0.10
505-08	23.80	0.06	0.013	24.76	0.45	0.05
Gossan ore						
505-15	0.73	0.51	0.034	34.83	- 0.56	0.05
484-34	50.00	-0.69	0.001	0.54	1.00	0.11
484-35	37.00	-0.70	0.005	4.25	0.57	0.06
Saprolite ore						
505-39	1.32	0.08	0.002	9.13	0.22	0.02
505-40	3.83	0.09	0.026	4.43	0.14	0.06
505-42	0.92	0.07	0.05	14.13	0.02	0.020

4 Discussion

This section is mainly dedicated to the geochemical behavior of the elements that exhibit high affinity with CuO in the hypogene mineralization, seeking to understand their fractionation along the gossan and the overlying saprolite. The remaining elements will be approached based on their linkage with the accessory minerals of the hypogene mineralization and host rocks.

4.1 Geochemical associations

The mineralogical distribution of main trace elements was determined using bivariate analysis (Pearson correlation coefficient). Thus, in the hypogene mineralization, the strong correlations between CuO and Au (0.87), Ag (0.93), Te (0.97), and Pb (0.83) reflect petzite, altaite, and galena inclusions in the chalcopyrite mass (Figs. 7A-C). There is also a strong correlation between CuO and In (0.88) and Se (0.94), in which the latter reflects possible S substitution, which is common in hydrothermal chalcopyrites (Loftus-Hills and Solomon 1967; Scott *et al.*, 2001).

The strong Bi × Pb correlation (0.90) may indicate Bi incorporation by galena, typically reported in hydrothermal deposits (Deady *et al*., 2022). Considering that this mineral is included in chalcopyrite, a good Bi × CuO correlation (0.56) was expected (Fig. 7D). The

strong As × U (0.90) and Mo × U (0.70) correlations suggest As and Mo are at least partially carried by uraninite, as reported by Alexandre *et al*. (2015).

The correlations between CuO and Ag (0.73), Te (0.55), Pb (0.57), Se (0.79), and Bi (0.56) are maintained in the gossan, although weaker, suggesting that after the dissolution of petzite, altaite, and galena, these elements were at least partially incorporated by the newly formed copper minerals (e.g., Atapour and Aftabi, 2007). Conversely, Au and In show no correlation with CuO nor Ag but are correlated with Fe_2O_3 (0.50 and 0.66, respectively). This fact suggests petzite (the only identified gold-bearing mineral) was solubilized, and gold was then complexed and precipitated preferentially with iron oxyhydroxides (e.g., Nickel, 1979; Plyusnin *et al*., 1981).

In the gossan, the most significant correlations are between Fe_2O_3 and Mo (0.88), Sc (0.65), Sn (0.72), Y (0.78), U (0.49), Zn (0.65), As (0.79), Be (0.88), Ga (0.64), and Ni (0.67), partially illustrated in Figs. 7E-H. They suggest iron oxyhydroxides are the main carriers of metals released by hypogene mineralization. These incorporations are possible by coprecipitation or adsorption (Andrew, 1984; Coughlin and Stone, 1995; Swedlund *et al*., 2009). The Fe_2O_3 × Sn correlation may also indicate the presence of relic cassiterite included in the iron oxyhydroxide micromass.

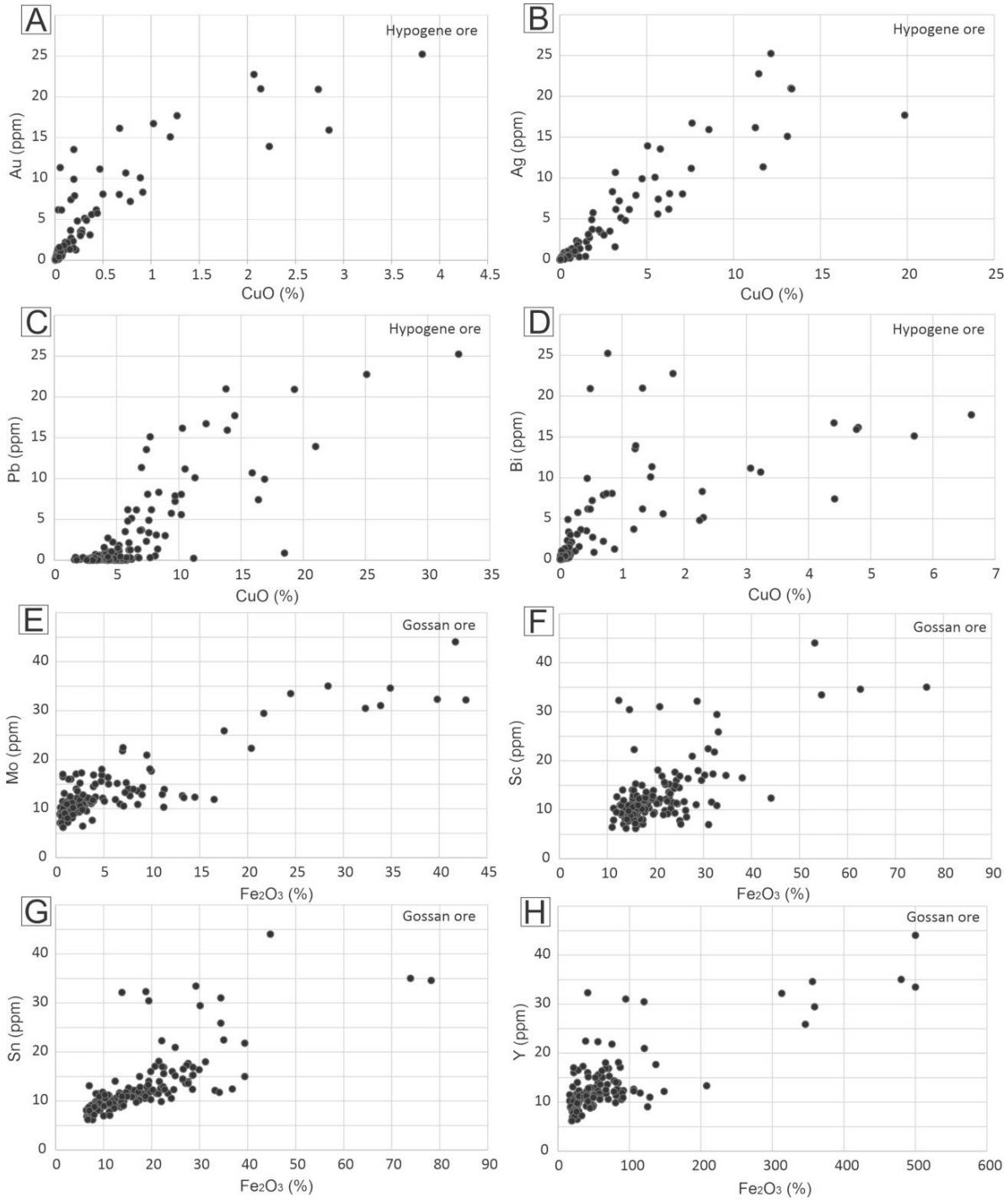

Fig. 7 Scatter diagrams for selected elements from hypogene mineralization, CuO × U (A), CuO × Ag (B), CuO × Pb (C), CuO × Bi (D); and gossan, Fe_2O_3 × Mo (E), Fe_2O_3 × Sc (F), Fe_2O_3 × Sn (G), Fe_2O_3 × Y (H).

In the saprolite, Fe_2O_3 correlates with Ga (0.81), Sc (0.70), Sn (0.78), V (0.73), Mn (0.57), Co (0.65), and Cr (0.57), as partially illustrated in Figs. 8 A–D, again suggesting their incorporation by iron oxyhydroxides (Smith, 1999). In weathering profiles, goethite usually presents low crystallinity and comprises nanometric particles with high surface area, thus representing an important cation immobilizer (Cornell and Schwertmann, 2003; Liu *et al.*, 2014). The geochemical correlations identified in the hypogene mineralization and gossan are

generally absent in the overlying saprolite, except for Fe_2O_3 with Ga, Sc, and Sn. On the other hand, V, Mn, Co, and Cr present a good correlation with Fe_2O_3 only in the saprolite, suggesting they were derived from host rock weathering.

Zircon exhibits a strong correlation with Ti in hypogene mineralization (0.99), in addition to the typical Zr × Hf (0.90) correlation. This behavior is maintained in the gossan (0.90) and saprolite (0.77) because their possible carriers (e.g., zircon and rutile) are stable in the supergene environment (e.g., Fralick and Kronberg, 1997; Harrison, 2005; Fu *et al*., 2008; Martínez *et al*., 2016).

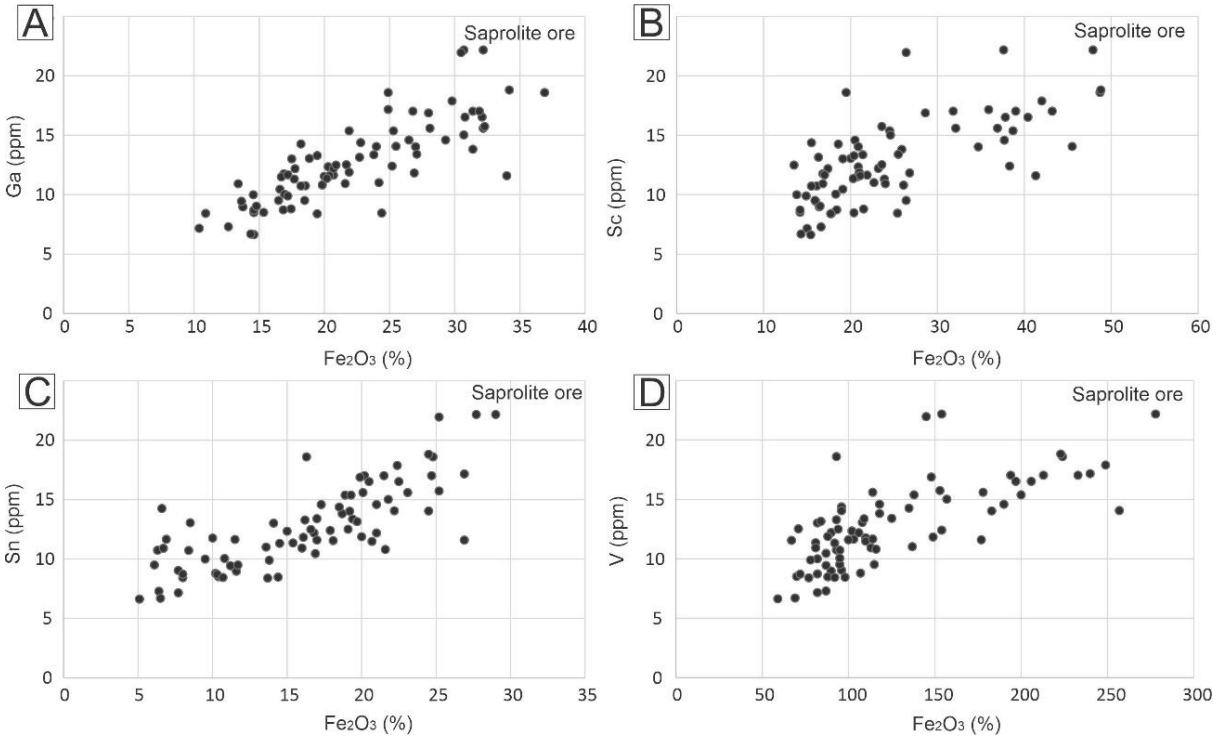

Fig. 8 Scatter diagrams for selected elements of the saprolite: Fe_2O_3 × Ga (A), Fe_2O_3 × Sc (B), Fe_2O_3 × Sn (C), Fe_2O_3 × V (D).

The chemical composition of the hypogene mineralization is fundamentally controlled by the alternation between disseminated and massive sulfide zones, that is, zones with the greater or lesser influence of the host rock, respectively. Thus, the two identified clusters (Euclidean distance of 0.8) reflect chloritites and hypogene mineralization contribution (Fig. 9A). This is supported by the strong correlation between CuO × Se, Cd, Bi, Sb, Te, Au, In, Y, and Pb previously presented, in addition to the identification of petzite, altaite, and galena inclusions.

Four clusters were recognized in the gossan (Euclidean distance of 0.8). Two of them correspond to the composition of the host rocks. The other two represent the chemical

composition of the gossan, in which one group can be distinguished by its similarity with Fe_2O_3 and the other with CuO (Fig. 9B). This association suggests that Cu and Fe minerals incorporated the same trace elements initially contained in the hypogene mineralization, with a few exceptions (Cs, U, Ta, Cd, Ge, Ni, and W) that also show affinity with the host rocks.

The four clusters identified in the saprolite are very distinct from those highlighted in the hypogene mineralization and gossan (Euclidean distance of 0.85). Two of them are related to the weathering products of the host chloritites; the third (Fe_2O_3, As, Ga, V, Sn, Cr, Sc, Nb, Ta, Co, and Mn) suggest incorporation or adsorption by iron oxyhydroxides; and the fourth (SO_3, Au, In, Y, Te, Pb, Bi, and Se) broadly is the only connection of the saprolite with the hypogene mineralization and gossan (Fig. 9C).

The two groups of elements exhibit high similarity in the three mineralization types (hypogene, gossan, and saprolite). The first (Au, In, Y, Te, Pb, Bi, and Se) corresponds to the components of hypogene mineralization, which continue to be associated with each other in the gossan and saprolite. The second group (Al_2O_3, Hf, Zr, Th, TiO_2, Ce, La, Ba, and Sr) is equivalent to the geochemical signature of the host rocks, which is preserved in the form of resistate or newly formed minerals.

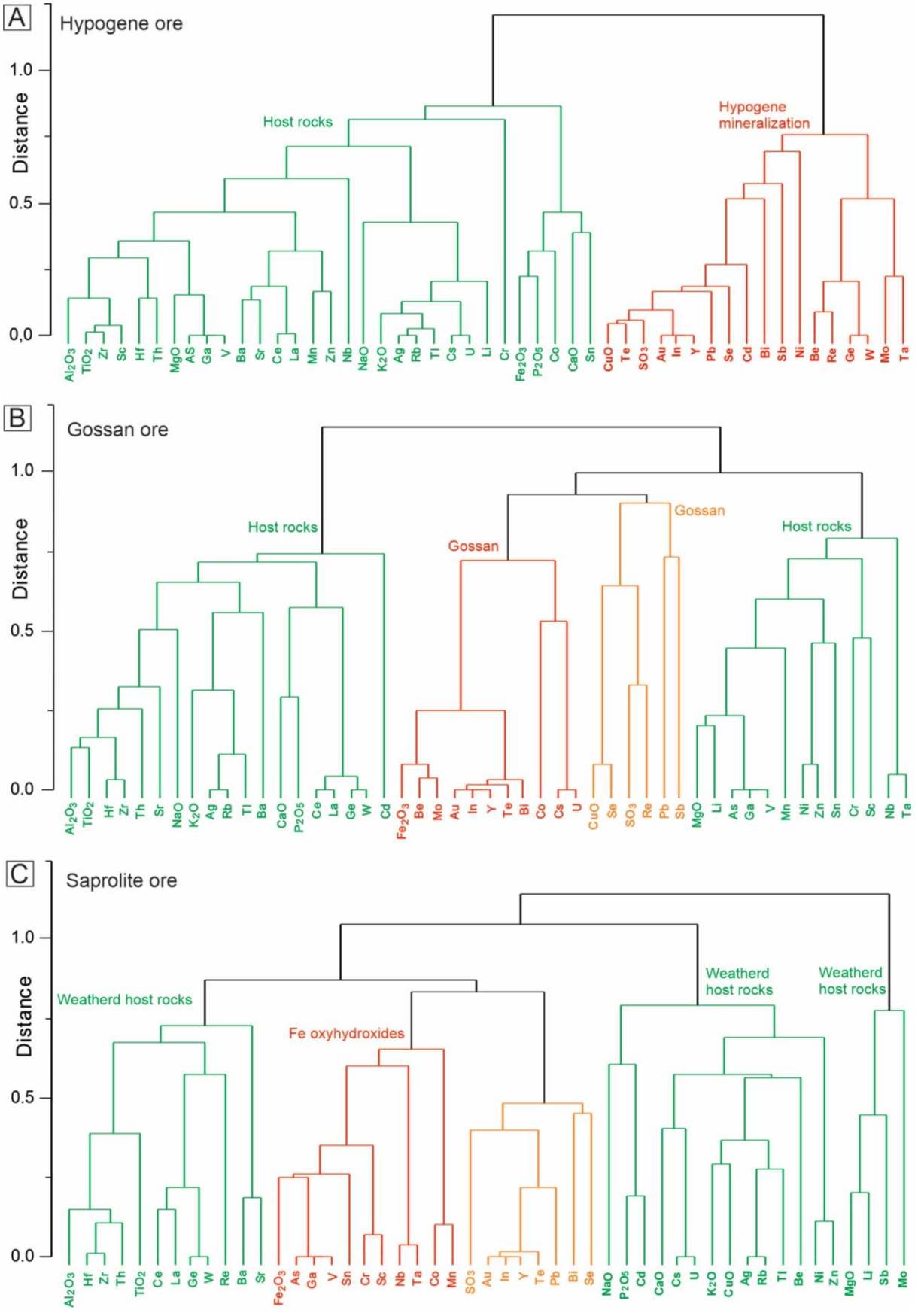

Fig. 9 Cluster diagram of whole-rock chemical composition data from drill hole A118-505, based on hypogene ore (A), gossan (B), and saprolite samples (C).

5.2. Geochemical fractionation

In the hypogene mineralization, the CuO, Se, Y, Ag, In, Sn, Pt, and Au concentrations reach values more than ten times higher than that of the UCC, reflecting the composition of chalcopyrite and its inclusions (Fig. 10A). In the gossan, the same elements remain above the UCC with the addition of P_2O_5, Fe_2O_3, Mo, Pd, and Ag (Fig. 10B). This is following the binary and cluster diagrams previously presented, which indicated similarity between the trace elements contained in the hypogene and gossan mineralizations. Se, Ag, Sn, Pt, Au, and Pd concentrations in the saprolite are more than ten times higher than in the UCC (Fig. 10C), following the hypogene mineralization and gossan. However, the general pattern for most elements differs from them due to the lower values, near or below the UCC contents. This contrast reflects the predominant influence of the chloritites on saprolite generation rather than hypogene mineralization and gossan.

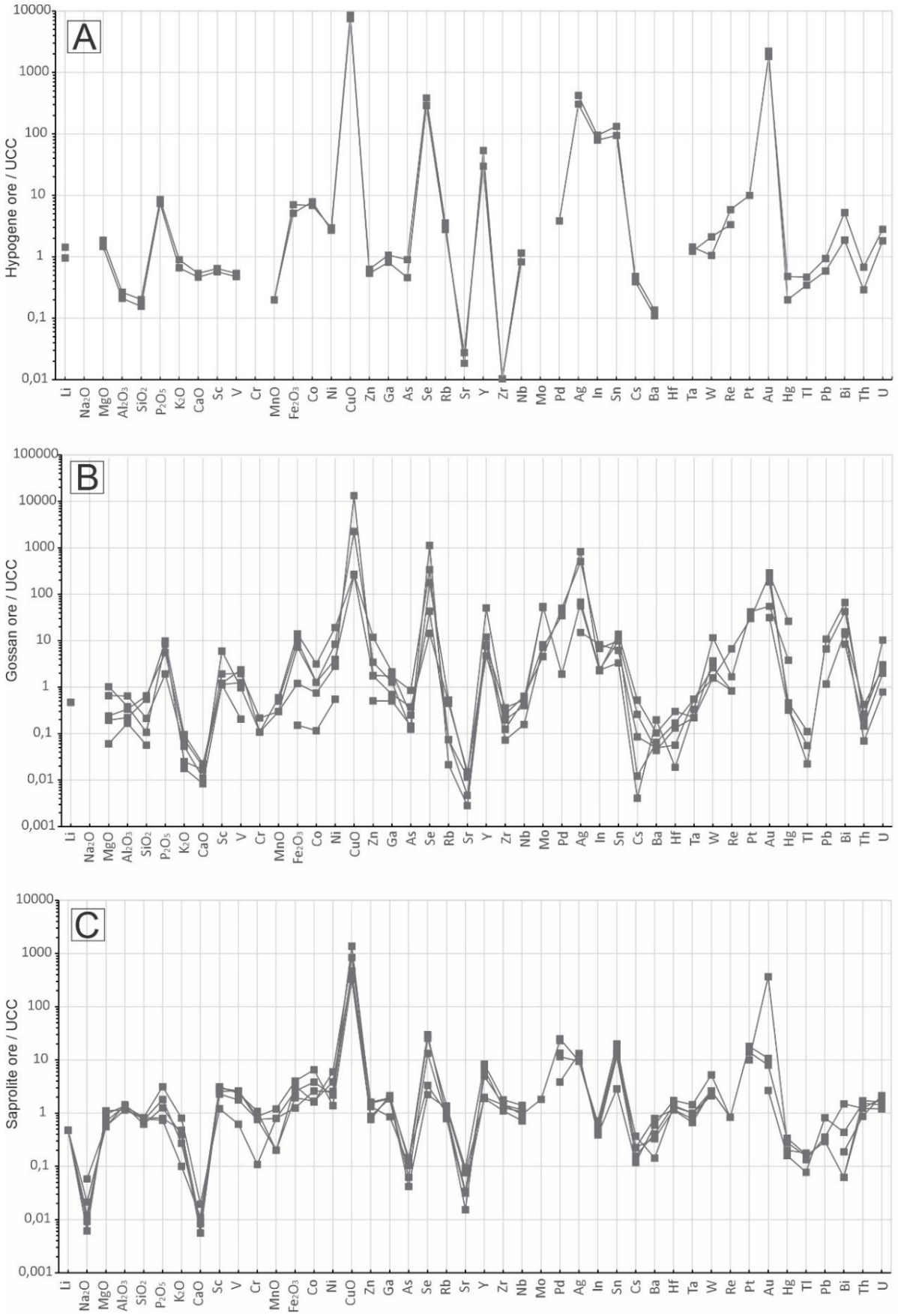

Fig. 10 Major and trace element distribution in hypogene ore (A), gossan (B), and saprolite (C), normalized to the chemical composition of the upper continental crust, UCC (Rudnick and Gao, 2003).

3.4 REE fractionation

The distribution patterns of REE normalized to the chondrites (Evensen *et al*., 1978) demonstrate they were fractionated during the supergene evolution of the deposit. In the hypogene mineralization, the HREE are enriched relative to the LREE, with an average $(La/Lu)_N$ of 0.08 (Fig. 11A). This contrast is attenuated in the gossan, where the average value of $(La/Lu)_N$ is 0.28, and it is reversed in the saprolite, where the HREE becomes enriched compared to the LREE and the average $(La/Lu)_N$ ratio is 3.95. Additionally, the negative Eu anomaly identified in the hypogene mineralization is absent in gossan and saprolite.

Several REE-bearing accessory minerals have been reported in the hypogene mineralization of the Alvo 118 deposit, including xenotime, monazite, britholite, gadolinite group mineral, and Be-Ba-HREE silicate (Xavier *et al*., 2008; Torresi *et al*., 2012). Their dissolution must have been responsible for the strong fractionation identified along the supergene evolution. Additionally, malachite and goethite have been reported as possible REE-bearing phases in supergene environments (e.g., Putter *et al*., 2010; Dutrizac and Soriano, 2018; Mondillo *et al*., 2019).

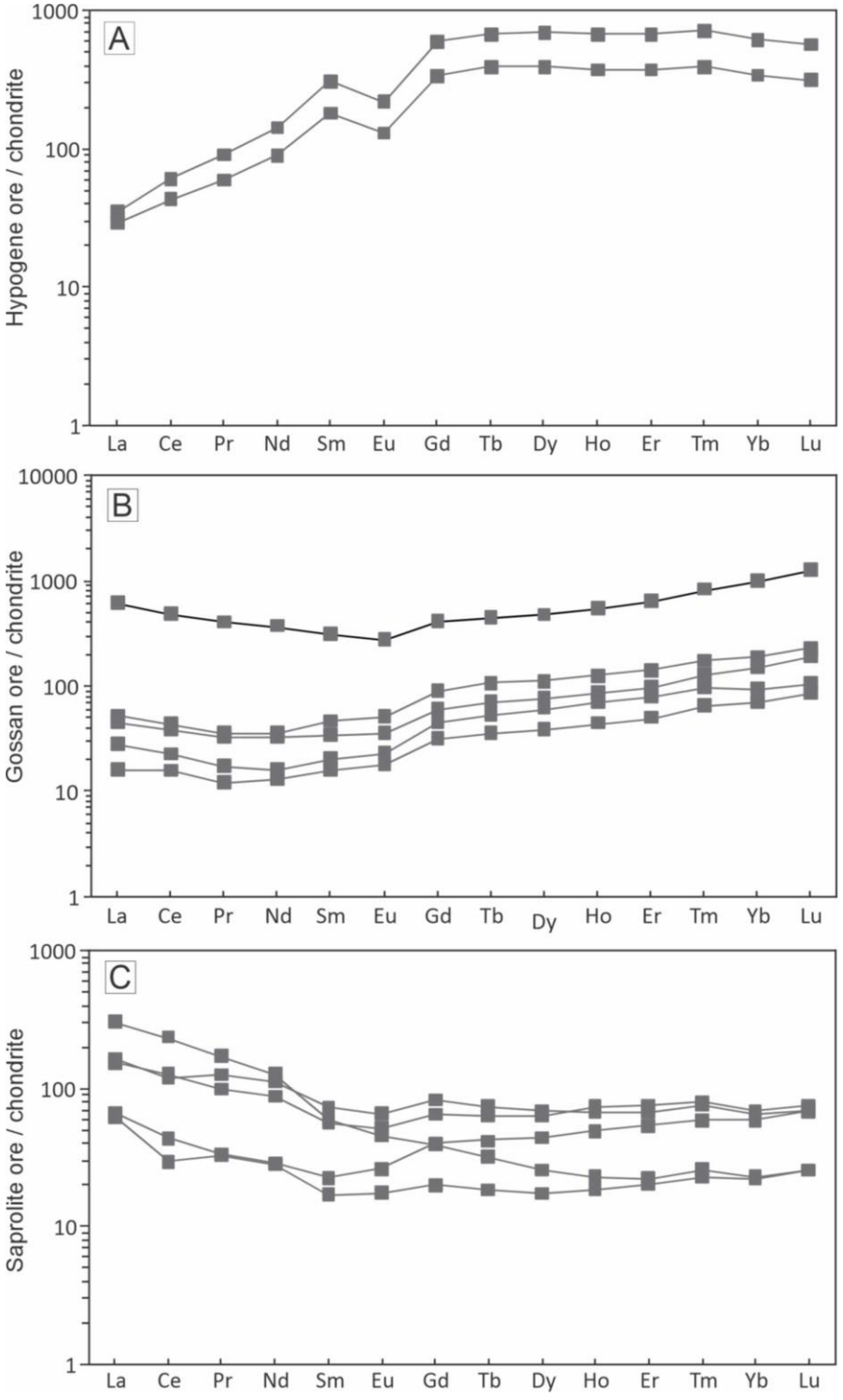

Fig. 11 Distribution pattern of REE in hypogene ore (A); gossan (B), and saprolite (C), normalized to the chondrites from Evensen *et al*. (1978).

5.5. Isotopic fractionation

The $\delta^{65}Cu$ values in the hypogene mineralization from Alvo 118 ($\delta^{65}Cu$ = +0.06 and +0.13‰) are consistent with massive and disseminated chalcopyrites from hydrothermal deposits, which are generally 0±1‰ (Graham *et al*., 2004; Maréchal *et al*., 1999; Zhu *et al*.,

2000). In the gossan, the goethite and malachite zones show slight positive and negative fractionations, respectively, relative to the hypogene mineralization (Fig. 12A). This fractionation is initially due to electron-exchange-driven redox reactions (Cu^{+}/Cu^{2+}) at the surface of the sulfides, which usually occur during the air and aqueous chemical reactions (Fernandez and Borrok, 2009).

The higher $\delta^{65}Cu$ values in the goethite zone compared with that of the hypogene mineralization are consistent with experimental and field studies, which indicate that redox reactions on hypogene sulfides produce isotopically heavier solutions (Mathur *et al*., 2005; Kimball *et al*., 2009) and that goethite can adsorb or coprecipitate Cu from such solutions, acquiring a heavier isotopic composition than that of the parent sulfide (Mathur *et al*., 2005). However, in many gossans, the development of a leaching zone overlying the oxidation zone results in successive cycles of alteration of the Cu-bearing neoformed minerals, including Fe oxyhydroxides, which are gradually depleted at ^{65}Cu, reaching lower $\delta^{65}Cu$ values compared with the hypogene sulfides (Mathur *et al*., 2005; Kříbek *et al*., 2016). That is not the case for the studied goethite zone, which was not affected by the leaching zone, resulting in the preservation of the heavier isotopic composition (Santos and Costa, 2022).

The depletion in $\delta^{65}Cu$ in the two samples from the malachite zone is consistent with the results obtained in several gossans worldwide, which are usually between −0.1 and +0.1‰ in oxidation zones (Maréchal *et al*., 1999; Ehrlich *et al*., 2004; Borrok *et al*., 2008; Fernandez and Borrok, 2009). Indeed, experimental studies have reported isotopic fractionation between the solution and malachite, in which malachite isotopic composition is lighter than the precursor solution and parent sulfide (Maréchal and Sheppard, 2002; Albarede, 2004; Plumhoff *et al*., 2021).

In the saprolite, the main carrier of Cu released after chalcopyrite dissolution might be goethite, typically by sorption or coprecipitation from isotopically heavier solutions compared with hypogene mineralization (Mathur *et al*., 2005). Thus, during adsorption, Fe oxyhydroxides typically accumulate the heavy isotope similar to the gossan goethite zone discussed above. However, the exposure of goethite to leaching close to the surface (Mason *et al*., 2005) leads to preferential loss of the heavy isotope, causing a reduction of $\delta^{65}Cu$ values. Thus goethites from the saprolite are isotopically lighter than those from the gossan goethite zone, showing an isotopic composition similar to the hypogene mineralization (Mathur *et al*., 2010, 2012).

The $\delta^{56}Fe$ values from Alvo 118 chalcopyrites are in the range of hydrothermal chalcopyrites from Lucky Strike, USA (−0.47‰ to 0.34‰) and Iryan Jaya, Indonesia, -2.01‰

to 1.08‰ (Rouxel *et al*., 2003; Graham *et al*., 2004). Iron isotopic fractionation is also related to electron-exchange-driven (Fe^{2+}/Fe^{3+}) redox reactions initially at the surface of the hypogene sulfides (Fernandez and Borrok, 2009). It reflects the different degrees of Fe oxidation in chalcopyrite and goethite (Fig. 12B).

Considering that goethite is the only iron-bearing mineral in the malachite zone, the increase in the $\delta^{56}Fe$ values compared with the hypogene sulfides is consistent with the Fe isotopic fractionation described in supergene environments dominated by redox, in which the oxide zone (e.g., malachite zone) shows higher $\delta^{56}Fe$ values than those of the hypogene sulfides and lower $\delta^{56}Fe$ than the those of the overlying leaching zone when present (Cheng *et al*., 2015). This is also supported by experimental studies, which indicate that Fe^{3+}-bearing phases are usually enriched in heavy isotopes compared with those carrying Fe^{2+} (Johnson *et al*., 2002; Welch *et al*., 2003; Butler *et al*., 2005). However, the goethite zone sample is depleted in heavy isotopes compared to hypogene mineralization, which was not expected. This may suggest some variation in the isotopic content of the precursor sulfide or that chalcopyrite is not the only Fe source, being chlorite a possible additional provenance.

The slightly negative fractionation of the saprolite compared with the hypogene mineralization indicates a low affinity because the sorption of Fe^{3+} onto goethite arising from the oxidation of aqueous Fe^{2+} into Fe^{3+} would typically favor heavy isotopes, causing a considerable increase in $\delta^{56}Fe$ (Bullen *et al*., 2001; Icopini *et al*., 2004; Fekiacova *et al*., 2013). This behavior reveals the low influence of the hypogene mineralization and gossan on saprolite Fe contents, which are more influenced by chloritite. Thus, chlorite influence must be responsible for isotopic values below the expected, as in the gossan goethite zone.

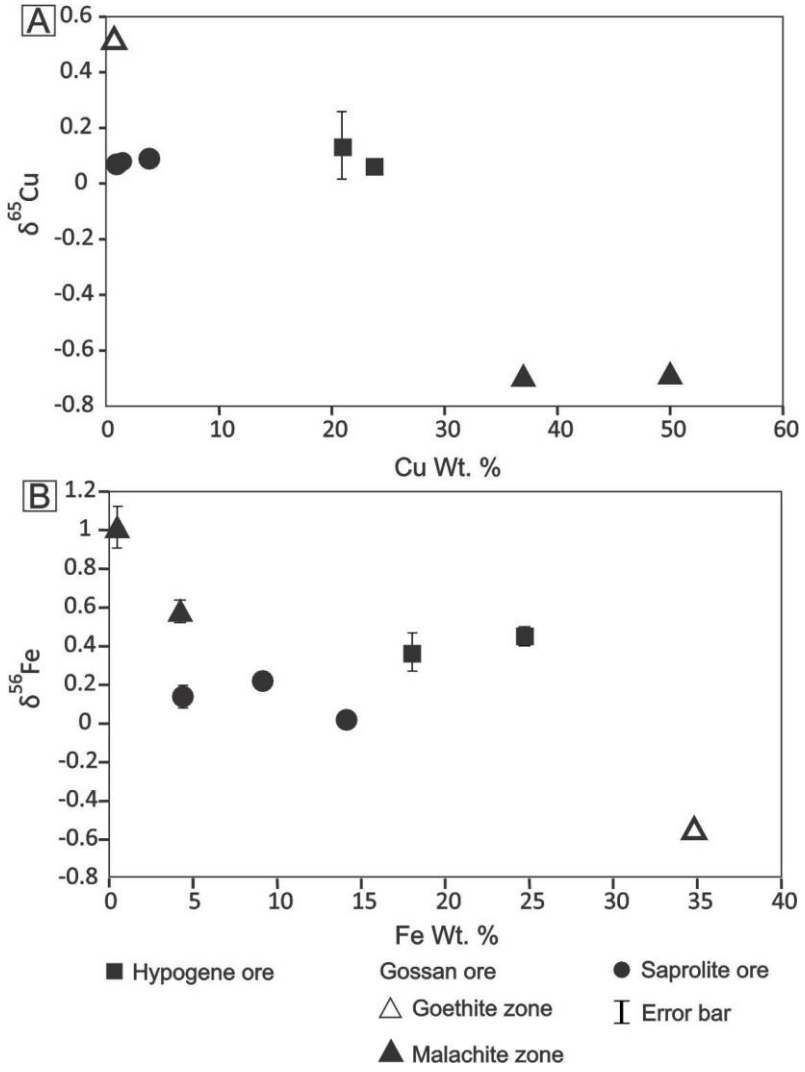

Fig. 12 Cu contents vs. δ^{65}Cu (A) and Fe contents vs. δ^{56}Fe (B) in the hypogene mineralization, gossan, and saprolite.

3.5 Geochemical evolution and exploratory implications

Statistical analyses showed that chalcopyrite is the main carrier of trace elements in the hypogene mineralization, either as a solid solution or in mineral inclusions. This is indicated by the correlation of Cu with Au, Ag, In, Y, Bi, Pb, Se, and U, which is consistent with previous studies on sulfide deposits (Demir *et al*., 2008; Helmy *et al*., 2014; Wang *et al*., 2014; Sadati *et al*., 2016; George *et al*., 2018).

The oxidation of S, with consequent chalcopyrite dissolution, represents the initial stage of the supergene evolution of the Alvo 118 deposit. This process culminates in the dissolution of petzite, altaite, uraninite, and stannite inclusions and the conversion of magnetite to hematite, while the cassiterite inclusions remain stable.

Metals released by the decomposition of the hypogene minerals were mainly incorporated into the gossan by the newly formed minerals from the goethite, malachite, cuprite, and libethenite zones (Santos and Costa, 2022). Conversely, these elements are at much lower concentrations in the gossan, as they have been predominantly lost from the system, as suggested by the multi-elemental diagrams. In this new environment, Ag, Te, Pb, Se, and Bi still show a strong correlation with Cu minerals (represented by CuO). However, U, Au, In, Y, ans Sn are more correlated with iron oxyhydroxides.

Iron oxyhydroxides have also incorporated other metals not correlated with CuO in hypogene mineralization, such as Sn, Zn, As, Be, Ga, Mo, Ni, and Sc. This process may occur via coprecipitation and/or adsorption, with ferrihydrite as the precursor (Rose *et al*., 1979; Fitzpatrick and Schwertmann, 1982; Thornber, 1985; Carlson, 1995; Liu *et al*., 2014).

The relatively good preservation of the gossan-hosting chloritites can be attributed to the slightly acidic to neutral conditions of the oxidation zone due to the low S/Cu ratio of chalcopyrite and the presence of carbonate-rich gangue minerals (e.g., Andrew, 1984; Thornber and Taylor, 1992; Taylor, 2011). This supports the restricted influence of the water table, as demonstrated by the δ^{65}Cu values, so that the chloritite minerals are mostly preserved from hydrolysis reactions. The granodiorites were more reactive with acidic solutions formed during chalcopyrite dissolution. Thus, kaolinite micromasses formed by feldspar hydrolysis are locally distributed in the libethenite zone. However, granodiorite distribution is more restricted than chloritites.

The deepening of the water table led to the development of a new evolutionary stage, with chemical remobilization dominated by hydrolysis reactions and saprolite formation. The vertical zoning of clay minerals in the saprolite suggests that chlorite in the coarse saprolite was progressively converted to vermiculite (e.g., Gilkes and Little, 1972; Aspandiar and Eggleton, 2002a). Conversely, in fine saprolite, vermiculite is converted into smectite and kaolinite (e.g., Ross *et al*., 1982).

Thus, most of the iron required for goethite formation was released during chlorite and vermiculite weathering (Aspandiar and Eggleton, 2002b). This is supported by the δ^{56} Fe values incompatible with the isotopic evolution derived only from the chalcopyrite-rich hypogene mineralization (Fig. 12A). Trace elements from the host rocks were then incorporated by goethite. That was demonstrated by the strong correlations of Fe_2O_3 with Ga, Sc, Sn, V, Mn, Co, and Cr, which was negligible in the hypogene mineralization and gossan.

In, Y, Te, Pb, Bi, and Se comprise the main Cu and Au pathfinder elements since they exhibit strongly associated in the hypogene mineralization and remain associated in the gossan and saprolite. In contrast, Al_2O_3, Hf, Zr, Th, TiO_2, Ce, La, Ba, and Sr are associated all over the deposit as a geochemical pattern of the host rocks, which are the saprolite's parent rocks.

6 Conclusions

This research described the geochemical and isotopic fractionation in the two evolutionary stages superimposed on the hypogene mineralization of the Alvo 118 deposit and host rocks, in which gossan and saprolite were formed.

In the hypogene mineralization, the most important trace elements are Ag, Te, Pb, Se, Bi, Au, In, Y, Sn, and U, mainly hosted by chalcopyrite and numerous inclusions of petzite, altaite, galena, uraninite, stannite, and cassiterite.

In the gossan, Ag, Te, Pb, Se, and Bi are associated with the newly formed Cu minerals, while Au, In, Y, Sn, and U show a more significant association with the iron oxyhydroxides, in addition to Zn, As, Be, Ga, Ga, Mo, Ni, Sc.

The $\delta^{65}Cu$ values reveal that the Alvo 118 gossan is immature and was preserved from intense leaching. Conversely, near the surface, the host rocks were converted into a typical saprolite horizon, compatible with lower $\delta^{65}Cu$ values. Additionally, the $\delta^{56}Fe$ values indicate a restricted contribution of the hypogene mineralization to the Fe content of the saprolite, more related to chloritite weathering.

In the saprolite, Ga, Sc, Sn, V, Mn, Co, and Cr are associated with the iron oxyhydroxides, and the last four are derived from the weathering of the host rocks as they do not correlate with Fe_2O_3 in the hypogene mineralization and gossan.

The association between Al_2O_3, Hf, Zr, Th, TiO_2, Ce, La, Ba, and Sr corresponds predominantly to the geochemical signature of the host rocks, with primary contribution from the chloritites. Conversely, the association formed of In, Y, Te, Pb, Bi, and Se represents the geochemical signature of the three mineralization types, representing the main Cu and Au pathfinders.

A**cknowledgments**

The authors thank Vale S.A. for access to exploration areas, logistical support during field activities, and access to drill cores and exploratory data; the geologist Clóvis Maurity for the intermediation of the partnership with Vale S.A.; and the Geosciences Institute of the

Federal University of Pará and the University of Bergen for the analytical facilities. This work was supported by the National Council for Scientific and Technological Development (CNPq) [305015/2016-8; 442871/2018-0].

References

Acker, J. G. and Bricker, O. P. (1992) The influence of pH on biotite dissolution and alteration kinetics at low temperature. *Geochimica et Cosmochimica Acta*. 56, 3073-3092. https://doi.org/10.1016/0016-7037(92)90290-Y

Albarede, F. (2004) The Stable Isotope Geochemistry of Copper and Zinc. *Reviews in Mineralogy and Geochemistry*, 55(1), 409–427. https://doi.org/10.2138/gsrmg.55.1.409

Albuquerque, M. A. C., Andrade, P. J. M. B., Maurity, C. and Kwitko, R. (2001) Geologia e Características das Mineralizações Cupríferas do Depósito Alvo 118 Província Mineral de Carajás, Pará, Brasil, in: *VII Simpósio de Geologia da Amazônia.* Belém, p 5–8.

Andreu, E., Torró, L., Proenza, J. A., Domenech, C., García-Casco, A., Villanova de Benavent, C., Chavez, C., Espaillat, J. and Lewis, J.F. (2015) Weathering profile of the Cerro de Maimón VMS deposit (Dominican Republic): textures, mineralogy, gossan evolution and mobility of gold and silver. *Ore Geology Reviews*, 65, 165–179. https://doi.org/10.1016/j.oregeorev.2014.09.015

Andrew, R. L. (1984) The geochemistry of selected base-metal gossans, southern Africa. *Journal of Geochemical Exploration*.22, 161–192. https://doi.org/10.1016/0375-6742(84)90011-6

Angélica, R. S.; Costa, M.L. and Pöllmann, H. (1996) Gold, wolframite, tourmaline-bearing lateritized gossans in the Amazon region, Brazil. *Journal of Geochemical exploration* 57, 201-215. https://doi.org/10.1016/S0375-6742(96)00037-4

Aspandiar, M. F. and Eggleton, R. A. (2002a) Weathering of chlorite: II. Reactions and products in microsystems controlled by solution avenues. *Clays and Clay Minerals*. 50, (6) 699–709. https://doi.org/10.1346/000986002762090100

Aspandiar, M. F. and Eggleton, R. A. (2002b) Weathering of chlorite: I. Reactions and products in microsystems controlled by the primary mineral. *Clays and Clay Minerals*. 50 (6): 685–698. https://doi.org/10.1346/000986002762090227

Alexandre, P., Kyser, K., Layton-Matthews, D., Joy, B. and Uvarova, Y. (2015) Chemical Compositions of Natural Uraninite. *The Canadian Mineralogist*. 53(4), 595–622. https://doi.org/10.3749/canmin.1500017

Atapour, H. and Aftabi, A. (2007) The geochemistry of gossans associated with Sarcheshmeh porphyry copper deposit, Rafsanjan, Kerman, Iran: Implications for exploration and the environment. *Journal of Geochemical Exploration*. 93(1), 47–65. https://doi.org/10.1016/j.gexplo.2006.07.007

Borrok, D. M., Wanty, R. B., Ridley, W. I., Wolf, R., Lamothe, P. J. and Adams, M. (2007) Separation of copper, iron, and zinc from complex aqueous solutions for isotopic measurement. *Chemical Geology*. 242(3), 400–414. https://doi.org/10.1016/j.chemgeo.2007.04.004

Borrok, D. M., Nimick, D. A., Wanty, R. B. and Ridley, W. I. (2008) Isotopic variations of dissolved copper and zinc in stream waters affected by historical mining. *Geochimica et Cosmochimica Acta*. 72, 329–344. https://doi.org/10.1016/j.gca.2007.11.014

Bullen, T. D., White, A. F., Childs, C. W., Vivit, D. V. and Schulz, M. S. (2001) Demonstration of significant abiotic iron isotope fractionation in nature. *Geology*. 29(8), 699. https://doi.org/10.1130/0091-7613(2001)029<0699:DOSAII>2.0.CO;2

Butler, I. B., Archer, C., Vance, D., Oldroyd, A. and Rickard, D. (2005) Fe isotope fractionation on FeS formation in ambient aqueous solution. *Earth and Planetary Science Letters*. 236, 430–442. https://doi.org/10.1016/j.epsl.2005.05.022

Carlson, L. (1995) Aluminum substitution in goethite in Lake Ore. *Bull. Geol. Soc. Finland*. 67(1), 19–28.

Cheng, Y., Mao, J., Zhu, X. and WangLiu, Y. (2015) Iron isotope fractionation during supergene weathering process and its application to constrain ore genesis in Gaosong deposit, Gejiu district, SW China. *Gondwana Research*. 27(3), 1283–1291. https://doi.org/10.1016/j.gr.2013.12.006

Cornell, R. M. and Schwertmann, U. (1996) *The Iron Oxides: Structure, properties reactions occurrence and uses.* Weinheim and New York (VCH Verlagsgeseiischaft mbH), 573 pp.

Costa, M. L., Angélica, R. S. and Fonseca, L. R. (1996) Geochemical exploration for gold in deep weathered lateritized gossans in the Amazon region-Brazil: a case history of the Igarapé Bahia deposit. *Geochimica Brasiliensis*. 13–26. http://dx.doi.org/10.21715/gb.v10i1.95

Coughlin, B. R. and Stone, A. T. (1995) Nonreversible Adsorption of Divalent Metal Ions (MnII, CoII, NiII, CuII, and PbII) onto Goethite: Effects of Acidification, FeII Addition, and Picolinic Acid Addition. *Environ Sci Technol*. 29(9), 2445-55. https://doi.org/10.1021/es00009a042

Craddock, P. R. and Dauphas, N. (2011) Iron Isotopic Compositions of Geological Reference Materials and Chondrites. *Geostandards and Geoanalytical Research*. 35(1), 101-123. https://doi.org/10.1111/j.1751-908X.2010.00085.x

Deady, E.; Moon, C.; Moore, K.; Goodenough, K.M. and Shail, R.K. (2022) Bismuth: Economic geology and value chains. *Ore Geology Reviews*. 143, 104722. https://doi.org/10.1016/j.oregeorev.2022.104722

Demir Y, Uysal I., Sadiklar M. B. and Sipahi, F. (2008) Mineralogy, mineral chemistry, and fluid inclusion investigation of Kostere hydrothermal vein-type deposit (Gumushane, NE-Turkey). *Neu Jahr Für Min*. 185(2), 215–232. https://doi.org/10.1127/0077-7757/2008/0122

Docegeo (1991) Departamento Nacional de Produção Mineral. Internal report.

Dutrizac, J. E. and Soriano, C. (2018) Behaviour of the rare earths during goethite (α-FeOOH) precipitation from sulphate-based solutions. *Hydrometallurgy*. 176, 87–96. https://doi.org/10.1016/j.hydromet.2018.01.015

Ehrlich, S., Butler, I., Halicz, L., Rickard, D., Oldroyd, A. and Matthews, A. (2004) Experimental study of the copper isotope fractionation between aqueous Cu(II) and covellite, CuS. *Chemical Geology*. 209, 259–269. https://doi.org/10.1016/j.chemgeo.2004.06.010

Evensen, N. M., Hamilton, P. J. and O'Nions, R. K. (1978) Rare-earth abundances in chondritic meteorites. *Geochimica et Cosmochimica Acta*. 42(8), 1199–1212. https://doi.org/10.1016/0016-7037(78)90114-X

Fekiacova, Z., Pichat, S., Cornu, S. and Balesdent, J. (2013) Inferences from the vertical distribution of Fe isotopic compositions on pedogenetic processes in soils. *Geoderma*. 209–210, 110–118. https://doi.org/10.1016/j.geoderma.2013.06.007

Fernandez, A. and Borrok, D. M. (2009). Fractionation of Cu, Fe, and Zn isotopes during the oxidative weathering of sulfide-rich rocks. *Chemical Geology*. 264(1–4), 1–12. https://doi.org/10.1016/j.chemgeo.2009.01.024

Fitzpatrick R. W., and Schwertmann, U. (1982) Al-substituted goethite — An indicator of pedogenic and other weathering environments in South Africa. *Geoderma*. 27(4), 335–347. https://doi.org/10.1016/0016-7061(82)90022-2

Fralick, P. W. and Kronberg, B. I. (1997). Geochemical discrimination of clastic sedimentary rock sources. *Sedimentary Geology*. 113, 111-124. https://doi.org/10.1016/S0037-0738(97)00049-3

Fu, B., Page, F. Z., Cavosie A.J., Fournelle, J., Kita, N.T., Lackey, J.S., Wilde, S.A. and Valley, J.W. (2008) Ti-in-zircon thermometry: Applications and limitations. *Contributions to Mineralogy and Petrology*. 156 (2), 197-215. https://doi.org/10.1007/s00410-008-0281-5

George L. L., Cook, N.J., Crowe, B. B. P. and Ciobanu, C. L. (2018) Trace elements in hydrothermal chalcopyrite. *Min Mag*. 82(1), 59–88. https://doi.org/10.1180/minmag.2017.081.021

Gilkes, R. J. and Little, I. P. (1972) Weathering of chlorite and some associations of trace elements in Permian phyllites in Southeast Queensland. *Geoderma.* 7 (3-4), 233-247. https://doi.org/10.1016/0016-7061(72)90008-0

Grainger, C. J., Groves, D. I., Tallarico, F. H. B. and Fletcher, I. R. (2008) Metallogenesis of the Carajás Mineral Province, Southern Amazon Craton, Brazil: Varying styles of Archean through Paleoproterozoic to Neoproterozoic base- and precious-metal mineralisation. *Ore Geology Reviews*. 33, 451–489. https://doi.org/10.1016/j.oregeorev.2006.10.010

Graham, S., Pearson, N., Jackson, S., Griffin, W. and O'Reilly, S. Y. (2004) Tracing Cu and Fe from source to porphyry: in situ determination of Cu and Fe isotope ratios in sulfides from the Grasberg Cu–Au deposit. *Chemical Geology*. 207, 147–169. https://doi.org/10.1016/j.chemgeo.2004.02.009

Harrison T. M., Aikman, A. Holden, P., Walker, A. M., McFarlane, C., Rubatto, D. and Watson, E. B. (2005) Testing the Ti-in-zircon thermometer. Eos Trans AGU. Abstr 86, V41F-1540

Helmy, H. M., Shalaby, I. M. and Abdel Rahman, H. B. (2014) Large-scale metal zoning in a late-Precambrian skarn-type mineralization, Wadi Kid, SE Sinai, Egypt. *Journal of African Earth Sciences*. 90, 77–86. https://doi.org/10.1016/j.jafrearsci.2013.11.015

Icopini, G. A., Anbar, A. D., Ruebush, S. S., Tien, M. and Brantley, S. L. (2004) Iron isotope fractionation during microbial reduction of iron: The importance of adsorption. *Geology*. 32(3), 205. https://doi.org/10.1130/G20184.1

Ildefonse, P., Manceau, A., Prost, D. and Toledo-Groke, M. C. (1986) Hydroxy-Cu-vermiculite formed by the weathering of Fe-biotites at Salobo, Carajás, Brazil. *Clays and Clay Min.* 3, 338–345.

Johnson, C. M., Skulan, J. L., Beard, B. L., Sun, H., Nealson, K. H. and Braterman, P. S. (2002) Isotopic fractionation between Fe(III) and Fe(II) in aqueous solutions. *Earth and Planetary Science Letters*, 195, 141–153. https://doi.org/10.1016/S0012-821X(01)00581-7

Kimball, B. E., Mathur, R., Dohnalkova, A. C., Wall, A. J., Runkel, R. L. and Brantley, S. L. (2009) Copper isotope fractionation in acid mine drainage. *Geochimica et Cosmochimica Acta.* 73(5), 1247–1263. https://doi.org/10.1016/j.gca.2008.11.035

Kříbek, B., Zachariáš, J., Knésl, I., Míková, J., Mihaljevič, M., Veselovský, F. and Bamba, O. (2016) Geochemistry, mineralogy, and isotope composition of Pb, Zn, and Cu in primary ores, gossan and barren ferruginous crust from the Perkoa base metal deposit, Burkina Faso. *Journal of Geochemical Exploration.* 168, 49–64. https://doi.org/10.1016/j.gexplo.2016.05.007

Liu, H., Chen, T. and Frost, R. L. (2014) An overview of the role of goethite surfaces in the environment. *Chemosphere*. 103, 1–11. https://doi.org/10.1016/j.chemosphere.2013.11.065

Loftus-Hills, G. and Solomon, M. (1967) Cobalt, nickel and selenium in sulphides as indicators or ore genesis. *Mineralium Deposita*. 2, 228–242. https://doi.org/10.1007/BF00201918

Mano, E. S., Caner, L., Petit, S. and Chaves, A.P. (2020) Mineralogical characterization of copper lateritic ore from the Furnas deposit - Carajás, Brazil. REM - *International Engineering Journal*. 73, 329–335. https://doi.org/10.1590/0370-44672019730113

Maréchal, C. N., Télouk, P. and Albarède, F. (1999) Precise analysis of copper and zinc isotopic compositions by plasma-source mass spectrometry. *Chemical Geology*. 156(1–4), 251–273. https://doi.org/10.1016/S0009-2541(98)00191-0

Maréchal, C. N. and Sheppard, S. M. F. (2002) Isotopic fractionation of Cu and Zn between chloride and nitrate solutions and malachite or smithsonite at 30 degrees and 50 degrees C. Goldschmidt Conference. *Geochim Cosmochim Acta* 66:A484

Martínez, M., Escobar, M., Morante, F., Márquez, G., Lorenzoa, E. and Álvarez, A. (2016) Ti/Zr ratio as a geochemical tool for the correlation of weathered coals from geological formations in two Latin American sedimentary basins, Energy Sources, Part A: Recovery,

Utilization, and Environmental Effects. 38:23, 3542-3548. http://dx.doi.org/10.1080/15567036.2016.1179361

Mason, T. F. D., Weiss, D. J., Chapman, J. B., Wilkinson, J. J., Tessalina, S. G., Spiro, B., Horstwood, M. S. A., Spratt, J. and Coles, B. J. (2005) Zn and Cu isotopic variability in the Alexandrinka volcanic-hosted massive sulphide (VHMS) ore deposit, Urals, Russia. *Chemical Geology*. 221(3–4), 170–187. https://doi.org/10.1016/j.chemgeo.2005.04.011

Mathur, R., Ruiz, J., Titley, S., Liermann, L., Buss, H. and Brantley, S. (2005) Cu isotopic fractionation in the supergene environment with and without bacteria. *Geochimica et Cosmochimica Acta*. 69(22), 5233–5246. https://doi.org/10.1016/j.gca.2005.06.022

Mathur, R., Dendas, M., Titley, S. and Phillips, A. (2010) Patterns in the Copper Isotope Composition of Minerals in Porphyry Copper Deposits in Southwestern United States. *Economic Geology*. 105(8), 1457–1467. https://doi.org/10.2113/econgeo.105.8.1457

Mathur, R., Jin, L., Prush, V., Paul, J., Ebersole, C., Fornadel, A., Williams, J. Z. and Brantley, S. (2012). Cu isotopes and concentrations during weathering of black shale of the Marcellus Formation, Huntingdon County, Pennsylvania (USA). *Chemical Geology*. 304–305, 175–184. https://doi.org/10.1016/j.chemgeo.2012.02.015

Moeller, K., Schoenberg, R., Pedersen, R. B., Weiss, D. and Dong, S. (2012) Calibration of the new certified reference materials ERM-AE633 and ERM-AE647 for copper and IRMM-3702 for zinc isotope amount ratio determinations. *Geostandards and Geoanalytical* Research. 36(2), 177-199. https://doi.org/10.1111/j.1751-908X.2011.00153.x

Moeller, K., Schoenberg, R., Grenne, T., Thorseth, I. H., Drost, K. and Pedersen, R. B. (2014) Comparison of iron isotope variations in modern and Ordovician siliceous Fe oxyhydroxide deposits. *Geochimica et Cosmochimica Acta*. 126, 422–440. https://doi.org/10.1016/j.gca.2013.11.018

Monteiro, H. S., Vasconcelos, P. M. P., Farley, K. A. and Lopes, C. A. M. (2018) Age and evolution of diachronous erosion surfaces in the Amazon: Combining (U-Th)/He and cosmogenic 3He records. *Geochimica et Cosmochimica Acta*. 229, 162–183. https://doi.org/10.1016/j.gca.2018.02.045

Mondillo, N., Balassone, G.; Boni, M.; Chelle-Michou, C., Cretella, S., Mormone, A., Putzolu, F., Santoro, L.; Scognamiglio, G. and Tarallo, M. (2019) Rare Earth Elements (REE) in Al- and Fe-(Oxy)-Hydroxides in Bauxites of provence and Languedoc (Southern France): Implications

for the Potential Recovery of REE as By-products of Bauxite Mining. *Minerals*. 9, 504. https://doi.org/10.3390/min9090504

Nickel, E. H. (1979) Gossan mineralogy viewed in the context of solution chemistry. In: Glover, J.E., Smith, R.E. (Eds.), Pathfinder and Multielement Geochemistry in Mineral Exploration: Geol. Dept. and Ext. Serv. University of Western Australia.

Ozdemir, A. and Sahinoglu, A. (2018) Important of Gossans in Mineral Exploration: A Case Study in Northern Turkey. Int J Earth Sci Geophys. 4:019. https://doi.org/10.35840/2631-5033/1819

Pires, G.L.C., Renac, C., Bongiolo, E.M. and Neumann R. (2020) Gossan mineralogy, textures, and gold enrichment over the Au (As, Bi, Ag) deposit in the Buracão Area (Brasília Fold Belt, Brazil): Implications for gold prospecting in weathering profiles. *J of Geoch Expl*. 218, 106615. https://doi.org/10.1016/j.gexplo.2020.106615

Plumhoff, A. M., Mathur, R., Milovský, R. and Majzlan, J. (2021). Fractionation of the copper, oxygen and hydrogen isotopes between malachite and aqueous phase. *Geochimica et Cosmochimica Acta* . 300, 246–257. https://doi.org/10.1016/j.gca.2021.02.009

Plyusnin, A. M., Pogrelnyak, Yu. F., Mironov, A. and Zhmodik, S.M. (1981) The behavior of gold in the oxidation of gold-bearing sulfides. *Geochem.* Int. 18, 116–123.

Porto, C. G. (2016) Geochemical exploration challenges in the regolith dominated Igarapé Bahia gold deposit, Carajás, Brazil. *Ore Geology Reviews*. 73, 432–450. https://doi.org/10.1016/j.oregeorev.2015.10.027

Putter, T., Mees, F., Decrée, S. and Dewaele. S. (2010) Malachite, an indicator of major Pliocene Cu remobilization in karstic environment (Katanga, Democratic Republic of Congo). *Ore Geol Rev.* 38, 90–100. https://doi.org/10.1016/j.oregeorev.2010.07.001

Rigon, J. C., Munaro, P., Santos, L. A., Nascimento, J. A. S. and Barreira, C. F. (2000) Alvo 118 copper–gold deposit—geology and mineralization, Serra dos Carajás, Pará, Brazil, in: *31 International Geological Congress.*

Ross, G. J., Wang, A. I., Ozkan, A. I. and Rees, H. W. (1982) Weathering of chlorite and mica in a New Brunswick podzol developed on till derived from chlorite-mica schist. *Geoderma*. 27, 255-267. https://doi.org/10.1016/0016-7061(82)90034-9

Rose, W. R., Hawkes, H. E. and Webb, J. S. (1979) *Geochemistry in Mineral Exploration*. Academic Press. 657 pp.

Rouxel, O., Dobbek, N., Ludden, J. and Fouquet, Y. (2003) Iron isotope fractionation during oceanic crust alteration. *Chemical Geology*. 202(1–2), 155–182. https://doi.org/10.1016/j.chemgeo.2003.08.011

Rudnick, R. L. and Gao, S. (2003) The Composition of the Continental Crust. In: Holland, H.D. and Turekian, K.K., Eds., Treatise on Geochemistry. The Crust, Elsevier-Pergamon, Oxford. 3, 1-64. http://dx.doi.org/10.1016/b0-08-043751-6/03016-4

Sadati, S. N., Yazdi, M., Mao, J., Behzadi, M., Adabi, M.H., Lingang, X., Zhenyu, C. and Mokhtari. M. A. A. (2016) Sulfide mineral chemistry investigation of sediment-hosted stratiform copper deposits, Nahand-Ivand area, NW Iran. *Ore Geology Reviews*. 72, 760–776. https://doi.org/10.1016/j.oregeorev.2015.09.018

Santiago, E. S. B., Xavier, R. P., Hagemann, S. G., Monteiro, L. V. S. and Cliff, J. (2021) Multiple sulfur isotopes constraints on origin and evolution of the Neoarchean and Paleoproterozoic Cu-Au systems from the Carajás Domain, Amazonian Craton, Brazil. *Ore Geology Reviews.* 29, 103872. https://doi.org/10.1016/j.oregeorev.2020.103872

Santos, P. H. S., Costa, M. L. (2022) Mineralogical and textural evolution of the Alvo 118 copper-bearing gossan: Implications for supergene metallogenesis in Carajás Mineral Province, Brazil. *Journal of South American Earth Sciences.* 104108. https://doi.org/10.1016/j.jsames.2022.104108

Schutesky, M. E. and Oliveira, C. G. (2020) From the roots to the roof: An integrated model for the Neoarchean Carajás IOCG System, Brazil. *Ore Geology Reviews*. 129, 103833. https://doi.org/10.1016/j.oregeorev.2020.103833

Scott, K. M., Ashley, P. M. and Lawie, D. C. (2001) The geochemistry, mineralogy and maturity of gossans derived from volcanogenic Zn–Pb–Cu deposits of the eastern Lachlan Fold Belt, NSW, Australia. *Journal of Geochemical Exploration*. *72*(3), 169–191. https://doi.org/10.1016/S0375-6742(01)00159-5

Silva, E. R. P. and Kotschoubey, B. (2000) Alteração supergênica do depósito de cobre-ouro do Salobo, Serra dos Carajás-PA - ênfase no comportamento do cobre. Rev. Bras. Geoc. 30, 623–630.

Suaréz, A., Prichard, H. M., Fisher, P. C. and McDonald, I. (2012) Platinum Group-Minerals in the Gossan from the Key West Cu-Ni-Pt Sulphide Occurrence (Nevada, USA). Revista de la sociedad española de mineralogía. 16, 242-243.

Smith, K. S. (1999). *Metal sorption on mineral surfaces: an overview with examples relating to mineral deposits.* In: Plumlee GS, Logsdon MS (eds) The environmental geochemistry of mineral deposits. Part A. Processes techniques and health issues, vol 6A. Reviews in economic geology, society of economic geologists, p 161–182. https://doi.org/10.5382/Rev.06.07.

Swedlund, P. j., Webster, J. G. and Miskelly, G. M. (2009) Goethite adsorption of Cu(II), Pb(II), Cd(II), and Zn(II) in the presence of sulfate: Properties of the ternary complex. *Geochimica et Cosmochimica Acta*. 73, 1548-1562. https://doi.org/10.1016/j.gca.2008.12.007

Taylor, R. (2011) *Gossans and leached cappings field assessment*. Springer, Townsville.

Toledo-Groke, M. C. M., Prost, D., Ildefonse, P., Melfi, A.J., Delvigne, J. and Parisot, J. C. (1985) Alteração dos minerais na zona supérgena da formação cuprífera do Salobo 3A (Serra dos Carajás) – Localização do cobre nos produtos secundários. *Rev. Bras. Geoc*. 15, 293–299.

Thornber, M. R. (1985) Supergene alteration of sulfides, distribution of elements during gossan forming process. *Chem. Geol*. 53, 279–301. https://doi.org/10.1016/0009-2541(85)90075-0

Thornber, M. R. and Taylor, G. F. (1992) *The mechanisms of sulphide oxidation and gossan formation*. 119-138. https://doi.org/10.1016/B978-0-444-89095-5.50015-8

Tornos, F., Velasco, F., Slack, J. F., Delgado, A., Gomez-Miguelez, M. G.; Escobar, J. M. and Gomez, C. (2016) The high-grade Las Cruces copper deposit, Spain: a product of secondary enrichment in an evolving basin. *Mineralium Deposita*. 52(1), 1-34. https://doi.org/10.1007/s00126-016-0650-3

Torresi, I., Xavier, R. P., Bortholoto, D. F. A. and Monteiro, L.V. S. (2012) Hydrothermal alteration, fluid inclusions and stable isotope systematics of the Alvo 118 iron oxide–copper–gold deposit, Carajás Mineral Province (Brazil): Implications for ore genesis. *Mineralium Deposita.* 47(3), 299–323. https://doi.org/10.1007/s00126-011-0373-4

Vasquez L. V., Rosa-Costa L. R., Silva C. G., Ricci, P. F., Barbosa, J. O., Klein, E. L., Lopes, E. S., Macambira, E. B., Chaves, C. L., Carvalho, J. M., Oliveira J. G., Anjos G. C. and Silva H.R. (2008) Geologia e Recursos Minerais do Estado do Pará: Sistema de Informações Geográficas – SIG: Texto Explicativo dos Mapas Geológico e Tectônico e de Recursos Minerais do Estado do Pará. Organizadores: M.L Vasquez, L.T. Rosa-Costa. Escala 1:1.000.000. Belém: CPRM.

Veiga, M. M., Schorscher, H. D., Fyfe, W. S. (1991) Relationship of copper with hydrous ferric oxides: Salobo, Carajás, PA, Brazil. *Ore Geology Reviews*. 6, 245–255. https://doi.org/10.1016/0169-1368(91)90025-3

Wang, G., Wang, Z., Shi, R., Zhang, Y. and Wang, K. (2014) Mineralogy and isotope geochemical characteristics for Xiaozhen copper deposit, Langao County, Shaanxi Province and their constraint on genesis of the deposit. *Geo J.* 19(2), 281–294. https://doi.org/10.1007/s12303-014-0044-4

Welch, S. A., Beard, B. L., Johnson, C. M. and Braterman, P. S. (2003) Kinetic and equilibrium Fe isotope fractionation between aqueous Fe(II) and Fe(III). *Geochimica et Cosmochimica Acta*. 67(22), 4231–4250. https://doi.org/10.1016/S0016-7037(03)00266-7

Williams, W. C., Meissl, E., Madrid, J., and de Machuca, B. C. (1999) The San Jorge porphyry copper deposit, Mendoza, Argentina: A combination of orthomagmatic and hydrothermal mineralization. *Ore Geology Reviews*. 14, 185–201. https://doi.org/10.1016/S0169-1368(99)00006-2

Xavier, R. P., Wiedenbeck, M., Trumbell, R. B., Dreher, A. M., Monteiro, L. V. S., Rhede, D., Araújo, C. E. G. and Torresi, I. (2008) Tourmaline B-isotopes fingerprint marine evaporites as the source of high-salinity ore fluids in iron-oxide-copper-gold deposits, Carajás Mineral Province (Brazil). *Geology*, 36, 743–746. https://doi.org/10.1130/G24841A.1

Yesares, L., Sáez, R., Ruiz, A. G., Nieto, J. M., Gómez, C. and Ovejero. G. (2017) Mineralogical evolution of the Las Cruces gossan cap (Iberian Pyrite Belt): From subaerial to underground conditions. *Ore Geology Reviews*. 80. 377–405. https://doi.org/10.1016/j.oregeorev.2016.05.018

Zhu, X. K., O'Nions, R. K., Guo, Y., Belshaw, N. S. and Rickard, D. (2000) Determination of natural Cu-isotope variation by plasma-source mass spectrometry: implications for use as geochemical tracers. *Chemical Geology*. 163, 139–149. https://doi.org/10.1016/S0009-2541(99)00076-5

6. THE GEOCHEMICAL IMPORTANCE OF IRON OXYHYDROXIDES AND ASSOCIATED MINERALS FOR COPPER ENRICHMENT IN SAPROLITE FROM A DENUDED AREA IN THE CARAJÁS MINERAL PROVINCE

Pabllo Henrique Costa dos Santos[1*], Marcondes Lima da Costa[1], Nilson dos Santos Ferreira[2], Mariella Alzamora Camarena[3], Rayara do Socorro Souza da Silva[4]

[1]Universidade Federal do Pará, Instituto de Geociências, Belém (Pará), Brazil

[2]Universidade Federal de Sergipe, Departamento de Física, Aracaju (Sergipe), Brazil

[3]Iniversidade Federal do Rio de Janeiro, Campus Xerém, Duque de Caxias (Rio de Janeiro), Brazil

[4]Instituto Tecnológico Vale Desenvolvimento Sustentável, Belém (Pará), Brazil

Abstract

The Carajás Mineral Province hosts one of the most extensive sulfide-bearing copper belts worldwide. The deposits are generally covered by thick regoliths, which may include gossans, laterites, colluviums, and soil. These covers represent exploration guides and, in some cases, can be mined along with the parent hypogene ore. Thus, precise determination of copper-bearing minerals is crucial for selecting the most appropriate metallurgical techniques. This research investigated the saprolite horizon overlying the Alvo 118 deposit. The parent rocks are chloritites hosting copper-bearing hypogene sulfides, partially converted to an immature gossan. The saprolite development was mainly controlled by chlorite weathering, still present as a relic but almost completely converted into kaolinite, with smectite and vermiculite as intermediates, forming a typical lower saprolite association. During this process, iron release from chlorite led to ferrihydrite, goethite, and hematite formation. Magnetite octahedrons, as relics of the hypogene ore, are surrounded by clay minerals. However, no minerals containing copper as a major component were initially identified. Thereafter, its presence in kaolinite was investigated through FTIR, which suggested no copper content. However, Mössbauer spectroscopy data allowed the quantification of the main iron-bearing minerals, in which goethite and ferrihydrite presented a strong correlation with CuO contents, with Pearson coefficients of 0.71 and 0.80, respectively. This data suggest that these are the main copper carriers of the deposit, in accordance with selective extraction results obtained in similar deposits. Acid leaching has been proposed as the most appropriate technique for extracting copper from this class of mineralization.

Keywords: Weathering, chlorite, goethite, ferrihydrite, Mössbauer

1 Introduction

In mineral provinces exposed to tropical or paleotropical conditions, ore minerals dissolution releases ions or ionic compounds, which can be incorporated into secondary minerals derived from the host rocks (Costa et al. 1996; Costa et al. 1999; Porto 2016). This process produces geochemical dispersion halos of significant economic relevance (Toledo-Groke et al. 1987; Veiga et al. 1991). Acknowledgment of their generation mechanisms is crucial for mineral exploration, especially in regions with dense vegetation and scarcity of outcrops.

The Carajás Mineral Province (PMC) hosts numerous IOCG copper deposits hosted by metavolcanic-sedimentary sequences discovered during exploration programs developed over the last five decades (Porto 2016; Grainger et al. 2008). The mineralizations, generally formed of Cu sulfides, were converted into gossans and later subjected to lateritization events, which commenced at 70 Ma (Costa et al. 1996; Vasconcelos et al. 1994). Deeper hypogene orebodies and respective gossans were not lateritized. On the other hand, the host rocks were converted into saprolite horizons near the surface, exhumed over the last 10 Ma, with the development of the Velhas/Itacaiúnas geomorphic surface (King et al. 1956; Monteiro et al. 2018). These saprolites, spread in the denuded areas around the Carajás Mountains, can reach 100 m thick, with a small reduction in copper contents compared to the underlying hypogene mineralizations (Toledo-Groke et al. 1987; Veiga et al. 1991).

The Alvo 118 deposit is located in a denuded area to the south of the Carajás Mountains and was brought to light after the exploration programs carried out by Docegeo in the 1990s and resumed by Vale in 2018. The deposit comprises massive and disseminated copper-sulfide orebodies subjected to two supergene alteration events. In the first stage, dominated by oxidoreduction, the primary mineralization was partially converted into an immature gossan profile at Depth (Santos and Costa 2022). In the second stage, the host rocks were weathered near the surface, developing a thick saprolite cover preserving high Cu contents (Albuquerque et al. 2001). Primary sulfide reserves are proximately 170 Mt at 1% Cu and 3 ppm Au, while supergene mineralization totals 55 Mt at 0.92% Cu and 0.3 ppm Au, of which 30% corresponds to gossan and 70% to saprolite (Docegeo 1991).

The high copper contents in the saprolite over the hypogene mineralization contrasts with the apparent absence of copper-bearing minerals. This fact raises questions about which phases could be involved in copper retention, which is an issue for metallurgical decisions. In that regard, some research studies have pointed to the role of phyllosilicates and iron and

manganese oxyhydroxides as copper-bearing phases in CMP saprolites (Toledo-Groke et al. 1987; Veiga et al. 1991; Mano et al. 2015; 2020).

Copper incorporation by oxyhydroxides can occur through isomorphic substitution or adsorption, while clay minerals can incorporate metals through ionic substitution into layers or adsorption into interlayer space (Ildefonse et al. 1986; Oliveira et al. 1995, Oliveira et al. 1996; Dube et al. 2001). Another metallurgical issue is the accurate determination of gangue minerals, which are potential chemical reagent consumers, depending on the dissolution kinetics and solubility of each phase (Chetty 2018; Thomas 2021).

This paper investigates the mineralogy and geochemistry of the weathering profile developed on the Alvo 118. In doing so, the dynamics of copper and other metals along the saprolite horizons, that is, their location in the various secondary phases, are established, resulting in implications for mineral exploration and metallurgy.

2 Geological and geomorphological setting

The most outstanding geomorphic unit in CMP are the Carajás Mountains, formed of a set of plateaus with elevations ranging from 500 to 750 m, occasionally reaching 900 m (Silva and Kotschoubey 2000; Porto 2016). The current drainage system has extensively eroded these mountains, resulting in flat to undulating lowlands with elevations of 250 to 350 m. The plateaus are generally capped by ferruginous duricrusts and latosols (Ker 1997; Eggleton 2001). However, the surrounding lowlands are normally covered by saprolites, exhumed by erosion of complete lateritic profiles (Maurity and Kotschoubey 1995; Silva and Kotschoubey 2000).

The Alvo 118 area comprises mafic to intermediate metavolcanic sequences, with mylonitic foliation and intense chloritic alteration typical of the Grão Pará Group (Itacaiúnas Supergroup) (Fig. 1A). They are crosscut by granodioritic, tonalitic, and gabbroic bodies, in addition to rhyolitic-dacitic and diabasic dikes (Tallarico et al. 2005; Torresi et al. 2012). These lithotypes are the host rocks of the hypogene mineralization and have been subjected to multiple events of hydrothermal alteration, including sodic, represented by albite and scapolite; potassic, indicated by biotite with alkali feldspar; chloritic; and quartz-sericite alteration (Torresi et al. 2012).

The hypogene mineralization forms sub-vertical tabular orebodies lined in the NW-SE direction. They comprise (1) massive sulfide veins with chalcopyrite, bornite, magnetite, hematite, and traces of Au-Ag tellurides, galena, and cassiterite; and (2) stockwork veins

formed of quartz and calcite, with disseminated chalcopyrite (Grainger et al. 2008; Torresi et al. 2012). Hypogene mineralization evolves upwards to form an immature gossan overlay by fresh chloritites. Thus, above the gossan, the host rocks are preserved from weathering but are converted into a saprolite horizon near the surface.

The Alvo 118 deposit is located in a lowland terrain 5 km NW of the Sossego copper mine. Both deposits are close to a relic plateau of the Carajás Mountains (Fig.1B, C). The weathering cover in this area presents an average thickness of 60 m and can locally reach 100 m. The soil displays colluvial features, with nodules and pebbles surrounded by a reddish clayey matrix formed of kaolinite and iron oxyhydroxides. Quartz and magnetite are the most frequent residual minerals (Toledo-Groke et al. 1987).

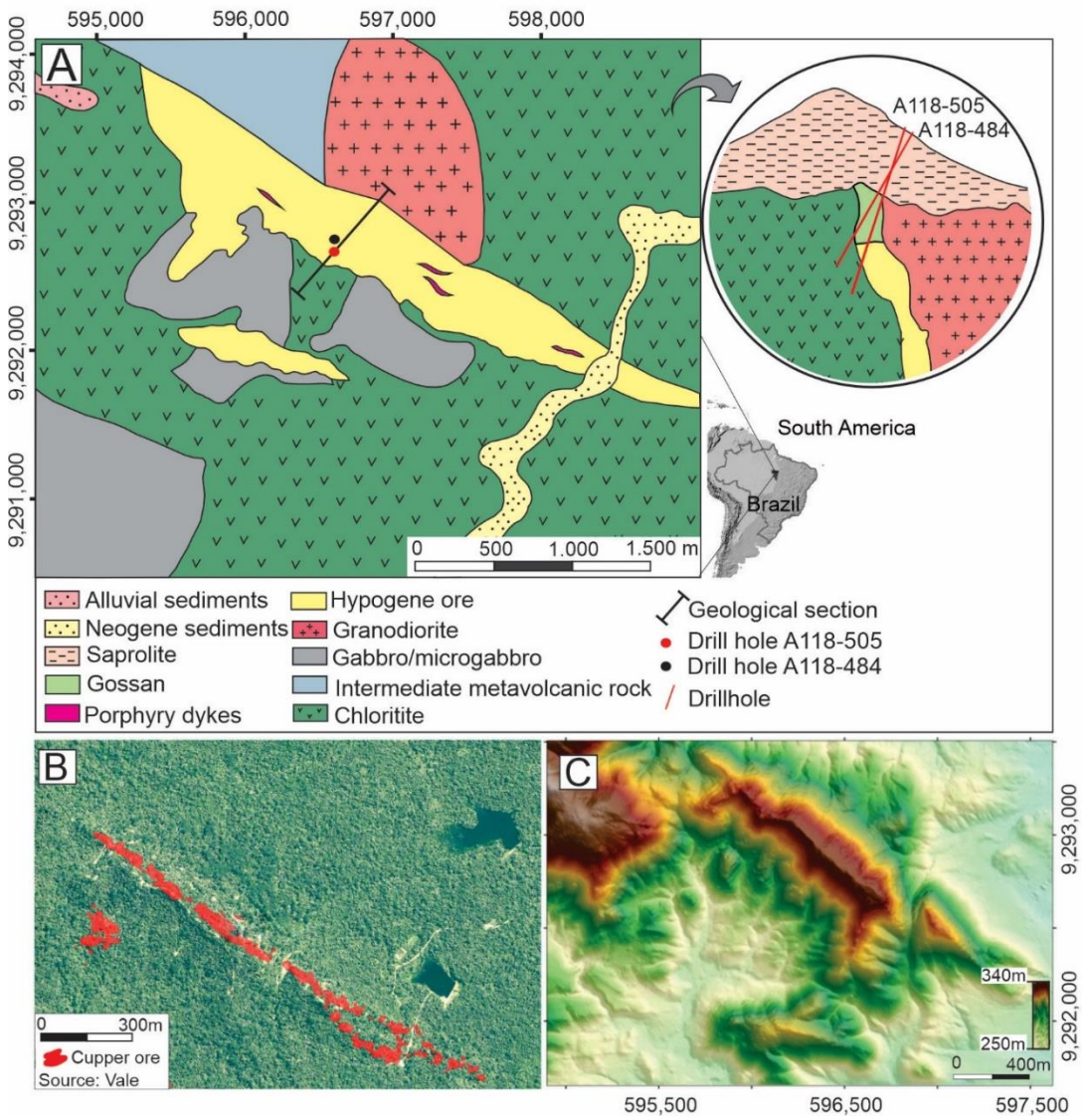

Fig. 1 A) Simplified geological map of the Alvo 118 deposit area, highlighting the spatial distribution of the hypogene mineralization, data compiled and modified (Vasques et al. 2008; Torresi et al. 2012; and Santos and Costa 2022). B) Satellite image of the deposit area, obtained from Google Earth Pro (2018), showing the dense vegetation that covers the deposit area (source: Vale). C) Digital elevation model displaying the relief of the study area (USGS 2018).

3 Analytical Methods

Petrographic descriptions were performed in outcrops at the Alvo 118 pilot mine and four drill holes. Subsequently, 152 samples were collected, including host rock, primary mineralization, gossan, and saprolite. The color classification was based on Munsell (1992). Mineralogical and microtextural investigations were conducted through polished sections analyzed in a LEICA DM 2700 P optical microscope with a LEICA MC 170 HD camera. The optical microscopy data were complemented with scanning electron microscopy observations (secondary electrons). Images were acquired with Zeiss SIGMAVP equipment. The operating conditions were: electron beam current of 80 μA, constant acceleration voltage at 10 kV, and

the working distance at 8.5 mm. Chemical analyses were carried out by an energy dispersive system (EDS) in the IXRF Sedona-SD equipment. The operating conditions were electron beam current at 80 μA, constant acceleration voltage at 20 kV, working distance at 8.5 mm, and counting time for element analysis at 30 s. The images and spectra were obtained in the Microanalysis Laboratory of the Federal University of Pará.

The X-ray diffraction (XRD) and Fourier-transform infrared spectroscopy (FTIR) analyses were performed after clay separation by sieving and centrifugation. Twenty 150 g aliquots were previously deflocculated in an ultrasonic cleaner and wet sieved at 63 μm. The passing fraction was centrifuged for 2 min at 1000 rpm. The suspension was collected in water, separated by decanting, and then centrifuged at 1800 rpm for 10 min. The suspension was again collected in water, decanted, and dried at 40°C for 48 h.

The XRD analyses were performed in the angular range of 4° to 75° 2θ on natural samples (oriented by decantation); subsequently, ethylene glycol solvated for 48 h and then heated at 550°C for 2 h. A Bruker D2 PHASER diffractometer was used, with Cu anode, Lynxeye detector (1D mode); 0.02° 2θ increment; 0.2 s step time; and 0.1 mm slit; operating at 300 W (30 kV and 10 mA). FTIR spectra were acquired on Bruker Vertex 70 equipment, with a deuterated L-alanine detector doped with triglycine sulfate, operating at room temperature (RT- DLaTGS). The analyses were controlled on Opus 7 software, in the region of 400 to 4000 cm^{-1}, in transmission mode, with a spectral resolution of 4 cm^{-1} and a mirror movement speed of 10 kHz. The XRD and FTIR readings were performed in the facilities of the Laboratory of Mineralogy, Geochemistry, and Applications (Federal University of Pará).

For the identification and quantification of the iron oxyhydroxides, ^{57}Fe Mössbauer spectroscopy analyses were carried out on raw samples at room temperature (298 K). The measurements were carried out in a conventional spectrometer, with transmission geometry and constant source acceleration (^{57}Co). The spectra were collected in the velocity range of approximately ± 10 mm/s. The velocity was calibrated with α-Fe standard at room temperature. The obtained spectra were refined using WinNormos-for-Igor software. The analytical procedures were carried out at the Brazilian Center for Physics Research.

Twelve samples of the hypogene mineralization, gossan, and saprolite were selected for pH and Eh measurements. Aliquots of 1 g were powdered and added to 10 ml of distilled water in falcon tubes, according to the procedures proposed by Teixeira et al. (2017). Five measurements were performed on each sample using an Orion Star A211 pH meter (Thermo Scientific).

A group of 40 samples with 10 kg each were analyzed for the determination of whole-rock chemical composition in the ALS facilities. The analyzed elements were Ag, Al, As, Ba, Be, Bi, Cd, Ce, Co, Cr, Cs, Fe, Ga, Ge, Hf, In, K, La, Li, Mg, Mn, Mo, Na, Nb, Ni, P, Pb, Rb, Re, S, Sb, Sc, Se, Sn, Sr, Ta, Te, Th, Ti, Tl, U, V, W, Y, Zn, and Zr. Aliquots of 0.25 g were digested with perchloric, nitric, hydrofluoric, and hydrochloric acids. The residue was digested with dilute hydrochloric acid and then analyzed in an inductively coupled plasma atomic emission spectrometer. Gold was determined by fire assay with ICP-AES finish, and Cu was analyzed by Niton X-ray fluorescence.

Additionally, the Fe_2O_3 and CuO contents of six selected samples were analyzed to support Mössbauer spectroscopy investigations. For Fe_2O_3 determination, 0.1 g aliquots were added to lithium borate and fused at 1025°C. The resulting melt was then cooled and dissolved in a mixture of nitric, hydrochloric, and hydrofluoric acids. For Cu, 0.4 g aliquots were digested in aqua regia. Both elements were analyzed in an inductively coupled plasma mass spectrometer.

4 Results

4.1 Bedrocks

The base of the investigated boreholes comprises foliated chloritites (35 to 43 m and 70 to 150 m deep), consisting of ~80% chlorite, ~15% plagioclase, and ~5% quartz, with accessory hematite. These rocks are crosscut by stockwork veins, formed of quartz and chalcopyrite, with accessory calcite, apatite, and fluorite (Fig. 2A). They are also intersected by massive sulfide veins, consisting of chalcopyrite matrix, with traces of nukundamite, involving chlorite plates (Fig. 2B, C), in addition to quartz, calcite, fluorite, and apatite. The 43 to 70 m interval is dominated by granodiorites, with ~40% quartz, ~35% oligoclase, and ~15% orthoclase, in addition to accessory biotite and hornblende (Fig. 2D). The granodiorites exhibit portions of intense chloritization, distributed along a network of chlorite veinlets, and display chalcopyrite disseminations (Fig. 2E).

The presence of sulfide mineralization resulted in the development of an immature gossan, similarly interspersed with the chloritites and granodiorites (Fig. 3A). Thus, the chloritites host goethite and malachite zone and the granodiorites host a cuprite and libethenite zones. The goethite zone consists of goethite micromass coating dissolution cavities (cavity-filling facies), filling the chloritite fracture system (fracture-filling facies), or forming a matrix involving quartz grains (breccia facies). In this zone, goethite is associated with chalcocite,

native copper, malachite, and pseudomalachite. The malachite zone comprises a malachite micromass with chrysocolla and ramsbeckite, surrounding cuprite, and tenorite nodules. The cuprite zone consists of cuprite micromass, with goethite and chalcocite relics involving millimetric quartz grains. The libethenite zone comprises a micromass formed of this mineral, together with malachite and pseudomalachite, distributed along granodiorite fractures (Fig. 3A).

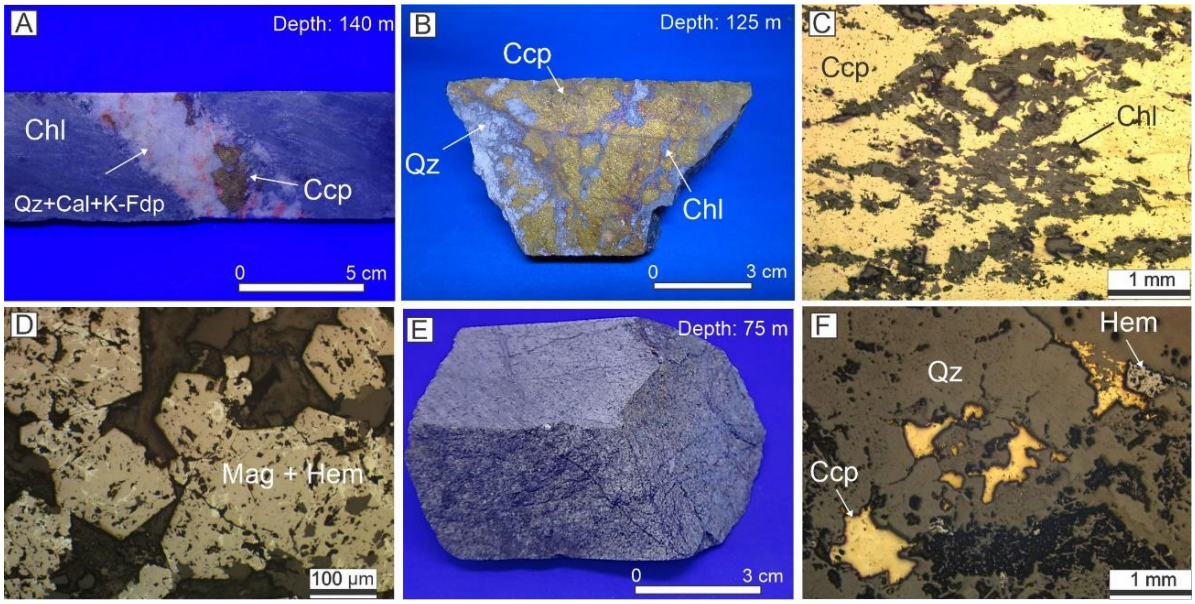

Fig. 2 Chloritite crosscut by quartz veins with minor chalcopyrite (disseminated mineralization) (A). Massive mineralization, formed of a chalcopyrite matrix with chloritite clasts (B). Chlorite surrounded by chalcopyrite, OM/RL (C). Magnetite partially hydrothermally altered to hematite, OM/RL (D). Granodiorite crosscut by chlorite veinlets (E). Chalcopyrite disseminations in granodiorite, OM/RL (F). Abbreviations: Chl (chlorite); Mag (magnetite); Hem (hematite); Qz (quartz); Ccp (chalcopyrite); Cal (calcite); K-Fdp (alkali feldspar); optical microscopy (OM); reflected light (RL).

4.2 Structure of the weathering profile

The host rocks of the hypogene mineralization and gossan evolve towards the surface to form a weathering cover, which extends for ~35 m, overlying fresh chloritites and, further down, the gossan (libethenite zone) (Fig. 3A). The weathering profile comprises a saprolite horizon. At the bottom, it includes a coarse saprolite, extending from 15 to 35 m and 29 to 35 m in the investigated boreholes. This zone preserves the typical foliation inherited from the chloritites. Thus, chlorite is still predominant but associated with a secondary plasma, including kaolinite and goethite, which provide a friable aspect and a yellow color (10YR 6/6) (Figs. 3B).

The top of the profile comprises a fine saprolite extending from 15 or 29 m deep to the surface in the investigated boreholes. It is formed of a friable clayey-sandy matrix consisting mainly of kaolinite with minor smectite and vermiculite, in addition to quartz grains. These

minerals are coated with iron oxyhydroxide films, which, depending on their distribution, can form red (10R 5/8), light red (10R 7/8), and yellow (2.5Y7/8) zones, with occasional white (10R 8/1) patches formed of kaolinite (Fig. 3C-E). The light red portion of the fine saprolite outcrops on the hillsides as a sandy-clayey matrix containing kaolinite veinlets (Fig. 3F, G).

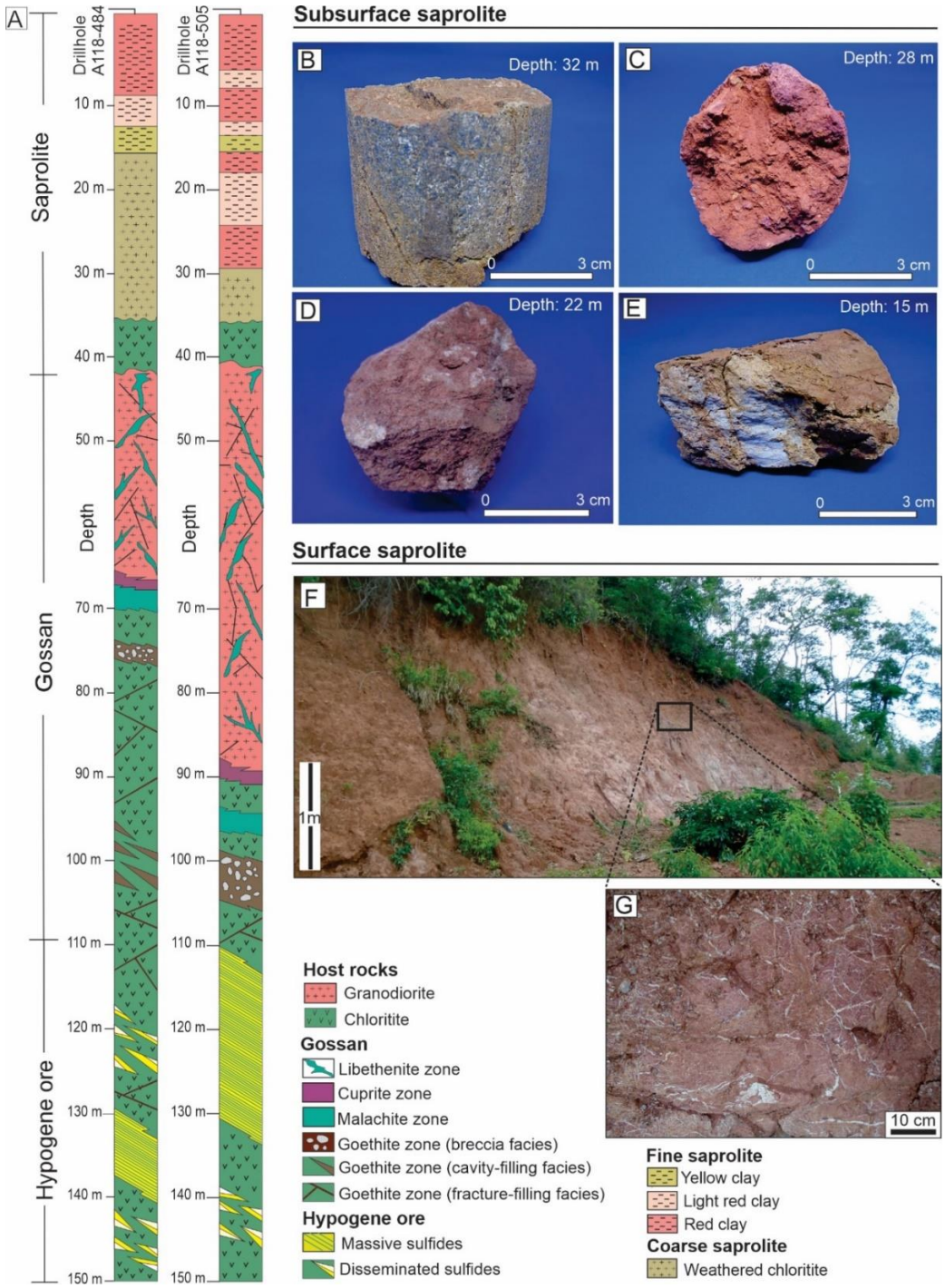

Fig. 3 Vertical distribution of the parent rocks and saprolite from the Alvo 118 deposit, modified from Santos and Costa (2022) (A). Weathered chlorite typical of the coarse saprolite (B). Typical samples of the fine saprolite, formed of clay- sandy mass with iron oxyhydroxide, in red (C), light red (D), and yellow (E) colors. Exposure of the fine saprolite on the hill slope (F). Kaolinite venules crosscutting the clay-sandy matrix in the fine saprolite (G).

Microscopic analyses reveal the preservation of chlorite in the coarse saprolite and confirm the maintenance of the original foliation (Fig. 4A). In the transition to the fine saprolite, the presence of goethite becomes more expressive, in botryoidal habit, preferentially along the chlorite cleavage planes (Fig. 4B). In the fine saprolite, kaolinite crystallites predominate, typically attached in the form of booklets (Fig. 4C). EDS data reveal that kaolinite is surrounded by goethite films, without the botryoidal habit previously described. The kaolinite matrix surrounds numerous magnetite octahedrons, either isolated or cemented (Fig. 4D, E). These crystals are relics of the parent rocks, suggesting that the saprolite was derived from mineralized protoliths. Hematite nodules are also found within the clayey matrix (Fig. 4F).

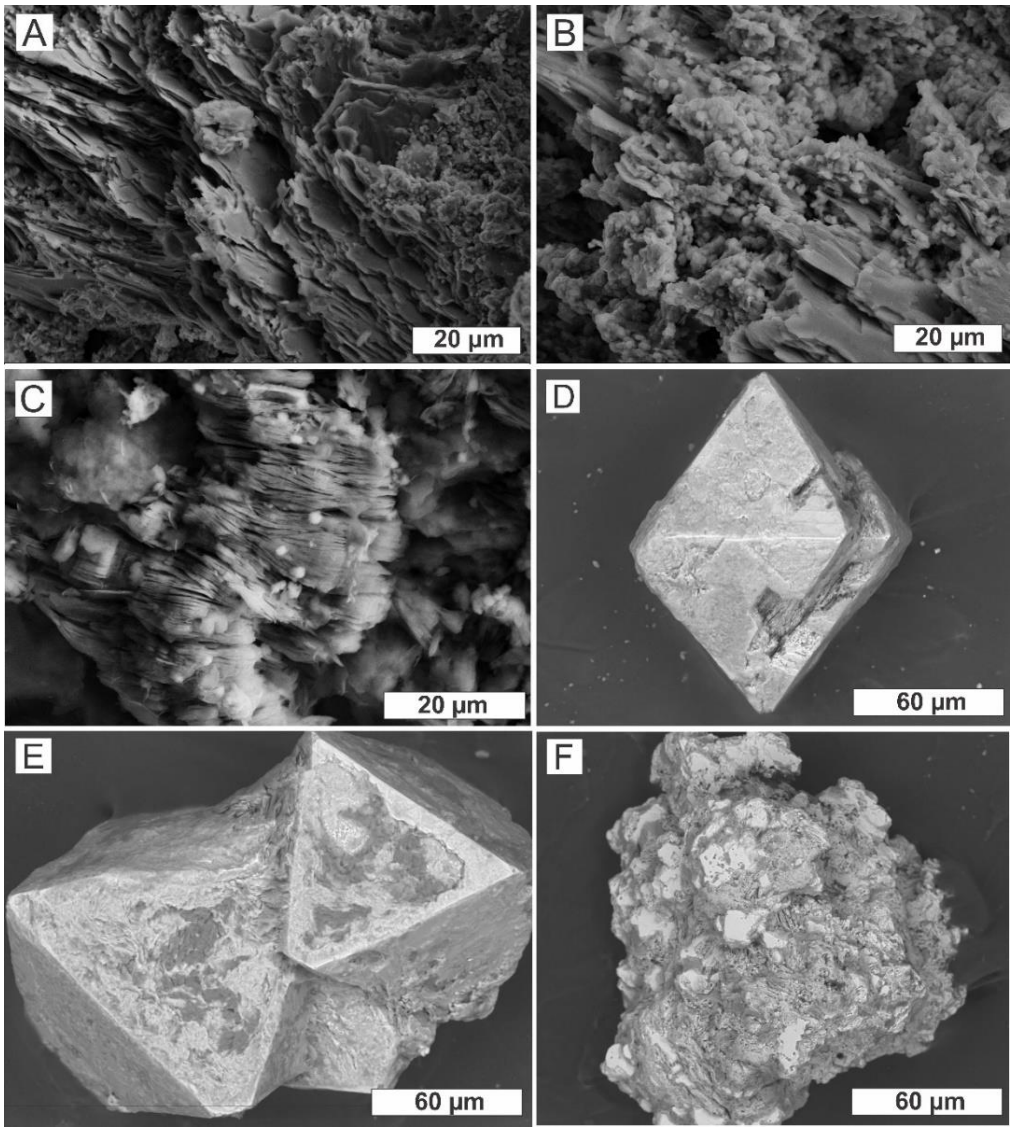

Fig. 4 Micromorphology of the coarse saprolite, represented by unweathered chlorite plates exhibiting relic foliation (A). Botryoidal goethite spread along chlorite cleavage planes (B). Typical micromorphology of fine saprolite, represented by kaolinite crystallites arranged in booklets (C). Octahedral crystals of magnetite in the fine saprolite, as single crystals (D) or forming aggregates (E). Typical hematite nodules from the saprolite (F).

4.2 Whole chemical composition of the studied saprolite

Fe_2O_3 and MgO contents are naturally expressive in the chloritites and the hypogene mineralization, both above the UCC, reflecting the presence of chlorite and, partially, chalcopyrite. On the other hand, in granodiorites, Fe_2O_3 and MgO contents are below the UCC, with high CaO, K_2O, and Na_2O. The TiO_2 contents in the chloritites are slightly higher in the chloritites than in the granodiorites (Table 1). These lithotypes host an immature gossan whose distribution is restricted and presents a low contribution to saprolite formation.

On the saprolite, the contents of Al_2O_3 (15.38 to 23.59%) and Fe_2O_3 (8.33 to 16.64%) are variable. The CaO, K_2O, and Na_2O contents are lower than those of the bedrock, while TiO_2 contents are slightly higher. MgO contents are also lower than chloritites values but higher than granodiorites. CuO content in a selected sample from the massive hypogene mineralization is 25.24%. However, in general, the mineralized zones are interspersed with chloritites, so the average content of the hypogene deposit is around 1%. This average content is slightly higher than the values of the saprolite, which range from 0.51 to 1.37%, with an average of 0.92%.

The concentrations of Au, Ag, Be, Co, Ga, La, Mn, Mo, No, P, Sc, Sn, U, V, W,Y, and Zr are always above the UCC and strongly oscillating. This reflects the intercalation of zones of non-mineralized rock with massive and disseminated mineralization, which is the typical spatial distribution pattern of the Alvo 118 deposit.

Table 1. Chemical composition of selected saprolite samples expressed in wt. % (major elements) and ppm (trace elements) and average composition of the upper continental crust (UCC) (Rudnick and Gao 2003).

Sample	Chlo.	Gran.	Miner.	Coarse saprolite		Fine saprolite					UCC
Depth	209 m	87 m	128 m	41 m	34 m	27 m	22 m	13 m	9 m	1 m	
% Al_2O_3	11.68	16.59	3.72	13.95	9.79	17.75	15.38	17.65	23.50	15.43	15.4
Fe_2O_3	16.52	3.57	31.89	10.77	14.81	13.62	11.72	14.38	8.33	16.64	5.04
CaO	1.36	3.42	0.84	0.01	0.03	0.01	0.01	0.03	0.06	0.04	3.59
K_2O	2.84	3.81	1.74	0.08	0.30	0.04	0.32	1.06	0.25	0.18	2.80
MgO	7.52	1.28	3.32	3.12	3.10	1.12	2.43	2.05	1.68	0.97	2.48
Na_2O	0.45	3.95	0.03	0.03	0.05	0.03	0.04	0.12	0.11	0.04	3.27
TiO_2	0.89	0.63	0.12	1.07	0.74	1.18	1.16	0.98	1.67	0.83	0.64
CuO	0.01	0.16	25.24	1.11	1.37	0.51	0.92	0.74	0.87	0.88	0.0035
S	0.01	0.07	10	n.d.	n.d.	n.d.	n.d.	n.d.	n.d.	0.01	-
ppm Au	0.0025	0.007	3.82	0.005	0.092	0.0025	0.0025	0.015	0.057	0.08	0.0015
Ag	0.05	0.13	12.15	0.87	1.88	1.72	0.35	0.34	0.31	0.77	0.053
As	0.7	0.4	10	0.2	0.9	0.9	0.3	0.5	0.8	2.2	4.8
Ba	470	620	70	140	120	90	210	220	560	280	628
Be	3.72	2.83	311	6.54	12.75	9.61	7.17	18.5	9.21	16.3	2.1
Bi	0.02	0.06	0.77	0.06	0.36	0.12	0.03	0.03	0.05	0.26	0.16
Cd	0.01	0.06	0.05	n.d.	0.03	n.d.	n.d.	n.d.	0.03	n.d.	0.09
Ce	289	84	75.4	30	50	27.1	31	21.2	162.5	237	63
Co	59.7	17.8	92.5	36.6	106	13.6	32.1	47	84.5	55.3	17.3
Cr	33	4	0.5	4	21	15	4	63	13	41	92
Cs	0.59	0.15	1.59	0.25	1.78	0.07	0.29	1.48	0.37	0.86	4.9
Ga	41.9	17.05	16.1	21.6	30.7	31.4	21.9	26.5	24.4	28	17.5
Ge	0.34	0.16	0.62	0.1	0.16	0.23	0.08	0.1	0.34	0.37	1.4
Hf	3.9	4.2	0.9	4.5	3.3	6.3	5	5.3	8.8	6.3	5.3
In	0.023	0.023	3.47	0.023	0.044	0.029	0.021	0.034	0.035	0.068	0.056
La	147	44.9	15.5	15.6	24.8	36.6	16.6	9.7	89.6	86	31
Li	14.3	17.7	15.5	11.9	14	7.3	7.3	6.8	5.1	3.6	24
Mn	727	420	77	322	771	142	275	306	605	1180	77.4
Mo	1.56	1.45	6.15	1.3	12.8	2.78	0.97	3.04	0.81	4.09	1.1
Nb	8.3	8.1	11.8	8.3	10.7	11.4	8.7	7.7	12.6	10	12
Ni	180.5	56.5	185	138	138	64.6	141.5	208	121	133	47
P	490	1610	2080	290	720	420	350	1110	750	880	65.4
Pb	3.1	6.2	32.5	6.1	4.3	4.3	5.9	4.5	9.7	12.1	17
Rb	93.8	185.5	167	10.8	39.3	3	19.2	105.5	19.2	21.8	84
Re	0.002	0.001	0.016	n.d.	n.d.	n.d.	n.d.	n.d.	n.d.	0.004	0.198
Sb	0.15	0.1	0.07	0.07	0.06	0.05	0.05	0.05	n.d.	n.d.	0.4
Sc	33.7	13	10.4	16.8	24.6	25.9	21	37.7	25.4	28.6	14.0
Se	0.5	0.5	15	1	2	n.d.	n.d.	n.d.	n.d.	n.d.	0.09
Sn	26.3	13.1	27.8	16	21.8	18.7	20	21	10.7	19.9	2.1
Sr	32	22.9	4.8	11.8	7.1	8.8	12.4	8.9	34.1	8.6	320
Ta	0.55	0.51	1.18	0.56	0.92	0.87	0.59	0.59	0.94	0.85	0.9
Te	0.09	0.025	13.85	0.11	0.45	0.11	0.025	0.07	0.06	0.42	-
Th	7.54	7.09	11.55	8.45	4.25	10.45	8.94	7.7	12.65	11.05	10.5
Tl	0.29	0.44	0.3	0.04	0.15	0.02	0.03	0.25	0.08	0.36	0.9
U	2.5	2.5	33	4.3	5.8	8.2	2.7	4.3	3.6	8.1	2.7
V	225	52	44	81	157	118	88	190	98	148	97
W	0.9	2.6	1.2	6.8	2.9	5.1	2.3	4.2	9.7	6.7	1.9
Y	65.2	24.8	500	32.3	136	231	22.7	56.6	73.8	231	21
Zn	61	40	30	63	42	24	76	101	68	63	67
Zr	139.5	158	4.3	206	132.5	255	205	208	344	241	193

Al_2O_3 and Fe_2O_3 contents oscillate and present opposite vertical distributions across most of the profile, reflecting the variable abundance of clay minerals and iron oxyhydroxides, respectively (Fig. 5A). CuO contents behave very closely to MgO. Both appear to distribute somewhat similarly to Al_2O_3, with no similarity to Fe_2O_3 (Fig. 5A). The TiO_2 contents present poor vertical variation, with values around 1%, compatible with the intermediate composition of the underlying granodiorites and chloritites. P_2O_5 behaves similarly to CuO, demonstrating that traces of pseudomalachite and libethenite may be present in the saprolite. K_2O contents are very low at the bottom of the profile (22 to 40 m), with a substantial increase at the top (above 22 m). Au contents oscillate strongly and reach up to 3% at 8 m depth (Fig. 5B).

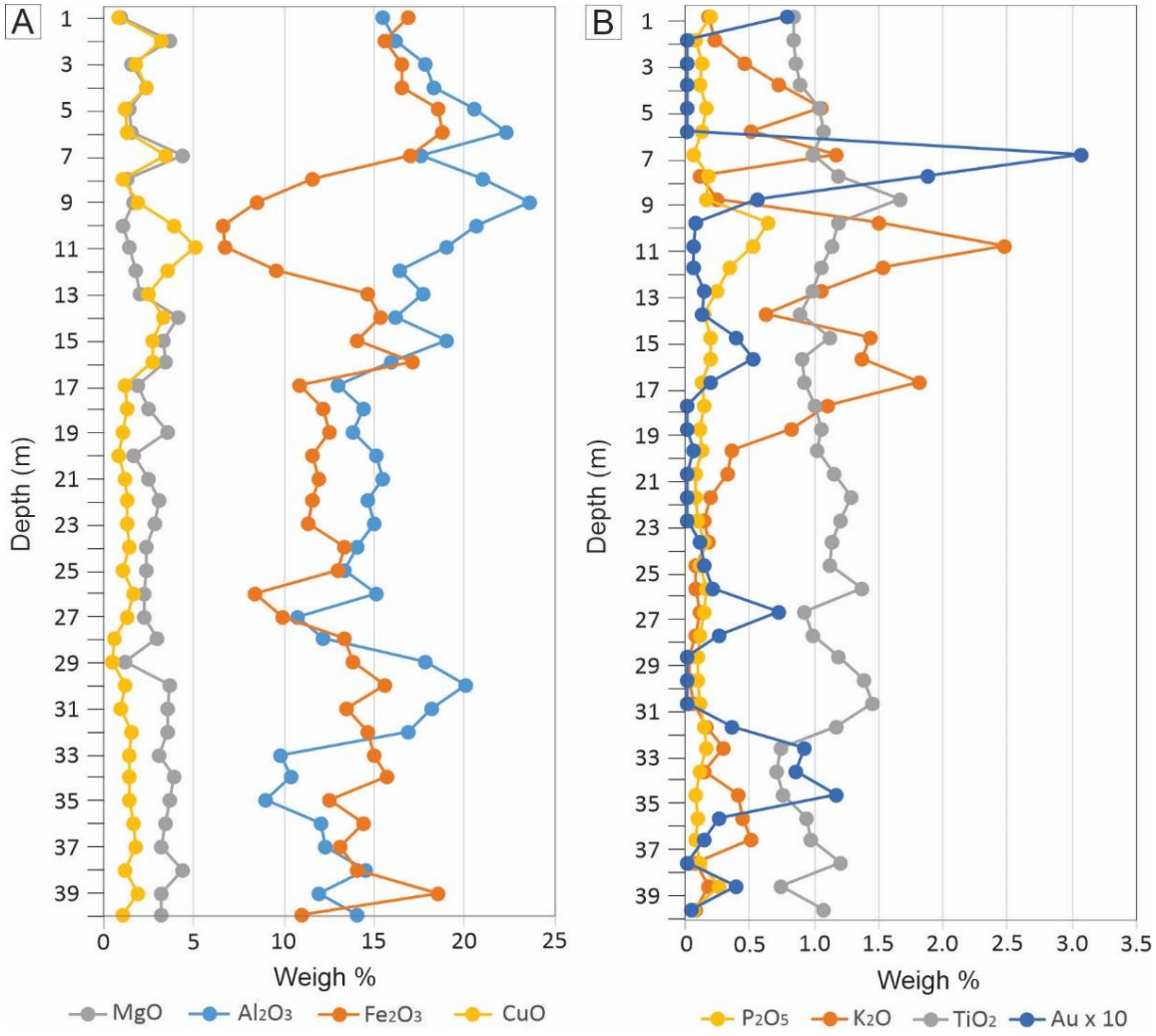

Fig. 5 Vertical distribution of selected major elements along the saprolite: MgO, Al_2O_3, Fe_2O_3, CuO (A); P_2O_5, K_2O, TiO_2, Au (B).

4.3 Clay minerals

Clay minerals identification followed the criteria established by Starkey et al. (1984) and Moore and Reynolds (1997). In the coarse saprolite, clay minerals are mainly represented

by chlorite and, towards the top (fine saprolite), kaolinite becomes progressively more abundant, associated with vermiculite and smectite, in addition to quartz and goethite.

Kaolinite was recognized from its major peak (001) between 7.10 and 7.12 Å in natural samples, which is not shifted after treatment with ethylene glycol and disappears after heating at 550°C (Fig. 6 A-D). Chlorite was identified from its highest intensity peak at 14.04 Å in natural samples, whose position remains unchanged after ethylene glycolation and heating at 550°C (Fig. 6A).

The 14.18 Å peaks indicated the presence of vermiculite in natural samples, remaining unchanged after ethylene glycol solvation (14.07 Å) and collapsing to 12.46 Å after heating at 550°C (Fig. 6B). Smectite peaks at 14.49 Å in the natural sample, expands to 16.54 Å after ethylene glycol solvation, and collapses to 9.91 due to heating (Fig. 6C). In some samples, smectite and vermiculite coexist (Fig. 6D).

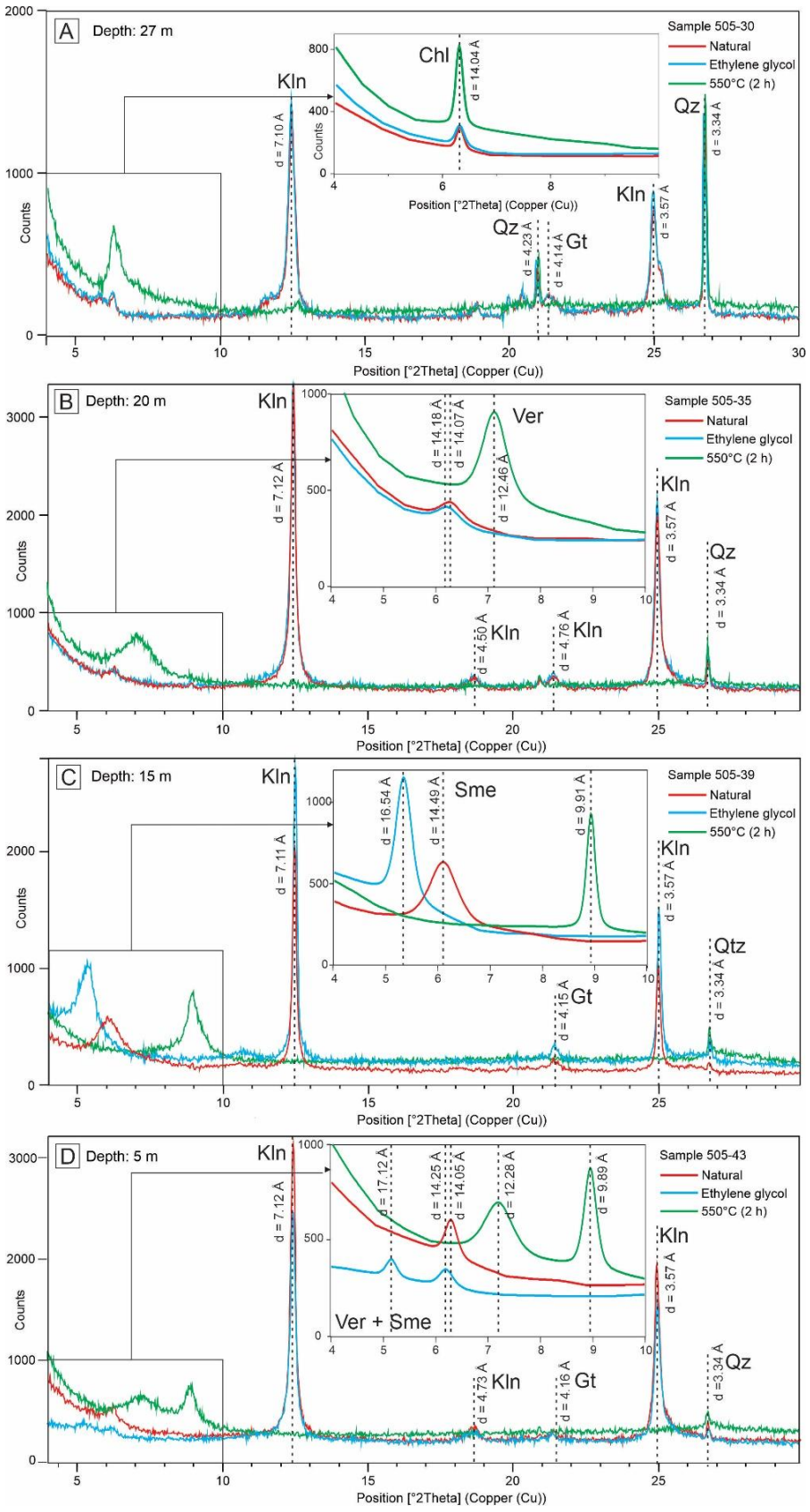

Fig. 6 X-ray diffractograms representative samples of different depths of the fine saprolite: 27m (A), 20m (B), 15m (C), 5m (D). Natural samples oriented by decantation in water (red). Ethylene glycol solvated samples (blue). Heated samples (green). Abbreviations: Kln (kaolinite), Chl (chlorite), Ver (vermiculite), Sme (smectite), Gt (goethite), Qz (quartz).

The transmittance spectra obtained in the mid-infrared (Fig. 7) demonstrate a typical pattern of kaolinite in all analyzed samples, with absorbance values similar to those obtained by Farmer (1998) and Madejová and Komadel (2001). Thus, the absorption bands at 431, 468, and 537 cm^{-1} are attributed to the Si-O, Si-O-Si, and Al-O-Si deformation vibrations, respectively. The bands at 695, 753, and 788 cm^{-1} are related to the Si-O bond, the first two being of the perpendicular type. The band at 912 cm^{-1} corresponds to the deformation of internal hydroxyl groups. The Si-O stretching plane is expressed at 1030 and 1112 cm^{-1} parallel and perpendicular to the bond, respectively. The band at 1635 cm^{-1} indicates the OH deformation vibration of water. The bands at 3619 and 3695 cm^{-1} are related to the stretching vibrations of internal hydroxyl groups. No absorption bands referring to smectites were detected, as expected at 3420 cm^{-1}, reflecting the presence of water molecules. Thus, the FTIR spectrum supports the predominance of kaolinite among clay minerals.

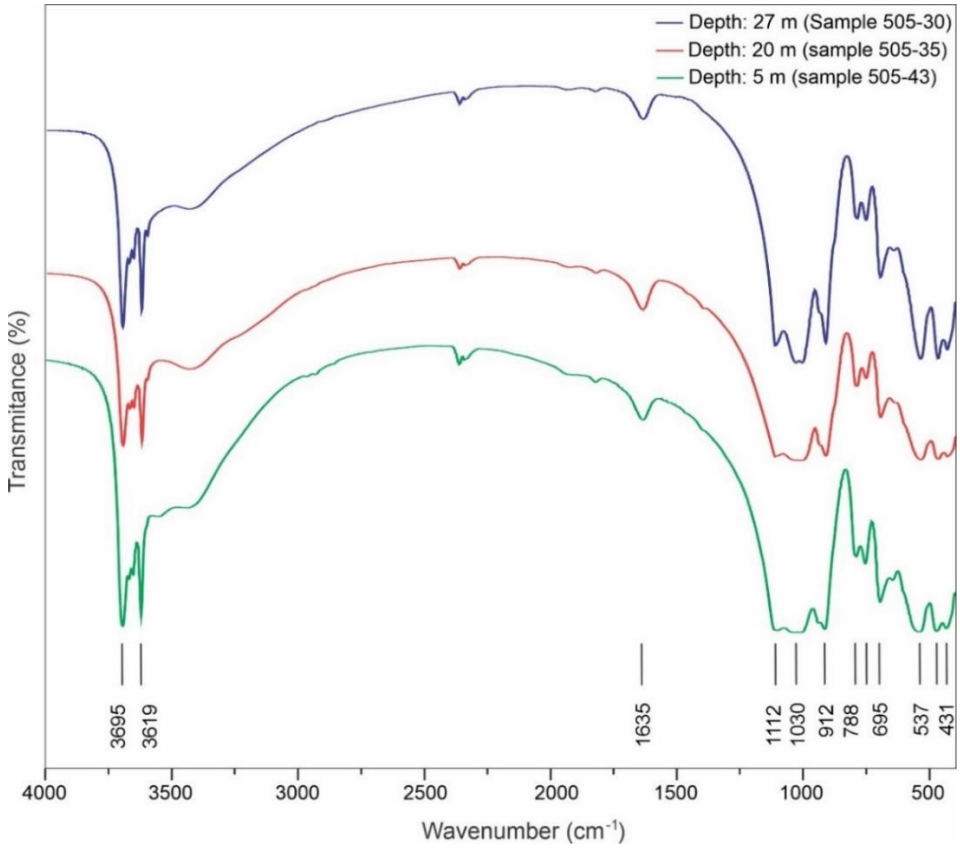

Fig. 7 FTIR spectra of selected samples from the fine saprolite samples, considered more representative of different depths.

4.4 Iron-bearing minerals

Room temperature Mössbauer spectra obtained from the saprolite samples are generally formed of four subspectra, represented by three dublets and one sextet (Fig. 8A-C,

E). However, samples 505-35 and 505-43 are more complex as they present an additional sextet (Fig. 8D, F). The hyperfine parameters obtained from refining the subspectra are shown in Table 2. Iron-bearing phases were identified by comparing the hyperfine parameters with those of the literature (Murad and Schwertmann 1980; Imbernon et al. 2011; Vandenberghe and De Grave 2012).

Thus two main groups were identified. The first is formed of goethite, ferrihydrite, chlorite, and hematite (samples 505-23, 505-25, 505-30, and 505-39), and the second group presents the same phases, in addition to magnetite (505-35 and 505-43). The relative areas suggest that chlorite is the most abundant iron-bearing phase in the coarse saprolite. However, goethite and hematite predominate in the fine saprolite, although chlorite contents are still high.

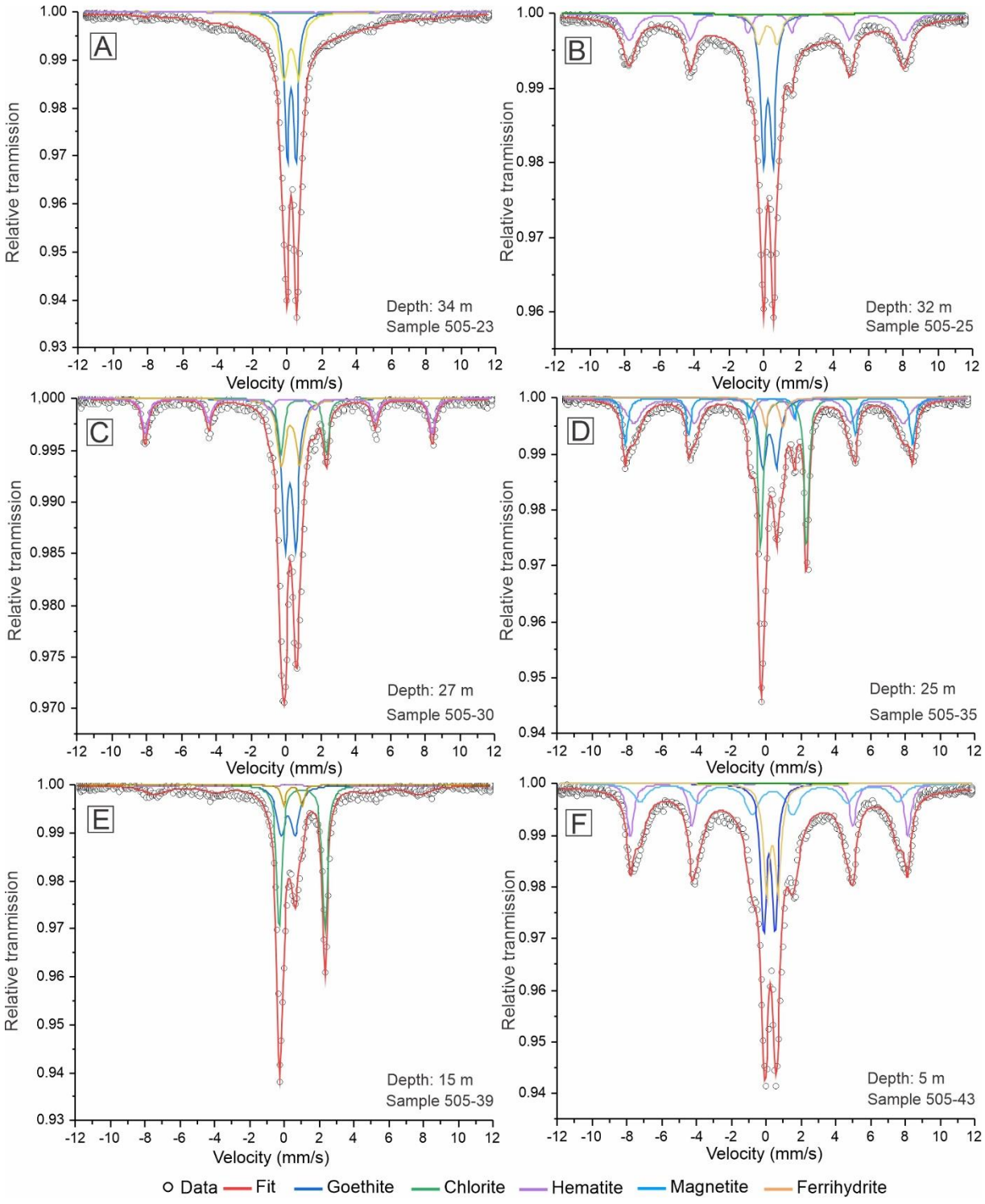

Fig. 8 Mössbauer spectra taken at room temperature for selected samples from the coarse (A, B) and fine saprolite (C, D, E, F).

Table 2. Hyperfine parameters obtained after Mössbauer spectra refinement, taken at room temperature for selected samples of the saprolite. B_{hf} (hyperfine field intensity); δ/Fe (isomeric shift relative to α-Fe); QS (quadrupole scattering); RA (relative subspectral area).

Sample	B_{hf} (T)	δ/Fe (mm s^{-1})	QS (mm s^{-1})	RA (%)	Mineral
505-23	-	0.2552	0.5031	21.648	Goethite
(34 m)	-	1.1155	2.6800	44.746	Chlorite
	-	0.2498	0.8654	33.114	Ferrihydrite
	51.569	0.2922	-0.1655	0.4913	Hematite
505-25	-	0.2509	0.55402	10.115	Goethite
(32 m)	48.952	0.26086	-0.2019	25.830	Hematite
	-	0.24238	1.074	5.010	Ferrihydrite
	-	1.2	2.7731	59.045	Chlorite
505-30	-	0.2554	0.6145	61.453	Goethite
(27 m)	-	1.0256	2.6022	11.152	Chlorite
	-	0.2724	1.0609	7.723	Ferrihydrite
	51.16	0.2662	-0.1826	19.672	Hematite
505-35	-	0.2129	0.7961	23.997	Goethite
(25 m)	-	1.0166	2.6294	21.414	Chlorite
	48.05	0.2684	-0.2212	35.341	Hematite
	51.24	0.2624	0.1740	13.226	Magnetite
	-	0.4707	1.0099	6.021	Ferrihydrite
505-39	-	0.2163	0.8132	36.747	Goethite
(15 m)	-	1.0287	2.6278	40.573	Chlorite
	47.073	0.2946	0.2809	18.339	Hematite
	-	0.5051	1.0743	4.341	Ferrihydrite
505-43	49.425	0.2725	-0.1966	13.231	Magnetite
(5 m)	45.964	0.2746	-0.2172	34.004	Hematite
	-	0.1832	0.6557	13.231	Ferrihydrite
	-	1.2413	2.5101	26.782	Chlorite
	-	0.3642	0.672	12.751	Goethite

5 Discussion

5.1 Mineralogical transformations and iron oxyhydroxide formation

The mineral association formed of kaolinite, chlorite, vermiculite, smectite, goethite, hematite, ferrihydrite, and quartz is frequently reported in saprolite profiles and, in many cases, has been associated with chlorite-bearing protoliths (Airey 1985; Murakami et al. 1996; Sirbu-Radasanu et al. 2022). Thus, the identified vermiculites are relics of the first stage of chlorite

weathering, which generally occurs from the oxidation of Fe^{2+} to Fe^{3+} and the removal of Fe and Mg (Gilkes and Little 1972; Ross and Kodama 1976; Schulze 2005).

As weathering progressed, the vermiculites were almost entirely converted into a mixture of kaolinite and iron oxyhydroxides (e.g., Murakami et al. 1996; Aspandiar and Eggleton 2002). The replacement of vermiculite with kaolinite needs significant chemical modifications, which involve the substitution of Al by Si in the tetrahedral sheets and Mg and Fe by Al in the octahedral sheets. For this to be feasible, dissolution and reprecipitation processes are required, with the incorporation of the major components of vermiculite by kaolinite, as both share the same polymerization pattern (Banfield and Eggleton 1998).

The presence of smectite in samples containing kaolinite and vermiculite or kaolinite alone indicates smectite formation could have occurred as an intermediate during the conversion of vermiculite to kaolinite (Murakami et al. 1996). On the other hand, smectite formation could also occur as an independent product of weathering of chlorite or feldspars that occur in minor amounts (Sirbu-Radasanu et al. 2022). The smectite formation from chlorite occurs from the removal of hydroxyl interlayers and reduction of sheet charge, mainly by organic compound complexation (Carnicelli et al. 1997; Castaldini et al. 2002). Mössbauer spectroscopy data reveal that chlorite, inherited from the protolith, is present throughout the entire saprolite, although not always detected by XRD (e.g., Sirbu-Radasanu et al. 2022).

Goethite and hematite were also identified in the entire saprolite associated with clay minerals. Additionally, Mössbauer spectroscopy investigations revealed the presence of ferrihydrite, which is difficult to identify by XRD. So, following similar studies, it is acceptable to infer that iron released during the conversion of chlorite to vermiculite was retained in the profile in the form of ferrihydrite. Over time, ferrihydrite precipitates underwent dehydration, forming goethite and, ultimately, hematite (Nickel and Daniels 1986; Mahmoud et al. 2018; Spier et al. 2018). Direct precipitation of goethite is rarely observed (Schwertmann and Murad 1983; Mahmoud et al. 2018). On the other hand, most of the magnesium released by chlorite was leached out due to its high mobility (Butt and Zeegers 1992; Butt et al. 2000).

Magnetite is one of the most common iron minerals in IOCG deposits (Barley et al. 1999; Montreuil et al. 2016). Generally, it is relatively resistant to oxidation in the surface environment and accumulates in weathering profiles (Graham et al. 1989). However, some magnetites can be partially oxidized to ferrihydrite, maghemite, and hematite (Habteselassie et al. 1996). The presence of relic magnetite octahedrons supports that the saprolite is derived

from mineralized chloritites since this is an accessory mineral typically identified in the hypogene mineralization.

This mineral association implies that the investigated saprolite corresponds to the lower portion of a thicker lateritic profile, with weak to moderate mineral transformations. In this environment, ferromagnesian minerals, such as chlorite, are partially preserved, resulting in the preservation of high MgO contents along the profile. Secondary minerals, such as smectites and vermiculites, less stable than kaolinite, are partially preserved (e.g., Butt and Zeegers 1992; Butt et al. 2000).

5.2 Geochemical incorporation

The distributions of Al_2O_3, Fe_2O_3, and MgO contents are mainly controlled by chlorite weathering, which is partially preserved in the coarse and fine saprolite due to decreased susceptibility to dissolution, caused by iron oxyhydroxides generation on its edges and planes (e.g., Acker and Briker 1992). These ferruginous films prevent the diffusion of the more mobile elements (Butt and Zeegers 1992; Butt et al. 2000).

The hypogene mineralization presents higher oxidation potential than the hosting chloritites, gossan, and saprolite, due to the abundance of chalcopyrite, which faces a rapid and profound change on the S oxidation state (Thornber and Taylor 1992) (Fig. 9). The chalcopyrite dissolution releases H^+, resulting in pH values between 4 and 5, in accordance to its typical low acidifying potential (Nickel 1984; Chávez 2000; Atapour and Aftabi 2007). Under such conditions, mineral inclusions in the chalcopyrite are also dissolved, leading to a redistribution of Cu, Au, Ag, Bi, Pb, Sn, Zn, and U, as will be discussed below.

Conversely, newly formation of gossan minerals and hydrolysis of chlorites from the host rocks results in the consumption of H^+, with pH elevation. The malachite predominance in gossan samples accounts for the more alkaline values (Brown 2005; Putter et al. 2010; Papineau 2020). Chlorites from the host rocks and kaolinite from the saprolite tend to consume H^+ during hydrolysis reactions, leading to higher pH values (Chávez 2000). These data demonstrate a minor effect of hypogene mineralization on the pH and Eh conditions of the saprolite.

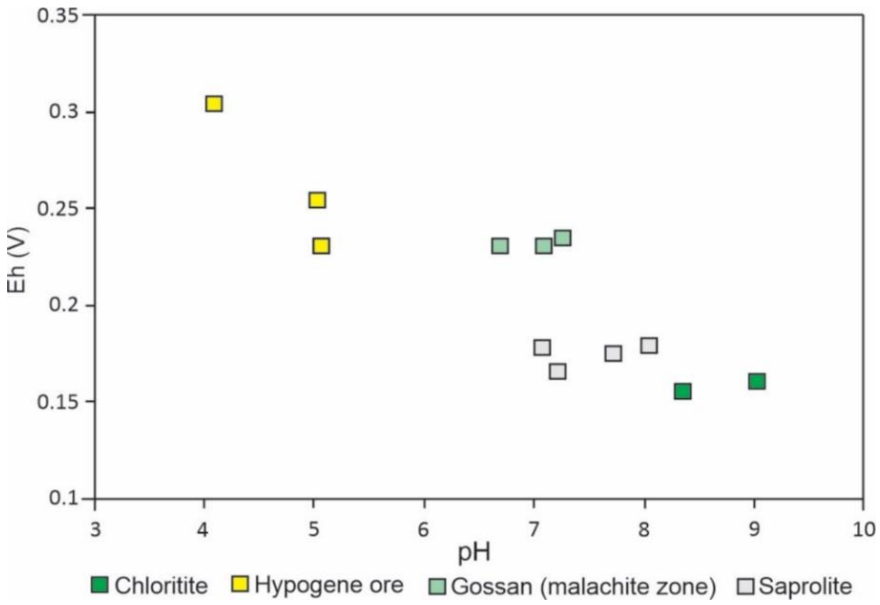

Fig. 9 pH-Eh conditions measured on selected samples of the hypogene mineralization, gossan, andsaprolite.

In addition, selected elements were used to determine the contribution of the hypogene mineralization to the saprolite geochemistry: Au, Ag, Bi, Pb, Sn, Zn, U. These metals, except Zn and Bi, are attributed to chalcopyrites and their mineral inclusions, like petzite, altaite, galena, cassiterite, stannite, sphalerite, and uraninite. In the studied deposit, the gossan is understood as a direct product of the hypogene mineralization, while the saprolite is derived from their host rocks.

Thus, the high chemical variance identified for all analyzed elements is related to the alternation of massive and disseminated sulfides, resulting in a gossan with equivalent spatial distribution (Fig. 10). So, the lower contents of most elements (except Zn) in gossan than in the hypogene mineralization are initially attributed to a more disseminated distribution of the newly formed minerals, rather than intense leaching.

However, the saprolite is not a direct product of the hypogene mineralization or gossan but is derived from their silicate host rocks. Hence, an increase in their average contents reflects their chemical retention capacity. The CuO average values in the saprolite are broadly higher or at the same level of gossan and hypogene mineralization. The same behavior is followed by Ag, Bi, Pb, Sn, and U (Fig. 10C-G). This behavior supports the high capacity of the saprolite minerals to retain metals in addition to Cu. No other minerals with Ag, Bi, Pb, Sn, or U as major components were recognized in the saprolite, except cassiterite inclusions in the magnetite octahedrons. However, iron oxyhydroxides are estimated to have contributed significantly to their partial retention (Butt and Zeegers 1992).

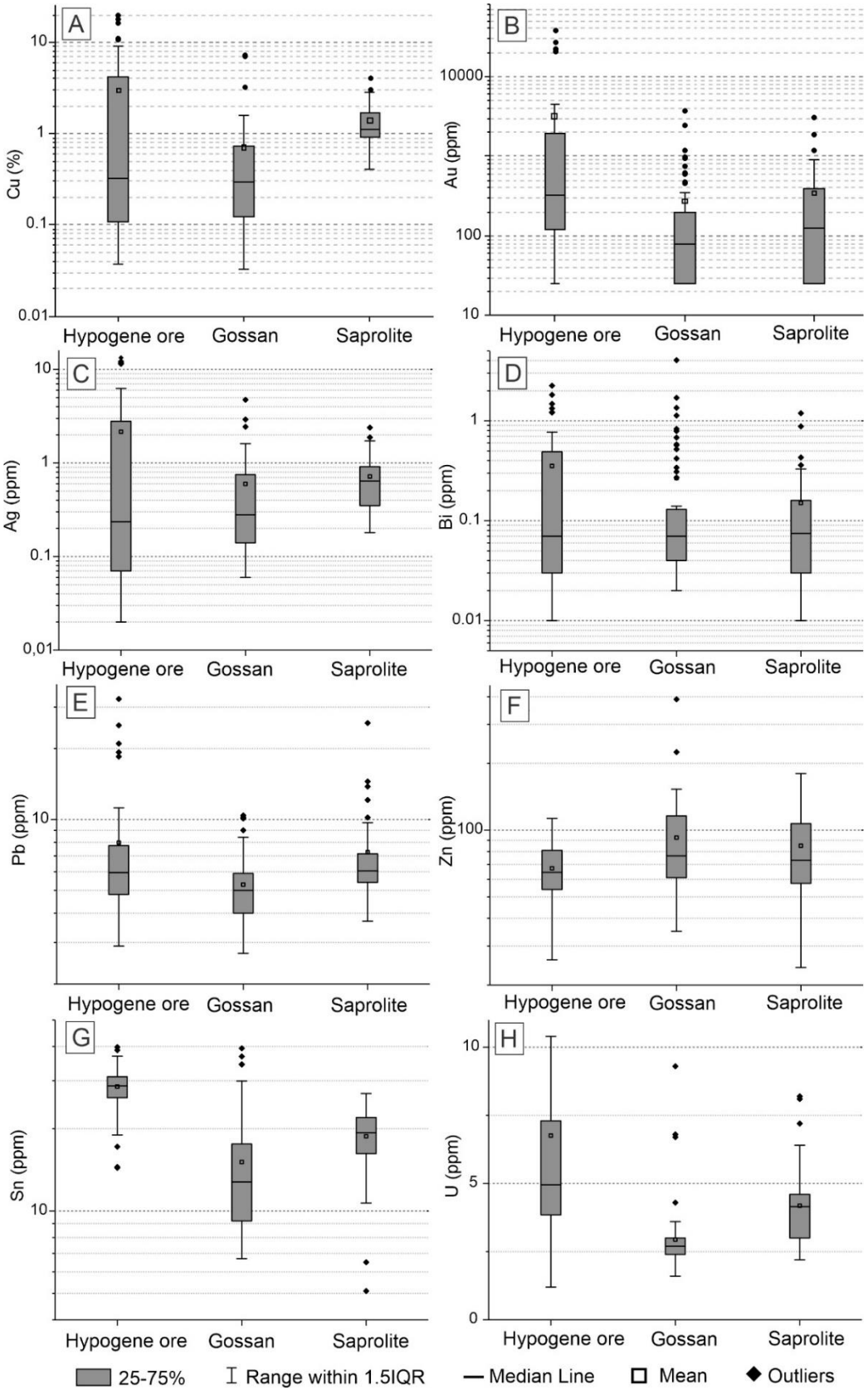

Fig. 10. Geochemical fractionation on selected elements in hypogene mineralization, gossan, and saprolite: Ag (A); Bi (B); Pb (C); Zn (D); Sn (E); and U (F).

5.3 Copper immobilization and metallurgical implications

Due to the minor abundance across the saprolite, chlorites, vermiculites, and smectites were considered to provide a low contribution to the economically relevant copper contents, although CuO values of up to 2% have been reported in natural and synthesized smectites (Mosser *et al*. 1990, 1992). On the other hand, as a major component, kaolinite seemed more prone to cause considerable copper retention, which is normally attributed to Cu/Al substitution in the octahedral sheets rather than to Cu^{2+} adsorption (Petit et al. 1995).

Under FTIR investigations, the presence of CuO in kaolinite would result in a broadening and loss of resolution of the 3619 to 3695 cm^{-1} bands (Petit et al. 1995), which was not observed in Alvo 118 samples. So, the behavior of OH stretching bands suggests that the CuO concentration in kaolinite is at least less than 10 ppm (Fig. 11). Thus, kaolinite, although predominant along the saprolite profile, would not justify the Cu contents around 1% identified in whole rock analyses.

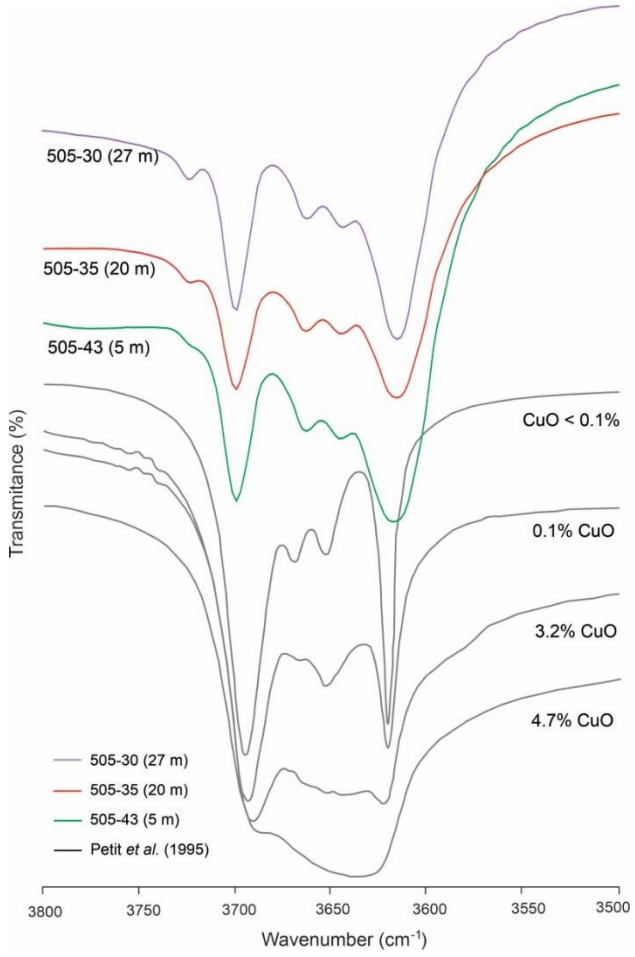

Fig. 11. Estimation of CuO content in kaolinites from the fine saprolite based on comparison with spectra obtained by Petit et al. (1995) from synthesized samples.

The estimation of the goethite, ferrihydrite, hematite, chlorite, and magnetite contents by Mössbauer spectroscopy allowed the determination of Pearson correlation with CuO contents. Thus, it was possible to estimate the strong correlation of copper with iron oxyhydroxides. Thus, the positive correlation between CuO contents in whole samples and goethite indicates that this mineral contributes significantly to copper retention in the saprolite (Fig. 12A). Moreover, the correlation of CuO contents with ferrihydrite is even higher, suggesting a greater ability of amorphous or low crystallinity ferruginous phases to incorporate copper (Fig. 12B). However, the distribution of hematite shows no correlation with CuO contents (Fig. 12C).

The strong correlation of CuO with ferrihydrite compared to goethite is in line with data obtained through selective extraction in the Salobo deposit (CMP), where iron oxyhydroxides present wide crystallinity variation and copper is mainly associated with the lower crystallinity phases (Veiga et al. 1991). The role of iron oxyhydroxides as base metal carriers is well-known and generally attributed to the high degree of structural imperfection and nanometer particle size, which results in increased surface activity (Strauss et al. 1997; Liu et al. 2014). The strong correlation of CuO with goethite and ferrihydrite contents contrasts with the weak Fe_2O_3 × CuO correlation ($r = 0.03$) due to the presence of other iron-bearing minerals, like hematite, chlorite, and magnetite, with weak correlation with CuO (Fig. 12C, D).

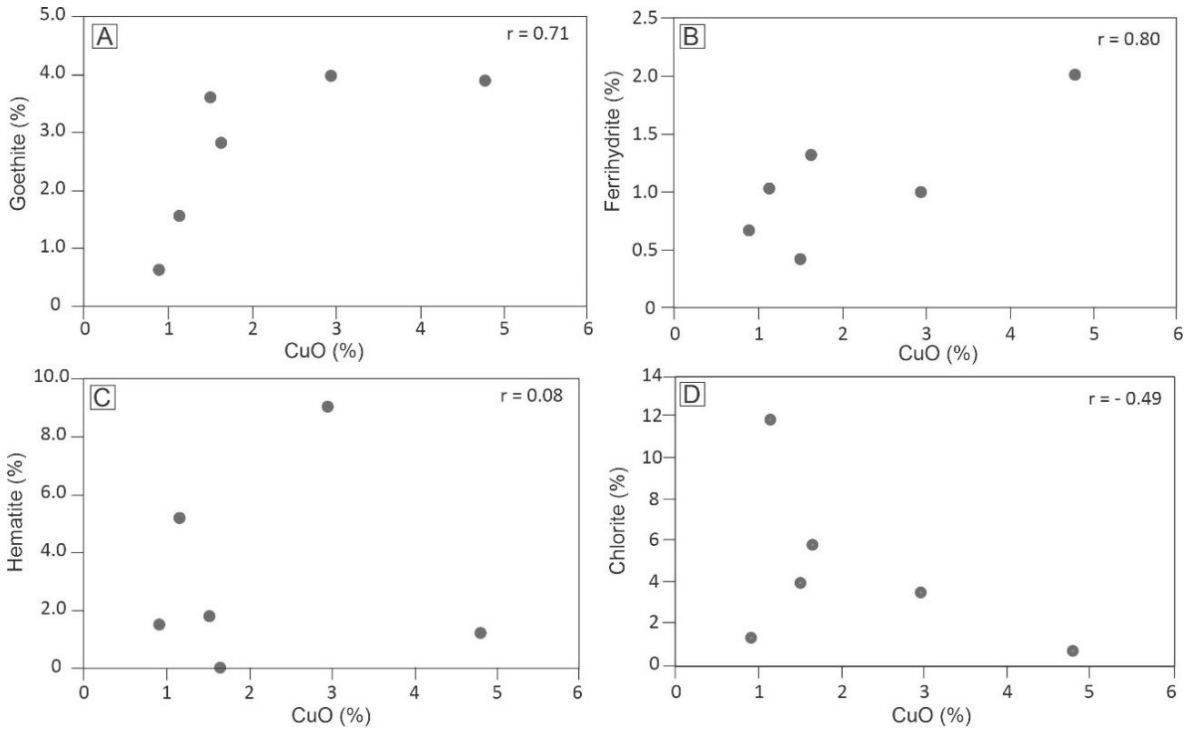

Fig. 12. A) Goethite x CuO. B) Ferrihydrite x CuO. C) Hematite x CuO. D) Chlorite x CuO.

For saprolite ores like those discussed in this paper, the establishment of metallurgical processes must consider that copper is carried by at least two different phases (goethite and ferrihydrite) with distinct strength bounds. Percolation leaching processes are commonly suggested for this class of mineralization. This technique removes Cu related to iron oxyhydroxides from a moderately acidic attack because iron oxyhydroxides, such as goethite and ferrihydrite, are strongly susceptible to breakdown to ferric ions in such conditions, releasing adsorbed metals like copper in this process (Jansen and Taylor 2003). For this purpose, acknowledgment of the associated phyllosilicates is essential as they are potential acidic consumers during the process (Veiga et al. 1991; Thomas 2021).

The predominance of kaolinites in Alvo 118 saprolite, with low contents of swelling clays, is beneficial for the percolation leaching as smectite can hold acid molecules in its structure (Chetty 2018; Thomas 2021). Conversely, chlorite, in more significant contents in the coarse saprolite, is more prone to acid consumption in strongly acidic environments during its incongruent dissolution (Snäll and Liljefors 2000; Tan et al. 2012; Jansen and Taylor 2003).

Percolation leaching technology has significantly evolved regarding reducing operation costs and recovery (Ghorbani et al. 2015; Thomas 2021; Schlesinger et al. 2022). Similar mineralized saprolites in the neighboring Sossego mine have been described but not

exploited (Toledo-Groke et al. 1987; Veiga et al. 1991). This aspect should be essential for maximizing Alvo 118 profitability.

6 Conclusions

The saprolite profile overlying the Alvo 118 deposit is derived from the underlying chlorites. No contribution of granodiorites was identified. Thus, weathering of the chlorite is the main controller of the mineralogical composition of the saprolite, where vermiculite and smectite are formed as intermediates, and kaolinite (predominant) is the final product. Iron released by chlorite was retained in the weathering profile as ferrihydrite, goethite, and hematite.

The sections of the parent rocks hosting hypogene copper ore at depth underwent the first stage of supergene alteration with the formation of an immature gossan. Near the surface, disseminated hypogene mineralization was weathered together with the chloritites. This process resulted in the formation of a saprolite horizon, exposed by subsequent erosion and displaying a mineralogical association typical of weak to moderate weathering, with abundant magnetite octahedrons still preserved in the kaolinite-vermiculite-smectite matrix.

Copper released from chalcopyrite formed a supergene dispersion halo in the saprolite, which also inherited Au, Ag, Bi, Pb, Sn, Zn, and U from the hypogene mineralization. Then, this investigation revealed that ferrihydrite and goethite played an essential role in copper incorporation across de weathering profile. There is no evidence of copper incorporation by clay minerals. Thus, percolation leaching is an appropriate copper extraction technique for this mineralization class, which is also favored by the low contents of expandible clay minerals.

A**cknowledgments**

The authors thank Vale for access to exploration areas, logistical support during field activities, and access to drill cores and exploratory data; the geologist Clóvis Maurity for the intermediation of the partnership with Vale; and the Geosciences Institute of the Federal University of Pará for the analytical facilities. This work was supported by the National Council for Scientific and Technological Development (CNPq) [305015/2016-8; 442871/2018-0].

References

Acker JG, Bricker OP (1992) The influence of pH on biotite dissolution and alteration kinetics at low temperature. Geochimica et Cosmochimica Acta 56:3073–3092. https://doi.org/10.1016/0016-7037(92)90290-Y

Albuquerque MAC, Andrade PJMB, Maurity C, Kwitko R (2001) Geologia e características das mineralizações cupríferas do depósito Alvo 118, Província Mineral de Carajás, Pará, Brasil. VII Simpósio de Geologia da Amazônia, 5–8

Aspandiar MF, Eggleton RA (2002) weathering of chlorite: I. Reactions and products in microsystems controlled by the primary mineral. Clays and Clay Minerals 50:685–698. https://doi.org/10.1346/000986002762090227

Atapour H, Aftabi A (2007) The geochemistry of gossans associated with Sarcheshmeh porphyry copper deposit, Rafsanjan, Kerman, Iran: Implications for exploration and the environment. J Geoch Exp 93(1):47–65. https://doi.org/10.1016/j.gexplo.2006.07.007

Airey PL (1986) Radionuclide migration around uranium ore bodies in the Alligator Rivers Region of the Northern Territory of Australia — Analogue of radioactive waste repositories — A review. Chemical Geology 55:255–268. https://doi.org/10.1016/0009-2541(86)90028-8

Banfield JF (1988) Transmission Electron Microscope Study of Biotite Weathering. Clays and Clay Minerals 36:47–60. https://doi.org/10.1346/CCMN.1988.0360107

Barley ME, Pickard AL, Hagemann SG, Folkert SL (1999) Hydrothermal origin for the 2 billion year old Mount Tom Price giant iron ore deposit, Hamersley Province, Western Australia. Mineralium Deposita 34:784–789. https://doi.org/10.1007/s001260050238

Brown AC (2005) Refinements for footwall red-bed diagenesis in the sediment-hosted stratiform copper deposits model. Econ Geol 100:765–771. https://doi.org/10.2113/gsecongeo.100.4.765

Butt CRM, Zeegers H (1992) Regolith Exploration Geochemistry in Tropical and Subtropical Terrains. Handbook of Exploration Geochemistry, 4. Elsevier, Amsterdam, 607pp.

Butt CRM, Lintern MJ, Anand RR (2000) Evolution of regoliths and landscapes in deeply weathered terrain — implications for geochemical exploration. Ore Geology Reviews 16:167–183. https://doi.org/10.1016/S0169-1368(99)00029-3

Carnicelli S, Mirabella A, Cecchini G, Sanesi G (1997) Weathering of Chlorite to a Low-Charge Expandable Mineral in a Spodosol on the Apennine Mountains, Italy. Clays and Clay Minerals 45:28–41. https://doi.org/10.1346/CCMN.1997.0450104

Castaldini M, Mirabella A, Sartori G, et al (2002) Soil development and microbial community along an altitudinal transect in trentino mountains. Developments in Soil Science 28: 217–228. https://doi.org/10.1016/S0166-2481(02)80019-8

Chávez W (2000) Supergene oxidation of copper deposits: zoning and distribution of copper oxide minerals. Soc of Econ Geol News 41:10–21. https://doi.org/10.5382/SEGnews.2000-41.fea

Chetty D (2018) Acid-gangue interactions in heap leach operations: a review of the role of mineralogy for predicting ore behavior. Min 8 (47):1–11. https://doi.org/10.3390/min8020047

Ghorbani Y, Franzidis JP, Petersen J (2015) Heap leaching technology – current state, innovations and future directions: A review. Min Proc Ext Met Rev 37:73-119. https://doi.org/10.1080/08827508.2015.1115990

Costa ML, Angélica RS, Fonseca LR (1996) Geochemical exploration for gold in deep weathered lateritized gossans in the Amazon region-Brazil: a case history of the Igarapé Bahia deposit. Geochimica Brasiliensis 10(1): 13–26.

Costa ML, Angélica RS, Costa NC (1999) The geochemical association Au–As–B–(Cu)–Sn–W in latosol, colluvium, lateritic iron crust and gossan in Carajás, Brazil: importance for primary ore identification. Journal of Geochemical Exploration 67:33–49. https://doi.org/10.1016/S0375-6742(99)00065-5

Docegeo (1991). Departamento Nacional de Produção Mineral. Internal report.

Dube A, Zbytniewski R, Kowalkowski T, Cukrowska E, Buszewski B (2001) Adsorption and migration of heavy metals in soil. Pol. J. Environ. Stud. 10, 1–10.

Eggleton RA (2001) The Regolith Glossary, Surficial Geology, Soils and Landscapes (Ed.) CRC LEME Pub. 144 pp.

Farmer VC (1998) Differing effects of particle size and shape in the infrared and Raman spectra of kaolinite. Clay Minerals 33:601–604.

Gilkes RJ, Little IP (1972) Weathering of chlorite and some associations of trace elements in Permian phyllites in Southeast Queensland. Geoderma 7:233–247. https://doi.org/10.1016/0016-7061(72)90008-0

Graham RC (1989) Weathering of Iron-Bearing Minerals in Soils and Saprolite on the North Carolina Blue Ridge Front: I. Sand-Size Primary Minerals. Clays and Clay Minerals 37:19–28. https://doi.org/10.1346/CCMN.1989.0370103

Grainger CJ, Groves DI, Tallarico FHB, Fletcher IR (2008) Metallogenesis of the Carajás Mineral Province, Southern Amazon Craton, Brazil: Varying styles of Archean through

Paleoproterozoic to Neoproterozoic base- and precious-metal mineralisation. Ore Geology Reviews 33:451–489. https://doi.org/10.1016/j.oregeorev.2006.10.010

Habteselassie MM, Mathison CI, Gilkes RJ (1996) Vanadium in magnetite gabbros and its behaviour during lateritic weathering, Windimurra Complex, Western Australia. Australian Journal of Earth Sciences 43:555–566. https://doi.org/10.1080/08120099608728276

Ildefonse P, Manceau A, Prost D, Toledo-Groke MC (1986) Hydroxy-Cu vermiculite formed by the weathering of Fe-biotites at Salobo, Carajás, Brazil. Clays Clay Miner 34:338-345. https://doi.org/10.1346/CCMN.1986.0340315

Imbernon RAL, Blot A, Pereira VP, Franco DR (2011) Characterization of Zn-bearing chlorite by Mössbauer (ME) and infrared spectroscopy (IR) - occurrence associated to the Pb-Zn-Ag deposits of Canoas, PR, Brazil. Braz J Geol 41(2):28-236. https://doi.org/10.25249/0375-7536.2011412228236

Jansen M, Taylor A (2003) Overview of gangue mineralogy issues in oxide copper heap leaching. International Project Development Services Pty Limited https://www.911metallurgist.com/blog/wp-content/uploads/2016/06/HEAP-LEACHING Mineralogy.pdf. Accessed 11 November 2022.

Ker JC (1997) Latossolos do Brasil: Uma Revisão. Rev. Geonomos 5 (1):17–40. https://doi.org/10.18285/geonomos.v5i1.187

King LC (1956) A Geomorfologia do Brasil Oriental. Revista Brasileira de Geografia 18: 147-265.

Liu H, Chen T, Frost RL (2014) An overview of the role of goethite surfaces in the environment. https://doi.org/10.1016/j.chemosphere.2013.11.065

Madejová J, Komadel P (2001) Baseline Studies of the Clay Minerals Society Source Clays: Infrared Methods. Clays and Clay Minerals 49:410–432. https://doi.org/10.1346/CCMN.2001.0490508

Mahmoudi E, Moore F, Asadi S (2018) Leached caps mineralogy and geochemistry as supergene enrichment fertility indicators, Meiduk and Parkam porphyry copper deposits, SW Iran. Journal of Geochemical Exploration 194:198–209. https://doi.org/10.1016/j.gexplo.2018.08.006

Mano ES, Caner, L, Chaves, AP (2015) Methodology for laterítics Cu-bearing clay minerals characterization. Holos 31 (7):3–12. https://doi.org/10.15628/holos.2015.3531

Mano ES, Caner L, Petit S, Chaves AP (2020) Mineralogical characterization of copper lateritic ore from the Furnas deposit - Carajás, Brazil. International Engineering Journal 73:329–335. https://doi.org/10.1590/0370-44672019730113

Maurity CW, Kotschoubey B (1995) Evolução recente da cobertura de alteração no platô N1-Serra dos Carajás-Pa: Degradação, pseudocarstificação, espeleotemas. Boletim do Museu Paraense Emílio Goeldi 7:331–362.

Monteiro HS, Vasconcelos PMP, Farley KA, Lopes CAM (2018) Age and evolution of diachronous erosion surfaces in the Amazon: Combining (U-Th)/He and cosmogenic 3He records. Geoch et Cosmo Acta 229:162–183. https://doi.org/10.1016/j.gca.2018.02.045

Montreuil J-F, Potter EG, Corriveau L, Davis WJ (2016) Element mobility patterns in magnetite-group IOCG systems: The Fab IOCG system, Northwest Territories, Canada. Ore Geology Reviews 72:562–584. https://doi.org/10.1016/j.oregeorev.2015.08.010

Moore DM, Reynolds, RC Jr (1997) X-Ray Diffraction and the Identification and Analysis of Clay Minerals, 2nd ed. 400 pp. Ed. Oxford University Press, New York.

Mosser C, Mestdagh M, D'Ecarreau, Herbillon AJ (1990) Spectroscopic (ESR, EXAFS) evidence of Cu for (Al-Mg) substitution in octahedral sheets of smectites. Clay Miner 25: 271-282. https://doi.org/10.1180/claymin.1990.025.3.03

Mosser C, Mosser A, Romeo M, Petit S, Decarreau A (1992) Natural and synthetic copper phyllosilicates studied by XPS. Clays Clay Miner 40:593-599. https://doi.org/10.1346/CCMN.1992.0400514

Murad E, Schwertmann U (1980) The Möessbauer spectrum of ferrihydrite and its relations to those of other iron oxides. Ame Min 65 (9-10):1044-1049.

Munsell Color (Firm) (1992) Munsell Soil Color Charts, Revised Ed., Baltmore.

Murakami T (1996) Weathering of Chlorite in a Quartz-Chlorite Schist: I. Mineralogical and Chemical Changes. Clays and Clay Minerals 44:244–256. https://doi.org/10.1346/CCMN.1996.0440210

Nickel EH (1984) The mineralogy and geochemistry of the weathering profile of the Teutonic Bore Cu-Pb-Zn-Ag sulphide deposit. J of Geoch Expl 22:239-263. https://doi.org/10.1016/0375-6742(84)90014-1

Nickel EH, Daniels JL (1986) Gossans. In: Wolf, K.H. (Ed.), Handbook of Strata-bound and Stratiform Ore Deposits. Elsevier, Amsterdam, pp. 261–390 Part 4, 13.

Oliveira SMB, Silva MLM, Toledo MCM (1995) The role of residual 2:1 phyllosilicates in lateritic metallogenesis: Ni and Cu deposits in Serra dos Carajás, Brazilian Amazônia. Geochimica Brasiliensis 9(2):161–171.

Oliveira SMB, Imbernon RAL, M. Partiti CS, Rechenberg HR (1996) Mössbauer spectroscopic study of iron oxides and oxyhydroxides in gossans. Geoderma 73:245–256. https://doi.org/10.1016/0016-7061(96)00035-3

Petit S, Decarreau A, Mosser C, Ehret G, Grauby O (1995) Hydrothermal Synthesis (250°C) of Copper-Substituted Kaolinites. Clays and Clay Minerals 43:482–494. https://doi.org/10.1346/CCMN.1995.0430413

Papineau D (2020) Chemically oscillating reactions in the formation of botryoidal malachite. Ame Mineral 105(4): 447–454. https://doi.org/10.2138/am-2020-7029

Porto CG (2016) Geochemical exploration challenges in the regolith dominated Igarapé Bahia gold deposit, Carajás, Brazil. Ore Geology Reviews 73:432–450. https://doi.org/10.1016/j.oregeorev.2015.10.027

Putter T, Mees F, Decrée S, Dewaele S (2010) Malachite, an indicator of major Pliocene Cu remobilization in karstic environment (Katanga, Democratic Republic of Congo). Ore Geol Rev 38:90–100. https://doi.org/10.1016/j.oregeorev.2010.07.001

Ross GJ, Kodama H (1976) Experimental alteration of a chlorite into a regularly interstratified chlorite vermiculite by chemical oxidation. Clays and Clay Miner 24, 183-190. https://doi.org/10.1346/CCMN.1976.0240406

Rudnick RL, Gao S (2003) The Composition of the Continental Crust. In: Holland, H.D. and Turekian, K.K., Eds., Treatise on Geochemistry, Vol. 3, The Crust, Elsevier-Pergamon, Oxford, 1-64.

Santos PHS, Costa ML (2022) Mineralogical and textural evolution of the Alvo 118 copper-bearing gossan: Implications for supergene metallogenesis in Carajás Mineral Province, Brazil. Journal of South American Earth Sciences, 104108. https://doi.org/10.1016/j.jsames.2022.104108

Schwertmann U, Murad E (1983) Effect of pH on the Formation of Goethite and Hematite from Ferrihydrite. Clays and Clay Minerals 31:277–284. https://doi.org/10.1346/CCMN.1983.0310405

Schlesinger ME, Sole KC, Davenport WG, Alvear Flores, GRF (2022) Hydrometallurgical copper extraction. In Extractive Metallurgy of Copper (pp. 361–406). Elsevier.

Schulze DG (2005) Clay minerals. In Hille, D. (Ed) Encyclopedia of Soils in the Environment. Elsevier, 246-254.

Sirbu-Radasanu DS, Huzum R, Dumitraş D-G, Stan CO (2022) Mineralogical and Geochemical Implications of Weathering Processes Responsible for Soil Generation in Mănăila Alpine Area (Tulgheş 3 Unit—Eastern Carpathians). Minerals 12:1161. https://doi.org/10.3390/min12091161

Snäll S, Liljefors T (2000) Leachability of major elements from minerals in strong acids. J Geoch. Expl 71(1):1-12. https://doi.org/10.1016/S0375-6742(00)00139-4

Spier CA, Levett A, Rosière CA (2018) Geochemistry of canga (ferricrete) and evolution of the weathering profile developed on itabirite and iron ore in the Quadrilátero Ferrífero, Minas Gerais, Brazil. Mineralium Deposita 54:983–1010. https://doi.org/10.1007/s00126-018-0856-7

Strauss R, Brummer GW, Barrow NJ (1997) Effects of crystallinity of goethite: II. Rates of sorption and desorption of phosphate. European Journal of Soil Science 48:101–114. https://doi.org/10.1111/j.1365-2389.1997.tb00189.x

Silva ERP, Kotschoubey B (2000) Alteração supergênica do depósito de cobre-ouro do Salobo, Serra dos Carajás-PA – Ênfase no comportamento do cobre. Revista Brasileira de Geociências 30(4):623–630.

Starkey HC, Blackmon PD, Hauff PL (1984) The routine mineralogical analysis of clay-bearing samples. In: pubs.er.usgs.gov.

Tan H, Skinner W, Addai-Mensah J (2012) Leaching behaviour of low and high Fe substituted chlorite clay minerals at low pH. Hydrom 125(6):100–108. https://doi.org/10.1016/j.hydromet.2012.05.015

Teixeira PC, Donagemma GK, Fontana A, Teixeira WG (2017) Manual de métodos de análise de solo. 3. ed. rev. e ampl. – Brasília, DF: Embrapa.

Tallarico FHB, Figueiredo BR, Groves DI, Kositcin N, McNaughton NJ, Fletcher IR, Rego JL (2005) Geology and SHRIMPU–Pb geochronology of the Igarapé Bahia Deposit, Carajás Copper–Gold Belt, Brazil: an Archean (2.57 Ga) example of iron–oxide Cu–Au–(U–REE) mineralization. Econ Geol 100:7–28. https://doi.org/10.2113/100.1.0007

Thomas M (2021) Understanding gangue acid consumption in copper sulfide heap leaching: Predicting the impact of carbonates, silicates and secondary precipitates. Miner Eng 171:107090. https://doi.org/10.1016/j.mineng.2021.107090

Thornber MR, Taylor, GF (1992) The mechanisms of sulphide oxidation and gossan formation 4:119–138. https://doi.org/10.1016/B978-0-444-89095-5.50015-8

Toledo-Groke MC, Melfi AJ, Parisot JC (1987) Comportamento do cobre durante o intemperismo das rochas xistosas cupríferas do Salobo 3A, Serra dos Carajás. Geochimica Brasiliensis, 2:187–200.

Torresi I, Xavier RP, Bortholoto DFA, Monteiro LVS (2011) Hydrothermal alteration, fluid inclusions and stable isotope systematics of the Alvo 118 iron oxide–copper–gold deposit, Carajás Mineral Province (Brazil): Implications for ore genesis. Mineralium Deposita 47:299–323. https://doi.org/10.1007/s00126-011-0373-4

USGS (2018) Shuttle Radar Topography Mission (SRTM).

Vandenberghe RE, De Grave E (2012). Application of Mössbauer spectroscopy in earth sciences. Möss Spec 91–185. https://doi.org/10.1007/978-3-642-32220-4_3

Vasconcelos PM, Renne PR, Brimhall GH, Becker TA (1994) Direct dating of weathering phenomena by 40Ar39Ar and K-Ar analysis of supergene K-Mn oxides. Geochimica et Cosmochimica Acta 58:1635–1665. https://doi.org/10.1016/0016-7037(94)90565-7

Vasques ML, Sousa, CS, Carvalho JML (2008) Mapa geológico e de recursos minerais do estado do Pará: Programa Geologia do Brasil, integração, atualização e difusão de dados da geologia do Brasil, escala 1:1.000.000.

Veiga MM, Schorscher HD, Fyfe WS (1991) Relationship of copper with hydrous ferric oxides: Salobo, Carajás, PA, Brazil. Ore Geology Reviews 6:245–255. https://doi.org/10.1016/0169-1368(91)90025-3

CONCLUSÕES

O depósito Alvo 118 apresenta uma evolução supergênica polifásica, marcada pela formação de um gossan imaturo em profundidade e por um horizonte saprolítico próximo à superfície, em que ambos apresentam elevados teores de cobre.

As investigações mineralógicas, texturais, química e isotópicas desenvolvidas nesta tese permitiram: (1) a reconstituição de um estágio da evolução supergênica da PMC até então pouco documentado, ou seja, a formação de gossan imaturo em profundidade; (2) estabelebecer o fracionamento geoquímico do cobre e outros metais em dois ambientes supergênicos distintos, gossan e horizonte saprolítico; e (3) estabelecer quais as fases minerais que justificam os elevados teores de cobre do horizonte saprolítico.

A formação do gossan em profundidade foi marcada por uma influência restrita do lençol freático e pela forte interação das soluções ácidas liberadas pelos sulfetos com os minerais de ganga (calcita e apatita) e, em parte, com os granodioritos. Por outro lado, os cloritito hospedeiros se mostraram pouco reativos. Assim, as sucessões minerais identificadas no gossan refletem a progressiva evolução das soluções mineralizantes de levemente ácidas a ligeiramente alcalinas. Paralelamente, há uma tendência de contínuo amento no potencial de oxidação do ambiente mineralizante, com algumas oscilações.

As zonas da goethita (*breccia facies*), malaquita e cuprita foram formadas a partir de mineralização sulfetada maciça, sendo as duas primeiras hospedadas por cloritito e a ultima, por granodioritos. Por outro lado, a *cavity-filling facies* da zona da goethita e a zona da libethenita são derivadas de mineralização disseminada, hospedadas por cloritito e granodioritos, respectivamente. Os principais elementos-traço identificados na calcopirita (Ti, Mn, Zn, Ni, V, Co) foram em parte incorporados ao gossan principalmente pela goethita. A malaquita está mais relacionada à retenção de Ba, Ca, Cr, Mn e Zn. Ouro e Pb estão restritos à cuprita, tenorita e cobre nativo.

A distribuição de metais na mineralização hipogênica é controlada principalmente pela calcopirita e suas inclusões, como petzita, altaíta, galena, uraninita, cassiterita e estannita. Estes minerais são carreadores de Au, Ag, Te, Pb, In, Se, Y, Bi, U e Sn. No gossan, Ag, Te, Pb, Se e Bi permaneceram associados e foram incorporados aos minerais de cobre neoformados. Por outro lado, Au, In, Y, U e Sn exibem maior afinidade com os oxi-hidróxidos de ferro, assim como, Zn, As, Be, Ga, Mo e Ni.

No saprólito, os oxi-hidróxidos de ferro incorporaram Ga, Sc, Sn, V, Mn, Co e Cr, em que os quatro últimos são derivados do intemperismo das rochas hospedeiras. A associação formada por Al_2O_3, Hf, Zr, Th, TiO_2, Ce, La, Ba e Sr corresponde à assinatura geoquímica das rochas hospedeiras, com contribuição dominante dos cloritito e secundária dos granodioritos. Por outro lado, a associação In, Y, Te, Pb, Bi e Se representa a assinatura geoquímica dos três tipos de mineralização, e, desse modo, constituem os rastreadores da mineralização de Cu e Au.

Os valores elevados de $\delta^{65}Cu$ confirmam que o gossan do depósito Alvo 118 é imaturo e esteve preservado do intemperismo clássico, dominado por processo de lixiviação. Adicionalmente, as rochas hospedeiras formaram um típico perfil de intemperismo, compatível com baixos valores de $\delta^{65}Cu$. Os valores de $\delta^{56}Fe$ corroboram esta interpretação, indicando restrita contribuição da mineralização hipogênica para os conteúdos de ferro do saprólito, mais influenciado pelo intemperismo da clorita.

O perfil saprolítico que recobre o depósito Alvo 118 é derivado dos cloritito subjacente, com pouca contribuição dos granodioritos, correspondento a um halo de dispersão supergênica da mineralização sulfetadas. Assim, o intemperismo da clorita é o principal controlador da composição mineralógica do saprólito, em que vermiculita e esmectita são intermediários e a caulinita é o produto final; e a principal fonte ferro ára formação dos oxi-hidróxidos de ferro.

Ferridrita e goethita, em especial, desempenharam importante papel como incorporadores de cobre no saprólito. Não há evidências da incorporação de cobre pelos argilominerais. Assim, a lixiviação ácida parece ser uma técnica apropriada para o beneficiamento deste tipo de mineralização.

O desenvolvimento do gossan do depósito Alvo 118 representa um estágio metalogenético supergênico preservado dos processos de lateritização que afetaram amplamente a região. Desse modo, ele difere da maioria dos gossan estudados até então na PMC. Outros depósitos com evolução supergênica equivalents devem estar distribuídos nas áreas denudadas do entorno da Serra dos Carajás, assim como em corpos mineralizados profundos localizados em outras regiões do mundo.

REFERÊNCIAS

Albuquerque M.A.C., Andrade P.J.M.B., Maurity C., Kwitko R. 2001. Geologia e Características das Mineralizações Cupríferas do Depósito Alvo 118 Província Mineral de Carajás, Pará, Brasil. In: VII Simpósio de Geologia da Amazônia, workshop I. Belém, p. 5-8.

Alpers C.N., Brimhall G.H. 1989, Paleohydrologic evolution and geochemical dynamics of cumulative supergene metal enrichment at La Escondida, Atacama Desert, Northern Chile. *Economic Geology*, **84**:229-255.

Andreu E., Torró L., Proenza J.A., Domenech C, García-Casco A, Villanova de Benavent C, Chavez C, Espaillat J, Lewis JF. 2015. Weathering profile of the Cerro de Maimón VMS deposit (Dominican Republic): textures, mineralogy, gossan evolution and mobility of gold and silver. *Ore Geology Reviews*, **65**:165-179.

Andrew R.L. 1984. The geochemistry of selected base-metal gossans, southern Africa. *Journal of Geochemical Exploration*, **22**:161-192.

Asmus B. 2013. Archaeometallurgy: Gossan or the iron cap. Disponível em: https://en.archaeometallurgie.de/gossan-iron-cap/. Acesso em 14 Novembro 2022.

Atapour A., Aftabi A. 2007. The geochemistry of gossans associated with Sarcheshmeh porphyry copper deposit, Rafsanjan, Kerman, Iran: Implications for exploration and the environment Habibeh. *Journal of Geochemical Exploration*, **93**:47-65.

Belogub E.V., Novoselov K.A., Yakovleva V.A., Spiro B. 2008. Supergene sulphides and related minerals in the supergene profiles of VHMS deposits from the South Urals. Ore Geology Reviews, **33**:239-254.

Borrok D.M. et al. 2007. Separation of copper, iron, and zinc from complex aqueous solutions for isotopic measurement. *Chemical Geology*, **242**(3):400-414.

Boyle D.R. 1993. Oxidation of massive sulfide deposits in the bathurstmining camp, New Brunswick. In: Alpers, C.N., Blowes, D.W. (eds.). Environmental Geochemistry of Sulfide Oxidation. American Chemical Society Symposium. **550**, p. 535-550.

Butt C.R.M. 2016. The Development of regolith exploration geochemistry in the tropics and sub-tropics. *Ore Geology Reviews*, **73**(3):380-393.

Callahan R.P., *et al*. 2019, Arrested development: Erosional equilibrium in the southern Sierra Nevada, California, maintained by feedbacks between channel incision and hillslope sediment production. *Geological Society of America Bulletin*, **131**:1179-1202.

Chávez W.X. 2021. Weathering of copper deposits and copper mobility: Mineralogy, geochemical stratigraphy, and exploration implications. *Society of Economic Geology Discovery*, **126**:16-27.

Chávez W.X. 2000. Supergene oxidation of copper deposits: zoning and distribution of copper oxide minerals. *Society of Economic Geology Discovery*, **41**:10-21.

Craddock P.R., Dauphas N. 2011. Iron Isotopic Compositions of Geological Reference Materials and Chondrites. *Geostandards and Geoanalytical Research*, **35**(1):101-123.

Costa M.L., Angélica R.S., Costa N.C. 1999. The geochemical association Au–As–B–(Cu)–Sn–W in latosol, colluvium, lateritic iron crust and gossan in Carajás, Brazil: importante for primary ore identification. *Journal of Geochemical Exploration*, **67**:33-49.

Costa M.L., Angelica, R.S., Fonseca, L.R. 1996. Geochemical exploration for gold in deep weathered lateritized gossans in the Amazon region-Brazil: A case history of the Igarapé Bahia deposit. *Geochimica Brasiliensis*, **10**(1):13-26.

Costa W.A.M., Costa M.LL. 1985. Os verdes minerais da Serra Verde (Região dos Carajás). In: II Simpósio de Geologia da Amazônia. Belém, p. 189-199.

Dill H.G. 2015. Supergene alteration of ore deposits: From nature to humans. *Elements*, **11**(5):311-316.

Dixon J.L., Heimsath A.M., Amundson R.C. 2009. The critical role of climate and saprolite weathering in landscape evolution. *Earth Surface Processes and Landforms*, **34**:1507-1521.

Galarza M.A., Macambira M.J.B., Villas, R.N. 2008. Dating and isotopic characteristics (Pb and S) of the Fe oxide–Cu–Au–U–REE Igarapé Bahia ore deposit, Carajás Mineral Province, Pará State, Brazil. *Journal of South American Earth Sciences*, **25**:377-397.

Grainger C.J., Groves, D.I., Tallarico, F.H.B., Fletcher, I.R. 2008. Metallogenesis of the Carajás Mineral Province, southern Amazon Craton, Brazil: Varying styles of Archean through Paleoproterozoic to Neoproterozoic base- and precious-metal mineralization. *Ore Geology Reviews*, **33**:451-489.

Goodfellow B.W., Hilley G.E., Webb S.M., Sklar L.S., Moon S., Olson, C.A. 2016, The chemical, mechanical, and hydrological evolution of weathering granitoid. *Journal of Geophysical Research: Earth Surface*, **121**: 1410-1435.

Haldar S.K. 2018. *Mineral Exploration Principles and Applications*, 2nd ed. Elsevier, Amsterdam, 378 p.

Hunt J., Lottermoser B.G., Parbhakar-Fox A., Veen E.V., Goemann, K. 2016. Precious metals in gossanous waste rocks from the Iberian Pyrite Belt. *Minerals Engineering*, **87**(1):45-53.

Ildefonse P., Manceau A., Prost D., Toledo-Groke M.C.M. 1986. Hydroxy-Cu-vermiculite formed by the weathering of Fe-biotites at Salobo, Carajás, Brazil. *Clays and Clay and Clay Minerals*, **34**:338-345.

Imbernon R.A.L. 1998. *Os chapéus de ferro associados aos depósitos de Canoas (Pb-Zn-Ag), Adrianópolis (PR) e O'Toole (Co-Ni-EGP), Fortaleza de Minas (MG) caracterização textural, mineralógica e geoquímica*. PhD Thesis, Universidade de São Paulo, São Paulo, 161 p.

Lebedeva M.I., Fletcher R.C., Balashov V.N., Brantley S.L. 2007. A reactive diffusion model describing transformation of bedrock to saprolite. *Chemical Geology*, **244**:624-645.

Lindenmayer Z.G., Pimentel M.M., Ronchi L.H., Althoff F.J., Laux J.H., Araújo J.C., Fleck A., Barcker C.A., Carvalho D.B., Nowatzki A.C. 2001. Geologia do depósito de Cu-Au de Gameleira, Serra dos Carajás, Pará. In: Jost H., Brodt J.A., Queiroz, E.T. (eds.). Caracterização de depósitos auríferos brasileiros, ADIMB, Brasília, p. 79-139.

Macheyeki, A. S., Li, X., Kafumu, D. P., Yuan, F. 2020. Elements of exploration geochemistry. In: Macheyeki A.S., Li X., Kafumu D.P., Yuan F. (eds.). *Applied Geochemistry*, Amsterdam, Elsevier, p. 1-43.

Mano E.S., Caner L., Petit S., Chaves A.P., 2020. Mineralogical characterization of copper lateritic ore from the Furnas deposit – Carajás, Brazil. *International Engineering Journal*, **73**:329-335.

Mathur R., Fantle M.S., 2015. Copper isotopic perspectives on supergene processes: implications for the global Cu cycle. *Elements*, **11**:323-329

Millot R, Gaillardet J, Dupre B, Allegre C.J. 2002. The global control of silicate weathering rates and the coupling with physical erosion: new insights from rivers of the Canadian Shield. *Earth and Planetary Science Letters*, **196**:83-98.

Moeller K., Schoenberg R., Pedersen R.B., Weiss D., Dong S. 2012. Calibration of the new certified reference materials ERM-AE633 and ERM-AE647 for copper and IRMM-3702 for zinc isotope amount ratio determinations. *Geostandards and Geoanalytical Research*, **36**(2):177-199.

Moeller K. et al. 2014. Comparison of iron isotope variations in modern and Ordovician siliceous Fe oxyhydroxide deposits. *Geochimica et Cosmochimica Acta*, **126**:422-440.

Moeskops P.G. 1977. Yilgarn nickel gossan geochemistry – a review, with new data. *Journal of Geochemical Exploration*, 8:247-258.

Monteiro, L.V.S., Xavier R.P., Hitzman R.W., Juliani C., Souza Filho, C.R., Carvalho E.R. 2008. Mineral chemistry of ore and hydrothermal alteration at the Sossego iron oxide–copper–gold deposit, Carajás Mineral Province, Brazil. *Ore Geology Reviews*, **34**: 317-336.

Monteiro H.S., Vasconcelos P.M.P., Farley K.A., Lopes C.A.M. 2018. Age and evolution of diachronous erosion surfaces in the Amazon: Combining (U-Th)/He and cosmogenic ^{3}He records. *Geochimica et Cosmochimica Acta*, **229**:162-183.

Nickel E.H. 1984. The mineralogy and geochemistryof the weathering profile of the teutonic bore Cu-Pb-Zn-Ag sulfide deposit. *Journal of Geochemical Exploration*, **22**:239-264.

Nordstrom D.K. 2011. Mine Waters: Acidic to circumneutral. *Elements*, **7**(6):393-398.

Oliveira N.M. 1991. *Caracterização mineralógica e geoquímica dos gossans portadores de ouro da região de São Bartolomeu-GO*. MS Dissertation, Universidade de São Paulo, São Paulo, 120 p.

Oliveira S.M.B., Silva .M.L.M., Toledo M.C.M. 1995. The role of residual 2:1 phyllosilicates in lateritic metallogenesis: Ni and Cu deposits in Serra dos Carajás, Brazilian Amazônia. *Geochimica Brasiliensis*, **9**(2):161-171.

Peterson R.C., Williamson M.C., Rainbird R.H. 2014. Gossan Hill, Victoria Island, Northwest Territories: An analogue for mine waste reactions within permafrost and implication for the subsurface mineralogy of Mars. *Earth and Planetary Science Letters* **400**:88-93.

Pires G.L.C., Renac C., Bongiolo E.M., Neumann R. 2020. Gossan mineralogy, textures, and gold enrichment over the Au (As, Bi, Ag) deposit in the Buracão Area (Brasília Fold Belt, Brazil): Implications for gold prospecting in weathering profiles. *Journal of Geochemical Exploration*, **218**:106615.

Porto C.G. 2016. Geochemical exploration challenges in the regolith dominated Igarapé Bahia gold deposit, Carajás, Brazil. *Ore Geology Reviews*, **73**:432-450.

Price J.R., Velbel M.A., Patino L.C.. 2005. Rates and time scales of claymineral formation by weathering in saprolitic regoliths of the Southern Appalachians from geochemical mass balance. *Geological Society of America Bulletin*, **117**:783-794.

Reich M., Vasconcelos P.M. 2015. Geological and economic significance of supergene metal deposits. *Elements*, **11**:305-310.

Reich M., Palacios C., Vargas G., Luo S., Cameron E.M., Leybourne M.I., Parada M.A., Zúñiga A., You C.F. 2009. Supergene enrichment of copper deposits since the onset of modern hyperaridity in the Atacama Desert, Chile. *Mineralium Deposita*, **44**(5):497-504.

Reis F.N., Villas R.N.N. 2002. Mineralização e alteração hidrotermal no depósito cupro-aurífero de Serra Verde, Província Mineral de Carajás. *Revista Brasileira de Geociências*, **31**:69-86.

Robb L. 2005. *Introduction to ore-forming processes*. Blackwell Publishig, Oxford, 373 p.

Scott K.M., Ashley P.M., Lawie D.C. 2001. The geochemistry, mineralogy and maturity of gossans derived from volcanogenic Zn–Pb–Cu deposits of the eastern Lachlan Fold Belt, NSW, Australia. *Journal of Geochemical Exploration*, **72**(3):169-91.

Silva E.R.P. 1996. Geologia e geoquímica das mineralizações supergênicas de ouro de ouro das áreas Salobo e Pojuca – Leste Serra dos Carajás. PhD Thesis, Universidade Federal do Pará, 217 p.

Silva E.R.P., Kotschoubey B. 2000. Alteração supergênica do depósito de cobre-ouro do Salobo, Serra dos Carajás-PA - ênfase no comportamento do cobre. *Revista Brasileira de Geociências*, **30**:623-630.

Silva M.G., Teixeira J.B.G., Pimentel M.M., Vasconcelos P.M., Arielo A., Rocha W.J.S.F. 2005. Geologia e mineralizações de Fe-Cu-Au do Alvo GT46 (Igarapé Cinzento, Carajás). In: Marini, O.J., Queiroz, E.T., Ramos, B.W. (eds.), Caracterização de Depósitos Minerais em Distritos Mineiros da Amazônia, ADIMB, p. 94-151.

Silva C.M.D., Villas, R.N. 1998. The Águas Claras C-sulfide Au deposit, Carajás Region, Pará, Brazil: Geological setting, wall-rock alteration and mineralization fluids. *Revista Brasileira de Geociências*, **28**:215-326.

Siqueira J.B., Costa J.B.S. 1991. Evolução geológica do duplex Salobo-Mirim. In: Simpósio de Geologia da Amazônia, Belém, 3, p 232-243.

Smith R.E., Sing B. 2007. Recognizing, in lateritic cover, detritus shed from the Archaean Gossan Hill Cu–Zn–Au volcanic-hosted massive sulphide deposit, Western Australia. *Geochemistry: Exploration, Environment, Analysis*, **7**:71-86.

Soares A.D.V., Macambira J.M.B., Vieira E.A.P., Massoti F.S., Souza C.I.J., Padilha J.L., Magni M.C.V. 2001. Depósito Cu (Au) Cristalino, Serra dos Carajás, PA: idade da mineralização com base em análises Pb-Pb em sulfetos (dados preliminares). In: Simpósio de Geologia da Amazônia, Belém.

Stavinga D., Jamieson H., Layton-Matthews D., Paradis S. Falck H. 2017. Geochemical and mineralogical controls on metal(loid) mobility in the oxide zone of the Prairie Creek Deposit, NWT. *Geochemistry: Exploration, Environment, Analysis*, 17(1):21-33.

Tallarico F.H.B., Figueiredo B.R., Groves D.I., Kositcin N., McNaughton N.J., Fletcher I.R., Rego J.L. 2005. Geology and SHRIMPU–Pb geochronology of the Igarapé Bahia Deposit, Carajás Copper–Gold Belt, Brazil: an Archean (2.57 Ga) example of iron–oxide Cu–Au–(U–REE) mineralization. *Economic Geology*, **100**:7-28.

Taylor G.F. 1984. Gossan profiles developed above stratabound sulphide mineralization. *Journal of Geochemical Exploration*, **22**:351-352.

Taylor R. 2011. *Gossans and leached cappings field assessment*. Springer, Townsville.

Taylor G.F., Appleyard E.C. 1983. Weathering of the zinc-lead lode, Dugald River, North-west Queensland: I The gossan profile. *Journal of Geochemical Exploration*, **18**:7-110.

Taylor G.F., Thornber M.R. 1992. Gossan and Ironstone Surveys In: Butt C.R.M., Zeegars, H. Editors (eds.). *Handbook of Exploration Geochemistry*. vol. 4. Regolith Exploration Geochemistry in Tropical and Subtropical Terrains. Amsterdam: Elsevier p. 139-202.

Teixeira P.C., Donagemma G.K., Fontana A., Teixeira W.G. 2017 Manual de métodos de análise de solo. 3. ed., Brasília, Embrapa.

Thornber M.R., Taylor G.F. 1992. The mechanisms of sulphide oxidation and gossan formation In: Butt C.R.M., Zeegars, H. Editors (eds.) *Handbook of Exploration Geochemistry* 4 p. 119-138.

Toledo-Groke M.C.M., Prost D., Ildefonse P., Melfi A.J., Delvigne J., Parisot J.C. 1985. Alteração dos minerais na zona supérgena da formação cuprífera do Salobo 3A (Serra dos Carajás) – Localização do cobre nos produtos secundários. *Revista Brasileira de Geociências*, **15**:293-299.

Torresi I., Xavier R.P., Bortholoto D.F.A., Monteiro L.V.S. 2012. Hydrothermal alteration, fluid inclusions and stable isotope systematics of the Alvo 118 iron oxide–copper–gold deposit, Carajás Mineral Province (Brazil): Implications for ore genesis. *Mineralium Deposita*, **47**:299-323.

Vasconcelos P.M., Reich M., Shuster D.L. 2015 The paleoclimatic signatures of supergene metal deposits. *Elements*, **11**(5):317-322.

Veiga M.M., Schorscher H.D., Fyfe W.S. 1991. Relationship of copper with hydrous ferric oxides: Salobo, Carajás, PA, Brazil. *Ore Geology Reviews*, **6**:245-255.

Velasco F., Herrero J.M., Suárez S., Yusta I., Alvaro A., Tornos T. 2013. Supergene features and evolution of gossans capping massive sulphide deposits in the Iberian Pyrite Belt. *Ore Geology Reviews*, **53**:181-203.

Volp K., Evins P., Meffre S. 2006. EPMA and LA-ICPMS dating of hydrothermal REE-minerals from the Estrela Copper Deposit, Carajás, Brazil. Goldschmidt Conference Abstracts, New York, Elsevier, 70.

White A.F., Brantley S.L. 2003. The effect of time on the weathering of silicate minerals: why do weathering rates differ in the laboratory and field? *Chemical Geology*, **202**(3-4): 479-506.

White A.F., Blum A.E. 1995. Effects of climate on chemical weathering in watersheds. *Geochimica et Cosmochimica Acta*, **59**:1729-1747.

Yesares L., Sáez R., Ruiz A.G., Nieto J.M., Gómez C., Ovejero G. 2017. Mineralogical evolution of the Las Cruces gossan cap (Iberian Pyrite Belt): From subaerial to underground conditions. *Ore Geology Reviews*, **80**:377-405.

ANEXO A – CONFIRMAÇÃO DE SUBMISSÃO AO GEOCHEMICAL JOURNAL

UFPA

Pabllo Henrique Costa dos Santos <phsantos@ufpa.br>

[GJ] Submission Confirmation for Geochemical and isotopic fractionation in the hypogene ore, gossan, and saprolite of the Alvo 118 deposit: Implications for Cu-Au exploration in regoliths of the Carajás

2 mensagens

Geochemical Journal Editorial Office <em@editorialmanager.com> 16 de novembro de 2022 23:07
Responder a: Geochemical Journal Editorial Office <gj@geochem.jp>
Para: Pabllo Henrique Costa dos Santos <phsantos@ufpa.br>

Dear Mr Santos,

Your submission entitled "Geochemical and isotopic fractionation in the hypogene ore, gossan, and saprolite of the Alvo 118 deposit: Implications for Cu-Au exploration in regoliths of the Carajás" has been received by journal Geochemical Journal

You will be able to check on the progress of your paper by logging on to Editorial Manager as an author. The URL is https://www.editorialmanager.com/gj/.

Your manuscript will be given a reference number once an Editor has been assigned.

Thank you for submitting your work to this journal.

Kind regards,

Geochemical Journal

UNIVERSIDADE FEDERAL DO PARÁ
INSTITUTO DE GEOCIÊNCIAS
PROGRAMA DE PÓS-GRADUAÇÃO EM GEOLOGIA E GEOQUÍMICA

UNIVERSIDADE FEDERAL DO PARÁ
PROGRAMA DE PÓS-GRADUAÇÃO EM GEOLOGIA E GEOQUÍMICA
TESE APROVADA COM DISTINÇÃO
Instituto de Geociências

PARECER

Sobre a Defesa Pública da Tese de Doutorado de PABLLO HENRIQUE DOS SANTOS

A banca examinadora da Tese de Doutorado de **PABLLO HENRIQUE DOS SANTOS** orientando do Prof. Dr. **Marcondes Lima da Costa** (**UFPA**), composta pelos professores doutores **Adriana Maria Coimbra Horbe (UNB), Edi Mendes Guimarães (UnB), Luiz Carlos Bertolino (CETEM)** e **Rômulo Simões Angélica (UFPA),** após apresentação da sua tese intitulada "**EVOLUÇÃO SUPERGÊNICA DO DEPÓSITO CUPRÍFERO ALVO 118 - PROVÍNCIA MINERAL DE CARAJÁS**", emite o seguinte parecer:

O candidato realizou sua apresentação de forma clara, bem organizada e segura no tempo estipulado. Na arguição mostrou domínio da temática abordada e respondeu às perguntas formuladas pela banca. O documento de tese foi apresentado na forma de três artigos, sendo um já publicado e um submetido, ambos a periódicos internacionais, e o terceiro artigo ainda não foi submetido. Dessa forma, todos os artigos atendem às exigências básicas para uma tese de doutorado.

A banca levantou alguns pontos relacionados ao documento, principalmente de forma e redação. Não obstante, considera que o tema é de grande importância para a região e para a compreensão tanto dos processos do intemperismo como dos depósitos minerais supergênicos relacionados à região Amazônica.

Finalmente, a banca examinadora decidiu por unanimidade aprovar a tese de doutorado, com **DISTINÇÃO**.

Belém, 15 de dezembro de 2022.

Prof. Dr. Marcondes Lima da Costa (Orientador – UFPA)

Prof.ª Dr.ª Adriana Maria Coimbra Horbe (Membro – UnB)

Prof.ª Dr.ª Edi Mendes Guimaraes (Membro – UnB)

Prof. Dr. Luiz Carlos Bertolino (Membro – CETEM)

Prof. Dr. Rômulo Simões Angélica (Membro – UFPA)